UNIVERSIDADE FEDERAL DO RIO GRANDE DO NORTE
CENTRO DE CIENCIAS EXATAS E DA TERRA
PROGRAMA DE PÓS-GRADUAÇÃO EM GEODINÂMICA E GEOFÍSICA

Crustal and upper mantle shear wave velocity structure and radial anisotropy beneath the Colombian Andes inferred from ambient noise and surface wave tomography

Hugo Esteban Poveda Nuñez

Orientador: Prof. Dr. Jordi Julià Casas

Tese de Doutorado apresentada ao Programa de Pós-Graduação em Geodinâmica e Geofísica da UFRN como parte dos requisitos para obtenção do título de Doutor em Geodinâmica e Geofísica.

Tese N° 53/PPGG
Natal, RN, Agosto de 2018

Crustal and upper mantle shear wave velocity structure and radial anisotropy beneath the Colombian Andes inferred from ambient noise and surface wave tomography

Hugo Esteban Poveda Nuñez

Tese de Doutorado aprovada em 29 de Agosto de 2018 pela banca examinadora composta pelos seguintes membros:

Prof. Dr. Jordi Julià Casas (Orientador) . . . . . DGEF/PPGG/UFRN

Prof. Dr. Walter Eugênio de Medeiros . . . . . DFEG/PPGG/UFRN

Prof. Dr. Francisco Hilário Rego Bezerra . . . . . DG/PPGG/UFRN

Prof. Dr. Marcelo Assumpção . . . . . IAG/USP

Prof. Dr. Germán Prieto . . . . . Dpto. Geociencias/UNAL

Universidade Federal do Rio Grande do Norte - UFRN
Sistema de Bibliotecas - SISBI
Catalogação de Publicação na Fonte. UFRN - Biblioteca Setorial Prof. Ronaldo Xavier de Arruda - CCET

Nuñez, Hugo Esteban Poveda.
Crustal and upper mantle shear wave velocity structure and radial anisotropy beneath the Colombian Andes inferred from ambient noise and surface wave tomography / Hugo Esteban Poveda Nuñez. - 2018.
242f.: il.

Tese (doutorado) - Universidade Federal do Rio Grande do Norte, Centro de Ciências Exatas e da Terra, Programa de Pós-Graduação em Geodinâmica e Geofísica. Natal, 2018.
Orientador: Jordi Julià Casas.

1. Velocidade sísmica - Tese. 2. Tomografia de ruído ambiente - Tese. 3. Vulcanismo relacionado à subducção - Tese. 4. Anisotropia radial - Tese. I. Casas, Jordi Julià. II. Título.

RN/UF/CCET CDU 550.344.094.5

Elaborado por Joseneide Ferreira Dantas - CRB-15/324

Acknowledgments

It is my greatest fortune that professor Jordi Julià has been my thesis supervisor. Without his insightful supervision, confidence and support, I would not have been able to complete this thesis. Thank you.

I also owe much to professor Martin Schimmel for many helpful discussions related to ambient noise studies and for sharing their cross-correlation and stacking codes.

My appreciation also goes to professor Walter Medeiros, for the excellent lessons about inverse problem, which proved fundamental and essential to accomplish my project.

My special thanks to the Brazilian Government and CAPES, for financial support, and granting access to students from various parts of the world to post-graduate education.

To the National Seismological Network of the Colombian Geological Survey for the data granted.

I want to extend my thanks to Flodoaldo Simões, Cicero Costa, Alessandro Dantas, Ana Nemocón, Diogo Coelho, Marcio Barboza, Daniel Evora and Luiz Rodrigo for their friendship, assistance and cooperation during my stay in Natal.

My deep gratitude to my friends and colleagues of the Colombian Geological Survey: Nelson Perez, Viviana Dionicio, Patricia Pedraza, Edwin Mayorga, Juan Carlos Bermudez, Carlos Fajardo, Lina Paola Aguirre, Daniel Martinez, Camilo Muñoz and Santiago Velásquez.

I also thank my family who encouraged during the time of my research. This thesis is very dedicated to my parents Elda and Hugo, who supported me with love and understanding.

Resumo

O objetivo deste trabalho é investigar como os processos relacionados à subducção no noroeste da América do Sul deformam e alteram a composição da placa superior, assim como a relação entre fluidos crustais e vulcanismo ativo/inativo. Para esse fim, este estudo desenvolveu: (1) Correlações cruzadas de ruído sísmico ambiente para os componentes vertical, radial e transversal entre todos os possíveis pares de estações permanentes implantadas pelo Serviço Geológico da Colômbia entre 2012 e 2016, que foram usadas para reconstruir as funções empíricas de Green para ondas Rayleigh e Love na região; (2) Novas medições de velocidade de ondas supeficiais de grupo para ondas Rayleigh e Love a partir de fontes de terremotos regionais e distantes; (3) Novos Mapas de ondas de superfície de fase e grupo entre 7 e 150 s para as ondas Love e Rayleigh, a partir de tomografia de ruído ambiente e ondas de superfície; (4) Novos mapas de velocidad das ondas V_{SV} e V_{SH} para a crosta e manto superior (até 140 km); e, (5) Um modelo 3D de anisotropia radial do noroeste da América do Sul. Os modelos de velocidade da onda S e de anisotropia radial para a crosta e manto superior para o noroeste da América do Sul foram desenvolvidos a partir de 1.300 funções de Green empíricas a partir de correlações cruzadas de ruído ambiente, e de 11.000 percursos de ondas de superfície de fontes de terremotos. As curvas de dispersão de fase e grupo para as ondas Rayleigh e Love foram medidas no intervalo de 7 a 150 s no conjunto de dados total, e invertidas tomograficamente para produzir mapas de fase e de grupo para ondas Rayleigh e Love numa grade de 0.5° x 0.5° para tomografia de ruido sismico e de 1.0° x 1.0° para tomografía de on-

das de superficie. Perfis de velocidade para V_{SV} e V_{SH} en função da profundidade foram construídos a partir da inversão conjunta das curvas de dispersão de grupo e fase em cada nó da grade da tomográfica até 140 km de profundidade.

Os modelos de velocidade revelam zonas de baixa velocidade a 25-35 km de profundidade sob regiões de vulcanismo ativo e inativo, sugerindo a presença de magmas que levam a assinatura da subducção segmentada na placa superior. As regiões de baixa velocidade crustal exibem anisotropia radial negativa ($V_{SH} < V_{SV}$) sob vulcões ativos, sugerindo a presença de diques magmáticos subverticais alimentando o volcanismo, enquanto anisotropia radial positiva ($V_{SH} > V_{SV}$) sob regiões vulcânicas inativas é consistente com o armazenamento de magma em soleiras. A 40 km de profundidade, velocidades baixas sob as cordilheiras Central e Oriental exibem anisotropia radial positiva (até 15%), que é interpretado como armazenamento de magmas relacionados à subducção na crosta inferior. Baixas velocidades da onda S com anisotropia radial positiva são observadas na Bacia Inferior do Magdalena em todos os níveis crustais, o que é consistente com velocidades altas e baixas alternadas dentro do pacote sedimentar, tensões extensionais, cisalhamento sub-horizontal e/ou magmas sub-litosféricos que atravessaram uma placa caribenha fraturada. Em níveis crustais superiores a médios, anisotropia radial negativa e altas velocidades coincidem com os principais terrenos tectônicos (Maciço de Santa Marta, Batólito de Antioquia, Maciço de Santander, Batólito de Ibagué), enquanto a anisotropia positiva e as velocidades baixas caracterizam as principais bacias costeiras (por exemplo, Bacia Inferior do Magdalena, Bacia de Tumaco). Em terrenos tectônicos, a anisotropia negativa pode ser explicada através de tectônica de escape, enquanto a anisotropia positiva sob as bacias costeiras pode ser resultante de uma combinação de soleiras, tectônica extensional e/ou cisalhamento sub-horizontal.

Palavras-chave: Tomografia de ruído ambiente, Tomografia de ondas de superfície, Anisotropia radial, Vulcanismo relacionado à subducção, América do Sul.

Abstract

The objective of this work is to investigate how subduction-related processes in NW South America deform and alter the composition of the overriding plate, as well as the relationship between crustal fluids and active/inactive volcanism. To that end, this study developed: (1) Vertical, radial and transverse ambient seismic noise cross-correlations between all possible pairs of permanent stations deployed by the Colombian Geological Survey between 2012 to 2016, to reconstruct empirical Green's functions for inter-station Rayleigh and Love waves in the region; (2) New surface-wave group-velocity measurements for Rayleigh and Love waves from regional and teleseismic earthquake sources; (3) Surface-wave dispersion maps of phase and group velocity variation between 7 and 150 s for Love and Rayleigh waves; (4) New maps of V_{SV} and V_{SH} velocity at crustal and upper mantle depths (down to 140 km); and, (5) a 3D model of radial anisotropy for NW South America. S-wave velocity and radial anisotropy for the crust and upper mantle under NW South America have been developed from 1,300 empirical Green's functions from ambient noise cross-correlations and from 11,000 fundamental-mode, surface-wave trains from earthquake sources. Phase- and group-velocity curves for Rayleigh and Love waves were measured in the 7-150 s period range from the combined dataset, and tomographically inverted to produce maps of phase- and group-velocity variation in a 0.5° x 0.5° grid for ambient noise and 1.0° x 1.0° for surface waves. V_{SV} and V_{SH} velocity-depth profiles were constructed from the joint inversion of local group and phase dispersion curves at each node in the tomographic grid down to 140 km depth.

The S-velocity models reveal zones of slow velocity at 25-35 km depth under regions of both active and inactive volcanism, suggesting the presence of melts that carry the signature of segmented subduction into the overriding plate. The regions of slow crustal S-velocity display negative radial anisotropy ($V_{SH} < V_{SV}$) under active volcanoes, suggesting the presence of sub-vertical magmatic dykes feeding the volcanics, and positive radial anisotropy ($V_{SH} > V_{SV}$) under inactive volcanic regions, consistent with magma storage along flat-lying sills. At 40 km depth, slow velocities under the Central and Eastern cordilleras display positive radial anisotropy (up to 15%), which is interpreted as storage of subduction-related magmas in the lower crust. Slow S-velocities with positive radial anisotropy are observed in the Lower Magdalena Basin at all crustal levels, consistent with a combination of alternating fast and slow velocities within the sedimentary package, extensional stresses, sub-horizontal shear, and/or sub-lithospheric melts from a fractured Caribbean flat slab. Negative radial anisotropy is also observed under Lower Magdalena Basin at upper mantle levels, coinciding with the location of the Caribbean flat slab. At upper to mid crustal levels negative radial anisotropy and high velocities coincide with major tectonic terrains (Santa Marta Massif, Antioquia Batholith, Santander Massif, Ibague Batholith), while that positive anisotropy and slow velocities characterizes major coastal basins (e.g., Lower Magdalena Basin, Tumaco Basin). In tectonic terrains, negative anisotropy may be explained through escape tectonics, while positive anisotropy under the coastal basins could be resulting from a combination of flay-lying magmatic sills, extensional tectonics, and/or sub-horizontal shear.

Keywords: Ambient noise tomography, Surface wave tomography, Radial anisotropy, Subduction-related volcanism, South America.

Table of Contents

List of figures

List of tables

Chapter 1

Introduction

Subduction is an important tectonic process that plays a major role in the dynamics of the Earth. The sinking of cold oceanic lithosphere into the mantle is associated with extensive recycling of hydrated materials (sediments, hydrated oceanic crust and upper mantle) and the growth of continents (e.g. (Condie 2005)). In addition, subduction zones are sites that are usually related to natural hazards such as volcanic activity, earthquakes, and tsunamis (Turcotte & Schubert 2002). The study of subduction-related processes can also address questions related to the nature of the plate-driving forces, and the mechanism of deformation in the upper plate and its magmatic overprint.

Seismological observations have traditionally provided valuable information about the nature of the crust and underlying mantle (Romanowicz 1991, Rawlinson et al. 2010). They have also been the main tool for exploring the structure of subduction zones at great depths and related processes. In particular, crustal thickness variations, bulk elastic properties, Vp/Vs ratio and P- and S-wave velocity variations and seismic anisotropy have provided important information of tectonic and geological processes all around the planet. For this reason seismologists have dedicated significant time and effort to knowing the internal structure of the Earth.

One of the most important seismological tools to map the structure of the Earth has

been seismic tomography and, perhaps to a lesser extent, seismic anisotropy. In the last decade, improvements in measuring surface-wave dispersion from earthquake-generated surface waves and empirical Green's functions (EGFs) extracted from ambient noise cross-correlations have allowed the crust and lithospheric mantle to be imaged in unprecedented detail. Surface-wave tomography (SWT) has been successfully utilized to image the continental lithosphere at several scales (Feng et al. 2004, Ritsema et al. 2004, Rosa et al. 2016). Tomographic images from naturally-occurring surface-waves, however, rarely provide information at periods shorter than 20 s, which are required to image the upper and middle crust. Fortunately, the cross-correlation of continuous recordings of ambient seismic noise for pairs of stations has recently been shown to be a powerful method for surface-wave imaging at local-to-regional scales (Sabra et al. 2005, Snieder 2004, Bensen et al. 2008, Lin et al. 2008a, Villaseñor et al. 2007). Since both ANT and SWT methods are, in principle, sensitive to the same bulk properties of the solid Earth, combining the two methods to produce measurements in a broad band of frequencies has become an important tool for investigating lithospheric structure as a whole.

In addition, the study of seismic anisotropy allows to learn about the deformation history of the crust and upper mantle, their magmatism, and flow patterns resulting from tectonic processes. In the recent years. it has become popular to investigate the patterns of deformation in the crust through radial anisotropy (Becker et al. 2008). Traditionally, seismic anisotropy studies had utilized SKS phases from distant earthquake sources (Porritt et al. 2014, Bastow et al. 2015, Idárraga-García et al. 2016, Becker et al. 2008), inferring the orientation of anisotropic fabrics in the lithosphere and/or flow patterns in the asthenospheric mantle; most recently, radial anisotropy has been considered for inferring patterns of fluid flow and/or direction of ductile deformation in the crust through the V_{SV} and V_{SH} discrepancy in Rayleigh and Love waves (Das & Rai 2017, Lynner et al. 2018, Spica et al. 2017, Yudistira et al. 2017).

The recent deployment of seismic stations by the Colombian Geological Survey in

the Colombian Andes, and the availability of seismological data from other international networks has allowed the application of several methods to improve our knowledge of the lithospheric structure under northwestern South America (van der Hilst & Mann 1994, Taboada et al. 2000, Corredor 2003, Gutscher et al. 2000, Vargas & Mann 2013, Idárraga-García et al. 2016, Syracuse et al. 2016). Those studies have demonstrated that the geometry of the Nazca and Caribbean plates at depth is complex, as evidenced by the presence of two Wadati Benioff zones displaced ∼250 km from each other at about ∼5.5°N. However, few studies have focused on the structure of the overriding South American plate and the relationships to subduction-related processes. Refraction surveys, for instance, were performed in southern Colombia as part of the Nariño Project (Aldrich et al. 1973, Ocola et al. 1975, Meissnar et al. 1976, Meyer et al. 1976, Mooney et al. 1979), producing a crustal cross-section for the region; and a 1D velocity model for the Colombian crust was developed by Ojeda and Havskov (2001), seeking to improve accuracy in the location of crustal seismicity. On a more regional scale, crustal thickness was surveyed by Poveda et al. (2015), based on receiver functions analysis and a published compilation of crustal thickness observations; and images of lateral P- and S-wave velocity variation between 12.5 and 155 km depth were developed by Syracuse et al. (2016), but interpretations focused on the deep structure. A regional-scale investigation of lateral seismic velocity variation of the overriding South American plate is thus still missing.

The present configuration of the northwestern corner of South America is the result of the interaction between two major oceanic plates (Nazca, Caribbean), and three continental blocks (Northern Andes, Panamá and Maracaibo). The crustal rocks in this corner of the continent keep a record of the amalgamation and disassembly of western Pangaea, pieces of South America rifted away from North America (Spikings et al. 2015). More recently, the collision of the Caribbean province created new crust that was added to the Atlantic margin during Early and Late Cretaceous times (Escalona & Mann 2011), and the subsequent collision of the Panamá arc in western Colombia during Middle Miocene

times (Restrepo & Toussaint 1988, Taboada et al. 2000, Cediel et al. 2003) completed the present make-up of NW South America. These terrains were later reworked and altered by convergence-related processes. The composition of the South America upper plate is presently being deformed by subduction-related volcanism, which reaches as far north as $\sim$5.5°N latitude. Volcanism is active along the Central Cordillera and inactive along the Eastern Cordillera, and is offset at $\sim$5.5°N latitude by $\sim$250 km in the EW direction, following the pattern delineated by intermediate, subduction-related seismicity (Wagner et al. 2017, Pennington 1981).

The NW corner of South America thus constitutes a unique tectonic setting to investigate how subduction-related processes deform and alter the overriding plate, and the relationship between crustal fluids and active/inactive volcanism. Currently, there are no investigations connecting how subduction systems alter and deform the upper plate.

In this study, vertical, radial and transverse ambient seismic noise cross-correlations between all possible pairs of permanent stations deployed by the Colombian Geological Survey between 2012 to 2016 in NW South America were computed to extract empirical Green's functions for inter-station Rayleigh and Love waves in the region, and develop maps of phase and group velocity variation between 7 and 38 s. The resulting ambient noise tomography (ANT) maps were then combined to map radial anisotropy with depth through the Love-Rayleigh wave discrepancy (Lynner et al. 2018, Moschetti et al. 2010a, Spica et al. 2017). Moreover, group-velocity maps in the 40 to 150 s period range were also constructed through surface wave tomography (SWT) of Love and Rayleigh waves from regional and teleseismic sources, and combined with the shorter-period ANT results to develop joint V_{SV} and V_{SH} velocity models at crustal and upper mantle depths (down to 140 km).

Shear velocities show an excellent correlation with surface geology at shallow depths, and reveal low-velocity patterns at mid-crustal depths (25-35 km) that correlate with active and inactive surface volcanism in the central portion of the Eastern Cordillera and the

southern flank of the Central Cordillera, respectively. These low-velocity anomalies are interpreted as magmas derived from the mantle wedge above the Nazca and Caribbean plates. More strikingly, a similar low-velocity anomaly is also observed under the Lower Magdalena Basin, where flat subduction of the Caribbean plate has prevented the occurrence of surface volcanism. We argue that this low-velocity region represents either the signature of fluid expulsion near crustal faults or upwelling magmas from the underlying asthenosphere, which would have breached the flat-subducting Caribbean plate through a preexisting fracture and pond at mid-crustal levels within the overriding plate.

Radial anisotropy reveals positive anisotropy for the upper crust where the principal sedimentary basins (e.g. LMB, TB, EC) are located, coinciding with sub-horizontal layering of Quaternary sedimentary sequences, while negative anisotropy overlaps with active volcanism (CC) and igneous-metamorphic (SMM, SM) terrains. In the middle crust, negative anisotropy regions are found under active volcanic complexes, consistent with storage along sub-vertical magmatic dykes; in contrast, positive radial anisotropy is observed under inactive volcanism along the EC, suggesting storage along flat-lying sills. In the upper mantle negative radial anisotropy under the LMB is found consistent with the proposed extent of Caribbean flat subduction.

This thesis contains six chapters. In Chapter 1 (this chapter), I present the motivation of this research and outline the main results of my investigations. In chapter 2 the Colombian geological and tectonic framework is described. Chapter 3 is dedicated to describing the techniques and methods used in this research. In Chapter 4, published as Poveda et al. (2018), I present the first ambient noise tomography of the Colombian Andes and surrounding regions, and provide a 3-D shear velocity model for the upper and middle crust. In Chapter 5, I determine lateral variations in radial anisotropy from ambient noise and surface wave tomography, and analize the relationship between crustal fluids and active/inactive volcanism under the Colombian Andes. In Chapters 6 and 7, the discussion and concluding remarks are presented, final considerations on the results obtained.

Chapter 2

Geology and Tectonic setting

Northwestern South America corresponds to the area in which the Colombian Territory is located, being limited to the north and west by the Atlantic and Pacific oceans, respectively. The northern Andes extend through Ecuador, Colombia, and Venezuela; in Colombia, they are structured into three main ranges (Eastern, Central and Western Cordilleras) and two intervening valleys (Middle Magdalena Valley, and Cauca-Patia Valley), where the Magdalena and Cauca rivers are respectively located. The Eastern Llanos, an extensive zone with flat and slightly undulating topography located eastwards, is part of the South American shield that extends further toward the Brazilian plains. The Macarena range, a small and isolated range from the Andean Cordillera is found within the western half of the Eastern Llanos. The Caribbean region is a flat area that encompasses a pyramidal structure (Santa Marta Massif) to the north, and where the Magdalena and Cauca rivers come together to flow into the Atlantic Ocean. The presence of a small mountain range (Baudo range) in the western most portion of Colombia, parallel to the Pacific coast, completes the physiographic landscape of the region.

The Northwestern region (Figure 2.1) has undergone significant tectonic deformation over geological time, which resulted from the interaction among three tectonic plates (South American, Nazca and Caribbean), and a number of tectonic blocks (Panama arc,

North Andean and Maracaibo). The Nazca plate is moving east with respect to the South American continental plate at $\sim$5 cm/year (Trenkamp et al. 2002) with a variable angle of subduction between 30° and 40° beneath the NAB, the convergence being accommodated along of Pacific subduction zone, and numerous fault systems along the Andean belts and intervening valleys. Pacific subduction is manifested through active seismicity throughout the region and volcanism in the Central Cordillera between Peru and latitude 5.5°N within Colombia. The Panama arc (also know as Panama-Chocó Block) behaves as a rigid indenter that is in collision with the NAB. As a result, the Panamá arc is under compression and has an ENE movement with respect to the remaining South American continent, indicative of an escape caused by indentation (Freymueller et al. 1993, Trenkamp et al. 2002). The Caribbean plate, on the other hand, is converging at 1-2 mm/yr ESE with respect to South America. Several authors proposed that the Caribbean Plate subducts beneath the North Andean Block at a shallower dip (Mora-Bohórquez et al. 2017, Vargas & Mann 2013, Yarce et al. 2014) without subducted-related volcanism, being responsible for extensional deformation in the Lower Magdalena Basin. Seismicity in this area is reduced with respect to the Pacific region, and active volcanims is absent. The Caribbean plate and NAB interaction place the triangularly-shaped Santa Marta Massif under compression. It has been proposed that this portion of the NAB is a separate tectonic block that accommodates deformation in the area. This postulated block - known as the Maracaibo Block (MaB) – would thus be being expulsed north eastwards with respect to South America as a result of plate convergence (Taboada et al. 2000).

The northern Andes and the Caribbean region behave as a coherent tectonic unit known as the North Andean Block (NAB), which can thus be regarded as a collage of several terrains that accreted against the Guyana Shield at different stages through Earth's history (Restrepo & Toussaint 1988, Cediel et al. 2003). The latest addition to the NAB was the Panamá arc, which includes the Baudó Range, and represents an oceanic arc covered by oceanic sediments (Case et al. 1971, Restrepo & Toussaint 1988, Taboada

et al. 2000, Cediel et al. 2003). The Panamá arc is thus seen as an exotic terrain within the NAB (Duque-Caro 1990, Taboada et al. 2000).

2.1 Geology

The geology of each of the Colombian cordilleras is varied, reflecting the diverse histories of subduction, collision, accretion and uplift that has characterized the western margin of Colombia through the geological ages (Restrepo & Toussaint 1988, Spikings et al. 2015, Cediel et al. 2003). To the west, the Baudo range represents an oceanic, basic and ultramafic magmatic arc covered by oceanic sediments (Case et al. 1971, Restrepo & Toussaint 1988, Taboada et al. 2000). The Western Cordillera is composed by a sequence of allochthonous accreted oceanic mafic and ultra mafic terrains of MORB composition, accreted during Cretaceous and Early Cenozoic times (Weber et al. 2015). The proposed tectonic scenario that gives rise to the geology of the western cordillera and neighboring areas is due to the oblique subduction of the Caribbean Oceanic plateau under South America (Figure 2.2), during the Upper Cretaceous to the Eocene (Pindell & Kennan 2009, Spikings et al. 2015, Weber et al. 2015). Subduction gave rise to an oceanic and continental plutonic arc (Weber et al. 2015).

The Central Cordillera is made of Paleozoic metamorphic rocks with intrusions of Mesozoic and Tertiary plutons of continental affinity, with deposit of Tertiary to Quaternary volcanic and volcano-sedimentary sequences (Bustamante et al. 2016, Restrepo-Moreno et al. 2009). The history of the Central Cordillera maintains a records of the fragmentation of Pangea that ocurred in the lower Triassic (240 ma). This area remained passive until 209 Ma within Pangaea, where a magmatic arc related to the oblique subduction of the Pacific plate (Farallon plate) between early Jurassic to early Cretaceous was originated, accompanied by extensional and retro-arc settings (Figure 2.3) generated by a roll-back of the plate (Spikings et al. 2015, Bustamante et al. 2016). The intense magmatism in the

Jurassic is represented mainly in the Ibague and Segovia (located in the San Lucas range - SLR) batholiths in the Central Cordillera.

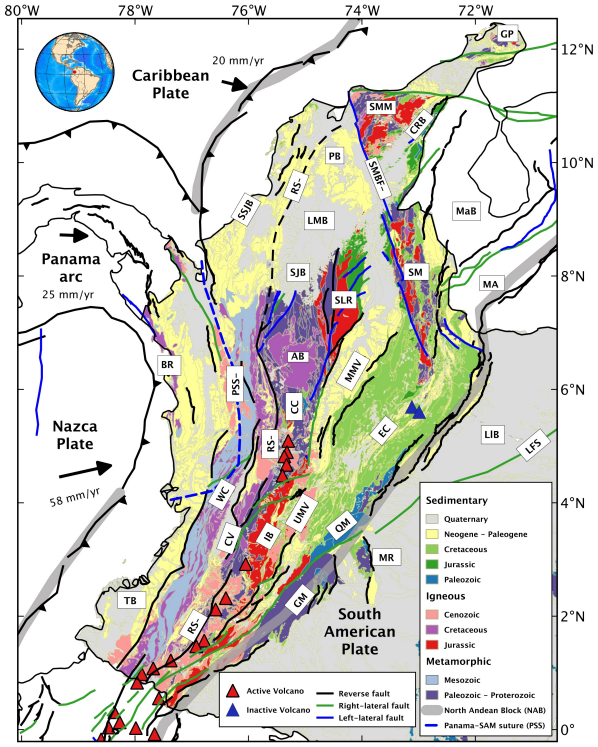

Figure 2.1: Simplified tectonic and geologic setting of the northern Andes. Geologic provinces from Gómez et al. (2007). Major faults from Veloza et al. (2012). Plate motions relative to South America from Trenkamp et al. (2002). Gray thick lines mark the boundary of the North Andean Block (NAB); Area with vertical lines marks the location of the Panamá arc; Red Triangles: Active Volcanoes; Blue triangles: Inactive Volcanoes. The different provinces are: SMM: Santa Marta Massif; Mab: Maracaibo Block; SMBF-: Santa Marta- Bucaramanga Fault; SM: Santander Massif; MA: Merida Andes; SSJB: Sinú and San Jacinto Basin; CRB: Cesár-Rancheria Basic; PB: Plató Basin; LMV: Lower Magdalena Valley; SJB: San Jorgé Basin; SLR: San Lucas Range; AB: Antioqueño Batholith; BR: Baudo Range; MMV: Middle Magdalena Valley; RS-: Romeral Suture; CPB: Panamá-Chocó Block; AB: Antioqueño Batholith; CC: Central Cordillera; EC: Eastern Cordillera; LIB: Llanos Basin; LFS: Llanos Faults system; WC: Western Cordillera; CV: Cauca Valley; IB: Ibagué Batholith; SMV: Superior Magdalena Valley; QM: Quetame Massif; GM: Garzón Massif and CV: Cauca Valley; MR: Macarena Ranges; TB: Túmaco Basin (adapted of Poveda et al. 2018)

The Eastern Cordillera is covered by sequences of continental and marine sediments of several ages and contains Precambrian basement rocks with meta-sedimentary supracrustals of Lower Paleozoic age and oceanic affinity (Gómez et al. 2007). The Eastern Cordillera has been interpreted as a wide Mesozoic extensional basin that was subsequently inverted by Andean compression and orogeny (Dengo & Covey 1993, Egbue et al. 2014). Next to the Eastern Cordillera are the Eastern LLanos, an extensive foreland basin associated to the Andean Orogen that overlays the Guyana craton with Lower Paleozoic and Tertiary sediments (Farris et al. 2011).

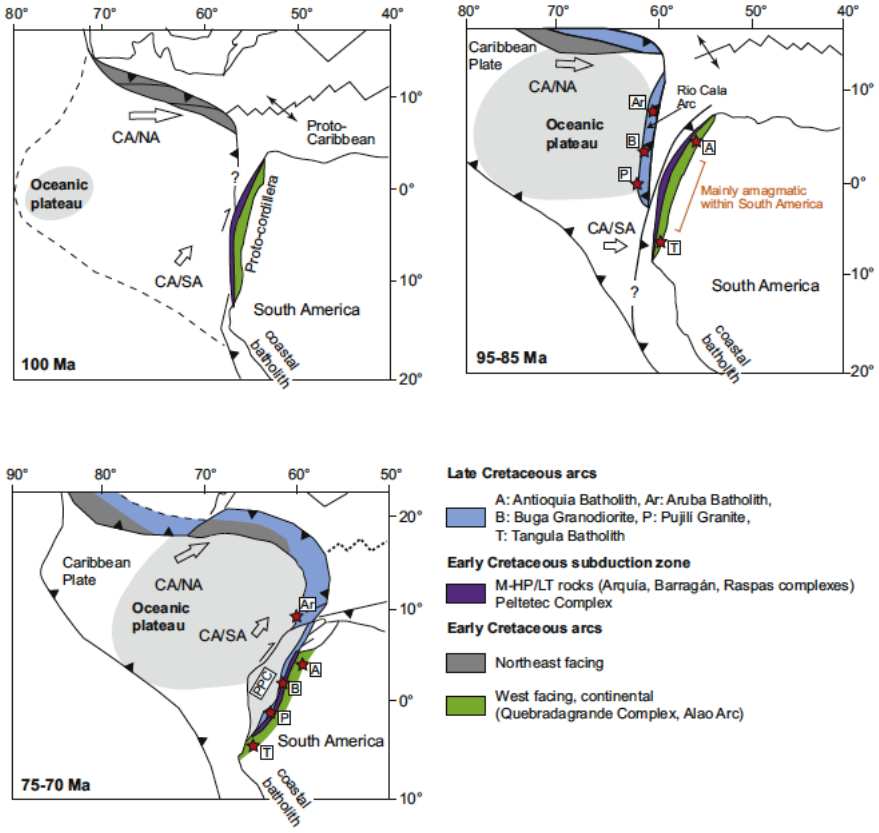

Figure 2.2: Reconstruction for northwestern South America of formation of oceanic plateau and collision and overlying with South America (adapted of Spikings et al. 2015)

The main inter mountain valleys of NW South America include the Cauca-Patia Valley, which divides the Western Cordillera from the Central Cordillera and is made of volcanic and sedimentary rocks of oceanic and continental affinity, and the Middle Magda-

lena Valley, which intervenes between the Central and the Eastern Cordillera and is covered by sequences of continental and marine sediments of several ages (Gómez et al. 2007).

The Caribbean region can be geologically described as an Oligocene-to-Recent forearc basin - the Lower Magdalena Basin (LMB) - overlying the shallowly dipping Caribbean slab (Bernal-Olaya et al. 2015, Mora-Bohórquez et al. 2017). The LMB is in turn composed of several subduction-related basins, such as the Plató, San Jorge, and Sinú-San Jacinto basins, and is bounded to the West by Sinú-San Jacinto fold-and-thrust belt. The Plató and San Jorge basins consist of Paleogene sediments overlying Precambrian and Paleozoic metamorphic basement rocks, while the Sinú–San Jacinto fold-and-thrust belt is regarded as an accretionary wedge that includes rocks of Cretaceous age as well as Tertiary and Quaternary lacustrine sediments. The sedimentary prism making the Sinú-San Jacinto basin extends offshore along the margin of the northern South American Plate, with thicknesses of up to 10 km (Toto & Kellogg 1992, Flinch 2003, Montes et al. 2010, Lara et al. 2013). In the northernmost corner of the northern Andes outcrops the Santa Marta Massif, which includes Jurassic volcanics and Paleozoic metamorphic rocks, along with volcano-sedimentary Cretaceous materials (Cardona et al. 2011).

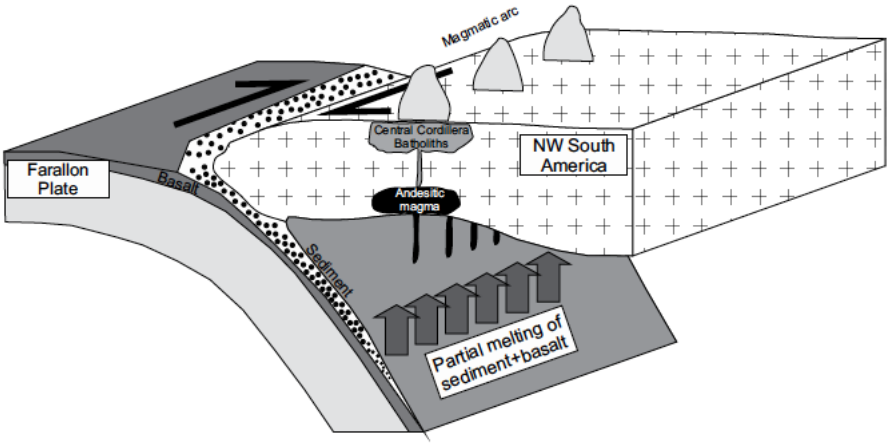

Figure 2.3: Model for the generation of the Early Jurassic to Early Cretaceous magmatic arc in the Northern Andes of Colombia (Adapted of Bustamante et al. 2016).

2.2 Tectonic Setting

Several studies have been conducted in order to investigate the precise contact geometry between the Nazca and Caribbean plates, although this still remains a matter of debate. An initial model was proposed by (Pennington 1981). Through selection of hypocentral locations of earthquakes and focal mechanisms in the region, two distinct segments of subducted lithosphere were identified beneath the Colombian Andes: the Bucaramanga segment, related to subduction of the Caribbean Plate; and the Cauca segment, related to subduction of the Nazca Plate. This implied the existence of a slab tear at depth separating the postulated segments. The Bucaramanga segment would be subducting in the N109°E direction and dipping at 20°-25°, while the Cauca segment would be subducting in the N35°E direction with a 35° dip. Taboada et al. (2000), from seismological data, and seismic tomography among other observations, suggests an overlapping zone between 5.2°N and 7°N between the Nazca Plate and the Paleo Caribbean Plateu (thus called by the authors). This interaction produced a major E-W transpressive shear zone at 5.5°N, where the Bucaramanga seismic nest is located, associated with the Paleo-Caribbean Slab. This hypothesis is adopted by Cortes and Angelier (2003), based on a study of focal mechanisms.

At the same time, from three-dimensional analysis of CMT solutions, Corredor (2003) argues that the limit between Caribbean and Nazca plates is around 10°N. Corredor (2003) proposes, at 5.5°N, a fault zone overlap associated with the termination of volcanism. More recently, Vargas and Mann (2013), from relocated hypocenters, coda-Q tomography and regional magnetic and gravity data, propose that the Caribbean and Nazca plates are separated by a 240 km EW trending slab tear at 5°N latitude - the Caldas tear – separating subduction in the Caribbean and Nazca slabs. Recent tomographic images by Chiarabba et al. (2016) place the tear entirely within the Nazca plate, pushing the boundary of this plate north and implying an EW trending slab torn separating a steeply subducting

segment to the south from a flat subducting segment to the north. The latter is taken into account by Syracuse et al. (2016), from hypocentral relocations, joint inversion of local body wave arrivals, surface-wave dispersion measurements, and gravity data, propose that the region at 5.5°N is a non-overlaping slab tear of the Nazca plate, where intermediate-depth seismicity is shifted 200 km toward the East, beneath the Eastern Cordillera. Within the Nazca flat-slab, north of the slab tear, slab colission at 7.5°N, marks the location of the Bucaramanga seismic nest. This last study is in agreement with Wagner et al. (2017), which is based on observations of seismicity and ages of volcanoes.

In figures 2.5 and2.4 the Taboada et al. (2000) and Syracuse et al. (2016) models are displayed for comparison. Some differences can be observed in the interpretation of the northern limit of the Nazca plate, and the location and origin of the seismicity of the Bucaramanga nest. The two models agree that the Caribbean Plate presents flat subduction, as in most models do.

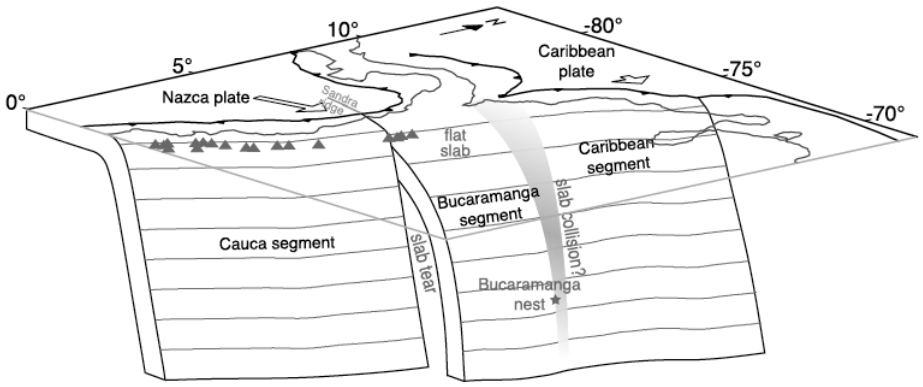

Figure 2.4: 3D schematic of the plate geometry proposed in Syracuse et al. (2016)

2.3 Seismicity

Figure 2.6 displays observed seismicity in NW South America (2011-2015) relocated by Syracuse et al. (2017). The seismicity shows patterns that are related to the main faults

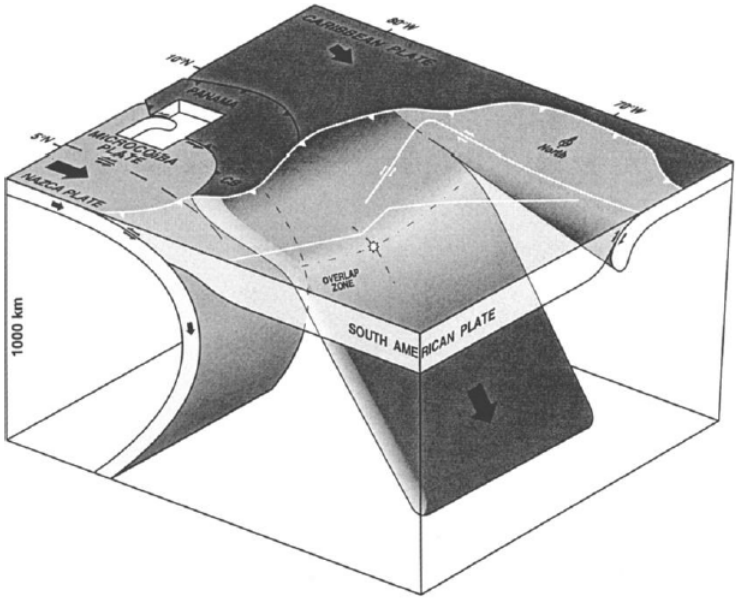

Figure 2.5: 3D schematic of the plate geometry proposed in Taboada et al. (2000)

and tectonic structures: (i) in the center and eastern border of the Eastern Cordillera, between 2°N to 4°N, seismicity concentrates between 0 and 30 km depth; (ii) offshore the Pacific Ocean relatively shallow earthquakes (<60 km) show variations from north to south related to the subducted oceanic crust of the Nazca plate; (iii) intermediate and shallow seismicity is observed in the Darien range in Panamá, which is explained by the interaction of the Chocó-Pánama Block with South America; (iv) finally, there is a concentration of shallow earthquakes along the Salinas fault system, at the middle and Upper Magdalena Valley, which extends to the Santa Marta-Bucaramanga fault.

With the recent expansion of the Red Sismológica Nacional de Colombia (RSNC), a greater number of seismic events have been identified and located in the northern part of Colombia, throughout the Lower Magdalena Valley (LMB) and the Sinú-San Jacinto folded belts. However, the seismicity under the LMB continues to be diffuse, which can be explained by the low rate of convergence between the Caribbean and South American plates (Trenkamp et al. 2002). Also, a mixture of seismicity between 10 and 50 km is observed over the Sierra Nevada de Santa Marta.

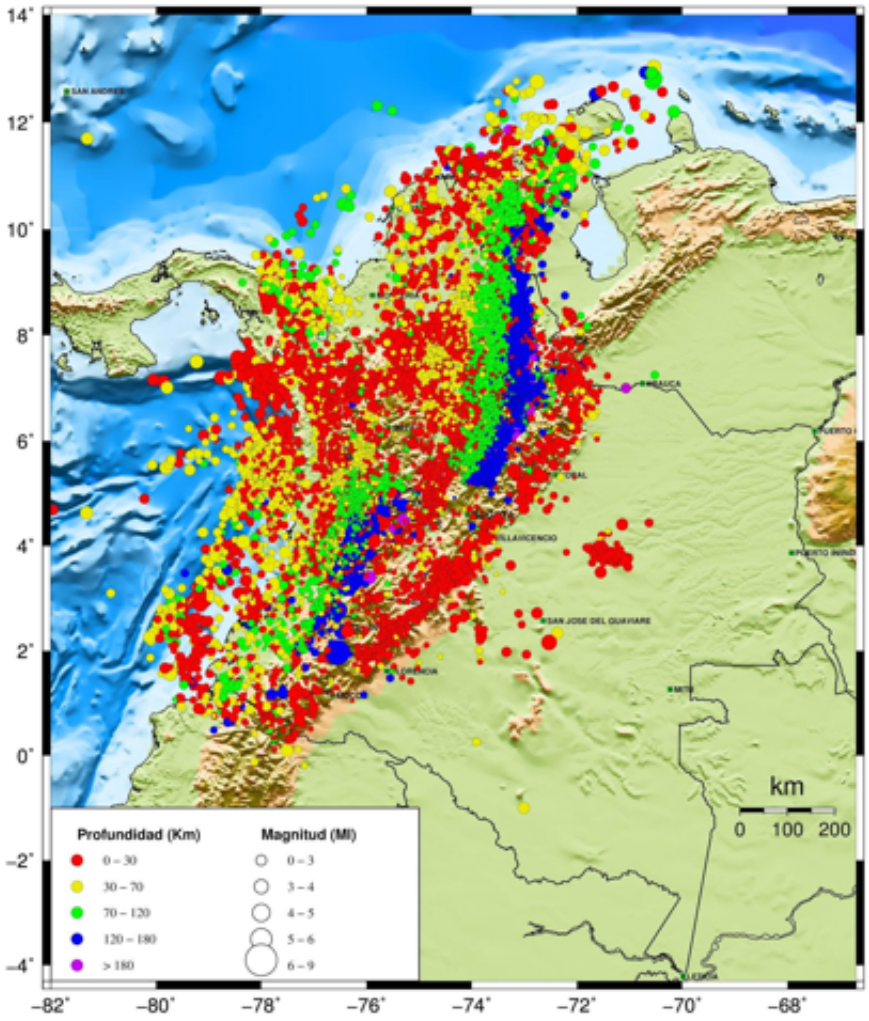

Figure 2.6: Seismicity recorded between 2011-2015, relocated at Syracuse et al. 2016

Regarding intermediate-depth seismicity (60 - 200 km), two patterns are observed associated to the subduction systems in the region. Between 2°N and 5.5°N, under the CC and the CV, seismicity is linked to the subduction of the Nazca plate (Pennington 1981, Taboada et al. 2000, Vargas & Mann 2013). Intermediate seismicity in this area has been interpreted recently as a region with high volumes of dehydrated fluids (Chang et al. 2017). North of 5.5°N and until 11°N, to the east, under the LMB and the EC, there is a second region with intermediate seismicity overlapping with that of the Bucaramanga nest (Zarifi et al. 2007, Prieto et al. 2012), probably associated with Caribbean plate subduction ((Vargas & Mann 2013, Taboada et al. 2000)). North of 5.5N, the seismicity between 2°N-5.5°N seems to be displaced to the east, generating an offset in intermediate-depth seismicity. Recent studies, (Syracuse et al. 2016, Wagner et al. 2017) have proposed that in this region there is a tear ("the Caldas Tear" Vargas and Mann, 2013) of the Nazca plate, extending towards the north and containing the seismicity of the Bucaramanga nest. Different hypotheses have been proposed to explain wether the seismicity north of 5.5°N is related to the Caribbean Plate, the Nazca Plate or an overlap of both (van der Hilst and Mann, 1994, Taboada et al., 2000; Cortés and Angelier, 2005, Vargas and Mann, 2013, Bernal-Olaya et al., 2015a, Chiarabba et al., 2016, Syracuse et al., 2016, Wagner et al., 2017). Finally, for deep seismicity (> 200 km), some events have been recorded in the south of the country, along the border with Perú. These events are associated with the Wadati-Benioff zone of Nazca plate.

Interesting, a cluster of shallow events is observed between ∼71°W and ∼3.8°N. The reported sequence started in 2013 and continueed until 2014. This seismicity has been associated to anthropogenic sources and coincides with an increase in oil production in late 2013 (Gómez-Alba et al. 2016).

Chapter 3

Methods

In this chapter, I present the fundamentals of ambient seismic noise processing to obtain the Empirical Green's function (EGFs) between two receivers. I also review processing techniques used for obtaining surface wave dispersion curves from cross-correlation of seismic ambient noise recordings, followed by inversion procedures to obtain surface-wave velocity maps. These maps were inverted for V_{SV} (from Rayleigh wave), V_{SH} (from Love wave), and the Voigt average and radial anisotropy. These procedures are reviewed, as well.

3.1 Ambient seismic noise

Ambient seismic noise is the ubiquitous signal captured in the seismometers in the absence of seismic events and explosions. In the past, ambient seismic noise was considered unusable, interferring with earthquake signals recorded by seismometers. In the last years, it has been realized that seismic ambient noise due to Earth's surface continuous vibrations over a wide frequency range provides continuous sampling of the Earth's interior at different scales. Ambient noise can provide coherent information for interdisciplinary studies of the Earth. In Seismology, ambient noise can be transformed into a deterministic

seismic responses.

Seismic noise can be induced by natural or anthropogenic sources, containing a wide spectrum of frequencies. The sources that generate noise have different origins, and are classified by their spectral content. The principal sources of ambient noise are generated by pressure fluctuations on the ocean's bottom along the coastlines, interactions of ocean waves traveling in opposite directions, and atmospheric perturbations (Prieto 2012, Bromirski 2009). Microseismic noise can be classified as either primary (single frecuency) and secondary (double frecuency) (Bromirski 2009). Primary microseism propagates periods similar to those of ocean waves (10–20 s), which are generated by ocean gravity waves near the coast, while secondary microseism is generated by the nonlinear interaction between direct and reflected ocean waves at a period band of 5-10 s (Tanimoto 2007). Higher frequencies have a local origin, closer to the sensor, and their generation is usually related to anthropogenic activities (e.g., machinery, explosions, etc.). In the absence of anthropogenic sources and earthquakes, simple and double frequency microseismic noise are clearly observed. Figure 3.1 shows the probability density function for station Prado (PRA) located in the Eastern Cordillera; high probability occurs in a band between 1 and 10 s, where the sources of the microseismic noise dominate. Note how the ambient noise signal falls within the HNM and LNM standard noise curves of (McNamara 2004).

Micro-seismic peaks can be considered as constituted mainly by surface waves. Changes in the oceans' levels as ocean waves propagate across them, produce pressure differences in the seabed that generate Rayleigh and Love surface waves. This occurs because the seismic noise is excited by shallow sources (Bromirski 2009). However, global body waves can be generated by storms over the oceans, propagating through the Earth's mantle and reflecting at major interfaces (Prieto 2012). By utilizing the correlation of ambient noise recordings, the dispersive nature of the surface waves can be extracted and used to obtain the shear wave velocity at varying depths and scales.

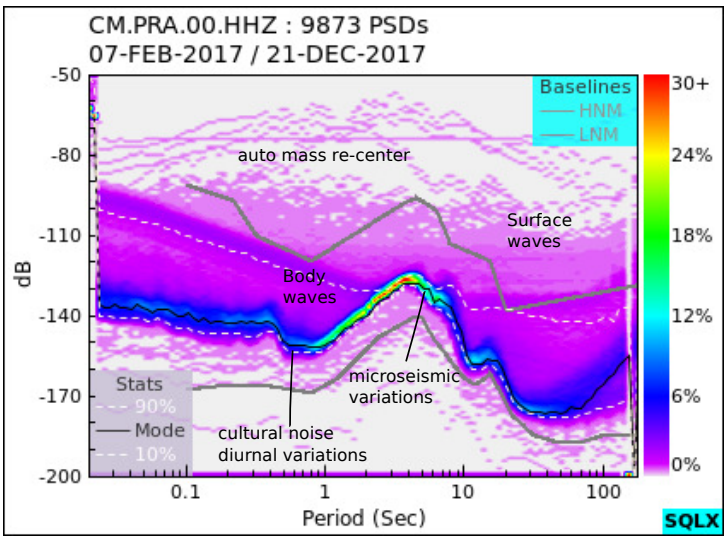

Figure 3.1: Probability Density Function for station Prado (PRA), located in the Eastern Cordillera, for 2017.

3.2 Seismic imaging with ambient noise

The pioneering work of Aki (1957) showed that it is possible to obtain the phase velocity of the surface waves under a seismic array from ambient noise. The technique, known as the SPatial AutoCorrelation method (SPAC) (Aki 1957), makes use of the frequency wavenumber (f-k) filtering of (Capon 1973) to obtain the dispersion relation and investigate the shallow S-wave velocity structures from recordings of ambient noise. Later on, Claerbout (1968) proposed that the temporal average of this spatial correlation could be used to retrieve the very impulse response itself. Based on these ideas, Campillo and Paul (2003), Shapiro and Campillo (2004) and Shapiro et al. (2005), presented a tomographic model of the upper and middle crustal using the long-term correlations of ambient noise recordings between station pairs. The approach was supported by the assumption that the surface wave Green's function between two stations could be extracted from cross-correlations of a diffusive wavefield (Weaver & Lobkis 2002) recorded simultaneously at several stations pairs. The empirical Green's functions are composed by the surface waves packets because the noise sources occur at shallow depths, with more energy in the

fundamental mode.

The emergence of the Green's function from the cross-correlation of simultaneously recorded ambient noise records is based on the assumption of an homogeneous distribution of noise sources and the proportionality of the cross-correlation to the Green's function (Weaver & Lobkis 2002, Snieder 2004). This is a complete Green's function of the medium that is symmetric in time, including all reflections, propagation modes and scattering.

The cross-correlation $C(\tau)$ is a quantitative measure of the similarity between two time series, $f(t)$ and g(t). The cross-correlation is defined as

$$C(\tau) = \langle f(t) * g(t) \rangle = \int_{-\infty}^{\infty} f(t)g(t+\tau)dt, \tag{3.1}$$

where t is time, and τ is the lag time of $g(t)$ with respect to $f(t)$. The cross-correlation between seismic recordings of ambient noise generated by independent sources, is described as (Wapenaar et al. 2010):

$$C(t) = G(r_B, r_A, t) + G(r_B, r_A, -t) \propto \langle p(r_B, t) * p(r_A, -t) \rangle, \tag{3.2}$$

where $G(r_B, r_a, t)$ is the Green's function between r_A and r_B, and $p(r,t)$ is the wave-field function describing the noise at r and at time t. Thus, by cross-correlating traces of seismic noise recorded at two receivers on the surface, it is possible to build the wave-field as if there were a source in one of the receiver's locations (Wapenaar et al. 2010). Accordingly, with seismic array deployments at the surface, noise can be cross-correlated for each sensor pair, as if each of them were a virtual source.

Green's function retrieval from cross-correlations between stations pairs thus relies on some measure of similarity between continuous seismic signals from different noise sources recorded at each station. There are several methods for calculating this similarity, such as the correlation (Bensen et al. 2007) and coherency (Prieto et al. 2009) functions.

The most commonly used in ambient noise tomography is the correlation function.

3.3 Ambient noise data processing

3.3.1 Preprocessing, time and frequency-domain normalization

The processing of ambient seismic noise to retrieve the empirical Green's function can be divided into three stages: 1) preprocessing, 2) cross correlation, and 3) stacking. The aim of the preprocessing stage is to decrease the influence of earthquake signals and instrumental irregularities from the time series prior to cross correlation, the ambient noise bandwidth. It begins with cutting the continuous recordings into non-overlapping, 1 day-long segments, which are then demeaned, detrended, and tapered. Instrumental responses are deconvolved from the daily time series, bandpass-filtered between 0.01 and 0.2 Hz, and decimated to 1 sample per second. Time- and frequency-domain normalization is then applied to remove the signature of seismic waveforms within the frequency band of interest. Time-domain normalization is implemented through 1 bit normalization, preserving the phase and neglecting amplitude variations within the time series (Bensen et al. 2007, Larose 2004); frequency-domain normalization or spectral whitening is implemented through normalization of spectral amplitudes to a unit value without altering the phase, effectively broadening the frequency band of the ambient noise recordings (e.g., Bensen et al. 2007). After time-frequency normalization is applied to all 1 day long segments, cross correlations are computed in the time domain for all station pairs for frequencies between 0.01 and 0.2 Hz. Figure 3.2 illustrates the preprocessing steps for the San Jacinto station located in the Lower Magdalena Basin (LMB).

After preprocessing, the horizontal components (N, E) must be rotated into the great-circle-path according to inter-station orientations, in order to produce the radial (R) and transverse (T) components. The pre-processed traces are finally cross-correlated in the time domain to develop vertical-vertical (ZZ) and radial-radial (RR) cross-correlations,

related to Rayleigh wave energy, and transverse-transverse (TT) cross-correlations, associated to Love wave energy (see figure 3.4).

3.3.2 Cross-correlations and stacking

The next stage in the data processing consists of obtaining the daily cross-correlations for all possible station pairs. To that purpose, it was used the geometrical normalized cross-correlation (CCGN). This method is insensitive to amplitude changes between data sets, but is biased towards the large amplitude portions within the considered correlation windows (Schimmel 1999). It is defined as:

$$C_{CCGN}(t) = \frac{\sum_{\tau=\tau_0}^{\tau_0+T} u_1(t+\tau)u_2(\tau)}{\sqrt{\sum_{\tau=\tau_0}^{\tau_0+T} u_1(t+\tau)^2 \sum_{\tau=\tau_0}^{\tau_0+T} u_2(\tau)^2}}, \tag{3.3}$$

where u_1 and u_2 are the seismic noise recordings, and τ, T and t are the lag time, the correlation window length and the time sample, respectively. Throughout this work, a $T = 86400$ s and lag-times of -1000 to 1000 s were used.

Individual cross-correlations are then stacked into average cross-correlation functions representing each Julian day to improve signal-to-noise ratio (Bensen et al., 2007). Stacking of the calculated ambient-noise cross-correlations was achieved through the time-frequency phase-weighted stack (tf-PWS) of (Schimmel et al. 2011). The tf-PWS is an improvement with respect to the original phase weighted stack (PWS) developed by (Schimmel & Paulssen 1997). The original PWS performed the stacking after weighting each sample of the linear stack with a measure of coherence independent of amplitude, as defined by the instantaneous phase of the analytic signal. The time domain PWS is expressed as

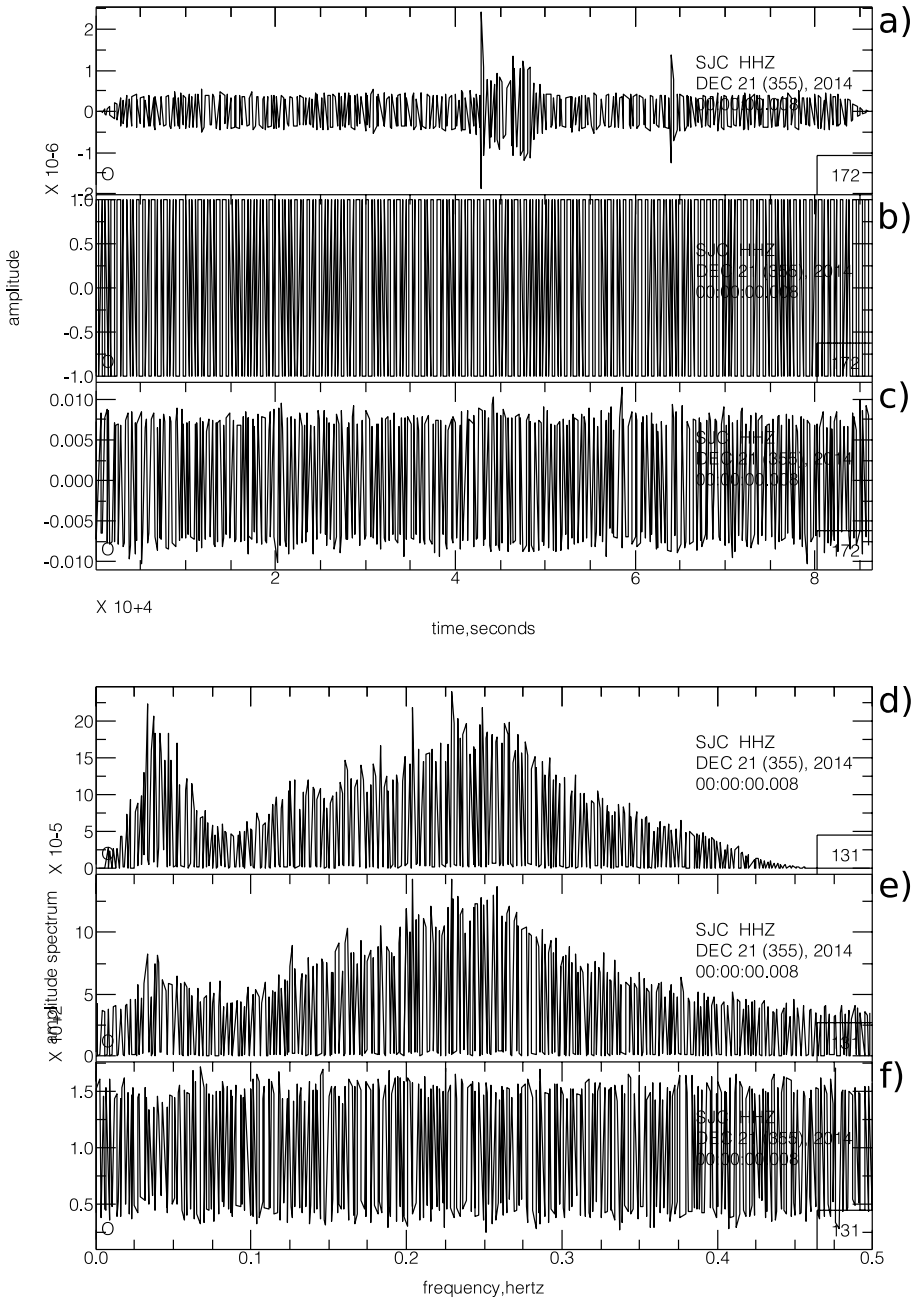

Figure 3.2: Illustration of pre-processing steps with ambient seismic noise recordings at station SJC. a), b) and c) display the raw data (resampling, demeaned and detrended), one-bit normalization, and spectral whitening in the time domain, respectively, for a 1 day-long time series recorded on the vertical component of station SJC; d), e) and f) display the same time series as in a), b) and c) Fourier-transformed into the frequency domain. The final trace used for cross-correlation is shown in panel c). The 1 day-long time series was recorded on 21/12/2014. Note how the spurious signals (earthquakes) in the original waveform disappear after the pre-processing steps.

$$g(t) = \frac{1}{N}\sum_{j=1}^{N} S_j(t) \left| \frac{1}{N}\sum_{k=1}^{N} e^{i\phi_k(t)} \right|^{\nu}, \tag{3.4}$$

where N is the number of stacked traces, S_j is the j-th trace to be stacked, $\phi(t)$ the instantaneous phase of the trace (Bracewell 1965), and ν is the power intensity of the phase-weight.

The tf-PWS makes use of the S-transform (Stockwell et al. 1996) to obtain a time-frequency representation for each cross-correlogram, so that the stacking is controlled with frequency-dependent resolution while maintaining a close relationship between the time-averaging and the Fourier spectrum (Stockwell et al., 1996). The tf-PWS phase stack analogy with the PWS phase stack is defined as:

$$c_{ps}(\tau, f) = \left| \frac{1}{N}\sum_{j=0}^{N} \frac{S_j(\tau, f) e^{i2\pi f\tau}}{|s_j(\tau, f)|} \right|^{\nu}, \tag{3.5}$$

where $S_j(\tau, f)$ is the S-transform of the j-th cross-correlogram and ν is a value that adjusts coherent and less coherent signal stacking. The tf-PWS is obtained through the product of the phase stack $c_{ps}(\tau, f)$ and the S-transform of the linear stack $S_{ls}(\tau, f)$ of the N-daily cross-correlations,

$$S_{pws}(\tau, f) = c_{ps}(\tau, f)^{\nu} S_{ls}(\tau, f). \tag{3.6}$$

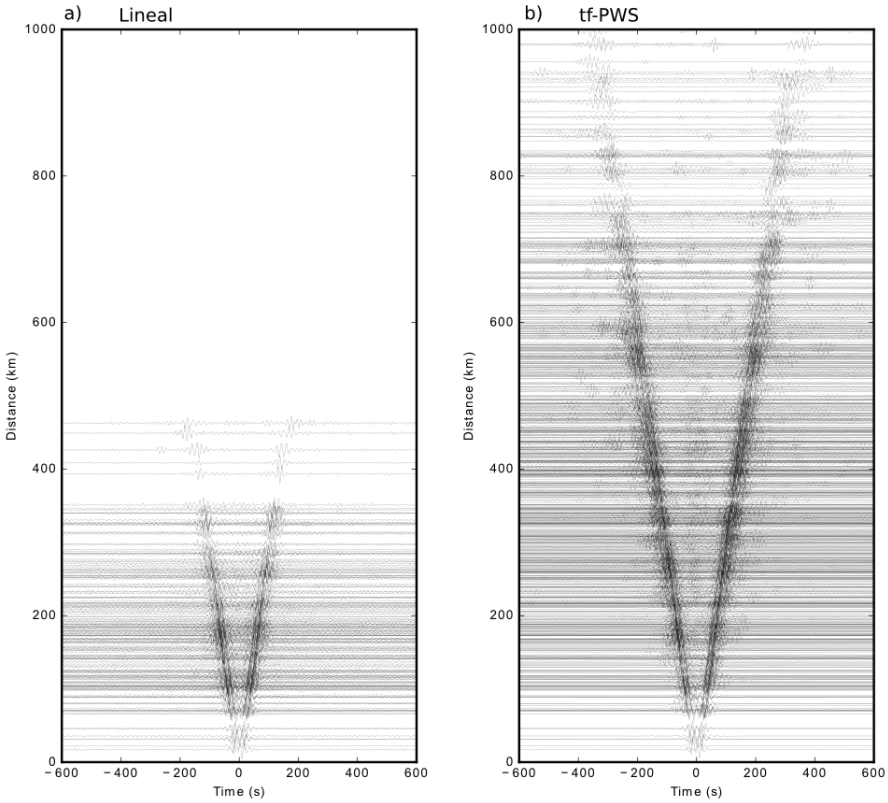

Figure 3.3: Extracted Rayleigh waves from ambient noise for the all stations with SNR > 20. All traces are band-pass filtered between 10 and 50 s and normalized. Left panel displays those cross correlations that were linearly stacked; right panel, cross correlations stacked with tf-PWS.

The $c_{ps}(\tau, f)$ weights the coherent portions of the linear stack in the time-frequency domain (Schimmel et al. 2011). The time–frequency dependent phase coherence attenuates incoherent noise, because it allows for the determination of weak amplitude signals that are more phase-coherent than the background noise. Signals obtained with this method have a signal-to-noise ratio (SNR) greater than those obtained with conventional methods (e.g. the classical correlation and stack method) (Bensen et al. 2007, Lin et al. 2008b, Villaseñor et al. 2007, Yang et al. 2007). Figure 3.3 shows the Rayleigh wave cross-correlations with SNR greater than 20 computed with linear and tf-PWS. Note that, for this value of SNR, half of the cross correlations calculated with the linear stack are lost.

Figure 3.4 displays the final cross-correlation stacks for Rayleigh (ZZ, RR) and Love waves (TT).

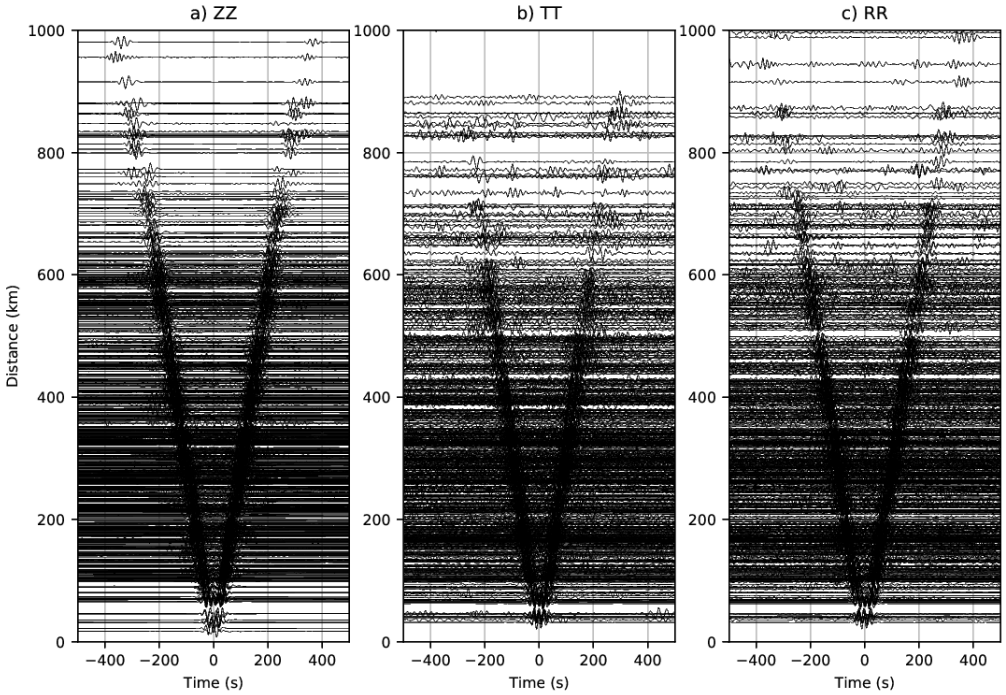

Figure 3.4: Rayleigh and Love waves extracted from ambient seismic noise for all station pairs. a) and c) Rayleigh wave; b) Love wave

3.4 Group and phase velocity estimation

3.4.1 Frequency Time ANalysis (FTAN) method

The empirical Green's functions from ambient noise cross-correlation are dominated by energy that is propagated as surface waves (Shapiro & Campillo 2004). Therefore, we can apply the time-frequency analysis (FTAN) of (Levshin & Ritzwoller 2001) to determine group velocity. This approach is constructed by applying a series of narrow bandpass filters to the signal, to then retrieve the group delay at each frequency by tracing the maximum of the signal envelope. The FTAN method also includes a phase-matched filter (Herrin & Goforth 1977) that cleans dispersion curves from multi-pathed signals.

One major advantage is that the procedure can be easily automated.

Dispersion measurements are obtained by considering the analytic signal in the frequency domain,

$$s(t) = f(t) + iH[f((t)] = A(t)e^{i\phi(t)}, \tag{3.7}$$

where $H[f(t)]$ is the Hilbert transform of $f(t)$, $A(t)$ is the envelope, and $\phi(t)$ is the instantaneous phase. To build a frequency-time function, Gaussian filters are applied to the analytic signal,

$$G_n(\omega) = e^{-\alpha(\frac{\omega-\omega_n}{\omega_n})^2}, \tag{3.8}$$

where ω_n is the central frequency and α is a tunable distance-dependent parameter that defines the width of the filter. The filtered analytical signal is then transformed back into the time domain through an inverse Fourier transform:

$$s(\omega_n, t) = \frac{1}{2\pi}\int_{-\infty}^{\infty} G_n(\omega)S(\omega)e^{i\omega t}d\omega, \tag{3.9}$$

where $S(\omega)$ is the Fourier transform of $s(t)$, defined as $S(\omega) = \int_{-\infty}^{\infty} s(t)e^{i\omega t}dt$.

Group velocity is taken from the 2D envelope function $|A(t,\omega_n)|$. In particular, the group delay time, $t(\omega_n)$, is determined from the envelope peak, so that group velocity is calculated as

$$U(\omega_0 = r/t(\omega_0)), \tag{3.10}$$

where r is the distance between stations. Group velocity estimation is improved if the instantaneous frequency $\omega = |d\phi(t,\omega_0/dt)|_{t=t(\omega_0)}$ is used instead of the central frequency

(Bensen et al. 2007).

Phase velocity, on the other hand, is measured using the method outlined in (Lin et al. 2008a), by which the phase velocity φ at a given period can be calculated from the equation

$$\varphi = kr + \omega t + \lambda + 2\pi N + \frac{\pi}{2} + \frac{\pi}{4}, \tag{3.11}$$

where k is the wave number, r is the interstation distance, ω is the instantaneous frequency, t is the observed group-delay time, λ is the source phase or initial phase, and $2\pi N$ represents the phase ambiguity (with $N = 0, \pm 1, \pm 2, ...,$). The additional $\pi/2$ phase represents the phase shift from the negative time derivative, and the $\pi/4$ phase arises from interference of the non-stationary terms in a homogeneous noise source distribution (Lin et al. 2008a, Snieder 2004). The phase ambiguity $2\pi N$ is assessed by comparing the long-period phase velocity measurements to a reference curve, which is based on the preliminary Earth model of (Dziewonski & Anderson 1981). A detailed example of FTAN processing is displayed in figure 3.5.

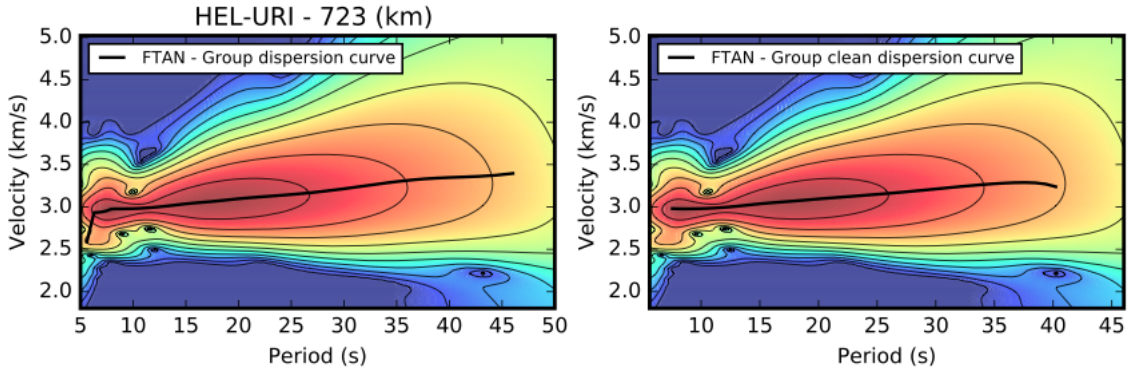

Figure 3.5: Example of frequency-time analysis (FTAN) showing Rayleigh wave group velocity after phase-match filtering for the raypath between stations HEL and URI (723 km).

3.4.2 Multiple Filter Analysis (MFA)

To develop dispersion measurements from earthquakes sources, the instrumental response was first removed from the recorded waveforms, which were then converted to displacement, demeaned, detrended and re-sampled to one sample per second. The best way to assess the effect of noise in a signal is to look at the seismograms over a range of frequencies. Thus, plotting the observations for a range of frequency bands is a good first step for finding reliable dispersion curves. An example is shown in figure 3.6.

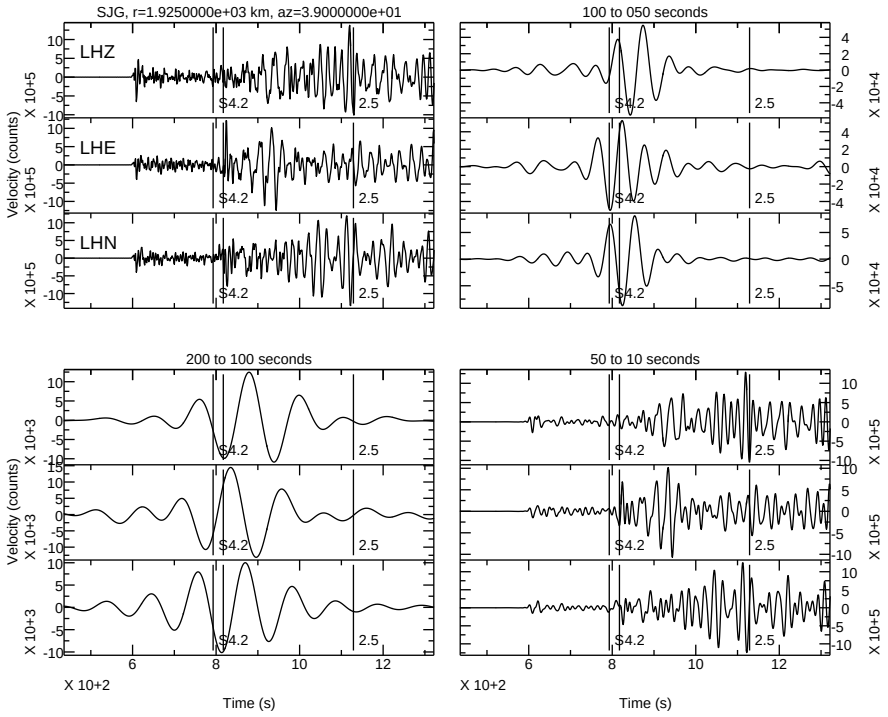

Figure 3.6: Example for an event near the west coast of Colombia (15/11/2004 09:02:00, Mw = 7.2) recorded at station SJG, in the Caribbean region (1924 km). The panel in the upper left is unfiltered and the title in that panel lists the distance (r) and the azimuth of the seismometer. The other three panels show the results of band-pass filtering the seismograms using a four-pole, two-pass Butterworth filter for different period ranges. The corner periods of the filters are shown above each panel. The data units are counts, which for most sensors indicates that a velocity seismogram is shown.

Dispersion was measured through the Multiple Filter Analysis (MFA) of (Dziewonski et al. 1969), as implemented in the PGSWMFA package (PGplot Surface Wave Multiple Filter Analysis) of Ammon, (1998), after isolating the fundamental mode through application of a phase-match filter (Herrin & Goforth 1977). Similarly to FTAN, the MFA approach uses a series of narrow bandpass Gaussian filters that isolate the wave trains around the central frequency of each filter. The group velocity for each frequency can then be determined by dividing the raypath length by the travel time of the maximum of the envelope. To obtain Love-wave measurements, we can apply the same filter to data rotated into the transverse direction. A detailed example of waveform processing for periods between 30 - 200 s, is shown in Figure 3.7.

3.5 Quality control and uncertainty estimation

3.5.1 Convergence analysis for EGFs and dispersion curves

One parameter to adjust in the computation of EGFs is the amount of data to be stacked in order to obtain reliable group-velocity measurements. To this purpose, waveform similarity was calculated for several trajectories through the zero-lag cross correlation between a reference trace (taken as the stacked cross-correlation of the maximum number of days available) and a subset of cross-correlations from the stack of a fixed number of days selected randomly at 30 days increment until matching the reference trace. Then, a plot of similarity versus number of random subset days was built and the minimum number of days after which the cross-correlation remains stable was chosen. Two examples are shown in figures 3.8 and 3.9 for two trajectories (HEL-ROSC and HEL-FLO2), with inter-station distances of 198 and 509 km, respectively. For HEL-ROSC, with a interstation path of 198 km, the convergence is very fast, with the minimum number of days at 150; for greater distances (>500 km), at least 300 days are necessary for convergence. This process was repeated for even longer distances, finding that for distances greater than

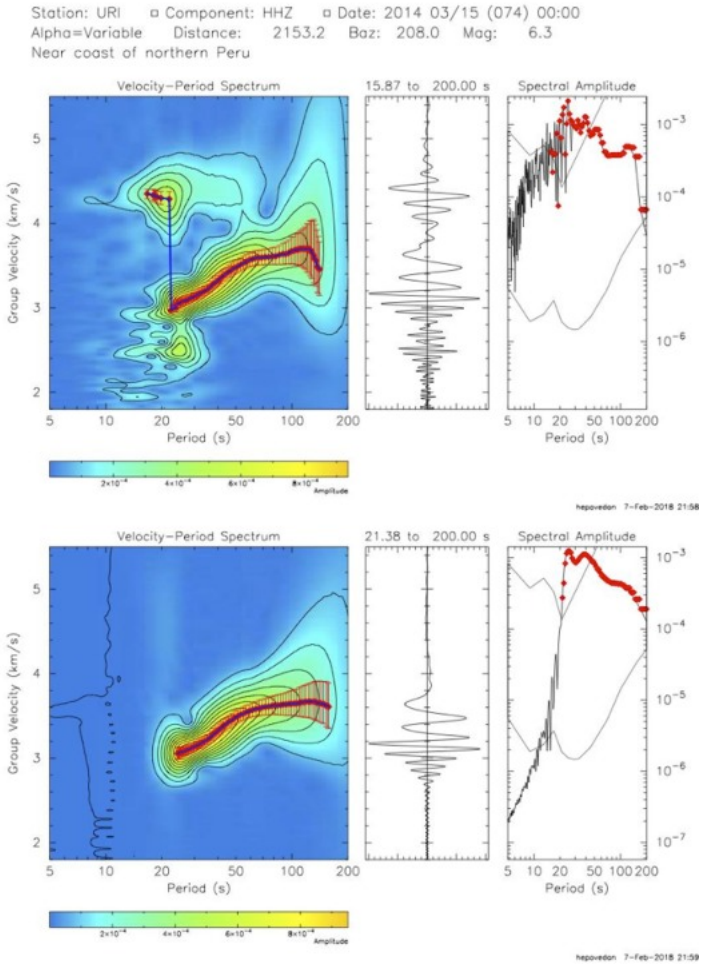

Figure 3.7: Example of group velocity measurement using the PGSWMFA program for station URI in the Guajira peninsula. The top panel shows the contours of the velocity-period spectrum which are used to make the dispersion measurement, along with uncertainty. The top-center figure shows the Rayleigh waveform, while the top-right figure shows the spectral amplitude as a function of period. Bottom panel shows the procedure after applying the phase-match filter.

800 km, at least 700 days were needed to achieve convergence, especially for the longest periods. Naturally, trajectories that did not achieve convergence were discarded.

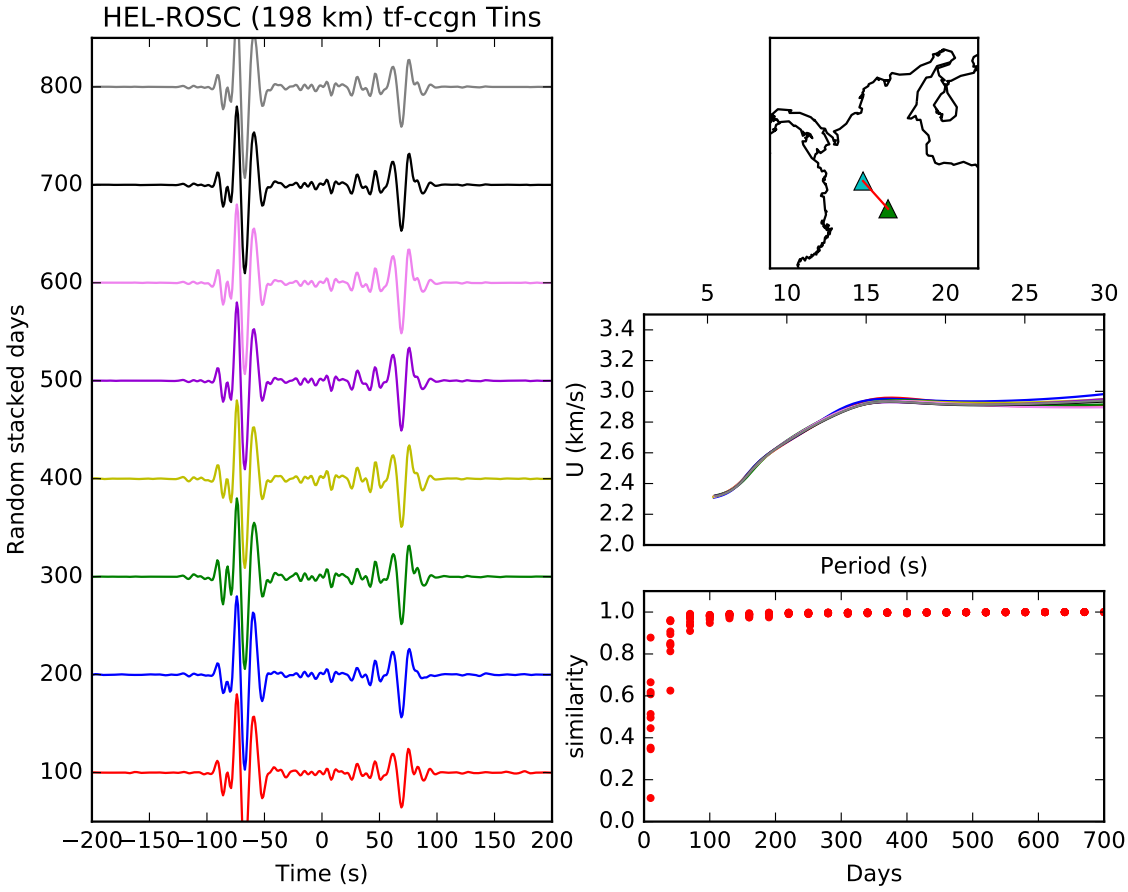

Figure 3.8: Analysis of signal stability and convergence for HEL-ROSC (198 km); the left panel shows empirical Green's function (EGF) convergence for progressive stacking randomly selected days, color coded to match the dispersion curves (right panel). The top-right panel shows the station locations. The center-right panel displays group- and phase-velocity dispersion curves for Rayleigh and phase velocities waves. The bottom-right panel displays the similarity value as a function of random number of days. Convergence is achieved in 150 days.

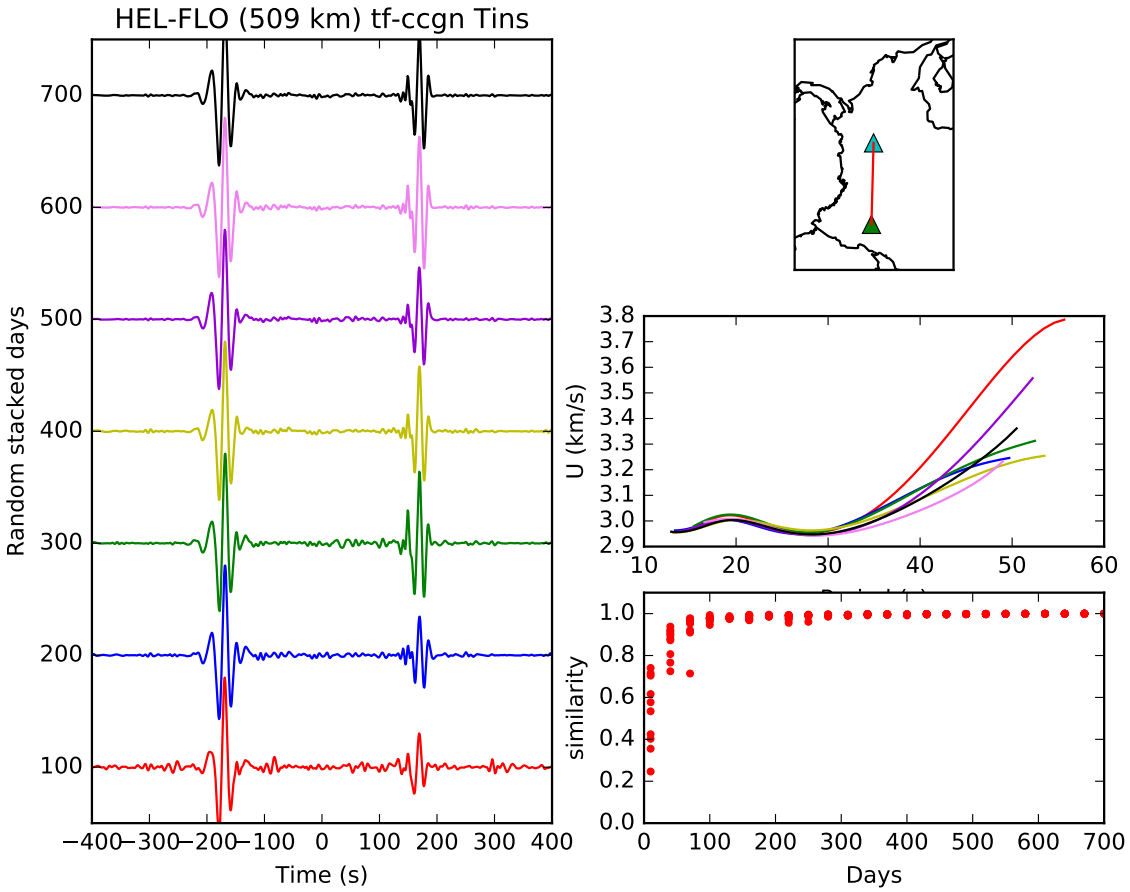

Figure 3.9: Analysis of signal stability and convergence for HEL-FLO (509 km). The left panel shows the empirical Green's function (EGF) convergence for progressive stacking of randomly selected days, color coded to match the dispersion curves (right panel). The top-right panel show the stations. The center-right panel displays group- and phase-velocity dispersion curves for Rayleigh waves. The bottom-right panel displays the similarity as a function of random number days. Convergence is achieved in 300 days.

Also, in order to assess the performance of stacking methodologies (linear *vs* time-frequency phase weight-stack), convergence was assessed for several methodologies. It was observed that the time-frequency phase weight-stack reaches convergence with fewer days than the linear stack. This is illustrated in figure 3.10, for an interstation path of 217 km, for which convergence is reached with 100 days with the tf-PWS and 150 days with the linear stack.

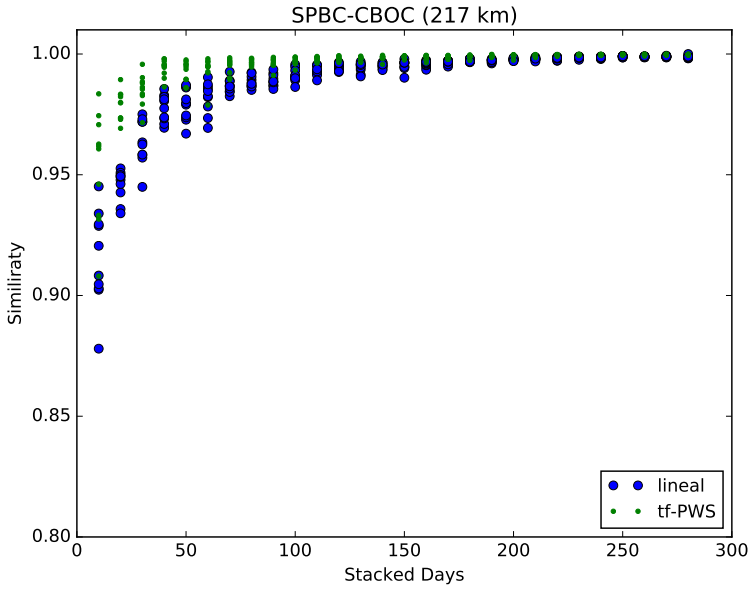

Figure 3.10: Comparison of waveform convergence of cross-correlation stacks for two different stacking approaches, the linear stack (blue points) and the tf-PWS (green points). Note that convergence is reached faster with the tf-PWS stack.

Following Bensen et al. (2007), dispersion measurements from cross correlations with interstation distances less than three wavelengths and with SNR < 7 were rejected. The SNR was calculated for periods between 5 to 40 s. In general, higher values of SNR were observed with tf-PWS procedure, since the tf-PWS allows to eliminate incoherent phases and increases the contribution of coherent, low-energy phases (Schimmel & Gallart 2007). Figure 3.11 displays the SNR values for the tf-PWS and linear stacks.

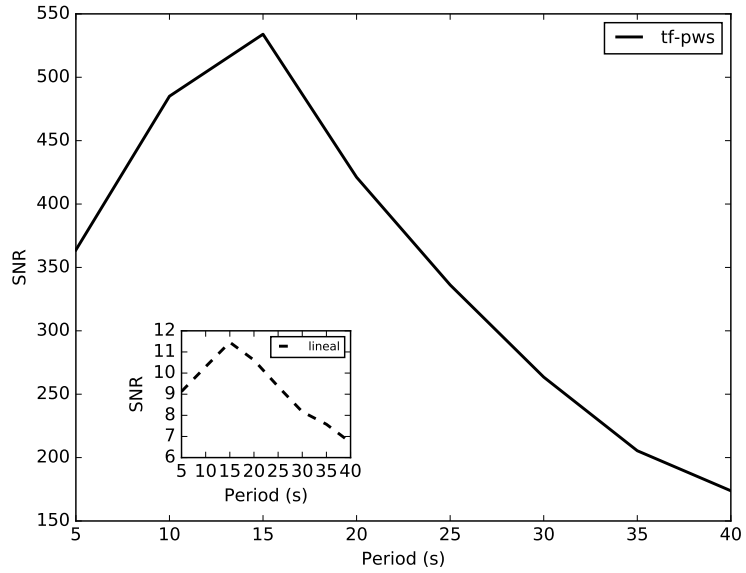

Figure 3.11: SNR averaged over all cross-correlations between all station pairs (solid line) computed with the tf-PWS stacking approach. The inset shows the SNR computed with the linear stacking approach.

To evaluate the uncertainties for dispersion velocities in each dispersion curve, the procedure of (Bensen et al. 2007) was applied. In that approach, dispersion curves are calculated from correlations developed within different periods of the year and with a fixed time lenght. Thus, if the dispersion curve is computed from cross-correlation of 3-months of data, using a year of data, there are up to twelve 3-month stacks: January-February-March, February-March-April, and so on. The dispersion curve uncertainty for each trajectory is then obtained from the standard deviation of the dispersion curves from the triplets. The standard deviation of a trajectory is calculated only if it has at least four triplets with SNR > 7; otherwise, the uncertainty for the trajectory is set on the average standard deviation of all trajectories with enough triplets. An example for the trajectory is shown in figure 3.12. The figure shows that for periods between 7 and 40 s the average group velocity uncertainties for Rayleigh wave are less than 0.1 km/s, dropping significantly for intermediate periods to 0.04 km/s. For phase velocities, the standard deviation is much smaller, ranging from 0.002 to 0.07 km/s.

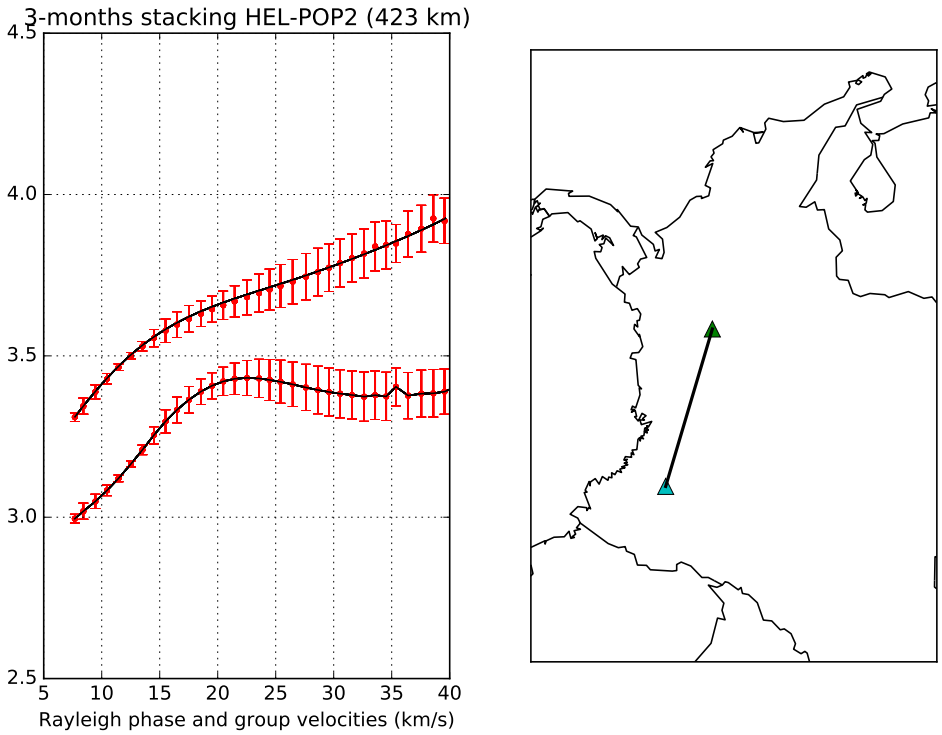

Figure 3.12: Example of assessment of uncertainty of dispersion measurements for the HEL-POP2 raypath. Left: Rayleigh group and phase velocity (black lines) with standard deviation from twelve 3-months (blue vertical lines) stacks. Right: Raypath between HEL and POP2 stations.

3.6 Tomographic inversion

The inter-station dispersion curves computed from ambient noise and those resulting from earthquakes sources, are inverted tomographically to produce phase and group velocity maps for NW South America at periods from 7 to 150 s. The non-linear, 2-D tomographic inversion technique developed by (Rawlinson & Sambridge 2003) is considered. Traveltimes through the 2-D model are computed using the fast marching algorithm (FMM) of (Sethian 1996), in which a finite-difference method is used to solve for the eikonal equation (forward problem). This technique brings considerable benefits over conventional ray-tracing methods, as it is more stable and successfully finds the first-

arrival times for diffraction paths in shadow zones. The inversion algorithm, on the other hand, uses a gradient method based on the subspace technique of (Kennett et al. 1988), where the minimization is carried out simultaneously along several search directions that together span a subspace of the original model space (Rawlinson & Sambridge 2004, Rawlinson & Sambridge 2003).

3.6.1 Fast Marching Method (FMM)

The fast marching method (FMM) is a grid-based numerical scheme for tracking the evolution of monotonically advancing interfaces, via finite-difference solution of the eikonal equation. In its simplest form, the FMM uses the first-order upwind difference scheme:

$$\begin{bmatrix} \max(D_{ijk}^{-x}T, -D_{ijk}^{+x}T, 0)^2 \\ +\max(D_{ijk}^{-y}T, -D_{ijk}^{+y}T, 0)^2 \\ +\max(D_{ijk}^{-z}T, -D_{ijk}^{+z}T, 0)^2 \end{bmatrix}^{\frac{1}{2}} = s_{ijk}, \tag{3.12}$$

where the finite difference operator notation used is defined as

$$D^{+x}T = \frac{T(x+\delta x) - T(x)}{\delta x}, \tag{3.13}$$

$$D^{-x}T = \frac{T(x) - T(x-\delta x)}{\delta x}, \tag{3.14}$$

with D_{ijk} the slowness at grid point (i, j, k). Realize that eq. (3.12) is a non-linear equation (quadratic) for the traveltime T_{ijk} for which, out the two possible solutions, the larger value is always the correct value. The FMM of Sethian and Popovici (1999) systematically constructs traveltimes T in a downwind fashion from known values upwind using a narrow band scheme. The the scheme is illustrated in Figure 3.13, where the narrow band represents the propagating wavefront, and the grid points are labelled as either alive, close

or far, depending on whether they have had the narrow band passing through them, they are inside it, or are yet to be touched by it, respectively.

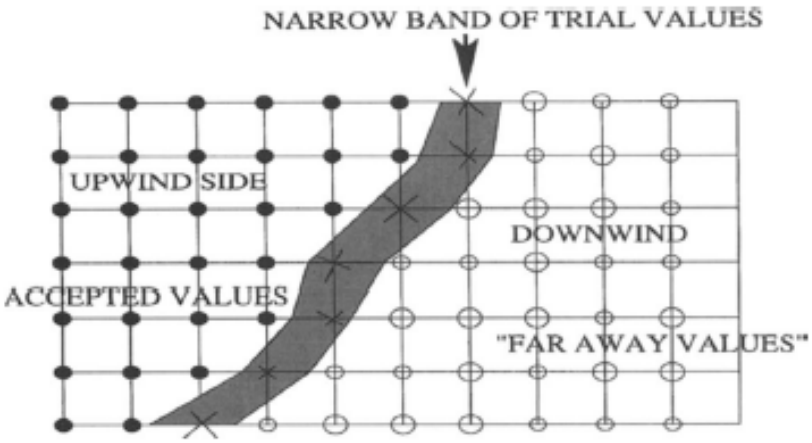

Figure 3.13: Upwind scheme, adapted of Sethian and Popovici (1999).

The FMM begins from a source point (or wavefront), and computes the traveltimes at neighboring node points using, for example, Eq. (3.11) to generate the first stage of the narrow band. The point with minimum traveltime is then accepted as alive (it is a true first-arrival traveltime), and all points neighboring this alive point are updated (if close) or calculated for the first time (if far), in which case they become close and the narrow band progresses downwind (see Figure 3.14).

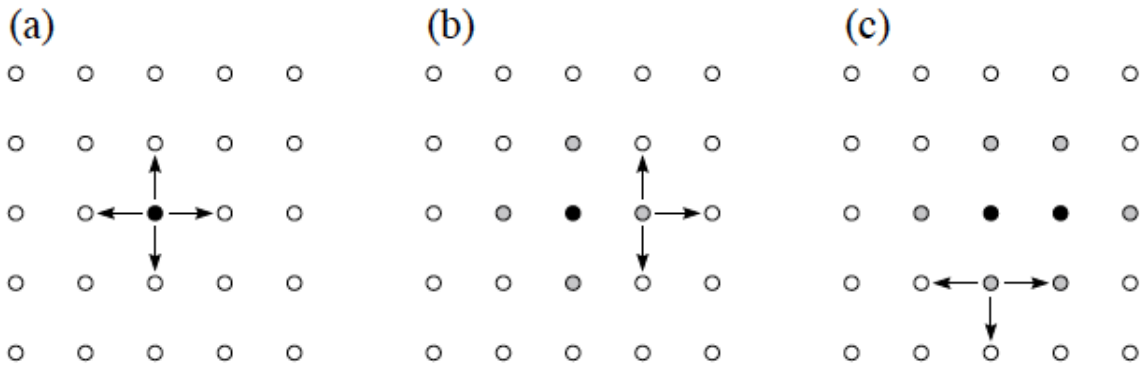

Figure 3.14: (a) Starting from the source point (black dot) in the center of a grid, traveltimes to the four neighboring grid points are determined using eq. (3.11). (b) The smallest of these four values (grey dots) must be correct one, so all close neighbors to this point that are not alive (white dots) have their values computed, and added to the narrow band defined by the grey dots. (c) The smallest of these six close points again must be the correct one, so all neighboring points have their values computed (or recomputed). Figure adapted of Rawlinson and Sambridge (2003)

3.6.2 Subspace inversion method

The second stage is the inversion procedure, which follows an iterative, non-linear scheme known as the subspace approach (Kennett et al. 1988). The scheme provides a model for the local phase and group velocities that best explains the interstation traveltimes. The subspace approach significantly reduces the computational effort during the inversion.

The functional to be inverted consists of a data residual term and two regularization terms:

$$S(\mathbf{m}) = (\mathbf{g}(\mathbf{m}) - \mathbf{d}_{\text{obs}})^{\text{T}} \mathbf{C}_d^{-1} (\mathbf{g}(\mathbf{m}) - \mathbf{d}_{\text{obs}}) + \varepsilon (\mathbf{m} - \mathbf{m}_0)^{\text{T}} \mathbf{C}_m^{-1} (\mathbf{m} - \mathbf{m}_0) + \eta \mathbf{m}^{\text{T}} \mathbf{D}^{\text{T}} \mathbf{D} \mathbf{m}, \tag{3.15}$$

where $\mathbf{g}(\mathbf{m})$ represents the predicted traveltimes from ~~the~~ model $\mathbf{m}$, $\mathbf{m_0}$ is an initial estimate of the model, $\mathbf{d_{obs}}$ is a vector of traveltimes, $\mathbf{C_d}$ is the data covariance matrix filled

with variances based on uncertainty from the 3-months stacks, and $\mathbf{C_m}$ is the *a priori* model covariance matrix with uniform *a priori* variances based on a model parameter uncertainty. **D** is the derivative operator, which has the role of smoothing the model, and ε and η are the damping and smoothing parameters, respectively.

To overcome the non-linearity of **g**, the minimization of the objective function is performed using an iterative approach:

$$\mathbf{m_{n+1}} = \mathbf{m_n} + \delta\mathbf{m}, \tag{3.16}$$

where $\delta\mathbf{m}$ is found iteratively using the subspace method. At each iteration, the subspace method restricts the minimization of the quadratic approximation of $S(\mathbf{m})$ to a *p*-dimensional subspace of the original model space, so that the perturbation $\delta\mathbf{m}$ occurs in the space spanned by a set of *p* *M*-dimensional basis vectors $\{a^j\}$. The perturbation is expressed as

$$\delta\mathbf{m} = \sum_{j=1}^{n} \mu_j \mathbf{a}^j = \mathbf{A}\mu, \tag{3.17}$$

where $\mathbf{A} = \mathbf{a}^j$ is the M×p projection matrix. The component μ determines the length of the corresponding vector $\mathbf{a^j}$ that minimizes the objective function $S(\mathbf{m})$ in the space spanned by $\mathbf{a}^j$. The final expression for the model update can be written as:

$$\delta\mathbf{m} = -\mathbf{A}[\mathbf{A}^T(\mathbf{G}^T\mathbf{C}_d^{-1}\mathbf{G} + \varepsilon\mathbf{C}_m^{-1} + \eta\mathbf{D}^T\mathbf{D})\mathbf{A}]^{-1}\mathbf{A}^T\hat{\gamma}, \tag{3.18}$$

where **G** is the Fréchet matrix of partial derivatives. Since the projection matrix **A** is orthonormal, A model update $\delta\mathbf{m}$ is readily obtained by the inversion of a relatively small part of the $n \times n$ matrix. After each update of the model, the surface waves are retraced through the updated model using the fast marching method described above, and the terms of **A**, $\hat{\gamma}$ and **G** are then re-computed.

The tomographic inverse problem is generally ill-posed in a Hadamard's sense (Tikhonov & Arsenin 1977), implying the existence of many solutions but, above all, the presence of instability; that is, small perturbations in $\mathbf{d_{obs}}$, such as noise present in the seismological observations, can result in large variations in the solution. The solution to this difficulty lies in the regularization of the solution (Tikhonov & Arsenin 1977), that is, in the introduction of constraints in the inversion functional (second and third terms in eq. (3.14)). One of the most standard ways of estimating the ideal value of the regularization is the so-called *L-curve* criterion or *trade-off* curve. This criterion is based on the fact that the dependency of data misfit with respect to a model characteristic is supposed to have shape of letter L. The most appropriate model is chosen as that corresponding to the corner of the L-curve, where ~~the~~ sufficient decrease of the data misfit is achieved by the model with the smallest complexity.

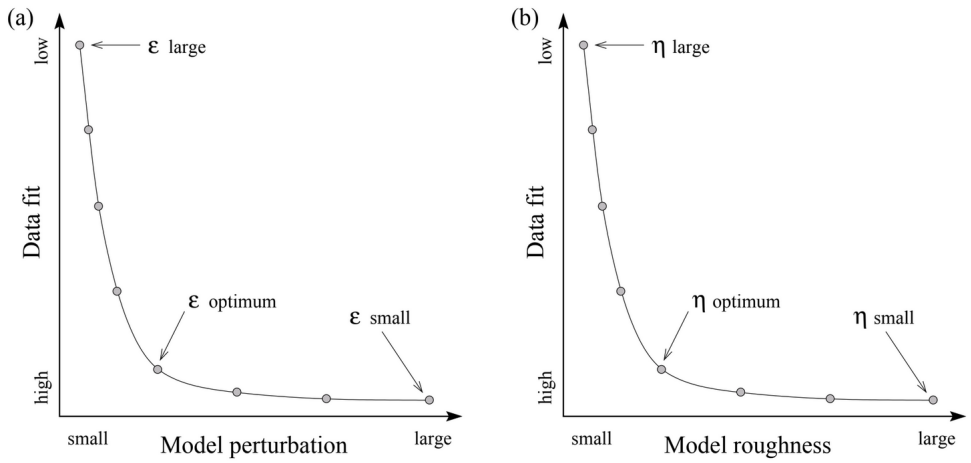

Figure 3.15: Schematic diagram of trade-off curves that could be used to choose appropriate damping or smoothing parameters for an inversion. A number of separate (eight in these examples) inversions with different values of ε or η are required in order to construct these curves. (a) Data fit (RMS) *vs* model perturbation for different values of ε. (b) Data fit (RMS) *vs* model roughness for different values of η. Adapted from Rawlinson and Sambridge 2005.

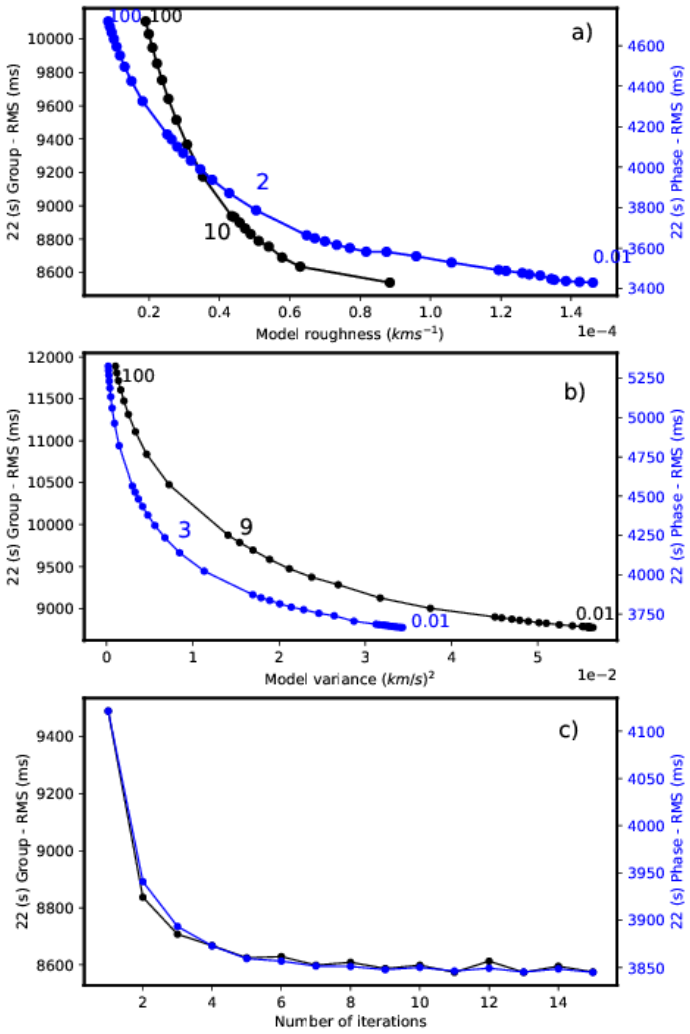

Figure 3.16: Trade-off curves for Rayleigh-wave phase- and group-velocity tomography at 22 s period. (a) Data misfit (RMS) *vs* model roughness for different values of η. (b) Data misfit (RMS) *vs* model perturbation for different values of ε. (c) RMS data misfit variation *vs* number of iterations; note that with 4 iterations convergence is reached.

The regularization parameters (ε e η) are chosen by inspecting the *trade-off* between RMS (root mean square) misfit and model roughness, and RMS misfit and model variance, respectively. Model roughness is defined as $\mathbf{m}^T\mathbf{D}^T\mathbf{Dm}$ and model variance as

$(\mathbf{m}-\mathbf{m}_0)^{\mathrm{T}}C_m^{-1}(\mathbf{m}-\mathbf{m}_0)$ (see eq. (3.14) and figure 3.15). The choice of parameters is done systematically as described in (Rawlinson & Sambridge 2005). Figure 3.16 displays sample trade-off curves for both group and phase velocity corresponding to tomographic inversions at 22 s period, demonstrating values of $\varepsilon = 9$ and $\eta = 10$ for group velocities, and $\varepsilon = 3$ and $\eta = 2$ for phase velocities. Parameters for tomographic inversions at other periods are similar, ranging between 0.3 and 10 for smoothness (ε) and between 0.3 and 9.0 for damping (η). Similar plots are built to investigate the required number of iterations, demonstrating that 6 iterations generally suffice to achieve convergence.

3.7 Inversion for Shear-wave velocity

Local dispersion curves can be extracted from the tomographic maps for each grid point, and the resulting dispersion curves can then be inverted to obtain 1D velocity-depth profiles of S-wave velocity. To this purpose, two methodologies were adopted: the Neighborhood Algorithm (NA) (Sambridge 1999), and a Linearized Inversion Method (Ammon et al. 1990).

3.7.1 Neighborhood Algorithm (NA)

The Neighborhood Algorithm (NA) (Sambridge 1999) was used to invert Rayleigh phase and group velocities for S-velocity structure. The NA is a global optimization method similar to genetic algorithms (Lomax & Snieder 1994) and simulated annealing (Sen & Stoffa 1991). These methods work by exploring the range of possible solutions in a quasi-random form. The result is a family of solutions that includes the best-fitting models in the parameter space. The neighborhood algorithm (NA) is a direct search scheme, so it does not require the presence of an initial model or linearization of the inverse problem (Wathelet 2008).

The NA makes use of Voronoi cells to model the misfit function across the parameter

space and offers a robust sampling of the solution space. The formal Voronoi cell definition is as follows: let $P = [m_1, ..., m_{n_p}]$ be a set of points in the d-space, where $2 \leq n_p \leq \infty$, and let $m_1 \neq m_j$ for $i \neq j$. The Voronoi cell about point m_i is given by:

$$V(m_i) = \left\{x| \parallel x - m_i \parallel \leq \parallel x - m_j \parallel \text{for} j \neq i, (i, j = 1, ..., n_p)\right\} \tag{3.19}$$

The Voronoi cell formulation is later utilized to resolve the forward problem with the formulation proposed in (Dunkin 1965) to evaluate the misfit function for different solutions. The misfit functions are defined through the L2-norm between the dispersion curve predicted by the model and the one constructed from the tomographic maps. The misfit function is given as:

$$||(m_a - m_b)|| = [(m_a - m_b)^T C_M^{-1} (m_a - m_b)]^{1/2}, \tag{3.20}$$

The equation above represents the distance between models m_a and m_b. C_M is a matrix that non-dimensionalizes the parameter space.

The sequence of steps taken during the application of the NA are as follows:

- Generation of n_s model samples, uniformly in parameter space and with associated Voronoi cells.
- Calculation of the misfit functions from the generated models and ranking of the n_r lowest misfit models.
- Creation of n_s new models inside the Voronoi cells for the n_r lowest misfit models by uniform random walk.
- Reiterate from step 2.

The software package Dinver (http://www.geopsy.org), implemented by Wathelet 2008, combines the forward modeling algorithm of Dunkin (1965) with an improved version of

the original NA. This implementation has been applied successfully by several authors (e.g. (Behr et al. 2010, Kao et al. 2013, Köhler et al. 2012)).

3.7.2 Linearized Inversion Method

A second method to invert for Shear velocities is the the linearized, iterative inversion scheme described in Ammon et al. (1990), in which the RMS misfit between observed and predicted dispersion velocities is minimized in a least-square sense, with smoothness constraints on the inverted velocity-depth profile. The method was originally developed for the inversion of receiver functions, and expanded to the joint inversion of receiver functions and surface wave dispersion in Julià et al. (2003). It can be easily used for the inversion of dispersion curves alone from the joint inversion implementation.

Let's start by expressing forward problem as

$$\mathbf{y} = \mathbf{F}[\mathbf{x}], \tag{3.21}$$

where $\mathbf{y}$ is a N-dimensional vector of data points, $\mathbf{F}[]$ is a non-linear operator that maps vectors in the model space into vectors in the data space, and $\mathbf{x}$ is a M-dimensional vector that contains shear wave velocities for fixed-thickness layers at depth. Let's now expand eq. (3.21) in a Taylor series

$$\mathbf{y} \approx \mathbf{F}[\mathbf{x_0}] + \nabla\mathbf{F}|_{\mathbf{x_0}} \cdot [\mathbf{x} - \mathbf{x_0}], \tag{3.22}$$

where $\mathbf{x_0}$ is the starting model. To make the dependence of the final model with respect to the initial model more explicit, eq. (3.22) can be re-arranges as

$$\mathbf{y} - \mathbf{F}[\mathbf{x_0}] + \nabla\mathbf{F}|_{\mathbf{x_o}} \cdot \mathbf{x_0} = \nabla\mathbf{F}|_{\mathbf{x_o}} \cdot \mathbf{x}, \tag{3.23}$$

or, alternatively, as

$$\mathbf{y}' = \nabla \mathbf{F}|_{\mathbf{x_0}} \cdot \mathbf{x}, \tag{3.24}$$

where $\mathbf{y}'$ is the modified vector of residuals. The solution is then obtained in a linearized and iterative fashion as

$$\mathbf{x_{i+1}} = (\nabla \mathbf{F}|_{\mathbf{x_i}})^{-\mathbf{1}} \cdot \mathbf{y}'. \tag{3.25}$$

The inverse operator $(\nabla \mathbf{F}|_{\mathbf{x_i}}) = \mathbf{G}^{-\mathbf{1}}$ is obtained by minimizing the functional φ, composed of a least squares term and a smoothing parameter

$$\varphi = (\Delta y - G\Delta x)^T (\Delta y - G\Delta x) + \theta((\Delta x)^T A^T A(\Delta x) - G\Delta x) \tag{3.26}$$

where θ is an adjustable parameter that controls the trade-off between fitting the waveform and the smoothness of the model. This value is computed through *L-curve* analysis. The matrix A constructs the second difference of the model m.

Chapter 4

Upper and middle crustal velocity structure of the Colombian Andes from ambient noise tomography (Paper I)

The following article, entitled ***Upper and middle crustal velocity structure of the Colombian Andes from ambient noise tomography: Investigating subduction-related magmatism in the overriding plate***, reports on the results obtained from ambient noise cross-correlations at 52 broadband stations in NW South America. 3-D maps of S-velocity variation were produced for the region for the upper and middle crust. The results suggest that slow S velocities under the Central Cordillera have been attributed to accumulation of magmas in the middle crust generated in the underlying mantle wedge. In addition, evidence of magmatic activity was reported under the inactive volcanoes of the Eastern Cordillera. Slow S-velocities in the Caribbean middle crust were related to asthenospheric melts that would have breached the Caribbean flat slab through a vertical tear. This manuscript was accepted in 13 JAN 2018 and published online 23 JAN 2018 in *Journal of Geophysical Research - Solid Earth (JGR)*. DOI: 10.1002/2017JB014688

Upper and middle crustal velocity structure of the Colombian Andes from ambient noise tomography: Investigating subduction-related magmatism in the overriding plate.

E. Poveda[1], J. Julià[1, 2], M. Schimmel[3], and N. Perez-Garcia[4, 5]

[1]Programa de Pós-Graduação em Geodinâmica e Geofísica, Universidade Federal do Rio Grande do Norte, Natal, RN CEP 59078-090, Brazil

[2]Departamento de Geofísica, Universidade Federal do Rio Grande do Norte, Natal, RN CEP 59078-970, Brazil

[3]Institut de Ciències de la Terra "Jaume Almera", CSIC, 08028 Barcelona, Spain

[4]Red Sismológica Nacional, Dirección de Geoamenazas, Servicio Geológico Colombiano, Bogotá, Colombia

[5]Now, Ecopetrol S.A., Bogotá, Colombia

Corresponding author: Esteban Poveda (hepovedan@unal.edu.co)

Key Points:

- The magmatic signature of the subducting Nazca plate is mapped at mid-crustal depths under the Central Cordillera.
- Asthenospheric magmas might have breached the Caribbean flat slab through a pre-existing vertical tear.
- Fluid migration on major faults might also explain observed low velocitiy anomalies under the Lower Magdalena Basin.

Abstract

New maps of S-velocity variation for the upper and middle crust making up the northwestern most corner of South America have been developed from cross-correlation of ambient seismic noise at 52 broadband stations in the region. Over 1300 empirical Green's functions, reconstructing the Rayleigh-wave portion of the seismic wave-field, were obtained after time- and frequency-domain normalization of the ambient noise recordings and stacking of 48 months of normalized data. Inter-station phase- and group-velocity curves were then measured in the 6-38 s period range and tomographically inverted to produce maps of phase- and group-velocity variation in a 0.5˚ x 0.5˚ grid. Velocity-depth profiles were developed for each node after simultaneously inverting phase- and group-velocity curves and combined to produce 3-D maps of S-velocity variation for the region. The S-velocity models reveal a ~7 km thick sedimentary cover in the Caribbean region, the Magdalena Valley, and the Cordillera Oriental, as well as crustal thicknesses in the Pacific and Caribbean region under ~35 km, consistent with previous studies. They also display zones of slow velocity at 25-35 km depth under regions of both active and inactive volcanism, suggesting the presence of melts that carry the signature of segmented subduction into the overriding plate. A low velocity zone in the same depth-range is imaged under the Lower Magdalena Basin in the Caribbean region, which may represent either sub-lithospheric melts ponding at mid-crustal levels after breaching through a fractured Caribbean flat slab or fluid migration through major faults within the Caribbean crust.

Key words: ambient noise tomography; Colombian Andes; subduction-related magmatism.

1. Introduction

The recent tectonic evolution of Northwestern South America has been shaped by the complex interactions of up to three different lithospheric plates: South America, Caribbean, and Nazca. It is accepted that this corner of the continent maintains a record of Grenvillian basement, originated during the amalgamation and disassembly of western Pangaea *[Spikings et al., 2015]*. The subsequent collision of the Caribbean Igneous province created new crust, which was added to the Pacific margin during Early and Late Cretaceous times *[Escalona and Mann, 2011],* and emplaced the Panama arc in western Colombia during Middle Miocene times *[Restrepo and Toussaint, 1988; Taboada et al., 2000; Cediel et al., 2003]*. These terrains were later reworked and altered by convergence-related processes. The end result is the present configuration of the Colombian Andes (north of the Ecuadorian border) into three main ranges - the Eastern Cordillera, the Central Cordillera, and the Western Cordillera – and two intervening valleys - the Middle Magdalena Valley, and the Cauca-Patía Valley – separating the ranges (Figure 1). The origin and composition of these three main ranges are essentially different, each of them deriving from distinct tectonic processes driven by plate convergence [*Taboada et al.*, 2000; *Cediel et al.*, 2003]. The composition of the South American plate is presently being altered by subduction-related volcanism, which reaches as far north as ~6^{o}N latitude. Volcanism is active along the Central Cordillera and inactive along the Eastern Cordillera, and is offset at 5^{o}N latitude by ~270 km in the EW direction, following the pattern delineated by intermediate, subduction-related seismicity [*e.g. Pennington, 1981; Vargas and Mann, 2013*]. The NW corner of South America thus constitutes a unique tectonic setting to investigate how subduction-related processes deform and alter the composition of the overriding plate.

Passive-source seismic studies in the region have focused mainly on the relative geometry of the subducting Nazca and Caribbean plates under South America [*Pennington,* 1981*; van der Hilst and Mann,* 1994*; Vargas and Mann,* 2003*, Chiarabba et al.,* 2016*; Syracuse et al.,* 2016]. An early study by *Pennington* [1981], for instance, used patterns of seismicity and focal mechanisms to define two separate segments of subducted lithosphere – Cauca and Bucaramanga – that were associated to the Nazca and Caribbean plates, respectively. The segments were found to be dipping at different angles, thus defining a slab window within the South American mantle that explained the offset of intermediate-depth seismicity and surface volcanism. The detailed geometry of the slab window was later refined through seismic tomography, suggesting either superposition of the Nazca and Caribbean plates [*van der Hilst and Mann*, 1994], tearing of the Caribbean slab [*Vargas and Mann*, 2013], tearing of the Nazca slab [*Chiarabba et al.,* 2016], or even multiple tears segmenting the subducting plates [*Corredor,* 2003; *Syracuse et al.,* 2016]. Fewer studies have focused on the structure of the overriding South American plate. Refraction surveys, for instance, were performed in southern Colombia as part of the Nariño Project [*Aldrich et al.*, 1973; *Ocola et al.*, 1975; *Meissnar et al.*, 1976; *Meyer et al.*, 1976; *Mooney et al.*, 1979], producing a crustal cross-section for the region; and a 1D velocity model for the Colombian crust was developed by *Ojeda and Havskov* [2001], seeking to improve accuracy in location of crustal seismicity. On a more regional scale, crustal thickness was surveyed by *Poveda et al.* [2015], based on receiver functions analysis and a published compilation of crustal thickness observations; and images of lateral P- and S-wave velocity variation between 12.5 and 155 km depth were developed by *Syracuse et al*. [2016], although with no tectonic interpretation at crustal levels. In spite of these efforts, therefore, a regional-scale investigation of lateral

seismic velocity variation of the overriding South American plate is still missing.

Surface-wave tomography has been successfully utilized to image the continental lithosphere at several scales [*e.g. Feng et al.,* 2004, *Ritsema et al.,* 2004]. Tomographic images from naturally-occurring surface-waves, however, rarely provide information at periods shorter than 20 s, which are required to probe into the upper and middle crust [*Levshin and Ritzwoller*, 2001]. Fortunately, the modal representation of ambient seismic noise for a diffuse wavefield with an homogeneous source distribution has demonstrated that surface-wave imaging at local-to-regional scales can be performed with ambient seismic noise [*Sabra et al.,* 2005; *Snieder*, 2004]. Indeed, an ever increasing number of ambient seismic noise studies have been produced during the last decade mapping different parts of the globe [*e.g. Shapiro et al.*, 2005; *Yao et al.*, 2006; *Stehly et al.*, 2006; *Bensen et al.*, 2007; *Yang et al.*, 2007; *Lin et al.*, 2007; *Villaseñor et al.*, 2007; *Saygin and Kennett*, 2010; *Ward et al.*, 2013; *Mottaghi et al.*, 2013; *Boué et al.*, 2014; *Abdetedal et al.*, 2015; *Haned et al.*, 2016]. These studies have conclusively demonstrated that empirical Green's function recovery from average cross-correlations of ambient noise between pairs of seismic stations is capable of providing tight constraints on upper and middle crustal structure.

In this study, we use information derived from cross-correlations of ambient seismic noise between pairs of permanent seismic stations in NW South America to reconstruct the surface-wave portion of the empirical Green's functions and develop surface-wave tomographic images at periods sampling upper and mid-crustal levels. More specifically, we utilize seismic stations deployed by the Colombian Geological Survey between 2012 to 2015 in and around the Andean

region to reconstruct the empirical Green's functions for all possible pairs of stations, and develop high-quality, Rayleigh-wave group- and phase-velocity tomographic images at periods between 6 and 38 s. Our tomographic study includes more than ~780 interstation raypaths that sample the region, derived from ~1300 empirical Green's functions imaging the upper and middle crust at an unprecedented resolution in the region. The group and phase-velocity maps are further inverted for isotropic S-wave velocity structure, building a detailed 3D S-velocity model for the middle and upper crust under NW South America. The resulting images show an excellent correlation with surface geology at shallow depths, and reveal low-velocity patterns at mid-crustal depths (25-35 km) that correlate with active and inactive surface volcanism in the central portion of the Eastern Cordillera and the southern flank of the Central Cordillera, respectively. These low-velocity anomalies are interpreted as magmas derived from the mantle wedge above the Nazca and Caribbean plates. More strikingly, a similar low-velocity anomaly is also observed under the Lower Magdalena Basin, where flat subduction of the Caribbean plate has prevented the occurrence of surface volcanism. We argue that this low-velocity region represents either the signature of fluid expulsion near crustal faults or upwelling magmas from the underlying asthenosphere, which would have breached the flat-subducting Caribbean plate through a preexisting fracture and pond at mid-crustal levels within the overriding plate.

2. Geology and Crustal Structure

2.1. Geology and tectonic setting

NW South America is broadly divided into the northern Andes, the Caribbean region, and the

Eastern Llanos. The northern Andes comprise the Andean regions of Ecuador, Colombia, and Venezuela, which are structured into three main ranges (Eastern Cordillera, Central, Cordillera, and Western Cordillera) and two intervening valleys (Middle Magdalena Valley, and Cauca-Patia Valley). Precambrian and Paleozoic rocks form the basement of the Eastern Cordillera and the Central Cordillera, immediatelly West of the Guyana Shield. The Eastern Cordillera is covered by sequences of Cretaceous sedimentary rocks, while the Central Cordillera is dotted by instances of Meso-Cenozoic batholits related to subduction of the Nazca plate. Cenozoic andesitic volcanism dominates the southern portion of the Central Cordillera (Figure 1). The Western Cordillera, on the other hand, consists of oceanic rocks that accreted during Cretaceous and early Cenozoic times, and are covered by sedimentary rocks. The division between the Western and the Central Cordilleras are the Cauca Valley and the Romeral Fault System, which separate the accreted oceanic part from the provinces of continental affinity next to the Guyana shield (Figure 1). The separation between the Central and the Western Cordilleras is marked by the presence of the Middle Magdalena Valley, which is covered by sequences of Cretaceous, Paleogene, Neogene, and Quaternary sedimentary rocks from the Eastern and the Central Cordilleras. In the northernmost corner of the northern Andes outcrops the Santa Marta Massif, which includes Jurassic volcanics and Paleozoic metamorphic rocks, along with volcano-sedimentary Cretaceous materials [*Cardona et al.*, 2011].

The Caribbean region can be geologically described as an Oligocene-to-Recent forearc basin - the Lower Magdalena Basin (LMB) - overlying the shallowly dipping Caribbean slab *[Bernal-Olaya et al., 2015b; Mora-Bohórquez et al., 2017]*. The LMB is in turn composed of several subduction-related basins, such as the Plató, San Jorge, and Sinú-San Jacinto basins, and is

bounded to the West by Sinú-San Jacinto fold-and-thrust belt. The Plató and San Jorge basins consist of Paleogene sediments overlying Precambrian and Paleozoic metamorphic basement rocks, while the Sinú–San Jacinto fold-and-thrust belt is regarded as an accretionary wedge that includes rocks of Cretaceous age as well as Tertiary and Quaternary lacustrine sediments. The sedimentary prism making up the Sinú-San Jacinto basin extends offshore along the margin of the northern South American Plate, with thicknesses of up to 10 km [*Toto and Kellogg*, 1992; *Flinch*, 2003; *Montes et al.*, 2010; *Lara et al.*, 2013; *Bernal-Olaya et al.*, 2015b]. The Eastern Llanos represent an extensive foreland basin associated to the Andean orogen that overlays the Guyana craton [*e.g., Farris et al.*, 2011].

The northern Andes and the Caribbean region behave as a coherent tectonic unit known as the North Andean Block (NAB), which can thus be regarded as a collage of several terrains that accreted against the Guyana Shield at different stages through Earth's history [*Restrepo and Toussaint*, 1988; *Cediel et al.*, 2003]. The latest addition to the NAB is the Panamá arc, which includes the Baudó Range and represents an oceanic, basic and ultramafic magmatic arc covered by oceanic sediments [*Case et al.*, 1971; *Restrepo and Toussaint*, 1988; *Taboada et al.*, 2000; *Cediel et al.*, 2003]. *Flueh et al.,* [1981] reported sedimentary sequences with thicknesses between 7.5 and 10 km under the Panama arc. The Panama arc is thus seen as an exotic terrain within the NAB [*Duque-Caro,* 1990; *Taboada et al.,* 2000].

The present geology of northwestern South America is partly the result of a complex interplay between the South American (overriding) plate and the (subducting) Nazca and Caribbean plates. An initial model of this interplay was proposed by *Pennington* [1981]. Through careful selection

of hypocentral locations of earthquakes and focal mechanisms in the region, the author identified two distinct segments of subducted lithosphere beneath the Colombian Andes: the Bucaramanga segment, related to subduction of the Caribbean Plate; and the Cauca segment, related to subduction of the Nazca Plate. These two segments would have resulted from the collision of the Panamá istmus against South America and buoyancy of partially subducted bathimetric features, implicitly implying the existence of a slab tear at depth separating the postulated segments. The Bucaramanga segment would be subducting in the N109^{o}E direction and dipping at 20^{o}-25^{o}, while the Cauca segment would be subducting in the N35^{o}E direction with a 35^{o} dip.

Although several studies have been conducted to investigate the precise contact geometry between the Nazca and Caribbean plates, this issue still remains a debate. Tomographic images developed by *van der Hilst and Mann* [1994], imaged oblique convergence of the Caribbean and Nazca slabs (including the Panama istmus segment), showing an overlap between latitudes 5.2^{o}N and 7^{o}N with both plates being simultaneously overridden by the South American plate. This interpretation was adopted in *Cortés and Angelier* [2005] and *Taboada et al.* [2000]. *Vargas and Mann* [2013], on the other hand, return to the slab tear model *of Pennington [1981]*. From additional earthquake locations accumulated during the intervening years, coda-Q tomography, and regional magnetic and gravity data, they propose the existence of a lithospheric, ~240 km wide, east-west trending slab tear at 5^{o}N latitude – the Caldas tear – that separates the shallowly-dipping Panama arc indenter from the more steeply dipping normal oceanic crust of the Nazca plate. Similar to *Pennington* [1981], they further propose that the tear would have resulted from the collision of the Panamá arc and buoyancy of a subducted oceanic ridge. Tomographic imaging by *Chiarabba et al.* [2016] places the tear entirely within the Nazca plate, pushing the

boundary of this plate north and indicating an EW trending slab tear separating a steeply subducting segment to the south from a flat subducting segment to the north. Finally, *Syracuse et al*. [2016] presented 3D models of P- and S-velocity variation for the mantle and hypocentral relocations based on the joint inversion of local body wave arrivals, surface-wave dispersion measurements, and gravity data. They imaged up to three separate slab fragments, separated by two slab windows: one at about 5°N, coinciding with the termination of active volcanism; and one at 7.5°N, marking the location of the Bucaramanga seismic nest. The region at ~5.5°N (Northern termination of volcanism) is interpreted as a non-overlaping slab tear of the Nazca plate, where intermediate-depth seismicity is shifted ~200 km toward the East, beneath Eastern Cordillera. A similar model had been previously proposed by *Corredor* [2003] from a three-dimensional model of CMT solutions and other seismicity in northwestern South America.

In spite of the many interpretations from tomographic imaging, all models seem to agree that the Nazca plate is subducting with an average angle of 35° in a nearly eastward direction, although with high variability along the subduction front and, therefore, presenting segmentation [*Gutscher et al.*, 1999]. The Caribbean Plate, on the other hand, would be subducting at shallower dip angle <10° in a WNW-ESE direction *[Bernal-Olaya et al., 2015a; Mora-Bohórquez et al., 2017]*, with no apparent signs of segmentation. All models also agree that the shift in intermediate-depth seismicity and surface volcanism would be the result of deep versus shallow subduction along the Colombian trench.

2.2. Crustal structure

The average crustal structure of the NW Andean region can be obtained from continental-scale models. *Chulick et al.*, 2013 for instance, presented contour maps and statistical analyses of the seismic structure of the crust and upper mantle, based on a large seismic compilation of multiple datasets. They reported an average crustal thickness of 38 km for South America, with a maximum crustal thickness estimate of 60 km for Colombia. *Feng et al.* [2007; 2004] and *Lloyd et al.* [2010], on the other hand, produced tomographic images from surface-wave dispersion with ~200 km resolution in the continent; although ray coverage is low for northern Colombia, crustal thickness is reported to be in the 40-50 km range. These values are consistent with thickness up to 45 km for the Colombian Andes and 33 km for the Lower Magdalena Basin reported from analysis of satellite gravity measurements from the GOCE mission by *van der Meijde et al*. [2013].

The most complete survey of crustal structure for the NW Andean region is the crustal thickness map presented in *Poveda et al.* [2015] from receiver function analysis, which has been updated here following the procedures described in their study. We include 11 new stations (Fig. 2) that improve the sampling of the Caribbean region and the Western and Central Cordillera. A close inspection of the figure reveals that the crust in the southern Pacific Coast is about 22 km thick, increasing to about 30 km under the Panama arc. The WC is characterized by thicknesses between 30 km south of 4°N and 40 km north of this latitude, similar to those observed under the Cauca Valley. Crustal thickness increases to 52-58 km beneath the northern Central Cordillera and to almost 60 km beneath some of the volcanoes of the Southern Cordilleran system; in the EC, crustal thickness is between 55 and 60 km. In the Middle Magdalena Valley, separating the CC from the EC, crustal thickness is around 45 km. In the Caribbean region, the crust is ~30 km

thick under the Sinú–San Jacinto Basin, and ~35 km thick under Lower Magdalena Basin, the Plató Basin, and the San Jorge Basin. These variations may be due to the shallowly dipping Caribbean slab [*Bernal-Olaya et al.*, 2015a]. Beneath the Santa Marta Massif, the uptaded crustal thickness map displays a crustal thickness of ~40 km, decreasing to ~30 km under the Guajira Peninsula.

Detailed velocity structure was developed from active-source profiling in southern Colombia as part of Nariño Project [*Aldrich et al.,* 1973; *Meyer et al.,* 1976; *Ocola et al.,* 1975], where the crust between 1◦N and 4◦N latitude, and 82◦W and 76◦W longitude was mapped with seismic refraction lines [*Meissnar et al.*, 1976]. In the off-shore portion, results revealed P-wave velocities of ~3.2 km/s for the upper crust (top 5 km) and 6.8 km/s for the lower crust (down to 15 km); on-shore, P-wave velocities ranged between 6.0 and 6.8 km/s for the upper and lower crusts, and were found to be ~8.0 km/s in the underlying mantle. Crustal thicknesses ranged between 30 and 40 km in the region, with upper and lower crustal thicknesses of 11-19 km and 15-25 km, respectively. *Bowland and Rosencratz*, 1988 investigated the upper crustal structure of the Caribbean sea region from multichannel seismic refraction, and found that oceanic crust is between 10 and 15 km thick, with P-velocities around 4.5 km/s in the upper crust, 7.0 km/s in the lower crust, and 8.2 km/s in the uppermost mantle.

From relocalization of hypocenters, *Ojeda and Havskov* [2001] developed a 1D crustal velocity model that improved location accuracy of local (crustal) seismicity, and *Ojeda and Ottemoller*, [2002] developed a local QLg tomography that defined several crustal regions according to attenuation values. *Ojeda and Havskov* [2001] developed a regional model with three layers for

the crust (32 km), with P-wave velocities of 4.8, 6.6 and 7.0 km/s with thicknesses of 4, 21 and 7.5 km respectively, and an upper mantle velocity between 8.0 and 8.1 km/s. A constant Vp/Vs ratio of 1.78 was determined for the entire data set. *Ojeda and Ottemoller* [2002], on the other hand, subdivided the central portion of the study area into 7 zones, according to attenuation characteristics of QLg. The principal regions with high attenuation correspond to active volcanic areas and the northeastern cordillera, which is characterized by young sedimentary rocks and lacustrine sediments, and high water content in the Bogotá altiplano.

Finally, as mentioned above, images of lateral P- and S-wave velocity variation for depths ranging between 12.5 and 155 km were produced in the recent tomographic study of *Syracuse et al.* [2016]. As the crustal slices in that study are directly comparable to our velocity models, we postpone the discussion of those images until section 6, where they will be compared to the results developed here from ambient noise tomography.

3. Data and Data Processing

3.1. The dataset

The dataset used in this study consists of the continuous recordings of the 50 seismic stations of the *Red Sismológica Nacional de Colombia* (RSNC), which is operated by the Colombian Geological Survey (SGC), and 3 nearby Global Seismograph Network (GSN) stations in Ecuador, Venezuela, and Panamá. In total, it makes a combined network of 53 permanent broadband stations that recorded continuously from 2012-04 through 2015-12. The equipment is quite heterogenous, and consists of a combination of Streckeisen STS-2, Güralp CMG-3T,

Güralp CMG3-ESP, Trillium 120p, Reftek 151-120A, and Reftek 152B-120 broadband sensors (flat response in velocity down to 120 s) feeding high-gain digitizers (Quanterra Q330, Güralp DM24, and Taurus) sampling continuously at 100 samples per second. We considered all accessible vertical component data within the recording time window from all the permanent stations. Figure 3 displays the location of the broadband stations, color-coded by recording time window duration, while Table 1 lists station coordinates and recording time windows. Realize that, because the network was gradually built, the amount of data available among the stations may vary. The final dataset offers good spatial and azimuthal coverage for the Colombian Andes and most of the Caribbean region of Colombia, with an average inter-station spacing of approximately 400 kilometers, and minimum and maximum inter-station distances of 20 km and 1300 km, respectively.

3.2. Empirical Green's functions

To retrieve the empirical Green's functions by cross-correlation, we followed the approach described in *Shapiro and Campillo*, [2004]*, Sabra et al.*, [2005] and *Bensen et al.* [2007], with modifications. Data processing can be divided into three stages: (i) pre-processing, (ii) cross-correlation, and (iii) stacking. Only vertical-component data were considered, which implies that only the Rayleigh wave portion of the empirical Green's function were reconstructed by cross-correlation. The aim of the pre-processing stage is to decrease the influence of earthquake signals and instrumental irregularities from the time-series prior to cross-correlation. It starts with cutting the continuous recordings into non-overlapping, 1-day long segments, which are demeaned, detrended, and tapered with a 5% cosine window. Instrumental responses are then

deconvolved from the daily time series to be bandpass-filtered between 0.01 and 0.2 Hz and decimated to 1 sample per second. Time- and frequency-domain normalization is then applied to remove the signature of seismicity within the frequency-band of interest. Temporal normalization is implemented through one-bit normalization, preserving the phase and neglecting amplitude variations within the time series [*Larose*, 2004; *Bensen et al.*, 2007]; frequency-domain normalization or "spectral whitening" normalizes spectral amplitudes to unit value without altering the phase, effectively broadening the frequency-band of the ambient noise recordings [*e.g. Bensen et al.,* 2007]. After time-frequency normalization is applied to all 1-day long segments, cross-correlations are computed in the frequency domain for all station pairs for frequencies between 0.01 to 0.2 Hz.

Stacking of the one-day long ambient-noise cross-correlations is achieved through the time-frequency phase-weighted stack (tf-PWS) of *Schimmel et al.* [2011]. The tf-PWS makes use of the S-transform [*Stockwell et al.*, 1996] to obtain a time-frequency representation for each cross-correlogram, so that the stacking is controlled with frequency-dependent resolution while maintaining a close relationship between the time-averaging and the Fourier spectrum [*Stockwell et al.*, 1996].

The time–frequency dependent phase coherence attenuates incoherent noise, because it allows for the determination of weak amplitude signals that are more phase-coherent than background noise. Signals obtained with this strategy have a signal-to-noise ratio (SNR) greater than those obtained with conventional methods [e.g. the classical correlation and stack method; *Villaseñor et al.,* 2007; *Yang et al.,* 2007; *Bensen et al.,* 2007; *Lin et al.,* 2008].

A total of 1286 cross-correlation stacks were constructed from the assembled dataset. A record section of cross-correlations is displayed in Figure 4, where only those cross-correlations with SNR > 20 are included for displaying purposes. The empirical Green's functions clearly emerge from the ambient seismic noise for distances ranging between about 50 km and over 1100 km. Moreover, travel times correspond to propagation velocities between ~2.1 and ~3.2 km/s, which are consistent with short-period, fundamental-mode, Rayleigh-wave propagation.

Selection of stable empirical Green's function was achieved through analysis of the coherence functional [*Schimmel et al.,* 2011], which measures the similarity of two time-series. First, waveform similarity was calculated using the zero-lag cross-correlation between a reference trace (correlogram with maximum stack size) and a subset of correlograms that correspond to a fixed number of days, which are selected randomly with 30 days increments to the maximum stack length. Then, a plot of similarity versus number of days was built, so that signal emergence and minimum number of days could be assessed for each Green's function for several interstation raypaths and azimuthal directions. Figures 5 and 6 illustrate the process through select examples corresponding to two different inter-station raypaths. The first raypath (Fig. 5e) travels through the central portion of the Colombian Andes in the N-S direction, and has an interstation distance of 423 km, while the second raypath (Fig. 6e) samples the Eastern portion of the Caribbean region and the Central Cordillera and has an interstation distance of 723 km. The figures reveal that, for distances greater than 700 km, about 450 days (Figure 6a,b) are necessary for convergence of the empirical Green's function; while for shorter raypaths of ~400 km, about 250 days seem to be enough (Figs 5a,b). This relatively large number of days required to achieve convergence contrasts with other studies in the stable portion of the continent, where just a few

weeks were enough to achieve convergence [e.g. *Dias et al.*, 2015]. We think that the observed rate of convergence is probably due to the intense seismic activity in the country, especially around the Bucaramanga nest [*Ojeda and Havskov*, 2001; *Zarifi et al.*, 2007; *Prieto et al.*, 2012], which could not be fully mitigated through the standard time-frequency normalization process. This might be especially true for the URI-HEL interstation path (Figure 6a), which intersects the Bucaramanga nest. Note how stacking of just 100 days is not enough to recover both the causal and acausal portions of the empirical Green's function, which is eventually recovered when adding additional one-day correlograms to the stack.

4. Phase- and Group-Velocity Tomography

4.1. Measuring group and phase velocity

The empirical Green's functions extracted in the previous section are dominated by surface-waves. Group velocity can thus be measured by applying the time-frequency analysis (FTAN) of *Levshin et al.* [1972] and *Levshin and Ritzwoller* [2001], which is based on the application of a series of narrow bandpass-filters to the signal. The FTAN method also implements a phase-matched filter that cleans dispersion curves from multi-pathed signals [*Herrin and Goforth*, 1977], so that the whole procedure can be easily automated [*Levshin and Ritzwoller,* 2001]. Phase velocity can be measured from the empirical Green's function as [*Lin et al.,* 2008]

$$\varphi(t) = kr + \omega t + \lambda + 2\pi N + \frac{\pi}{2} - \frac{\pi}{4}, \quad (1)$$

where k is the wavenumber, r the interstation distance, ω is the instantaneous frequency, t is the observed group-delay time, λ is the source phase or initial phase, and $2\pi N$ represents the phase ambiguity term (with $N = 0, \pm 1, \pm 2, ...,$). The phase corrections at the end of eq. (1) are specific to empirical Green's functions from ambient noise cross-correlations. The $\pi/2$ represents the phase shift from the negative time-derivative, and the $\pi/4$ arises from interference of the non-stationary terms in a homogeneous noise source distribution [*Lin et al.,* 2008; *Snieder,* 2004]. The phase ambiguity ($2\pi N$) is assessed by comparing the long-period phase-velocity measurements to a reference curve, which here is based on the PREM global earth model [*Dziewonski and Anderson*, 1981]. Sometimes, FTAN fails to measure the dispersion curve due to abrupt jumps or spectral gaps. To overcome this shortcoming, the period window is reduced sequentially in bands from 5-100 s down to 5-30 s, in steps of 10 s.

To measure dispersion velocity, we first reject empirical Green's functions with SNR < 7 at each period. The tf-PWS technique of *Schimmel et al,* [2011] is quite successful in attenuating incoherent noise in the stacked cross-correlations, so the SNR is improved dramatically after increasing the number of available daily cross-correlations. Following *Bensen et al*. [2007], we also eliminate dispersion measurements on cross-correlations with inter-station distances less than three wavelengths. To estimate uncertainties, we applied the repeatibility of measurements through seasonal variability. First, we selected 12 overlapping, 3 month-long time series for each interstation path for a time window between 2012 to 2015. The first 3-month stack will include data from January through March for each year between 2012 and 2015, the second 3-month stack will include data from February through April for each year between 2012 to 2015, and so on. After the dispersion curve for group and phase velocity is measured for all the 3-month long

cross-correlations, the standard deviation is calculated if at least half of the twelve 3-month stacks have a SNR greater than 7. If this criteria is not satisfied, the standard deviation is taken as the average value for all the raypaths.

Figures 5 and 6 also illustrate the measuring of dispersion velocities through two select empirical Green's functions. The figures reveal that the stability of the dispersion curves is slightly dependent on interstation distance, especially for periods longer than 20 s, where microseismic energy decays abruptly [*Bromirski*, 2009]. For the raypath through the central part of the Colombian Andes (Fig. 5), the dispersion curve reveals normal dispersion between 7-22 s with an average group velocity of ~3.2 km/s. The standard deviations, calculated from seasonal variability, are around 0.05 km/s and 0.03 km/s for group and phase velocity, respectively (Fig. 5c). For the raypath sampling the Eastern portion of the Lower Magdalena Basin and the Central Cordillera (Fig. 6), we observe a gradual increase in both phase and group velocity between 7-40 s, with standard deviations of ~0.07 km/s for group velocity and ~0.02 km/s for phase velocity (Fig. 6c). The final results of FTAN processing are shown in Figures 5d and 6d, where the dispersion curves for phase and group velocity are clean of spurious and multi-pathed signals. Also note how for the longer raypath (Fig. 6c), the dispersion curve obtained from the empirical Green's function is not stable at long periods when stacking only 100 days, in accordance with the lack of convergence of the empirical Green's function noted in the previous section.

The average group and phase velocity uncertainties, number of measurements that passed the quality control, average arrival time uncertainty, and average raypath length for each period are displayed in Figure 7. Figure 7a shows that for periods between 6 and 30 s the average group

velocity uncertainties are less than 0.1 km/s, dropping significantly for intermediate periods to ~0.05 km/s. For phase velocities, the standard deviation is much smaller, ranging from ~0.06 to ~0.1 km/s, with a minimum of 0.04 km/s at 14-22 s. Our uncertainties are similar to those reported in independent studies with similar datasets [*e.g. Lin et al.,* 2007; *Mottaghi et al.,* 2013; *Dias et al.*, 2015]. The greatest uncertainties are for periods > 30s, which we believe are due to the decrease in amplitude of the microseismic noise spectrum at those periods that make it difficult to recover the empirical Green's function. Travel time uncertainties as a function of period are displayed in Figure 7c, which will be used to weight the datasets in the tomographic inversion (section 4.2). Figures 7b and 7d show the number of raypaths and the average path length in each period for the selected observations, respectively, demonstrating that the optimal coverage is in the intermediate period range of 12-30 s.

4.2. Tomographic Inversion

The inter-station dispersion curves developed in the previous section are next inverted tomographically to produce phase and group-velocity maps of NW South America at different periods. The Fast Marching Surface Tomography (FMST) package of *Rawlinson and Sambridge* [2005] is utilized for the inversion. The formulation of the forward problem is based on the solution of the Eikonal equation by finite differentiation of the phase or group delays, thus mapping the evolution in time of the first-arriving wavefronts across the study area. This eikonal solver, known as the Fast Marching Method (FMM), is described in detail elsewhere [*Sethian*, 1996; *Sethian and Popovici*, 1999], and its migration to the surface-wave tomography problem can be found in *Rawlinson and Sambridge* [2005]. This methodology is advantageous when the

stations coverage is sparse, providing stable, robust solutions for wave propagation in heterogeneous media [*Rawlinson and Sambridge*, 2004]. The inversion procedure follows an iterative, nonlinear scheme know as the subspace method [*Kennett et al.*, 1988], which acts by projecting the quadratic approximation of the objective function of the inversion into a multi-dimensional subspace. Therefore, at each iteration, the optimization functional *S(m)* is projected into a subspace of dimension smaller than the original parameter space in order to reduce the computational effort in the local linearization. More details of the subspace method can be found in *Rawlinson and Sambridge* [2004]. Because of the size of the study area and the amount of data, we found that it is not necessary to project in greater than one dimension. The optimization functional is defined as,

$$S(m) = \Big(d - g(m)^T C_d^{-1}\big(d - g(m)\big)\Big) + \epsilon(m - m_0)^T C_m^{-1}(m - m_0) + \eta m^T D^T D m \quad (2)$$

where m_0 is the reference model, C_m is the *a priori* model covariance matrix, C_d is the data covariance matrix, and D is the second derivative smoothing operator. The parameters ϵ (≥ 0) and η (≥ 0) are the damping and smoothing regularization parameters, respectively. The smoothing parameter controls the trade-off between data misfit and model smoothness, while the damping parameter controls the trade-off between data misfit and proximity of the inverted model to a reference model m_0 [*Rawlinson and Sambridge*, 2005].

A discretized grid consisting of 0.5˚ × 0.5˚ cells was defined throughout the study area, with a constant initial velocity taken from the average observed group or phase velocity at each period. Uncertainties from 3 month-stacks (Figure 7c) were then included in the objective function (Eq.

4) to define the covariance matrices. Appropriate regularization parameters, ϵ and η, in the objective function were determined through L-curve analysis [*Aster et al.*, 2012]. We explored several combinations of regularization parameters by varying the damping and smoothing from 0 to 100 in steps of 0.01, 0.1, 1.0, and 10 for all periods. Figure 8 displays sample trade-off curves for both group and phase velocity tomographic inversions at 22 s, demonstrating values of $\epsilon = 9$ and $\eta = 10$ for group velocities and $\epsilon = 3$ and $\eta = 2$ for phase velocities. Parameters for tomographic inversions at other periods are similar, ranging between 0.3 and 10 for smoothness (ϵ) and between 0.3 and 9.0 for damping (η). Furthermore, the tomographic inversions converge after six iterations for the selected regularization values (Fig. 8c). Figure 8b, also shows that model variance decreases to an average of ~0.015 km^2/s^2 (group) and ~0.01 km^2/s^2 (phase) with our selected parameters or, equivalently, to average standard deviations of ~0.12 km/s and ~0.1 km/s, respectively. These values are within the confidence bounds of the observed dispersion curves obtained from the 3-month stacks and are sufficiently high to indicate that the data are not overfitted.

The robustness of the tomographic inversions depends mostly on the azimuthal coverage of the seismic raypaths. Figure 7b already showed that path density is best for periods between 12 to 30 s, with over 800 measurements for both group and phase velocities. However, the azimuthal raypath distribution is not uniform in the study region, being highest for the central part of Colombia and gradually decreasing towards the edges of the study area. To assess the bias due to poor raypath coverage, we used standard checkerboard tests at each period. The tests were performed using input models of alternating fast and slow velocity defined through a grid of nodes with B-spline cubic interpolation with the same grid size, same ray-path geometry, and

same regularization values as for the real model. Each input model had velocities varying ±0.5 km/s around a background velocity for each dispersion map. Additionally, Gaussian noise was added to the synthetic group and phase arrival times for all station pairs. A series of checkerboard tests mimicking the ray-path coverage of all inversion periods (i.e., 7 s, 14 s, 22 s, 30 s, 34 and 38 s) are shown in the Figure 9. The recovery is very good in the center of the study area, especially in the Andean region, but the recovery worsens in the northern part of the Caribbean region (Guajira peninsula), the Pacific coast bordering with Ecuador, and also towards the edges, especially at long periods. Nonetheless, the recovery of the velocity contrasts is excellent. Similar results hold for checkerboard tests using phase velocities (not shown).

4.3. Phase and Group Velocity Images

Figure 10 displays the tomographic results for group- and phase- velocity for periods of 7, 22 and 34 s; the remaining group and phase velocity maps can be found in the Supplementary Material section (Figures S1 and S2). The group and phase velocity maps are organized in order of increasing period, therefore increasing penetration depth into the crust. Group velocities, for instance, sample down to a depth approximately equal to one-third of their wavelength; thus, short periods (7 - 10 s) are a good indicator of sedimentary structure, while periods above 30 s are primarily sensitive to the S-wave velocity structure at ~30 km of depth. The tomographic maps at short periods (7 s) show an excellent correlation with surface geology (recall Figure 1). The main sedimentary basins, such as the Lower and Middle Magdalena valleys, the Túmaco basin along the Pacific coast, the Maracaibo Basin in Venezuela, and the sediments covering the Panamá arc, are clearly depicted by slow phase and group velocities, as well as the Eastern Cordillera between latitudes 4˚N - 6˚N, which is geologically expressed as a Cretaceous

sedimentary basin. In contrast, the provinces composed of igneous-metamorphic complexes, such as the Santa Marta massif, the Santander massif, the Central Cordillera - which includes the Antioquia and Ibagué batholiths (AB, IB) - the Western Cordillera, and the southern segment of the Eastern Cordillera - which encompasses the Garzon massif - are mapped with higher-than-average velocities.

At intermediate periods of 22 s a similar pattern is observed, especially for group velocities. This is because some of the sedimentary structure leaks into the longer periods, which keep some sensitivity to shallow structure as well as upper crustal structure. This is especially true for the accretionary wedge making up the Caribbean in the Sinú-San Jacinto fold-belt and the Lower Magdalena Basin regions along the Atlantic coast of Colombia, which consist of ~10 km thick deposits [*Toto and Kellogg*, 1992; *Vernette et al.*, 1992; *Montes et al.*, 2010; *Lara et al.*, 2013] and for the sedimentary basins along the Pacific coast that possess a similar accretionary wedge, although not as thick as in the Caribbean. Phase velocities, on the other hand, seem to be sampling deeper structure when compared to the corresponding group velocities. Slow velocities are still mapped within the Caribbean basins, but slow velocities also correlate with active volcanic regions along the Central and Eastern cordilleras. In contrast high-speed anomalies are observed along the Pacific coast and Eastern Llanos, perhaps resulting from a thinner crust under those regions. A similar interpretation seems to hold at periods of 34 s for both group and phase velocities, indicating that group velocities are no longer sensitive to shallow sedimentary structure, although slow velocities in the Panamá arc and the Lower Magdalena Basin might still be related to thick sedimentary depositions (recall section 2). Finally, faster phase velocities are observed in the Maracaibo and Caribbean basins, perhaps sensing mantle velocities under a thin

crust. The correlation of slow velocities under the Central Cordillera with active volcanics is, nonetheless, remarkable.

5. Shear-wave Velocity Models

5.1. Inverting dispersion for S-velocity

From the tomographic maps shown in Figure 10, local dispersion curves can be extracted from each grid point at successive periods ranging between 6 and 38 s, and the resulting phase- and group-velocity dispersion curves can then be jointly inverted to develop S-wave velocity-depth profiles for each grid point. Inversion of group and phase velocities has been performed through the Neighborhood Algorithm (NA) of *Sambridge* [1999a], as implemented in the software package Dinver (http://www.geopsy.org) of [*Wathelet*, 2008]. This tecnique has been applied successfully by several authors [e.g. *Behr et al.,* 2010; *Kao et al.,* 2013; *Köhler et al.,* 2015; 2012] to estimate isotropic layered models from dispersion data. The implementation combines computation of dispersion curves (forward problem) through the *Dunkin* [1965] formulation and an improved version of the original NA. The implementation is based on a powerful geometric sampling with Voronoi cells, which explores the model space in a quasi-random, sequential, and non-uniform manner, taking into account previous estimations of the cost function to generate new and better families of solutions. The misfit function is optimized in a least squares sense (L2-norm) between the dispersion curve predicted by the model and that constructed from the surface-wave maps. The velocity search in the NA is performed by varying 20% the velocity in each layer.

We considered two starting S-velocity models in order to assess the variability of the inversion results. The first starting model is a modified IASP91 model [*Kennett and Engdahl*, 1991] with Moho depths constrained from crustal thickness estimates developed by *Poveda et al.* [2015]. The Vp/Vs ratio is constrained to be between 1.60 and 1.85, consistent with typical values of the rocks in the continental crust [*Christensen*, 1996]; and density is kept to the values from IASP91 with a 10% perturbation. *Wathelet et al.*, [2004] demonstrated that influence of density in the dispersion curve is minimal. The second model is based on a crust of uniform shear wave velocity of 4 km/s with layer thickness of 4 km, with no *a priori* constraints on crustal thickness. Vp/Vs varies in the same way as for the first model. Finally, the density varies 20% around a starting density of 3.0 g/cm^3 for each layer.

The NA search in the model space starts with 100 models, and the 50 best Voronoi cells in the model space are then selected to generate 100 new models during several iterations. The inversion is stopped after 250 iterations, resulting in 25,000 shear velocity models being evaluated at each grid point. From the set of 25,000 models examined during the NA process, we select and average the 500 best-fitting models to obtain a representative model for each grid point. Figure 11 displays inversion examples at three select locations starting from the constrained IASP91 velocity model, where a good fit between observed and predicted dispersion curves can be observed. Optimal misfit values are around 0.06 km/s, with the corresponding best-fitting models being concentrated within a narrow portion of the model space. The select models are located in the Santa Marta massif (Fig. 11a), the Western Cordillera (Fig. 11b), and between the Western and Central cordilleras (Fig. 11c). Tests of depth-resolution for the

dispersion curves are given in the Supplementary Material (Fig. S3), showing that negative, delta-like anomalies interspaced at depths of 10, 20, 30 and 40 km, respectively, are recovered at the right depths for spikes shallower than 40 km. Our S-wave models are thus only reliable for depths down to ~35 km.

The uniqueness of the results is assessed from the similarity of the velocity models developed from the two starting models (constrained IASP91 and unconstrained, uniform crustal velocity). A detailed comparison is provided in the Supplementary Material (Fig. S4), showing histrograms of RMS between the inverted S-velocity models developed from the two starting models that reveal differences are small, especially in the upper crust. Somewhat larger differences begin to appear after 30 km, concluding that the dependence with the starting model is minimal. For interpretation, we will take the results from the IASP91 starting model with crustal thickness constraints. Maps of average misfit distribution between observed and predicted dispersion velocities are given in the Supplementary Material (Fig. S5). The misfit varies between 0.01 and 0.15 km/s, with overall better fits in the Andean Region (misfit < 0.06 km/s) than in the Caribbean and Pacific coasts (< 0.1 km/s, with local occurrences of 0.1-0.15 km/s).

Finally, to check the robustness of some crustal anomalies – specifically, those under thick sedimentary layers such as the Lower Magdalena Basin - we performed two synthetic tests (Figure S6). The first test consists of a spike test for the 30 s group velocity tomography, concluding that anomalies for this period are well recovered. The second test consists of an inversion of synthetic “data” generated after assuming a 30 km thick crust with a 10 km thick sedimentary layer. This second test demonstrates that, although sedimentary velocities are

smeared into the shallower basement (down to ~15 km depth), they do not pervade the entire crustal column.

5.2. Models of S-velocity variation

The suite of 1D S-velocity profiles were assembled to build maps of lateral S-velocity variation for depths ranging between 5 and 35 km. Solutions generated from the IASP91 model with Moho depth constraints were selected for the construction of the maps. The minimum curvature interpolation method of *Smith and Wessel* [1990], with a tension factor of T=0.25, was considered for this purpose. A number of velocity slices are presented in Figure 12 at depth intervals of 5 km. The S-velocity maps show features similar to the dispersion velocity maps, with shallow slices (5-10 km depth) mostly correlating with surface geology and deeper slices (25-35 km depth) mostly correlating with the location of active surface volcanism.

More in detail, at 5 km depth (Figure 12a), we find marked slow S-velocity values on the northwestern side of the Sinú and San Jacinto belts (~2.4 km/s), Maracaibo Basin (~2.7 km/s), the Eastern Cordillera between 4˚N-5˚N (~2.7 km/s), and the Pacific coastal basin (~2.5 km/s), all of them correlating with the presence of sedimentary rocks (Figure 1). High velocities of ~3.6 km/s characterize the northern Central Cordillera, especially in the Antioqueño Plateau and the Antioqueño Batholith. This region is characterized by the intrusion of Mesozoic quartz diorite batholiths and plutons [*Restrepo-Moreno et al.*, 2009], with metamorphic basement of Paleozoic and Precambrian ages [*Case et al.,* 1971]. Batholiths of Jurassic age [*Tschanz et al.*, 1974; *Cardona et al.*, 2011] present in the northernmost part of Colombia, such as the Santa Marta

massif, also correlate with relatively high velocities (~3.2 km/s). Finally, high-velocity values of ~3.3 km/s are observed in the Eastern Cordillera, Middle Magdalena Valley, and Central cordillera south of ~4˚N, correlating with mapped outcrops such as the Garzón Massif, the Quetame Massif, and with Jurassic plutonism under the Central Cordillera.

Similar patterns are observed at 10 km depth (Figure 12b), although some slow-velocity features start to fade away. This is the case of the Panamá arc, where velocity increases from 2.8 km/s to 3.1 km/s at 5 and 10 km, respectively, and the central segment of the Eastern Cordillera, where the velocity estimated is ~3.0 km/s. High velocities of ~3.6 km/s north of the Central Cordillera, nonetheless, remain.

At 20 km depth, low-velocity anomalies (~3.0 km/s) are observed throughout the Caribbean region (SSJB, PB, SJB) and the central segment of the Eastern cordillera (~3.3 km/s). In contrast, the northern segment of the central cordillera, the middle Magdalena Valley and the Santander Massif (EC northernmost flank), and Santa Marta massif display high velocities of ~3.7 km/s with little lateral variation among them. This high-velocity pattern extends further down to 25 and 30 km depth. At 25 km depth under the Pacific coast, South of 4˚N, high velocities (> ~4.0 km/s) are also observed. More interestingly, within the same depth-range, low-velocities of ~3.4 km/s are found under the volcanic complexes, especially under the volcanoes near the border with Ecuador and those located between 3˚N - 5.4˚N (Figure 12d).

At 30 - 35 km depth, we find high velocities (> 4.1 km/s) along the Pacific coast (Tumaco basin, Panama arc), part of the Western Cordillera, Lower Magdalena Basin, and the Llanos Basin,

probably reflecting thin crust. In the Central and Eastern Cordilleras slow velocities around 3.7 km/s dominate the regions, consistent with the presence of a crustal root. Slow velocities (< 3.5 km/s) along the southern Central Cordillera still correlate with active volcanic systems located on the surface, and similar slow velocities are also observed in the central part of the Eastern Cordillera, approximately coinciding with the location of inactive volcanism. Slow velocities are also observed at these depths in the southern flank of the Lower Magdalena Basin under the San Jorge Basin. A possible origin for these anomalies is discussed in the next section.

6. Implications for magmatism and (magmatic) overprint in the upper plate.

The velocity slices described in the previous section show a generally good agreement with previous studies [*Meyer et al.*, 1976; *Mooney et al.*, 1979; *Flueh et al.*, 1981] and, at shallow depths, correlate well with major surface geological features [*Gómez et al.*, 2007a; *Veloza et al.*, 2012]. Our results are directly comparable to those produced by *Syracuse et al.* [2016]. From the joint inversion of local P- and S-wave arrival times reported by the RSNC, regional surface wave dispersion in the 10-70 s period range, and gravity data from the Earth Gravitational Model 2008 [EGM2008; *Pavlis et al.,* 2012], *Syracuse et al*. [2016] produced images of lateral P- and S-wave velocity variation down to 155 km depth for the Colombian Andes and adjacent regions. The S-velocity depth-slices at 12.5 km and 32.5 km (see Fig. 6 in *Syracuse et al*., 2016) are – at long wavelengths - similar to our S-velocity maps at 10 and 35 km depth, respectively (Figs 12b and f), displaying similar patterns of fast and slow S-velocity throughout the area. At shallow crustal depths, for instance, both studies show slow velocities in the Lower Magdalena Basin and the Eastern Llanos, separated by faster velocities in the intervening cordilleras; and, at intermediate

crustal depths, both studies display slow velocities in the Lower Magdalena Basin and under the volcanic areas of the Eastern and Central cordilleras. Due to the inclusion of shorter periods in the development of our velocity models, however, the resulting velocity images have better resolution at short wavelengths. Our images, for instance, clearly depict the fast velocities characterizing the Antioqueño batholith at shallow depths (Fig. 12a,b) and successfully image the shift in volcanism following the trend marked by the Caldas tear at intermediate depths (Fig. 12d,e), which were not resolved by *Syracuse et al.* [2016].

6.1. Magmatic overprinting

Figures 12a-b show that the signature of sedimentary basins and accretionary wedges can be tracked through slow S-velocities (< 3.0 km/s) at shallow depths (5-10 km). In the Lower Magdalena Basin, slow S-velocities are observed along the Sinú-San Jacinto fold belt (SSJB), Plató-San Jorge basin, and Cesar-Rancheria basins, where sediment thickness can reach values of 3-12 km [*Toto and Kellogg*, 1992; *Vernette et al.*, 1992; *Montes et al.*, 2010; *Lara et al.*, 2013; *Sanchez and Mann*, 2015]; the Cesar Rancheria basin, however, is not clearly discriminated in the shear wave velocity maps because the dimensions (20–30 km) are lower than the resolution length (~50 km) of the velocity maps. Similarly, the Plató and San Jorge Basins - also characterized by thick sedimentary sequencies - display slow S-velocities. And slow velocities are also found in the Maracaibo Basin in Venezuela, where sediment thickness varies between 3 - 9 km [*Mann et al.,* 2006]. Slow velocities (2.8-3.0 km/s) are also observed under the central flank of the Eastern Cordillera (4˚N to 6.5˚N, figure 12a,b), which is considered a fold and thrust belt with Cretaceous sedimentary cover units [*Mora and Parra*, 2008; *Horton et al.*, 2015], and

the neighbouring Middle Magdalena Valley, which is covered by Quaternary-Neogene sedimentary rocks [*Mora et al.*, 2006; *Parra et al.*, 2009]. These anomalies do not show continuity at larger depths, as sedimentary basins are shallow features that are confined within the shallow crust.

Some shallow, high-velocity anomalies also lack continuity at depth. High velocities are, for instance, observed in the Ibagué Batholit and paralleling the volcanic line under the Central Cordillera; however, these anomalies are replaced by low-velocity anomalies at larger depths of 20-35 km (Figs 12c-f). As argued in the next section, we believe that velocity anomalies below those depths are dominated by the signature of subduction-related volcanism, implying that the geological formations observed at surface levels, which attest to the accretionary and deformational history of the northeastern Andean region, are being overprinted at depth by younger magmatism.

In contrast, some high-velocity anomalies do have continuity at depth. High velocities are observed in the Santa Marta Massif and Santander Massif (SM) down to ~30 km depth (Figs 12a-e), reflecting the presence of an outcropping crystalline basement, Jurassic Plutonism, and Precambrian metamorphic rocks [*Cardona et al.,* 2011]; and fast velocities are also observed along the Central Cordillera, which can be traced down to 35 km depth north of 5^{o}N latitude and extending laterally into the Middle Magdalena Valley (Figs 12a-f). According to *Montes et al.* [2005], this whole region represents a unique crustal block with a more rigid behavior and less deformation than the surrounding Eastern Cordillera, consistent with persistently fast velocities.

This would conversely attest to the lack of magmatic overprinting in these areas due to the absence of volcanic activity in this region. Magmatic overprinting at depth of surface geological features in the Colombian Andes seems thus to be dictated by the geometry and segmentation of the subducting Nazca and Caribbean slabs.

6.2. Subduction-related volcanism

Active volcanism in Colombia is presently found along the Central Cordillera, south of ~5^{o}N latitude (Fig. 1), and has been related to the subduction of the Nazca Plate along the Pacific margin of South America. This volcanism is generally described as mainly explosive in character and andesitic in composition [e.g. *Marín-Ceron et al.,* 2010]. The strong correlation between slow S-velocities at intermediate depths (25-35 km) and surface volcanism in the CC, makes us think that those velocities are related to magma production along the subduction front. The magmatic evolution of the Colombian Andes was investigated in *Weber et al.* [2002] from the analysis of deep crustal xenolith suites. They proposed a model for the deep Andean crust in which basaltic components (e.g. oceanic plateau) and minor sediment are incorporated into the subduction-accretion complex, with areas of possible melt formation within the mantle wedge, mantle-crust transition, and accreted lower crust. Considering that our observed S-velocities display a similar S-velocity range of 3.4–3.6 km/s within the entire 25–35 km depth-range, which exclude a purely thermal origin, and that the xenolith suite does not display evidence of pervasive crustal melting [*Weber et al.,* 2002], we conclude that the observed slow S-velocities likely correspond to subduction-related magmas ponding at mid-crustal depths.

More enigmatic is the presence of even slower S-velocities (3.2-3.6 km/s) in the same depth-range under the inactive volcanoes of the Eastern Cordillera (Fig. 12d-f). Volcanism in the EC is concentrated in the Paipa-Iza volcanic complex, which is believed to have formed during the late Pliocene when the Cordillera reached its present elevation [*Pardo et al.*, 2005]. Recent thermo and geochronological constraints on the eruption history of this complex developed from zircon fission-track analysis and U-Pb data have bracketed the time of this volcanic activity between 5.9 Ma and (at least) 1.8 Ma [*Bernet et al.*, 2016]. Interestingly, the study argues that hydrothermal activity, with water temperatures up to 73^{o}C, CO_2 gas seepages associated with regional faults, and a strong local geothermal gradient of 74 ^{o}C/km, support the existence of a magma chamber at shallow depths. If this inference were correct, an interpretation of the observed slow S-velocities under the volcanic complex as deriving from partial melts – similar to the interpretation under the active volcanism of the Central Cordillera – would be plausible. Indeed, bulk Vp/Vs ratios in the area are high, around 1.82-1.86 [*Poveda et al.,* 2015], as well as Lg attenuation [*Ojeda and Ottemoller,* 2002], consistent with the presence of partial melts in the crust. Our results therefore support *Bernet et al.* [2016]'s conclusion that volcanism under the EC might be inactive but not necessarily extinct. Moreover, magmatic activity in the region might help explain the non-isostatic residual topography of the region reported by [*Yarce et al.*, 2014], as the thermally perturbed asthenospheric wedge expected in the region [*Chiarabba et al.,* 2016] might provide the necessary buoyancy to explain the elevations.

Alternatively, low-velocities may also be an indication of aligned anisotropic minerals. High Vp/Vs ratios might be related to high pore fluid pressure and crack anisotropy [*Wang et al.*, 2012], and recent local S-splitting estimations [*Idárraga-García et al.,* 2016] display high

anisotropy values of 3.09% and 3.43% for the EC crust. Moreover, it is well known that the EC is a deformed NE-trending fold-and-thrust belt, and several authors have documented the crustal shortening, thickening and uplift that occurred in this region [*Colletta et al.*, 1990; *Dengo and Covey*, 1993; *Cortés et al.*, 2006; *Mora et al.*, 2010] during late Miocene [*Taboada et al.*, 2000; *Egbue et al.*, 2014]. The detachment surface depth under EC fold-and-thrust belt is postulated to be between 20 and 30 km depth [*Mora and Parra*, 2008], which correlates well with the termination of slow S-velocities at depth (Figure 12).

Even more enigmatic is the presence of similarly slow S-velocities under the Lower Magdalena Basin, where slower-than-average S-velocities are found for almost the entire depth-range (Fig. 12a-e). S-velocities are 2.4-2.8 km/s down to ~10 km depth, which have been found consistent with the accretionary prism reported earlier (section 6.1); S-velocities of 3.0-3.4 km/s at 20-30 km, however, are harder to explain. To help clarify this issue, a NW-SE trending cross-section crossing the LMB and EC regions is displayed in Figure 13a. The figure shows that the Caribbean region, like the Eastern Cordillera, consists of a shallow layer of slow (2.4-2.8 km/s) S-velocities overlying an also slow (3.0-3.4 km/s) upper-middle crust. Moreover, also like the EC, bulk Vp/Vs ratios in the Caribbean region are in the 1.82-1.86 range [*Poveda et al.,* 2015], which would again be consistent the presence of partial melts. Strikingly, this region is regarded as amagmatic.

We argue, nonetheless, that partial melts might be present within the Lower Magdalena basin. A recent study of field, geochemical, gechronological, biostratigraphical, and sedimentary provenance of basaltic and associated sediments in northern Colombia has revealed the existence

of Middle Miocene (13-14 Ma) mafic volcanism within the Caribbean continental margin [*Lara et al.,* 2013]. In particular, geochemical analysis showed that basalts were formed by asthenospheric melting at shallow depths mixed with some additional slab input and, together with biostratigraphic results, demonstrated that they were deposited in a platform setting. Considering the low-angle subduction of the Caribbean plate and the corresponding absence of a mantle wedge (recall section 2.1), the authors proposed the presence of a vertical tear in the subducting plate through which asthenospheric melts would have found their way through while acquiring the observed slab input. Vertical tears might result from along-strike extension related to the strong curvature of the subduction as it passes around the NW corner of South America, and this type of extension was invoked in *Bernal-Olaya et al. [2015a]* to explain the origin of the Plato and San Jorge basins within the Lower Magdalena Basin. Assuming a speed of 20 mm/yr for the Caribbean plate relative to the South American plate, and a position of the tear under the continental platform at 13-14 Ma, it is easy to calculate that the tear would be presently located 260-280 km further inland under the South American plate. This distance-range is consistent with the location of the Caribbean low S-velocity region (Fig. 12c-e), suggesting that the Caribbean slab might have been breached by asthenospheric melts that are now ponding at mid-crustal depths within the overriding plate.

As stated before (recall section 5.1 and Figure S6), we are confident that the mid-crustal, low-velocity anomaly under the Lower Magdalena Basin is not an artifact from the inversion procedure. Moreover, the trace of the Romeral Suture - which is regarded as a major fault separating the oceanic crustal rocks of the Western Cordillera from the continental-affinity basement to the East *[Restrepo and Toussaint, 1988; Taboada et al., 2000; Cediel et al., 2003]* -

is very consistent with the velocity contrast separating the Central Cordillera from the sedimentary units described above at shallow depths (Figs 12a-b), suggesting a continuation of this fault into the Lower Magdalena Basin (Fig. 12a) *[Taboada et al., 2000; Toro et al., 2004; Bernal-Olaya et al., 2015b]*. This consistency degrades at larger depths (Figs 12d-f), suggesting that the low-velocity anomaly under the Lower Magdalena Basin at mid-crustal depths is not related to sedimentary structure.

However, we do acknowledge that the large lateral extent of the anomaly is at odds with the lack of surface volcanism associated with it, and that alternative mechanisms might be at play. Low velocity zones may also be related to fluid migration along major faults zones, especially when coincident with large Vp/Vs ratios [*Zhao et al.*, 1996; *Thurber et al.*, 2003]. Such relationships have been recently invoked, for instance, to explain large Vp/Vs ratios within the western Hispaniola crust [*Corbeau et al.*, 2017] and, perhaps more importantly, to explain low velocity anomalies along the Sinú and Romeral Fault system *[Bernal-Olaya et al, 2015c]*. In the case of the Lower Magdalena Basin anomaly, the Romeral fault system – which, as described above, might actually be extending under the basin - could provide the paths for fluids emanating from the subducting Caribbean plate to infiltrate the surrounding continental mantle and reach mid-crustal depths. Fluid migration along the Romeral fault system would then explain both the low velocities reported in this study, as well as high bulk Vp/Vs ratios reported in the receiver function study of *Poveda et al, [2015]*. Moreover, fluid expulsion might also provide an alternative explanation for the mid-crustal, low-velocity anomaly under the Eastern Cordillera, as *Bernal-Olaya et al. [2015c]* have related low-velocities at depths > 80 km near the Bucaramanga earthquake nest with such phenomenon.

Finally, we note that our velocity slices cleary image the signature of the "Caldas tear" postulated by *Vargas and Mann* [2013] at crustal depths within the overriding plate. As mentioned in section 2, the “Caldas tear” is an E-W trending feature that extends for ~240 km and separates two slab segments that subduct at different angles. The projection of the Caldas tear is superimposed in our S-velocity model (Figure 12d and 12e), showing it can be traced down to 20-35 km depth.

7. Conclusions

We have presented the first ambient noise tomography of the Colombian Andes and surrounding regions from recordings of 53 broadband seismic stations belonging to the *Red Sismológica Nacional de Colombia* (RSNC). A total of 1300 empirical Green’s functions - identified as fundamental-mode, Rayleigh waves - were recovered, covering much of the country and furnishing new constraints in areas where previous information was limited. Our results resolve geological features with high accuracy at shallow levels, as well as patterns associated with magmatism and plate segmentation at mid-crustal depths. More specifically, slow S velocities under the Central Cordillera have been attributed to accumulation of magmas in the middle crust generated in the underlying mantle wedge, and evidence of magmatic activity has been reported under the inactive volcanoes of the Eastern Cordillera. Slow S-velocities in the Caribbean middle crust have been related to asthenospheric melts that would have breached the Caribbean flat slab through a vertical tear. Alternatively, migration of fluids along faults from expulsion of nearby subducting slabs could provide a feasible explanation for such velocity anomalies.

Acknowledgments

The authors want to express their gratitude to the Colombian Geological Survey (Servicio Geológico Colombiano, SGC) for generously providing the data for conducting this study; in particular to Marta Calvache, technical director of geological hazards of Colombian Geological Survey and Viviana Dionicio, coordinator of the Seismological Network (Red Sismológica Nacional de Colombia, RSNC). Raw data is freely available and accesible to the scientific community through written request and justification addressed to the Colombian Geological Survey (sismologo@sgc.gov.co). E.P. acknowledges support from the Coordenação de Aperfeiçoamento de Pessoal de Nível Superior (CAPES) through a 4-year scholarship to complete his Ph.D. J.J. thanks CNPq for his research fellowship (CNPq, grant number 308171/2012-8). M.S. acknowledges support by Brazilian Science Without Border Program, grant No. 40.2174/2012-7. N.P.G. thanks to Colombian Geological Survey, contract No. 393-2016. Maps were produced using Generic Mapping Tools (GMT) software [*Smith and Wessel*, 1990]. We also thank to editor Martha Savage, the reviewer Paul Mann and an anonymous reviewer for improved the final manuscript.

References

Abdetedal, M., Z. H. Shomali, and M. R. Gheitanchi (2015), Ambient noise surface wave tomography of the Makran subduction zone, south-east Iran: Implications for crustal and uppermost mantle structures, *Earthq. Sci.*, *28*(4), 235–251, doi:10.1007/s11589-015-0132-1.

Aldrich, L. T., D. E. James, A. T. Linde, G. R. Ocola, G. R. Poe, and I. S. Sacks (1973), Project Nariño, *Carnegie Inst. Washington, Yearb*, *72*, 247–249.

Aster, R. C., B. B. And, and C. H. Thurber (2012), *Parameter Estimation and Inverse Problems*,

Elsevier.
Behr, Y., J. Townend, S. Bannister, and M. K. Savage (2010), Shear velocity structure of the Northland Peninsula, New Zealand, inferred from ambient noise correlations, *J. Geophys. Res.*, *115*(B5), B05309, doi:10.1029/2009JB006737.
Bensen, G. D., M. H. Ritzwoller, M. P. Barmin, A. L. Levshin, F. Lin, M. P. Moschetti, N. M. Shapiro, and Y. Yang (2007), Processing seismic ambient noise data to obtain reliable broad-band surface wave dispersion measurements, *Geophys. J. Int.*, *169*(3), 1239–1260, doi:10.1111/j.1365-246X.2007.03374.x.
Bernal-Olaya, R., J. Sanchez, P. Mann, and M. Murphy (2015a), Along-strike Crustal Thickness Variations of the Subducting Caribbean Plate Produces Two Distinctive Styles of Thrusting in the Offshore South Caribbean Deformed Belt, Colombia, in *Memoir 108: Petroleum Geology and Potential of the Colombian Caribbean Margin*, pp. 295–322, AAPG.
Bernal-Olaya, R., P. Mann, and A. Escalona (2015b), Cenozoic Tectonostratigraphic Evolution of the Lower Magdalena Basin, Colombia: An Example of an Under- to Overfilled Forearc Basin, *Mem. 108 Pet. Geol. Potential Colomb. Caribb. Margin*, 345–398, doi:10.1306/13531943M1083645.
Bernal-Olaya, R., P. Mann, and C. A. Vargas (2015c), Earthquake, Tomographic, Seismic Reflection, and Gravity Evidence for a Shallowly Dipping Subduction Zone beneath the Caribbean Margin of Northwestern Colombia, *Mem. 108 Pet. Geol. Potential Colomb. Caribb. Margin*, 247–270, doi:10.1306/13531939M1083642.
Bernet, M., C. Urueña, S. Amaya, and M. L. Peña (2016), New thermo and geochronological constraints on the Pliocene-Pleistocene eruption history of the Paipa-Iza volcanic complex, Eastern Cordillera, Colombia, *J. Volcanol. Geotherm. Res.*, doi:10.1016/j.jvolgeores.2016.08.013.
Boué, P., P. Roux, M. Campillo, and X. Briand (2014), Phase velocity tomography of surface waves using ambient noise cross correlation and array processing, *J. Geophys. Res. Solid Earth*, *119*(1), 519–529, doi:10.1002/2013JB010446.
Bowland, C. L., and E. Rosencratz (1988), Upper Crustal structure of the Western Colombian basin, Caribbean sea, *Geol. Soc. Am. Bull.*, *100*(4), 534–546.
Bromirski, P. D. (2009), Earth Vibrations, , *324*(5930), 1026–1027, doi:10.1126/science.1171839.
Cardona, A., V. A. Valencia, G. Bayona, J. Duque, M. Ducea, G. Gehrels, C. Jaramillo, C. Montes, G. Ojeda, and J. Ruiz (2011), Early-subduction-related orogeny in the northern Andes: Turonian to Eocene magmatic and provenance record in the Santa Marta Massif and Rancheria Basin, northern Colombia, *Terra Nov.*, *23*(1), 26–34, doi:10.1111/j.1365-3121.2010.00979.x.
Case, J. E., L. G. Duran S, L. Alfonsp, and W. R. Moore (1971), Tectonic Investigations in Western Colombia and Eastern Panama, *Geol. Soc. Am. Bull.*, *82*(10), 2685, doi:10.1130/0016-7606(1971)82[2685:TIIWCA]2.0.CO;2.
Cediel, F., R. Shaw, and C. Cáceres (2003), Tectonic Assembly of the Northern Andean Block, *eds., Circum-Gulf Mex. Caribb. Hydrocarb. habitats, basin Form. plate tectonics*, *79*, 815–848.
Chiarabba, C., P. De Gori, C. Faccenna, F. Speranza, D. Seccia, V. Dionicio, and G. A. Prieto (2016), Subduction system and flat slab beneath the Eastern Cordillera of Colombia, *Geochemistry, Geophys. Geosystems*, *17*(1), 16–27, doi:10.1002/2015GC006048.
Christensen, N. I. (1996), Poisson's ratio and crustal seismology, *J. Geophys. Res. Solid Earth*,

101(B2), 3139–3156, doi:10.1029/95JB03446.
Chulick, G. S., S. Detweiler, and W. D. Mooney (2013), Seismic structure of the crust and uppermost mantle of South America and surrounding oceanic basins, *J. South Am. Earth Sci.*, *42*, 260–276, doi:10.1016/j.jsames.2012.06.002.
Colletta, B., F. Hebrard, J. Letouzey, P. Werner, and J. L. Rudkiweicz (1990), Tectonic style and crustal structure of the Eastern Cordillera, Colombia, from a balanced cross section, *Pet. Tectonics Mob. Belts*, Pages 81-100.
Corbeau, J. et al. (2017), Crustal structure of western Hispaniola (Haiti) from a teleseismic receiver function study, *Tectonophysics*, *709*(April 2013), 9–19, doi:10.1016/j.tecto.2017.04.029.
Corredor, F. (2003), Seismic strain rates and distributed continental deformation in the northern Andes and three-dimensional seismotectonics of northwestern South America, *Tectonophysics*, *372*(3–4), 147–166, doi:10.1016/S0040-1951(03)00276-2.
Cortés, M., and J. Angelier (2005), Current states of stress in the northern Andes as indicated by focal mechanisms of earthquakes, *Tectonophysics*, *403*, 29–58, doi:10.1016/j.tecto.2005.03.020.
Cortés, M., B. Colletta, and J. Angelier (2006), Structure and tectonics of the central segment of the Eastern Cordillera of Colombia, *J. South Am. Earth Sci.*, *21*(4), 437–465, doi:10.1016/j.jsames.2006.07.004.
Dengo, C. A., and M. C. Covey (1993), Structure of the Eastern Cordillera of Colombia: implications for trap styles and regional tectonics, *Am. Assoc. Pet. Geol. Bull.*, *77*(8), 1315–1337, doi:10.1306/BDFF8E7A-1718-11D7-8645000102C1865D.
Dias, R. C., J. Julià, and M. Schimmel (2015), Rayleigh-Wave, Group-Velocity Tomography of the Borborema Province, NE Brazil, from Ambient Seismic Noise, *Pure Appl. Geophys.*, *172*(6), 1429–1449, doi:10.1007/s00024-014-0982-9.
Dunkin, J. W. (1965), Computation of modal solutions in layered, elastic media at high frequencies, *Bull. Seismol. Soc. Am.* , *55*(2), 335–358.
Duque-Caro, H. (1990), The Choco Block in the northwestern corner of South America : Structural , tectonostratigraphic , and paleogeographic implications, *J. South Am. Earth Sci.*, *3*(I), 71–84, doi:https://doi.org/10.1016/0895-9811(90)90019-W.
Dziewonski, A. M., and D. L. Anderson (1981), Preliminary reference Earth model, *Phys. Earth Planet. Inter.*, *25*(4), 297–356, doi:10.1016/0031-9201(81)90046-7.
Egbue, O., J. Kellogg, H. Aguirre, and C. Torres (2014), Evolution of the stress and strain fields in the Eastern Cordillera, Colombia, *J. Struct. Geol.*, *58*, 8–21, doi:10.1016/j.jsg.2013.10.004.
Escalona, A., and P. Mann (2011), Tectonics, basin subsidence mechanisms, and paleogeography of the Caribbean-South American plate boundary zone, *Mar. Pet. Geol.*, *28*(1), 8–39, doi:10.1016/j.marpetgeo.2010.01.016.
Farris, D. W., C. Jaramillo, G. Bayona, S. A. Restrepo-moreno, C. Montes, A. Cardona, A. Mora, R. J. Speakman, M. D. Glascock, and V. Valencia (2011), Fracturing of the Panamanian Isthmus during initial collision with South America, *Geology*, *39*(11), 1007–1010, doi:10.1130/G32237.1.
Feng, M., M. Assumpção, and S. Van der Lee (2004), Group-velocity tomography and lithospheric S-velocity structure of the South American continent, *Phys. Earth Planet. Inter.*, *147*(4), 315–331, doi:10.1016/j.pepi.2004.07.008.
Feng, M., S. van der Lee, and M. Assumpção (2007), Upper mantle structure of South America

from joint inversion of waveforms and fundamental mode group velocities of Rayleigh waves, *J. Geophys. Res. Solid Earth*, *112*(4), 1–16, doi:10.1029/2006JB004449.

Flinch, J. F. (2003), Structural Evolution of the Sinu-Lower Magdalena Area (Northern Colombia), *AAPG Mem.*, *79*, 776–796.

Flueh, E. R., B. Milkereit, R. Meissner, R. P. Meyer, J. E. Ramirez, J. C. Quintero, and A. Udias (1981), Seismic refraction observations in northwestern Colombia at latitude 5.5°N, in *Zentralblatt fuer Geologie und Palaeontologie*, edited by U. Miller and U. Rosenfeld, pp. 231–242, Angew., Reg. Hist. Geol, Germany.

Gómez, J. et al. (2007a), Geological Map of Colombia, *INGEOMINAS, Proj. Geol. Map Colomb. Bogotá, Colomb. Available http//www2.sgc.gov.co/ getattachment/Geologia/Mapa- Geol. GMC_2007_1000K.pdf.aspx*.

Gómez, J. et al. (2007b), Mapa Geologico Colombia,

Gutscher, M.-A., J. Malavieille, S. Lallemand, and J.-Y. Collot (1999), Tectonic segmentation of the North Andean margin: impact of the Carnegie Ridge collision, *Earth Planet. Sci. Lett.*, *168*(3–4), 255–270, doi:10.1016/S0012-821X(99)00060-6.

Haned, A., E. Stutzmann, M. Schimmel, S. Kiselev, A. Davaille, and A. Yelles-Chaouche (2016), Global tomography using seismic hum, *Geophys. J. Int.*, *204*(2), 1222–1236, doi:10.1093/gji/ggv516.

Herrin, E., and T. Goforth (1977), Phase-matched filters: Application to the study of Rayleigh waves, *Bull. Seismol. Soc. Am.*, *67*(5), 1259–1275.

van der Hilst, R., and P. Mann (1994), Tectonic implications of tomographic images of subducted lithosphere beneath northwestern South America, *Geology*, *22*(5), 451–454, doi:10.1130/0091-7613(1994)022.

Horton, B. K., V. J. Anderson, V. Caballero, J. E. Saylor, J. Nie, M. Parra, and A. Mora (2015), Application of detrital zircon U-Pb geochronology to surface and subsurface correlations of provenance, paleodrainage, and tectonics of the Middle Magdalena Valley Basin of Colombia, *Geosphere*, *11*(6), 1790–1811, doi:10.1130/GES01251.1.

Idárraga-García, J., J.-M. Kendall, and C. A. Vargas (2016), Shear wave anisotropy in northwestern South America and its link to the Caribbean and Nazca subduction geodynamics, *Geochemistry, Geophys. Geosystems*, *17*(9), 3655–3673, doi:10.1002/2016GC006323.

Kao, H., Y. Behr, C. A. Currie, R. Hyndman, J. Townend, F.-C. Lin, M. H. Ritzwoller, S.-J. Shan, and J. He (2013), Ambient seismic noise tomography of Canada and adjacent regions: Part I. Crustal structures, *J. Geophys. Res. Solid Earth*, *118*(11), 5865–5887, doi:10.1002/2013JB010535.

Kennett, B. L. N., and E. R. Engdahl (1991), Traveltimes for global earthquake location and phase identification, *Geophys. J. Int.*, *105*(2), 429–465, doi:10.1111/j.1365-246X.1991.tb06724.x.

Kennett, B. L. N., M. S. Sambridge, and P. R. Williamson (1988), Subspace methods for large inverse problems with multiple parameter classes, *Geophys. J. Int.*, *94*(2), 237–247, doi:10.1111/j.1365-246X.1988.tb05898.x.

Köhler, A., C. Weidle, and V. Maupin (2012), Crustal and uppermost mantle structure of southern Norway: results from surface wave analysis of ambient seismic noise and earthquake data, *Geophys. J. Int.*, *191*(3), 1441–1456, doi:10.1111/j.1365-246X.2012.05698.x.

Köhler, A., V. Maupin, and N. Balling (2015), Surface wave tomography across the Sorgenfrei–

Tornquist Zone, SW Scandinavia, using ambient noise and earthquake data, *Geophys. J. Int.*, *203*(1), 284–311, doi:10.1093/gji/ggv297.

Lara, M., A. Cardona, G. Monsalve, J. Yarce, C. Montes, V. Valencia, M. Weber, F. De La Parra, D. Espitia, and M. López-Martínez (2013), Middle Miocene near trench volcanism in northern Colombia: A record of slab tearing due to the simultaneous subduction of the Caribbean Plate under South and Central America?, *J. South Am. Earth Sci.*, *45*, 24–41, doi:10.1016/j.jsames.2012.12.006.

Larose, E. (2004), Imaging from one-bit correlations of wideband diffuse wave fields, *J. Appl. Phys.*, *95*(12), 8393, doi:10.1063/1.1739529.

Levshin, A. L., and M. H. Ritzwoller (2001), Automated Detection, Extraction, and Measurement of Regional Surface Waves, *Pure Appl. Geophys.*, *158*(8), 1531–1545, doi:10.1007/PL00001233.

Levshin, A. L., V. Pisarenko, and G. Pogrebinsky (1972), On a frequency-time analysis of oscillations, *Ann. Geophys*, *28*, 211–218.

Lin, F.-C., M. H. Ritzwoller, J. Townend, S. Bannister, and M. K. Savage (2007), Ambient noise Rayleigh wave tomography of New Zealand, *Geophys. J. Int*, *170*, 649–666, doi:10.1111/j.1365-246X.2007.03414.x.

Lin, F. C., M. P. Moschetti, and M. H. Ritzwoller (2008), Surface wave tomography of the western United States from ambient seismic noise: Rayleigh and Love wave phase velocity maps, *Geophys. J. Int.*, *173*(1), 281–298, doi:10.1111/j.1365-246X.2008.03720.x.

Lloyd, S., S. van der Lee, G. S. França, M. Assumpção, and M. Feng (2010), Moho map of South America from receiver functions and surface waves, *J. Geophys. Res.*, *115*(B11), B11315, doi:10.1029/2009JB006829.

Mann, P., A. Escalona, and M. Verónica (2006), Regional geologic and tectonic setting of the Maracaibo supergiant basin, western Venezuela, *Am. Assoc. Pet. Geol. Bull.*, *90*(4), 445–477, doi:10.1306/10110505031.

Marín-Ceron, M., T. Moriguti, A. Makishima, and E. Nakamura (2010), Slab decarbonation and CO 2 recycling in the Southwestern Colombian volcanic arc, *Geochim. Cosmochim. Acta*, *74*(3), 1104–1121, doi:10.1016/j.gca.2009.10.031.

van der Meijde, M., J. Julià, and M. Assumpçao (2013), Gravity derived Moho for South America, *Tectonophysics*, *609*, 456–467, doi:10.1016/j.tecto.2013.03.023.

Meissnar, R. O., E. R. Flueh, F. Stibane, and E. Berg (1976), Dynamics of the active plate boundary in southwest colombia according to recent geophysical measurements, *Tectonophysics*, *35*(1–3), 115–136, doi:10.1016/0040-1951(76)90032-9.

Meyer, R. P., W. D. Mooney, A. L. Hales, C. E. Helsley, G. P. Woollard, D. M. Hussong, L. W. Kroenke, and J. E. Ramirez (1976), Project Nariño III: Refraction observation across a leading edge, Malpelo Island to the Colombian cordillera occidental, pp. 105–132.

Montes, C., R. D. Hatcher, and P. A. Restrepo-Pace (2005), Tectonic reconstruction of the northern Andean blocks: Oblique convergence and rotations derived from the kinematics of the Piedras–Girardot area, Colombia, *Tectonophysics*, *399*(1–4), 221–250, doi:10.1016/j.tecto.2004.12.024.

Montes, C., G. Guzman, G. Bayona, A. Cardona, V. Valencia, and C. Jaramillo (2010), Clockwise rotation of the Santa Marta massif and simultaneous Paleogene to Neogene deformation of the Plato-San Jorge and Cesar-Ranchería basins, *J. South Am. Earth Sci.*, *29*(4), 832–848, doi:10.1016/j.jsames.2009.07.010.

Mooney, W. D., R. P. Meyer, J. P. Laurence, H. Meyer, and J. E. Ramírez (1979), Seismic

refraction studies of the Western Cordillera, Colombia, *Bull. Seismol. Soc. Am.* , *69*(6), 1745–1761.

Mora-Bohórquez, J. A., M. Ibánez-Mejia, O. Oncken, M. de Freitas, V. Vélez, A. Mesa, and L. Serna (2017), Structure and age of the Lower Magdalena Valley basin basement, northern Colombia: New reflection-seismic and U-Pb-Hf insights into the termination of the central andes against the Caribbean basin, *J. South Am. Earth Sci.*, *74*, 1–26, doi:10.1016/j.jsames.2017.01.001.

Mora, A., and M. Parra (2008), The structural style of footwall shortcuts along the eastern foothills of the colombian eastern cordillera. Differences with other inversion related structures., *CT&F - Ciencia, Tecnol. y Futur.*, *3*, 7–21.

Mora, A., M. Parra, M. R. Strecker, A. Kammer, C. Dimaté, and F. Rodríguez (2006), Cenozoic contractional reactivation of Mesozoic extensional structures in the Eastern Cordillera of Colombia, *Tectonics*, *25*(2), 1–19, doi:10.1029/2005TC001854.

Mora, A., M. Parra, M. R. Strecker, E. R. Sobel, G. Zeilinger, C. Jaramillo, S. F. Da Silva, and M. Blanco (2010), The eastern foothills of the Eastern Cordillera of Colombia: An example of multiple factors controlling structural styles and active tectonics, *Geol. Soc. Am. Bull.*, *122*(11–12), 1846–1864, doi:10.1130/B30033.1.

Mottaghi, A. A., M. Rezapour, and M. Korn (2013), Ambient noise surface wave tomography of the Iranian Plateau, *Geophys. J. Int.*, *193*(1), 452–462, doi:10.1093/gji/ggs134.

Ocola, L. C., L. T. Aldrich, J. F. Gettrust, R. P. Meyer, and J. E. Ramirez (1975), Project Nariño I: Crustal structure under southern Colombian-northern Ecuador Andes from seismic refraction data, *Bull. Seismol. Soc. Am.*, *65*(6), 1681–1695.

Ojeda, A., and J. Havskov (2001), Crustal structure and local seismicity in Colombia, *J. Seismol.*, *5*(4), 575–593, doi:10.1023/A:1012053206408.

Ojeda, A., and L. Q. Ottemoller (2002), Q Lg tomography in Colombia, *Phys. Earth Planet. Inter.*, *130*(3–4), 253–270.

Pardo, N., H. Cepeda, and J. M. Jaramillo (2005), The Paipa Volcano, Easter Cordillera of Colombia,South America: Volcanic Stratigraphy, *Earth Sci. Res. J.*, *9*(1), 3–18.

Parra, M., A. Mora, C. Jaramillo, M. R. Strecker, E. R. Sobel, L. Quiroz, M. Rueda, and V. Torres (2009), Orogenic wedge advance in the northern Andes: Evidence from the Oligocene-Miocene sedimentary record of the Medina Basin, Eastern Cordillera, Colombia, *Geol. Soc. Am. Bull.*, *121*(5–6), 780–800, doi:10.1130/B26257.1.

Pavlis, N. K., S. A. Holmes, S. C. Kenyon, and J. K. Factor (2012), The development and evaluation of the Earth Gravitational Model 2008 (EGM2008), *J. Geophys. Res. Solid Earth*, *117*(B4), n/a-n/a, doi:10.1029/2011JB008916.

Pennington, W. D. (1981), Subduction of the Eastern Panama Basin and seismotectonics of northwestern South America, *J. Geophys. Res. Solid Earth*, *86*(B11), 10753–10770, doi:10.1029/JB086iB11p10753.

Poveda, E., G. Monsalve, and C. A. Vargas (2015), Receiver functions and crustal structure of the northwestern Andean region, Colombia, *J. Geophys. Res. Solid Earth*, *120*(4), 2408–2425, doi:10.1002/2014JB011304.

Prieto, G. A., G. C. Beroza, S. A. Barrett, G. A. López, and M. Florez (2012), Earthquake nests as natural laboratories for the study of intermediate-depth earthquake mechanics, *Tectonophysics*, *570–571*, 42–56, doi:10.1016/j.tecto.2012.07.019.

Rawlinson, N., and M. Sambridge (2004), Multiple reflection and transmission phases in complex layered media using a multistage fast marching method, *Geophysics*, *69*(5), 1338–

1350, doi:10.1190/1.1801950.
Rawlinson, N., and M. Sambridge (2005), The fast marching method: an effective tool for tomographic imaging and tracking multiple phases in complex layered media, *Explor. Geophys.*, *36*(4), 341, doi:10.1071/EG05341.
Restrepo-Moreno, S., D. Foster, D. Stockli, and L. Parra-Sanchez (2009), Long-term erosion and exhumation of the "Altiplano Antioqueño", Northern Andes (Colombia) from apatite (U–Th)/He thermochronology, *Earth Planet. Sci. Lett.*, *278*(1–2), 1–12, doi:10.1016/j.epsl.2008.09.037.
Restrepo, J., and J. Toussaint (1988), Terranes and continental accretion in the Colombian Andes, *Episodes*, *11*, 189–193.
Ritsema, J., H. J. van Heijst, and J. H. Woodhouse (2004), Global transition zone tomography, *J. Geophys. Res. Solid Earth*, *109*(B2), doi:10.1029/2003JB002610.
Sabra, K. G., P. Gerstoft, P. Roux, W. A. Kuperman, and M. C. Fehler (2005), Surface wave tomography from microseisms in Southern California, *Geophys. Res. Lett.*, *32*(14), n/a-n/a, doi:10.1029/2005GL023155.
Sambridge, M. (1999), Geophysical inversion with a neighbourhood algorithm - I. Searching a parameter space, *Geophys. J. Int.*, *138*(2), 479–494, doi:10.1046/j.1365-246X.1999.00876.x.
Sanchez, J., and P. Mann (2015), Integrated Structural and Basinal Analysis of the Cesar–Rancheria Basin, Colombia: Implications for its Tectonic History and Petroleum Systems, in *Memoir 108: Petroleum Geology and Potential of the Colombian Caribbean Margin*, AAPG.
Saygin, E., and B. L. N. Kennett (2010), Ambient seismic noise tomography of Australian continent, *Tectonophysics*, *481*(1–4), 116–125, doi:10.1016/j.tecto.2008.11.013.
Schimmel, M., E. Stutzmann, and J. Gallart (2011), Using instantaneous phase coherence for signal extraction from ambient noise data at a local to a global scale, *Geophys. J. Int.*, *184*(1), 494–506, doi:10.1111/j.1365-246X.2010.04861.x.
Sethian, J. A. (1996), A fast marching level set method for monotonically advancing fronts., *Proc. Natl. Acad. Sci.*, *93*(4), 1591–1595, doi:10.1073/pnas.93.4.1591.
Sethian, J. A., and A. M. Popovici (1999), 3-D traveltime computation using the fast marching method, *GEOPHYSICS*, *64*(2), 516–523, doi:10.1190/1.1444558.
Shapiro, N. M., and M. Campillo (2004), Emergence of broadband Rayleigh waves from correlations of the ambient seismic noise, *Geophys. Res. Lett.*, *31*(7), 8–11, doi:10.1029/2004GL019491.
Shapiro, N. M., M. Campillo, L. Stehly, and M. H. Ritzwoller (2005), High-resolution surface-wave tomography from ambient seismic noise., *Science*, *307*(5715), 1615–1618, doi:10.1126/science.1108339.
Smith, W. H. F., and P. Wessel (1990), Gridding with continuous curvature splines in tension, *GEOPHYSICS*, *55*(3), 293–305, doi:10.1190/1.1442837.
Snieder, R. (2004), Extracting the Green's function from the correlation of coda waves: a derivation based on stationary phase., *Phys. Rev. E. Stat. Nonlin. Soft Matter Phys.*, *69*(4 Pt 2), 46610, doi:10.1103/PhysRevE.69.046610.
Spikings, R., R. Cochrane, D. Villagomez, R. Van Der Lelij, C. Vallejo, W. Winkler, and B. Beate (2015), The geological history of northwestern South America : from Pangaea to the early collision of the Caribbean Large Igneous Province (290 – 75 Ma), *Gondwana Res.*, *27*(1), 95–139, doi:10.1016/j.gr.2014.06.004.

Stehly, L., M. Campillo, and N. M. Shapiro (2006), A study of the seismic noise from its long-range correlation properties, *J. Geophys. Res.*, *111*(B10), B10306, doi:10.1029/2005JB004237.

Stockwell, R. G., L. Mansinha, and R. P. Lowe (1996), Localization of the complex spectrum: the S transform, *IEEE Trans. Signal Process.*, *44*(4), 998–1001, doi:10.1109/78.492555.

Syracuse, E. M., M. Maceira, G. A. Prieto, H. Zhang, and C. J. Ammon (2016), Multiple plates subducting beneath Colombia, as illuminated by seismicity and velocity from the joint inversion of seismic and gravity data, *Earth Planet. Sci. Lett.*, *444*, 139–149, doi:10.1016/j.epsl.2016.03.050.

Taboada, A., L. A. Rivera, A. Fuenzalida, A. Cisternas, H. Philip, H. Bijwaard, J. Olaya, and C. Rivera (2000), Geodynamics of the northern Andes: Subductions and intracontinental deformation (Colombia), *Tectonics*, *19*(5), 787–813, doi:10.1029/2000TC900004.

Thurber, C., S. Roecker, K. Roberts, M. Gold, Powell L., and K. Rittger (2003), Earthquake locations and three-dimensional fault zone structure along the creeping section of the San Andreas fault near Parkfield, CA: Preparing for SAFOD, *Geophys. Res. Lett.*, *30*(3), 1112, doi:10.1029/2002GL016004.

Toro, J., W. Virginia, S. Le Cornec-lance, R. Malmaison, W. Sassi, and N. B. Floch (2004), Thermal and Kinematic Evolution of the Eastern Cordillera Fold and Thrust Belt, Colombia, *Am. Assoc. Pet. Geol.*, *1*, 79–115, doi:10.1306/1025687H13114.

Toto, E. A., and J. N. Kellogg (1992), Structure of the Sinu-San Jacinto fold belt — an active accretionary prism in northern Colombia, *J. South Am. Earth Sci.*, *5*(2), 211–222, doi:10.1016/0895-9811(92)90039-2.

Trenkamp, R., J. N. Kellogg, J. T. Freymueller, and H. P. Mora (2002), Wide plate margin deformation, southern Central America and northwestern South America, CASA GPS observations, *J. South Am. Earth Sci.*, *15*(2), 157–171, doi:10.1016/S0895-9811(02)00018-4.

Tschanz, C. M., R. F. Marvin, J. Cruz B., H. H. Mehnert, and G. T. Cebula (1974), Geologic Evolution of the Sierra Nevada de Santa Marta, Northeastern Colombia, *Geol. Soc. Am. Bull.*, *85*(2), 273, doi:10.1130/0016-7606(1974)85<273:GEOTSN>2.0.CO;2.

Vargas, C. A., and P. Mann (2013), Tearing and Breaking Off of Subducted Slabs as the Result of Collision of the Panama Arc-Indenter with Northwestern South America, *Bull. Seismol. Soc. Am.*, *103*(3), 2025–2046, doi:10.1785/0120120328.

Veloza, G., R. Styron, M. Taylor, and A. Mora (2012), Open-source archive of active faults for northwest South America, *GSA Today*, *22*(10), 4–10, doi:10.1130/GSAT-G156A.1.

Vernette, G., A. Mauffret, C. Bobier, L. Briceno, and J. Gayet (1992), Mud diapirism, fan sedimentation and strike-slip faulting, Caribbean Colombian Margin, *Tectonophysics*, *202*(2–4), 335–349, doi:10.1016/0040-1951(92)90118-P.

Villaseñor, A., Y. Yang, M. H. Ritzwoller, and J. Gallart (2007), Ambient noise surface wave tomography of the Iberian Peninsula: Implications for shallow seismic structure, *Geophys. Res. Lett.*, *34*(11), L11304, doi:10.1029/2007GL030164.

Wang, X.-Q., A. Schubnel, J. Fortin, E. C. David, Y. Guéguen, and H.-K. Ge (2012), High Vp/Vs ratio: Saturated cracks or anisotropy effects?, *Geophys. Res. Lett.*, *39*(11), n/a-n/a, doi:10.1029/2012GL051742.

Ward, K. M., R. C. Porter, G. Zandt, S. L. Beck, L. S. Wagner, E. Minaya, and H. Tavera (2013), Ambient noise tomography across the Central Andes, *Geophys. J. Int.*, *194*(3), 1559–1573, doi:10.1093/gji/ggt166.

Wathelet, M. (2008), An improved neighborhood algorithm: Parameter conditions and dynamic scaling, *Geophys. Res. Lett.*, *35*(9), 1–5, doi:10.1029/2008GL033256.
Wathelet, M., D. Jongmans, and M. Ohrnberger (2004), Surface-wave inversion using a direct search algorithm and its application to ambient vibration measurements, *Near Surf. Geophys.*, *2*(22), 211–221, doi:10.3997/1873-0604.2004018.
Weber, M. B. I., J. Tarney, P. D. Kempton, and R. W. Kent (2002), Crustal make-up of the northern Andes : evidence based on deep crustal xenolith suites, Mercaderes, SW Colombia, *Tectonophysics*, *345*(1–4), 49–82.
Yang, Y., M. H. Ritzwoller, A. L. Levshin, and N. M. Shapiro (2007), Ambient noise Rayleigh wave tomography across Europe, *Geophys. J. Int.*, *168*(1), 259–274, doi:10.1111/j.1365-246X.2006.03203.x.
Yao, H., R. D. van der Hilst, and M. V. de Hoop (2006), Surface-wave array tomography in SE Tibet from ambient seismic noise and two-station analysis - I. Phase velocity maps, *Geophys. J. Int.*, *166*(2), 732–744, doi:10.1111/j.1365-246X.2006.03028.x.
Yarce, J., G. Monsalve, T. Becker, A. Cardona, E. Poveda, D. Alvira, and Ordonez-Carmona Oswaldo (2014), Seismological observations in Northwestern South America: Evidence for two subduction segments, contrasting crustal thicknesses and upper mantle flow, *Tectonophysics*, *637*, 57–67, doi:10.1016/j.tecto.2014.09.006.
Zarifi, Z., J. Havskov, and A. Hanyga (2007), An insight into the Bucaramanga nest, *Tectonophysics*, *443*(1–2), 93–105, doi:10.1016/j.tecto.2007.06.004.
Zhao, D., H. Kanamori, H. Negishi, and D. Wiens (1996), Tomography of the Source Area of the 1995 Kobe Earthquake: Evidence for Fluids at the Hypocenter?, *Science (80-.).*, *274*(5294), 1891–1894, doi:10.1126/science.274.5294.1891.

Figure captions

Figure 1. Tectonic and simplified Geologic setting of the northern Andes. Geologic provinces from [*Gómez et al.,* 2007] and major faults from *Veloza et al.,* [2012]. Plate motions relative to South America from *Trenkamp et al.*, 2002. Gray thick line: Envelops of North Andean Block (NAB); Area with vertical lines: Panamá arc; Red Triangles: Active Volcanoes; Blue triangles: Inactive Volcanoes. The different provinces are: SMM: Santa Marta Massif; Mab: Maracaibo Block; SMBF-: Santa Marta- Bucaramanga Fault; SM: Santander Massif; MA: Merida Andes; SSJB: Sinú and San Jacinto Basin; CRB: Cesár-Rancheria Basic; PB: Plató Basin; LMB: Lower Magdalena Basin; SJB: San Jorgé Basin; SLR: San Lucas Range; AB: Antioqueño Batholith; BR: Baudo Range; MMV: Middle Magdalena Valley; RS-: Romeral Suture; Panamá arc; AB: Antioqueño Batholith; CC: Central Cordillera; EC: Eastern Cordillera; LIB: Llanos Basin; LFS:

Llanos Faults system; WC: Western Cordillera; CV: Cauca Valley; IB: Ibagué Batholith; SMV: Upper Magdalena Valley; QM: Quetame Massif; GM: Garzón Massif and CV: Cauca Valley; MR: Macarena Ranges; TB: Túmaco Basin; PSS: Panama South America suture.

Figure 2. Update of the interpolated crustal thickness map for NW South America from Poveda et al. (2015).

Figure 3. Broadband seismic stations used in this work. The color-coded represents recording time window duration in each station.

Figure 4. Extracted Rayleigh waves from ambient noise for the all stations with RMS > 20. All traces are band passed between 10 to 50 seconds and are normalized. The dashed lines show an average velocity between 2.1-3.2 km/s.

Figure 5. Analysis the signal stability and convergence for HEL-POP2; a) EGF convergence for different amount stack data, selected from random form; b) Similarity value in function of random days number, that show the convergence evolution. In this case the paths converge in ~250d; c) Dispersion curves for Rayleigh Group and Phase velocities, each color is associated to EGF in panel a). Uncertainties from 3-month stack is show; d) Example of frequency–time analysis (FTAN) diagram showing Rayleigh wave group velocity with phase match filter; e) Path between HEL and POP2 stations (423 km).

Figure 6. Similar that Figure 5. Analysis the signal stability and convergence for HEL-URI.

Figure 7. Statistics for the estimated group and phase speed maps to the observations taken after all stages of data rejection; a) Velocity uncertainty for group and phase versus period; b) Number of paths versus period; c) Travel time uncertainty versus period used for tomography inversion; d) Average of path length versus period.

Figure 8. L-curve for 22 s Group (black)- and phase (red) velocity tomography; a) RMS misfit with model roughness, selected values are 10 and 2 for group and phase respectively; b) RMS misfit and model Variance, selected values are 9 and 3 for group and phase respectively; c) RMS variation with number of iterations, note that with ~4 iterations the convergence is reached.

Figure 9. Checkerboard resolution tests and recovery for group velocities for 7, 14, 22, 30, 34, 38 s (large maps). The black polygon encompasses the region used in modeling crustal Vs, and the number in the upper left shows mean group velocity obtained from the real data set and number of paths. Small maps show input synthetic checkerboard test for each period.

Figure 10. Rayleigh-wave group and phase velocity maps for selected periods of 7, 22 and 34 s. Major faults (black lines) are superimposed from *Veloza et al*. [2012] same that Figure 1. The blue polygon encompasses the region used for the Vs inversion (section 4.2). The red and blue triangles show the active and inactive volcanoes respectively.

Figure 11. 1-D profiles of the Vs resulting from inversion. The colors illustrate the density distributions of models with misfits smaller than 0.1. The white line shows the observed data. a) Profile next to Santa Marta Massif (SMM; b) Profile under Western Cordillera (WC); c) Profile

south of CC.

Figure 12. Shear wave velocity maps for selected depths. The red and blue triangles indicate the active and inactive volcanoes respectively and major faults (blue lines) are superimposed from Veloza et al. [2012]. The thick black lines shows locations of profiles in Figure 13. The dashed red lines shows proposed "Caldas tear" [Vargas and Mann, 2013] and dashed blue line represents the Romeral Suture (RS) on Lower Magdalena Basin. Other features are labeled as in Figure 1 and depth is indicated in the lower right corner of each panel.

Figure 13. Cross-section on Lower Magdalena Basin and Andean regions (see figure 12a), and associated topographic profiles, showing several provinces (see figure 1). Segmented white lines are the top of the Caribbean slab and sediment thickness from *Bernal-Olaya et al.,* [2015c] and *Mora-Bohórquez et al.,* [2017].

Table 1. Seismic Station Parameters (Geographical Location and Recording Time Window)

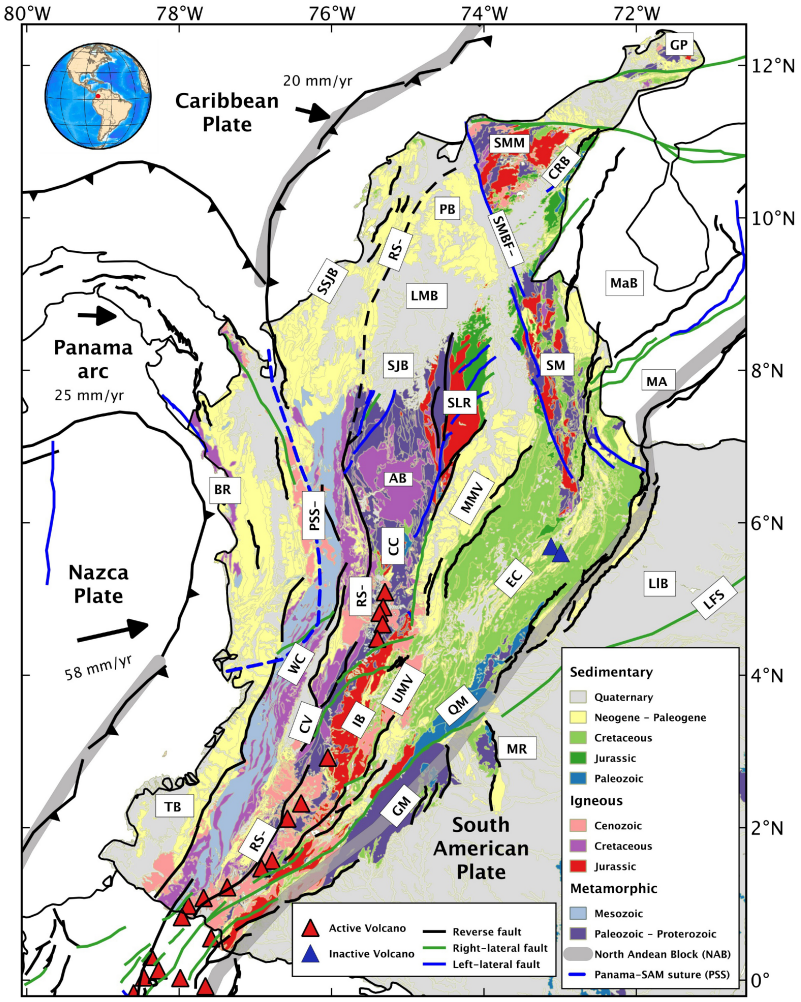
80°W
78°W
76°W
74°W
72°W
12°N
10°N
8°N
6°N
4°N
2°N
0°
Caribbean Plate
20 mm/yr
Panama arc
25 mm/yr
Nazca Plate
58 mm/yr
South American Plate
GP
SMM
CRB
PB
SMBF
RS
SSJB
LMB
MaB
SJB
SM
MA
SLR
AB
MMV
BR
PSS
CC
EC
LIB
LFS
WC
UMV
QM
CV
IB
MR
TB
GM
Active Volcano
Inactive Volcano
Reverse fault
Right-lateral fault
Left-lateral fault
Sedimentary
Quaternary
Neogene - Paleogene
Cretaceous
Jurassic
Paleozoic
Igneous
Cenozoic
Cretaceous
Jurassic
Metamorphic
Mesozoic
Paleozoic - Proterozoic
North Andean Block (NAB)
Panama-SAM suture (PSS)

Figure 1

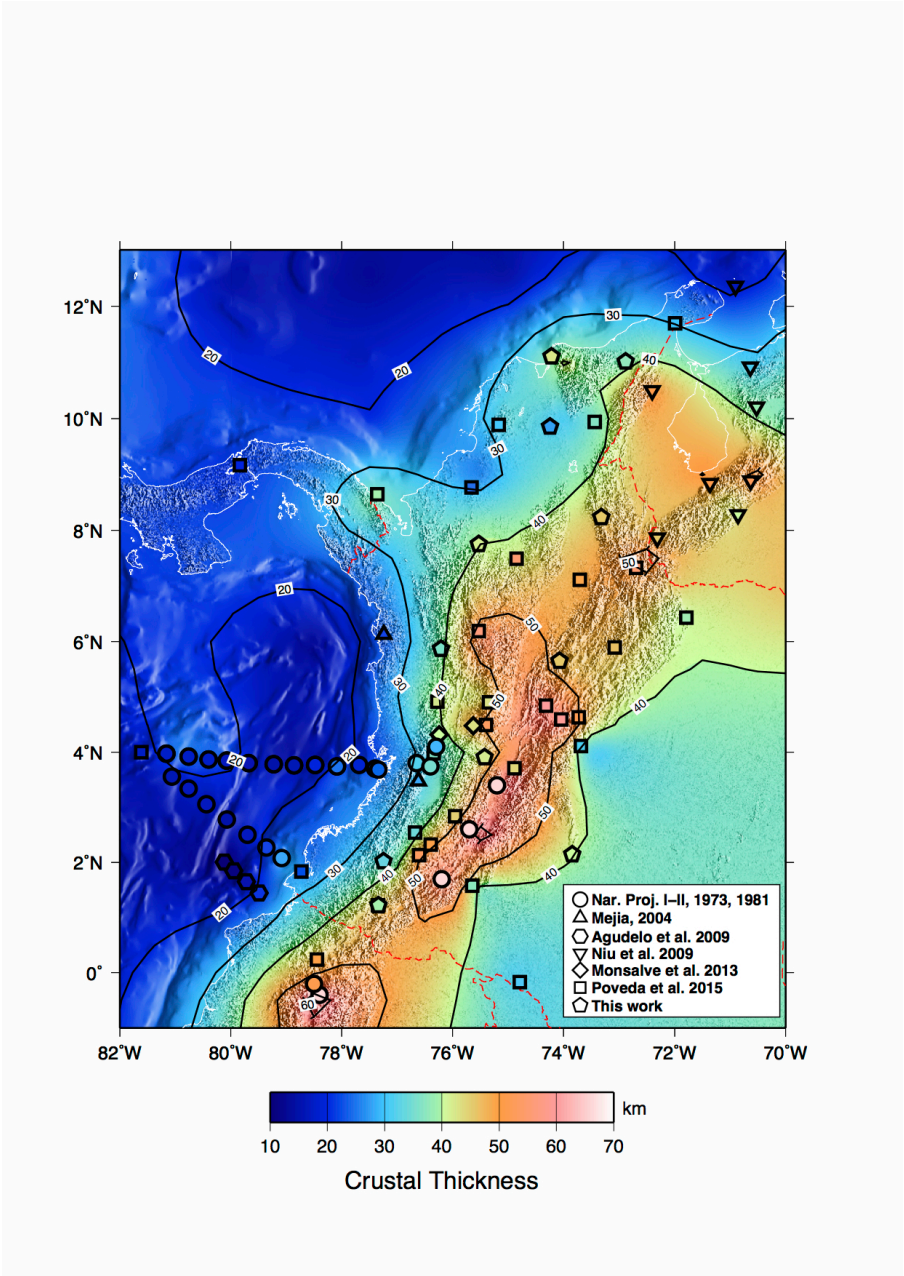
12°N
10°N
8°N
6°N
4°N
2°N
0°
82°W
80°W
78°W
76°W
74°W
72°W
70°W
Nar. Proj. I–II, 1973, 1981
Mejia, 2004
Agudelo et al. 2009
Niu et al. 2009
Monsalve et al. 2013
Poveda et al. 2015
This work
km
10
20
30
40
50
60
70
Crustal Thickness

Figure 2

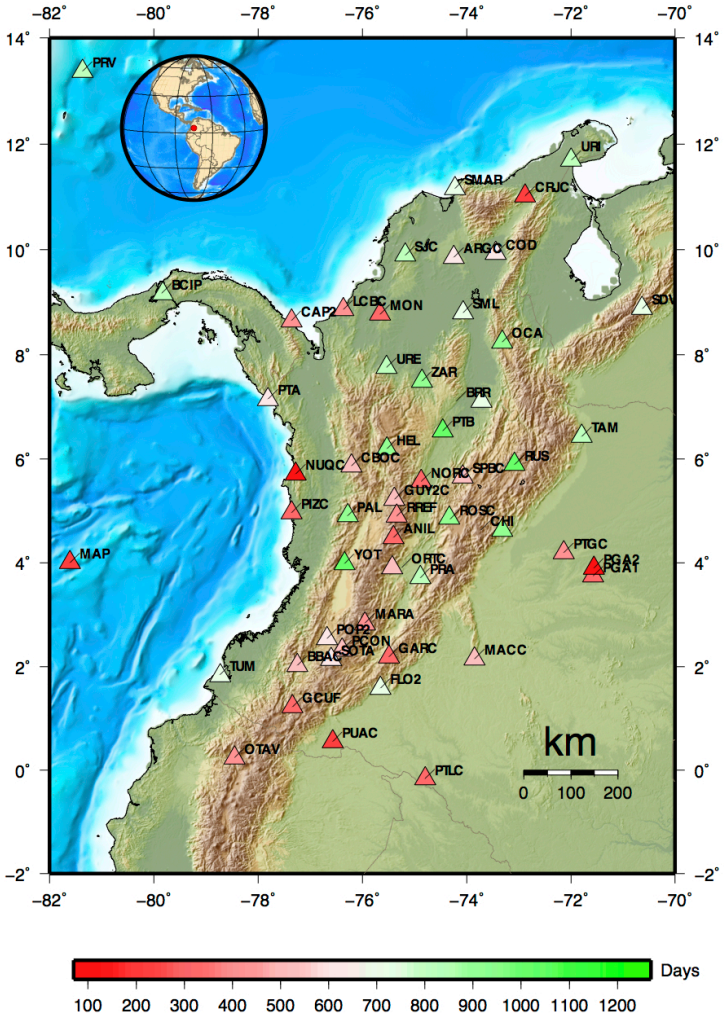
−82°
−80°
−78°
−76°
−74°
−72°
−70°
14°
12°
10°
8°
6°
4°
2°
0°
−2°
PRV
URI
SMAR
CRJC
SJC
ARGC
COD
BCIP
CAP2
LCBC
MON
SML
SDV
OCA
URE
ZAR
PTA
BRR
PTB
TAM
HEL
CBOC
NUQC
NORC
SPBC
RUS
GUY2C
PIZC
PAL
FREF
ROSC
CHI
ANIL
MAP
YOT
ORTC
PRA
PTGC
BGA2
PGAT
MARA
POP2
PCON
SOTA
GARC
MACC
BBAC
TUM
FLO2
GCUF
PUAC
OTAV
PTLC
km
0
100
200
Days
100
200
300
400
500
600
700
800
900
1000
1100
1200

Figure 3

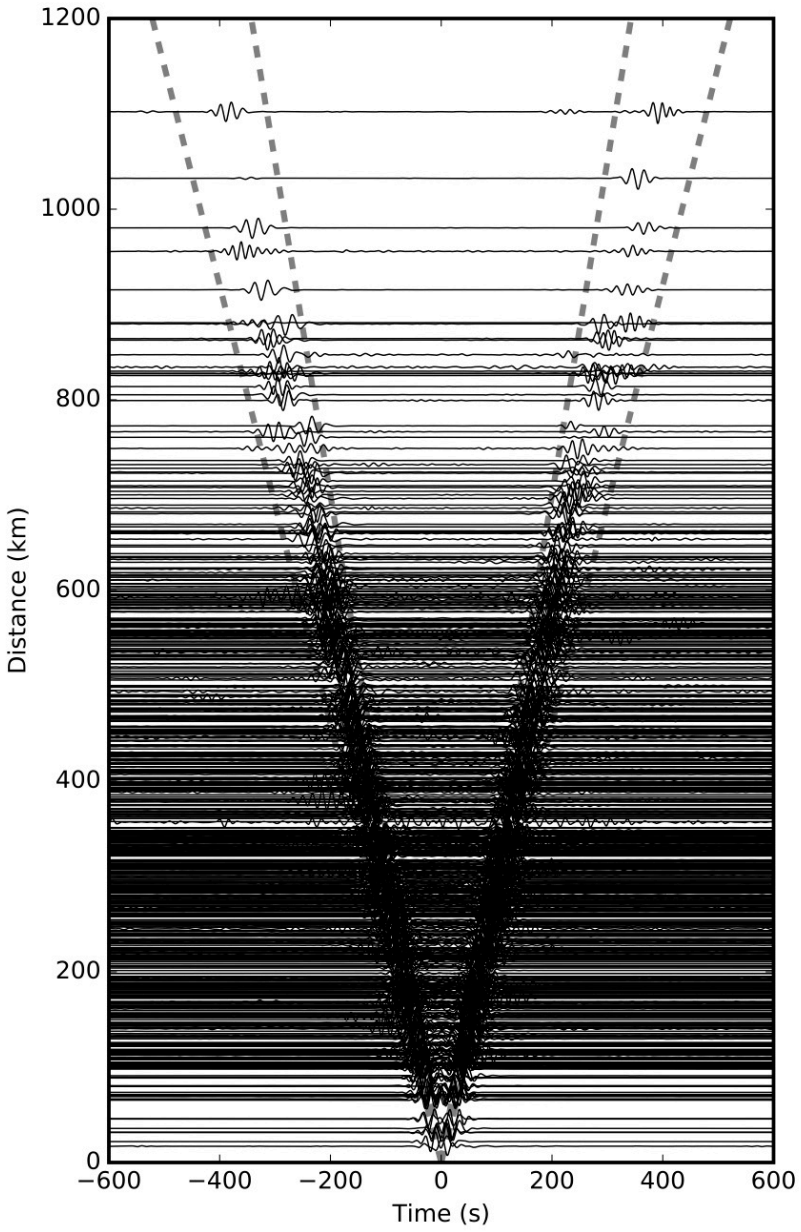
1200
1000
800
600
400
200
0
Distance (km)
−600
−400
−200
0
200
400
600
Time (s)

Figure 4

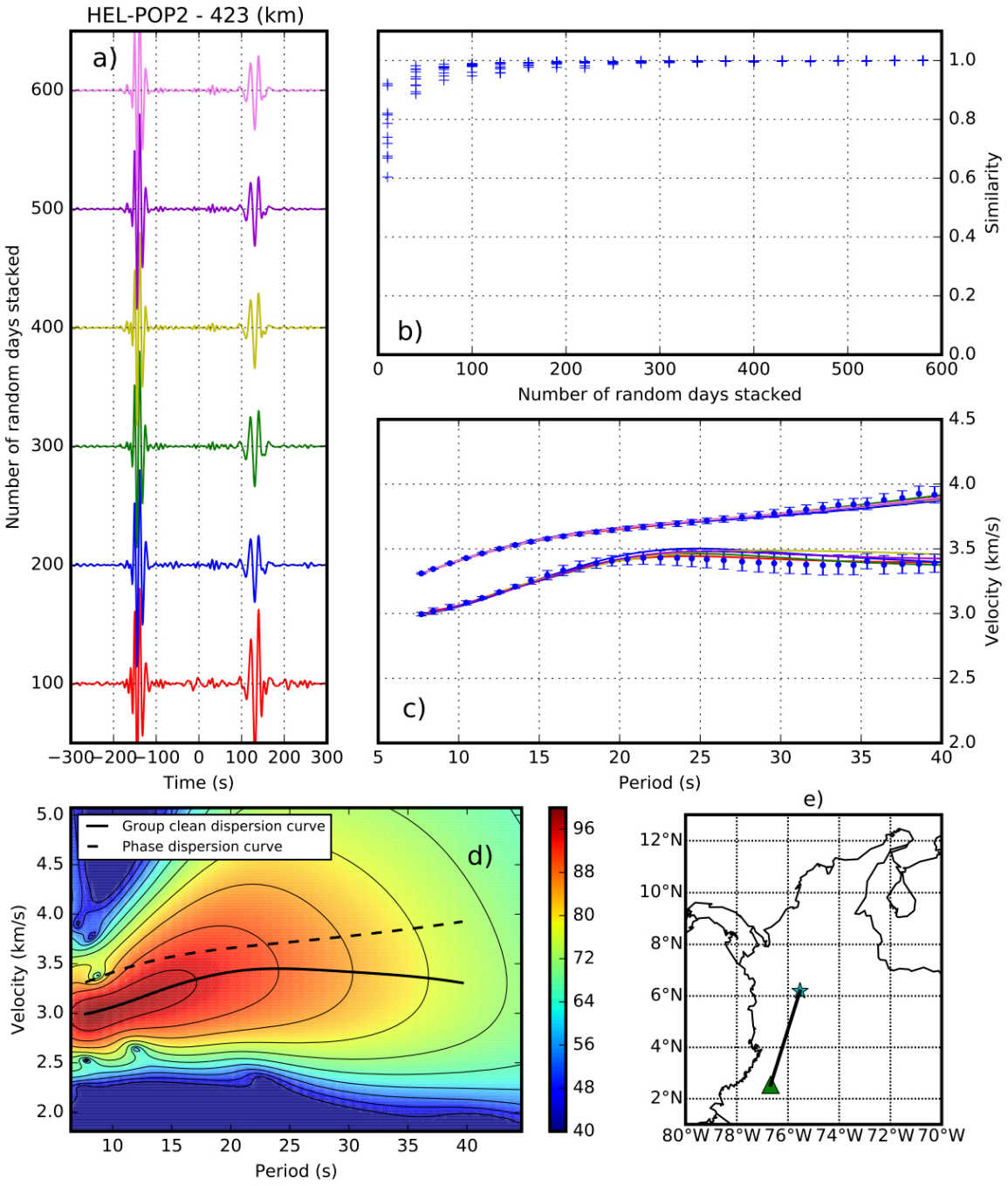
HEL-POP2 - 423 (km)
a)
Number of random days stacked
Time (s)
b)
Similarity
Number of random days stacked
c)
Velocity (km/s)
Period (s)
d)
Group clean dispersion curve
Phase dispersion curve
Velocity (km/s)
Period (s)
e)

Figure 5

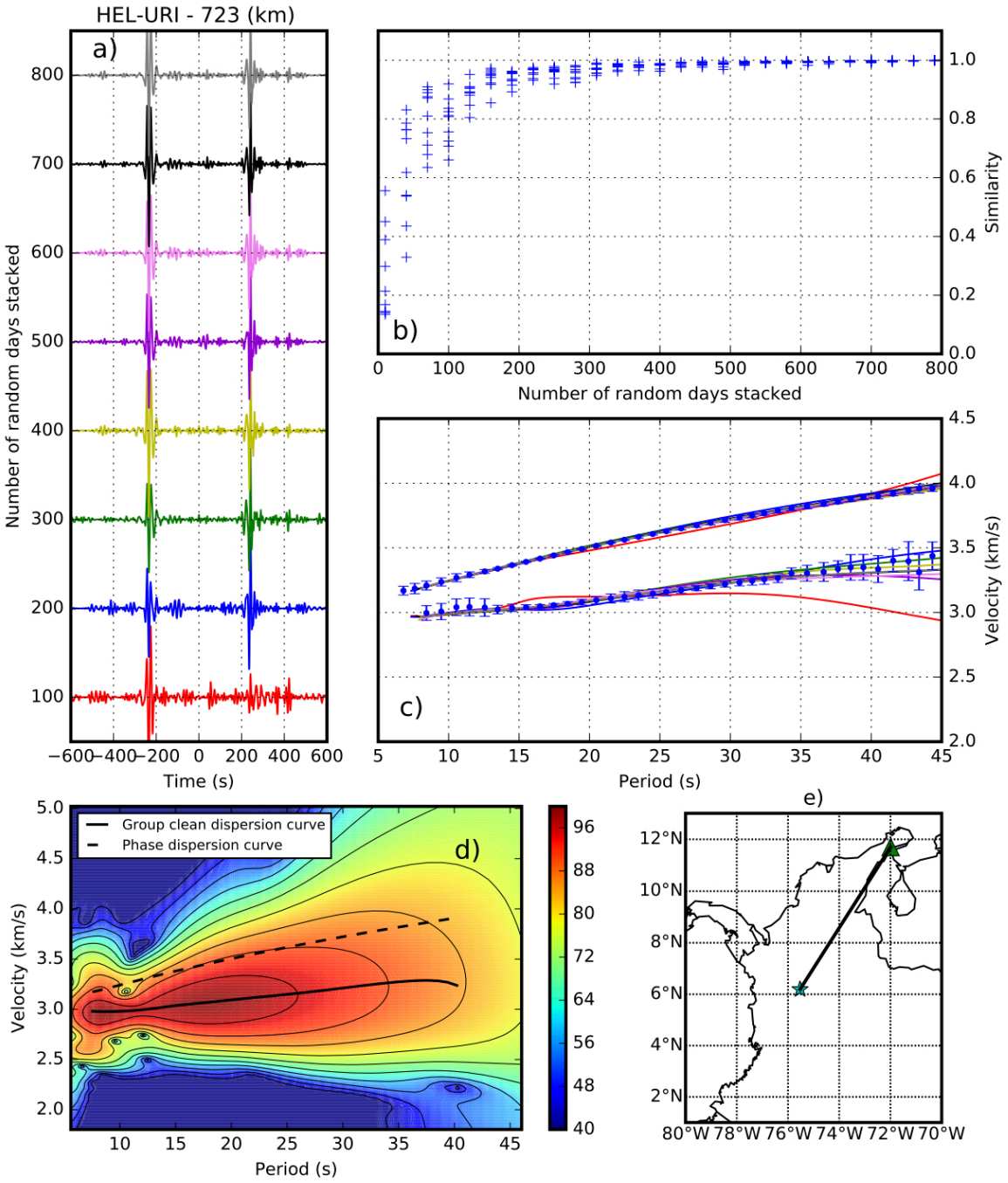
HEL-URI - 723 (km)
a)
b)
c)
d)
e)
Number of random days stacked
Time (s)
Similarity
Number of random days stacked
Velocity (km/s)
Period (s)
Group clean dispersion curve
Phase dispersion curve
Velocity (km/s)
Period (s)
12°N
10°N
8°N
6°N
4°N
2°N
80°W 78°W 76°W 74°W 72°W 70°W

Figure 6

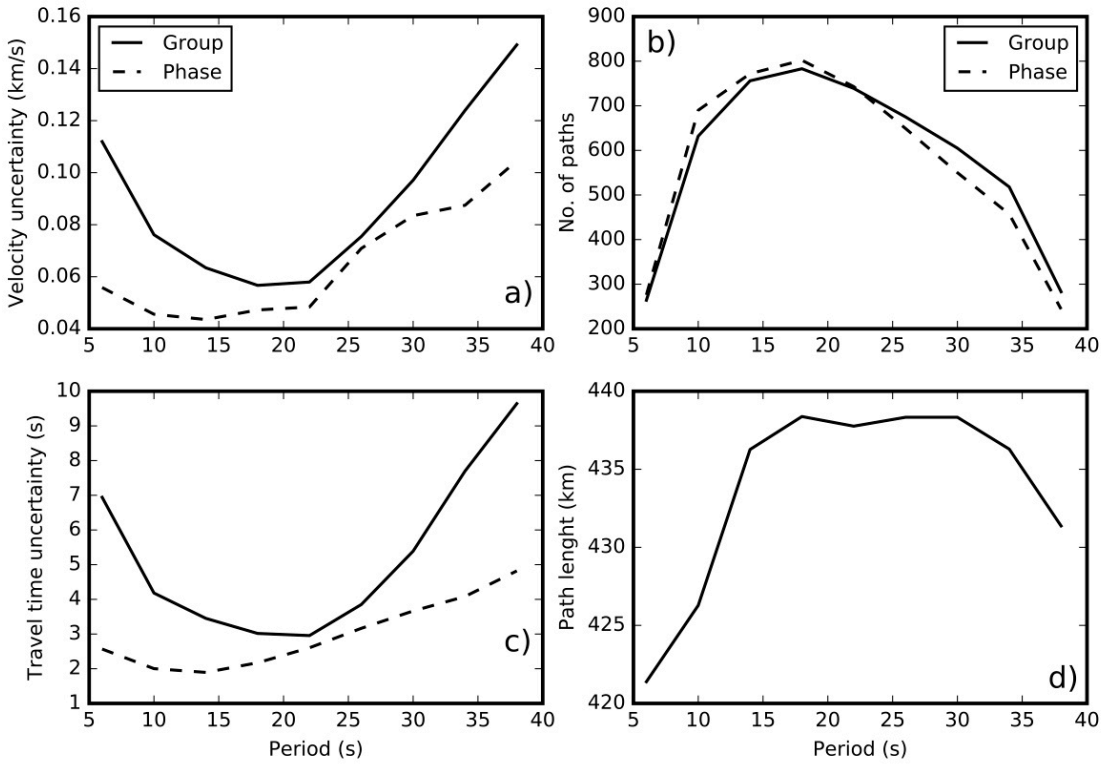
Velocity uncertainty (km/s)
Group
Phase
a)
No. of paths
b)
Travel time uncertainty (s)
c)
Path lenght (km)
d)
Period (s)
Period (s)

Figure 7

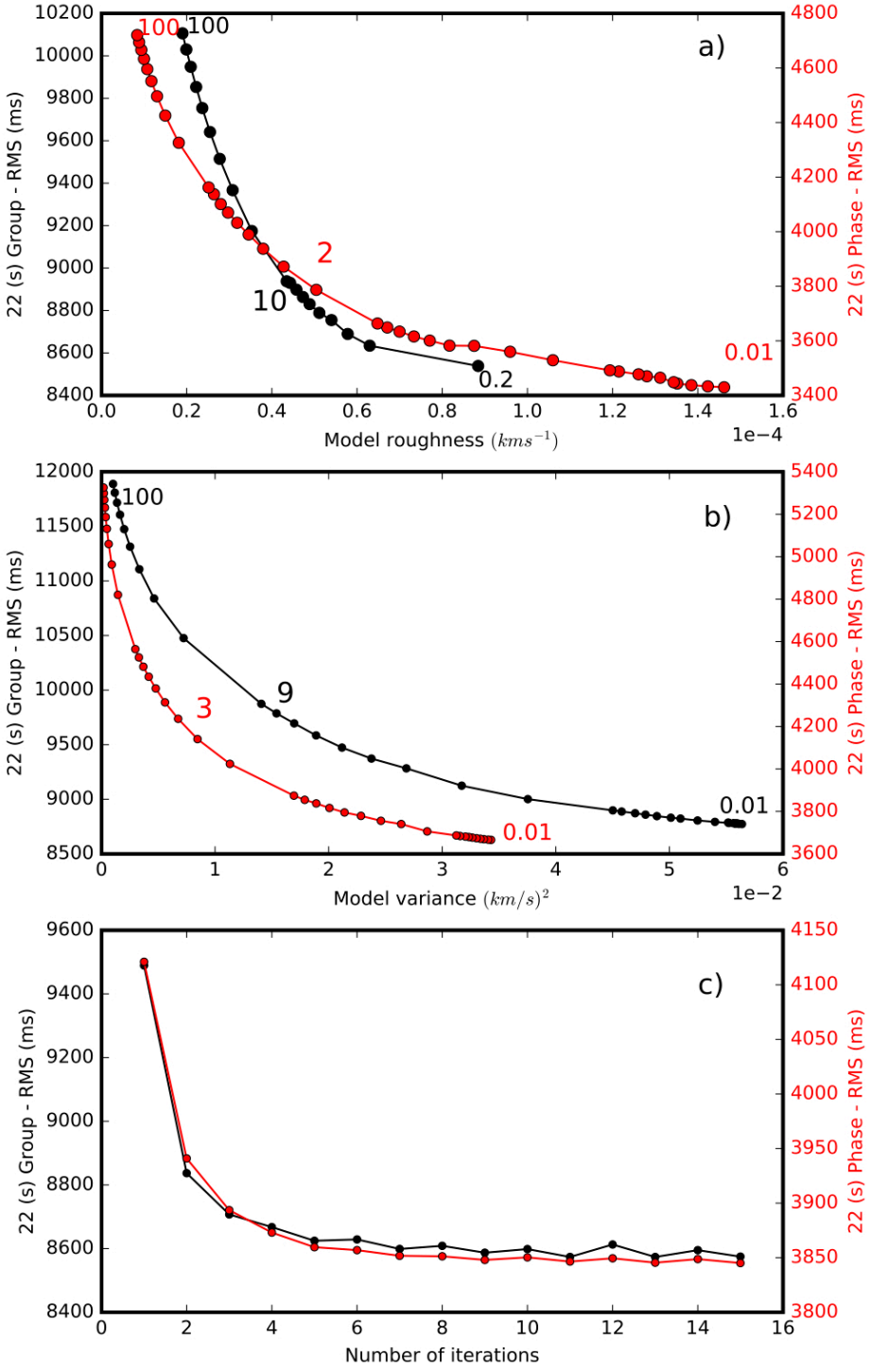
a)
100
100
2
10
0.2
0.01
22 (s) Group - RMS (ms)
22 (s) Phase - RMS (ms)
Model roughness (kms^{-1})
1e−4
b)
100
9
3
0.01
0.01
22 (s) Group - RMS (ms)
22 (s) Phase - RMS (ms)
Model variance $(km/s)^2$
1e−2
c)
22 (s) Group - RMS (ms)
22 (s) Phase - RMS (ms)
Number of iterations

Figure 8

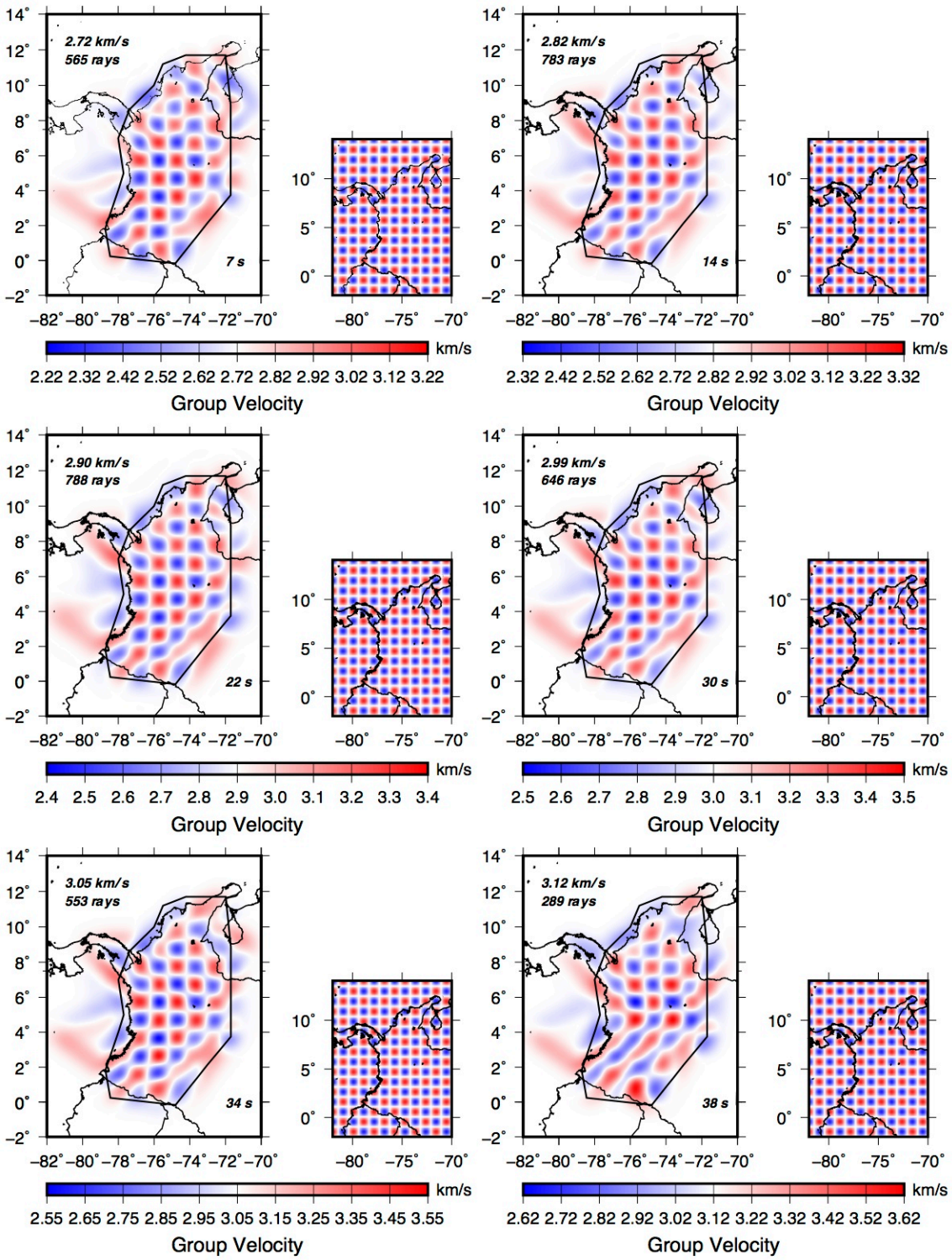
2.72 km/s
565 rays
7 s
2.82 km/s
783 rays
14 s
2.90 km/s
788 rays
22 s
2.99 km/s
646 rays
30 s
3.05 km/s
553 rays
34 s
3.12 km/s
289 rays
38 s
km/s
2.22 2.32 2.42 2.52 2.62 2.72 2.82 2.92 3.02 3.12 3.22
2.32 2.42 2.52 2.62 2.72 2.82 2.92 3.02 3.12 3.22 3.32
2.4 2.5 2.6 2.7 2.8 2.9 3.0 3.1 3.2 3.3 3.4
2.5 2.6 2.7 2.8 2.9 3.0 3.1 3.2 3.3 3.4 3.5
2.55 2.65 2.75 2.85 2.95 3.05 3.15 3.25 3.35 3.45 3.55
2.62 2.72 2.82 2.92 3.02 3.12 3.22 3.32 3.42 3.52 3.62
Group Velocity

Figure 9

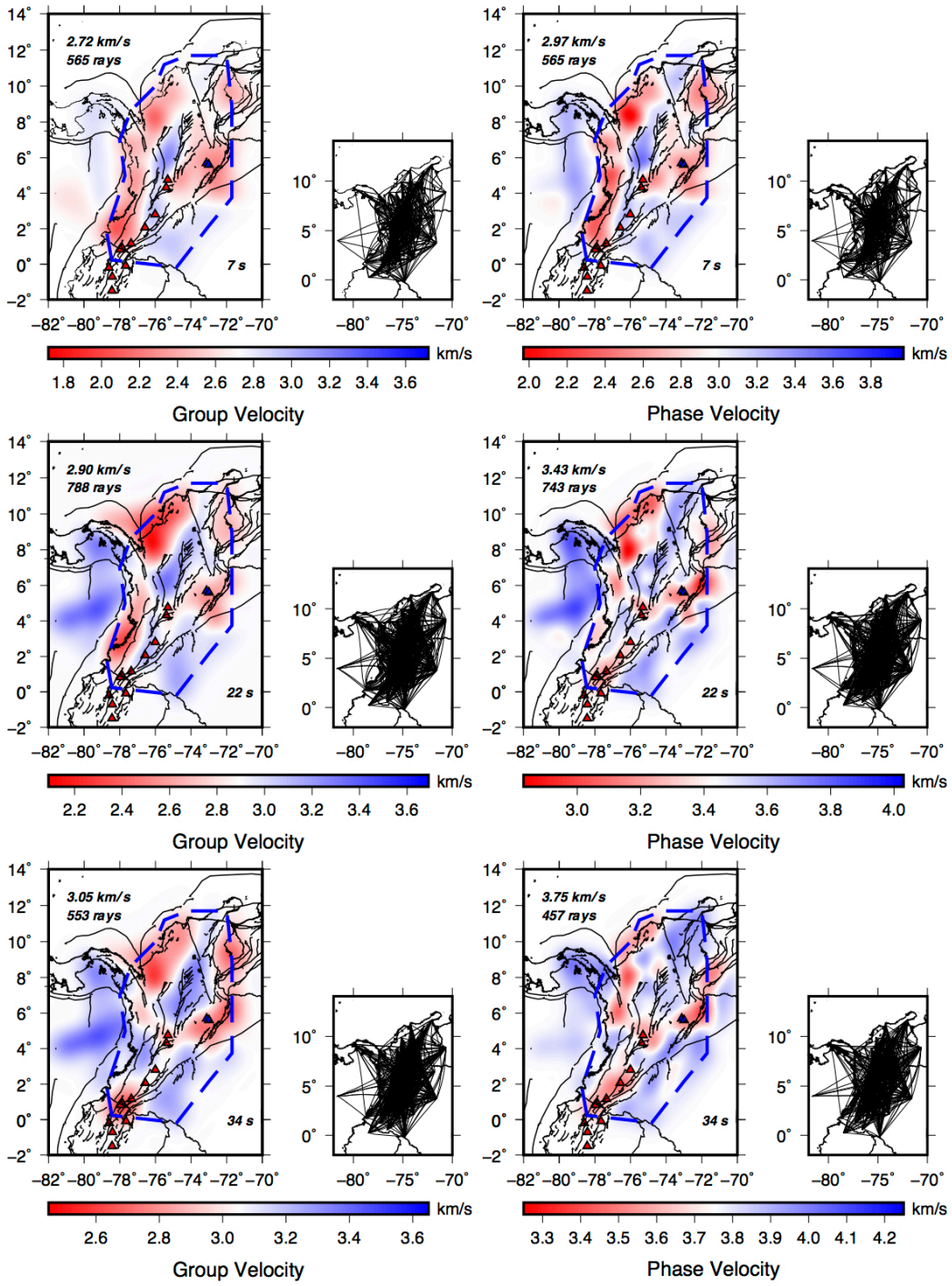
2.72 km/s
565 rays
7 s
2.97 km/s
565 rays
7 s
km/s
Group Velocity
Phase Velocity
2.90 km/s
788 rays
22 s
3.43 km/s
743 rays
22 s
3.05 km/s
553 rays
34 s
3.75 km/s
457 rays
34 s

Figure 10

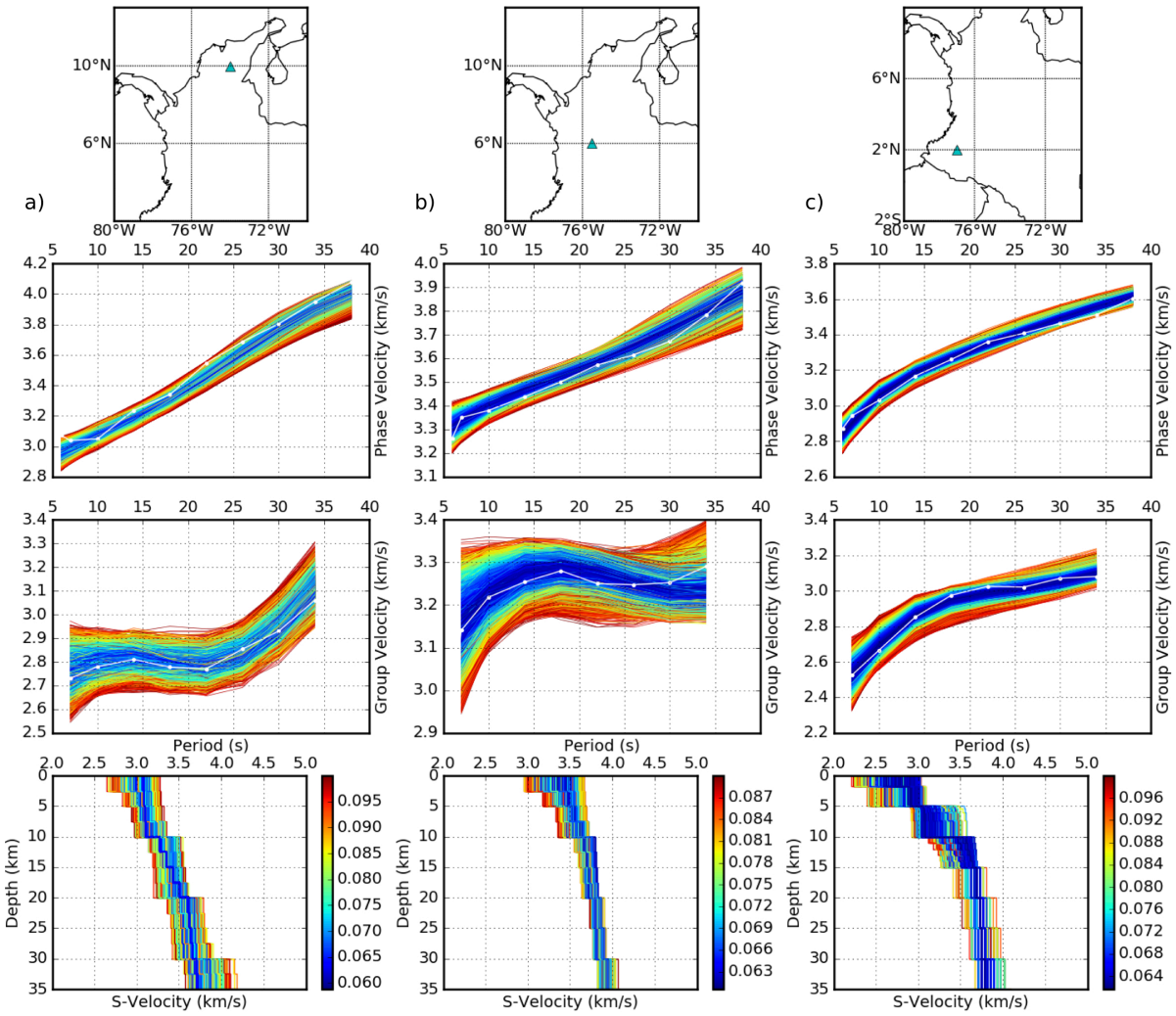
a)
b)
c)
10°N
6°N
2°N
2°S
80°W
76°W
72°W
Phase Velocity (km/s)
Group Velocity (km/s)
Period (s)
Depth (km)
S-Velocity (km/s)

Figure 11

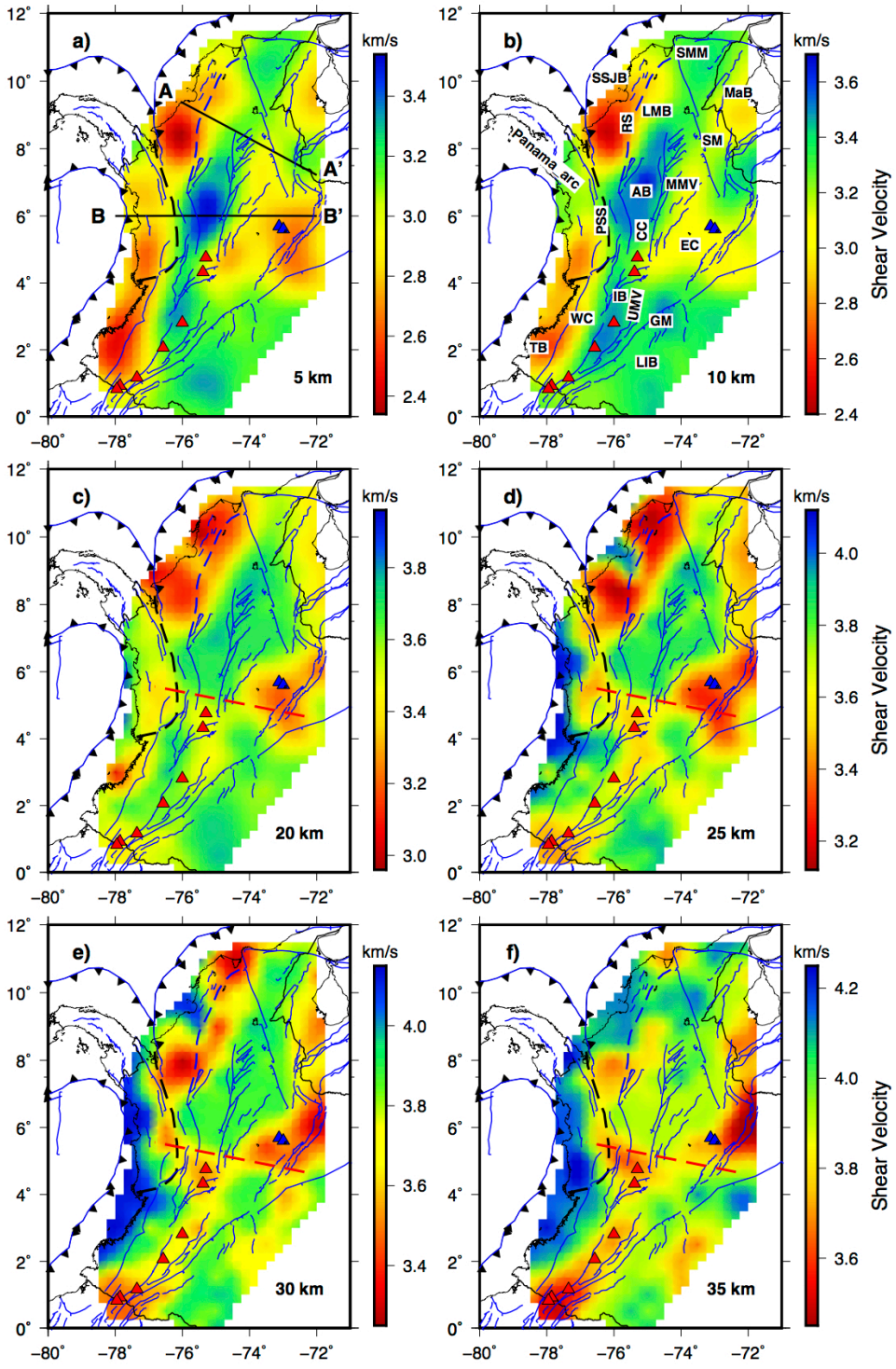
a)
A
A'
B
B'
5 km
km/s
3.4
3.2
3.0
2.8
2.6
2.4
b)
SMM
SSJB
MaB
LMB
RS
SM
Panama_arc
AB
MMV
PSS
CC
EC
IB
UMV
WC
GM
TB
LIB
10 km
Shear Velocity
3.6
3.4
3.2
3.0
2.8
2.6
2.4
c)
20 km
3.8
3.6
3.4
3.2
3.0
d)
25 km
4.0
3.8
3.6
3.4
3.2
e)
30 km
4.0
3.8
3.6
3.4
f)
35 km
4.2
4.0
3.8
3.6
12°
10°
8°
6°
4°
2°
0°
−80°
−78°
−76°
−74°
−72°

Figure 12

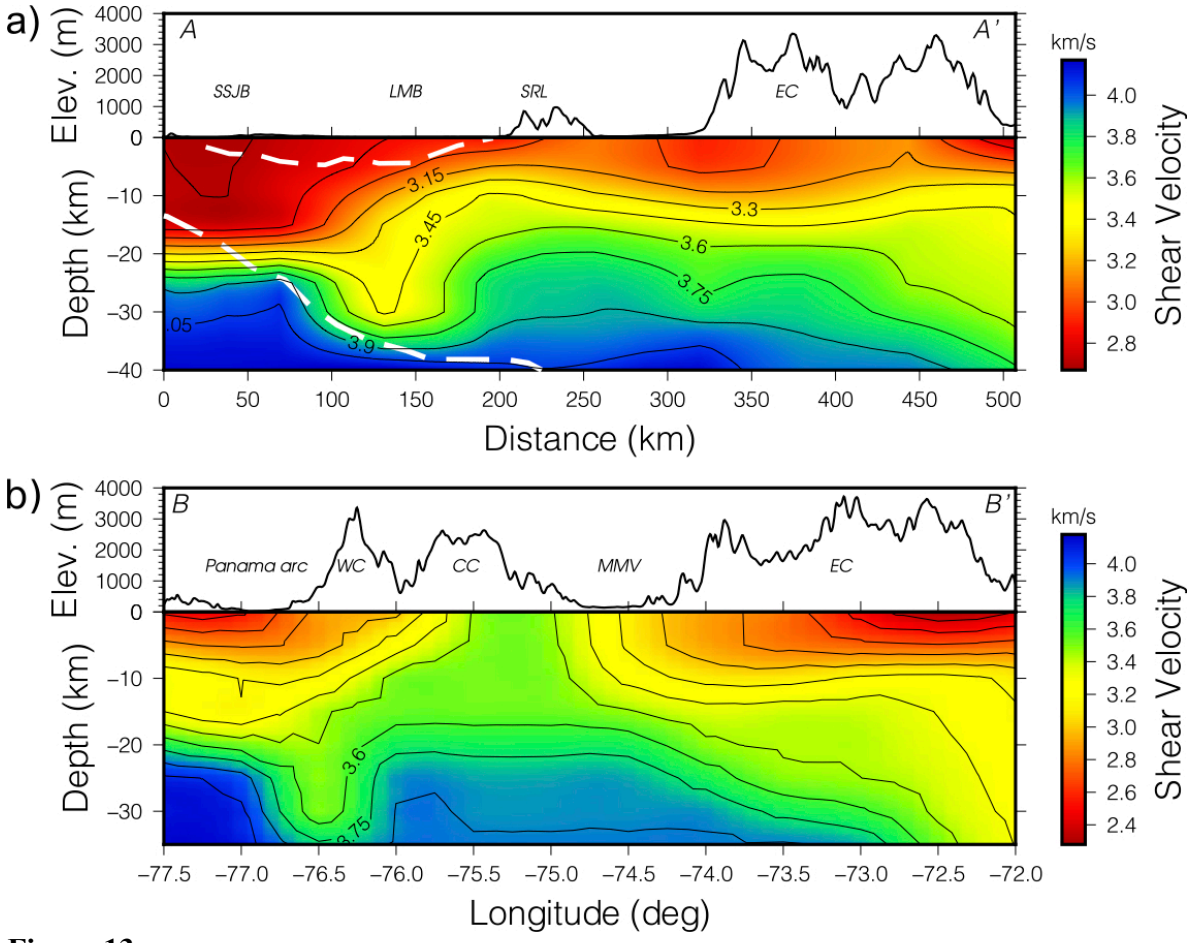
a)
A
A'
SSJB
LMB
SRL
EC
Elev. (m)
Depth (km)
Distance (km)
km/s
Shear Velocity
3.15
3.3
3.45
3.6
3.75
3.9
b)
B
B'
Panama arc
WC
CC
MMV
EC
Longitude (deg)

Figure 13

Table 1

Station	Latitude (deg)	Longitude (deg)	Recording time used (DD/MM/YY)	
ANIL	4.491	-75.403	04/05/2012	31/10/2015
ARGC	9.858	-74.246	26/04/2013	31/12/2015
BBAC	2.021	-77.247	27/04/2013	31/12/2015
BCIP	9.166	-79.837	01/01/2013	31/12/2015
BRR	7.107	-73.712	19/04/2012	03/12/2015
CAP2	8.646	-77.359	19/04/2012	03/07/2015
CBOC	5.864	-76.012	08/08/2013	31/12/2015
CHI	4.629	-73.318	19/04/2012	31/12/2015
COD	9.935	-73.444	19/04/2012	17/06/2014
CRJC	11.021	-72.881	27/11/2014	31/12/2015
FLO2	1.583	-75.653	19/04/2012	31/12/2015
GARC	2.187	-75.493	24/02/2014	31/12/2015
GCUF	1.226	-77.345	30/08/2012	31/10/2015
GUY2	5.223	-75.371	27/04/2013	31/12/2015
HEL	6.191	-75.529	19/04/2012	31/12/2015
LCBC	8.857	-76.368	19/11/2013	31/12/2015
MACC	2.145	-73.848	28/05/2013	31/12/2015
MAP	4.004	-81.606	19/04/2012	14/11/2015
MARA	2.822	-75.954	19/04/2012	17/08/2013
MON	8.778	-75.665	19/04/2012	31/12/2015
NOR	5.564	-74.869	06/04/2013	31/12/2015
NUQC	5.709	-77.277	18/08/2013	06/11/2013
OCA	8.238	-73.319	02/06/2012	31/12/2015
ORTC	3.909	-75.426	20/06/2013	31/12/2015
OTAV	0.237	-78.451	01/01/2013	31/12/2015
PAL	4.906	-76.283	19/04/2012	31/12/2015
PCON	2.327	-76.397	19/04/2012	03/06/2014
PGA1	3.747	-71.571	03/04/2014	31/12/2015
PGA2	3.901	-71.561	04/04/2014	16/06/2014
PIZC	4.965	-77.361	10/06/2014	31/12/2015
POP2	2.541	-76.676	19/04/2012	31/12/2015
PRA	3.714	-74.886	19/04/2012	31/12/2015
PRV	13.376	-81.364	31/05/2012	31/12/2014
PTA	7.147	-77.809	01/09/2012	31/12/2015
PTB	6.539	-74.456	19/04/2012	31/12/2015
PTGC	4.199	-72.134	09/10/2013	31/12/2015
PTLC	-0.171	-74.797	02/02/2013	31/12/2015
PUAC	0.549	-76.571	29/07/2014	19/05/2015
ROSC	4.844	-74.321	19/04/2012	31/10/2015
RREF	4.901	-75.347	19/04/2012	23/06/2015
RUS	5.893	-73.083	19/04/2012	31/12/2015
SDV	8.883	-70.634	01/01/2013	31/12/2015
SJC	9.897	-75.181	02/06/2012	31/12/2015
SMAR	11.163	-74.224	21/09/2012	31/12/2015
SML	8.801	-74.071	02/11/2012	31/12/2015
SOTA	2.135	-76.609	19/04/2012	23/05/2014
SPBC	5.652	-74.072	13/07/2013	31/12/2015
TAM	6.435	-71.791	28/07/2012	31/12/2015
TUM	1.824	-78.727	19/04/2012	31/12/2015
URE	7.752	-75.533	24/06/2012	31/12/2015
URI	11.702	-71.993	19/04/2012	31/12/2015
YOT	3.983	-76.345	19/04/2012	31/12/2015

JGR Solid Earth

Supporting Information for

Upper and middle crustal velocity structure of the Colombian Andes from ambient noise tomography: Investigating subduction-related magmatism in the overriding plate

Esteban Poveda[1], Jordi Julià[1, 2], Martin Schimmel[3], and Nelson Perez-Garcia[4, 5]

[1]Programa de Pós-Graduação em Geodinâmica e Geofísica, Universidade Federal do Rio Grande do Norte, Natal, RN CEP 59078-090, Brazil

[2]Departamento de Geofísica, Universidade Federal do Rio Grande do Norte, Natal, RN CEP 59078-970, Brazil

[3]Institut de Ciències de la Terra "Jaume Almera", CSIC, 08028 Barcelona, Spain

[4]Red Sismológica Nacional, Dirección de Geoamenazas, Servicio Geológico Colombiano, Bogotá, Colombia

[5]Now, Ecopetrol S.A., Bogotá, Colombia

Contents of this file

Figures S1 to S6

Introduction

This supporting information contains six figures that complement the text and figures provided in the manuscript.

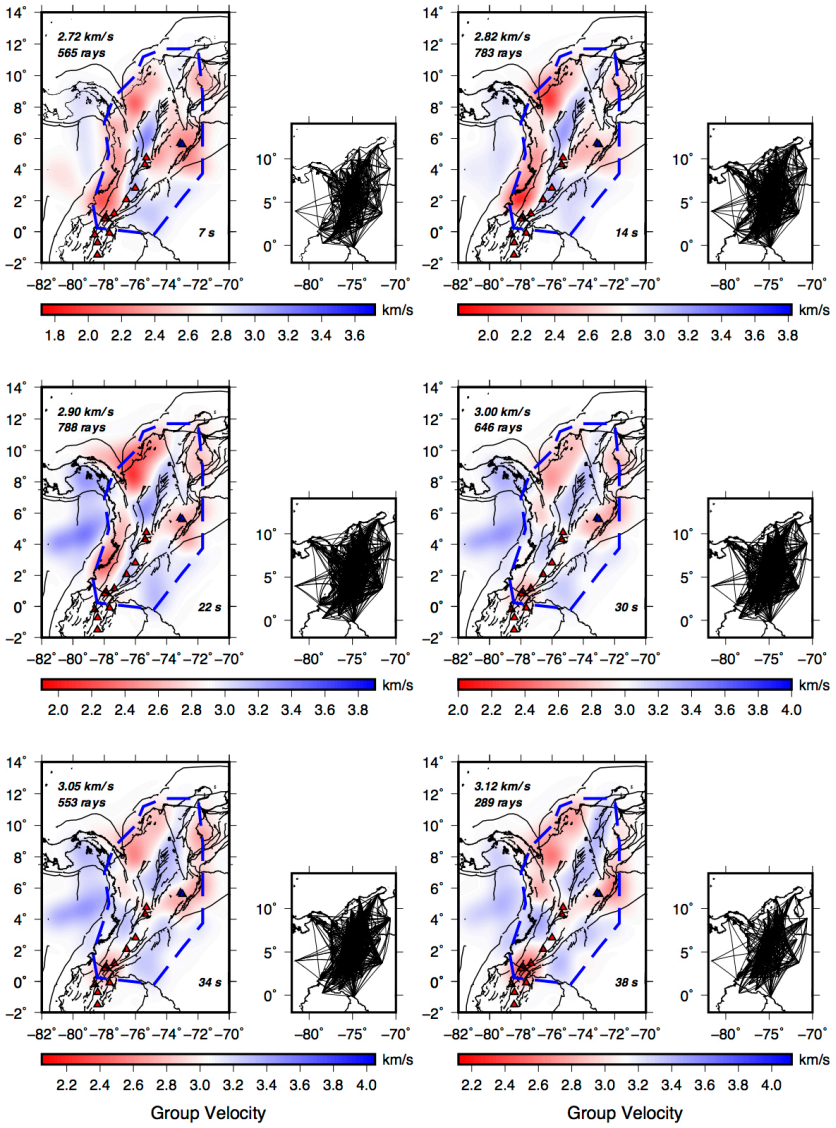

Figure S1. Rayleigh-wave group velocity maps for periods of 7, 14, 22, 30, 34, and 38 s. Major faults (black lines) are superimposed. The blue polygon encompasses the region used for the development of the 3-D S-velocity models. Smaller panels next to the tomographic slices show ray-path coverage for each period. Red and blue triangles display the location of active and inactive volcanoes, respectively.

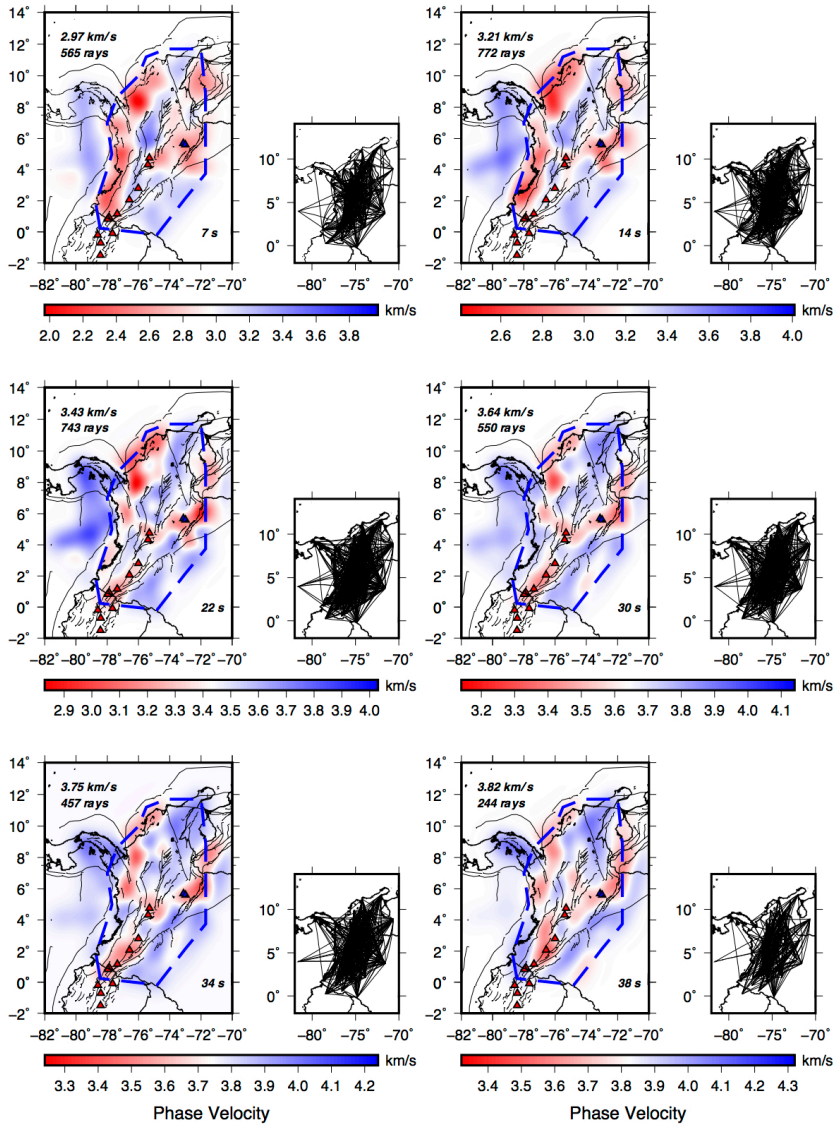

Figure S2. Rayleigh-wave phase velocity maps for periods of 7, 14, 22, 30, 34, and 38 s. Major faults (black lines) are superimposed. The blue polygon encompasses the region used for the development of the 3-D S-velocity models. Smaller panels next to the tomographic slices show ray-path coverage for each period. Red and blue triangles display the location of active and inactive volcanoes, respectively.

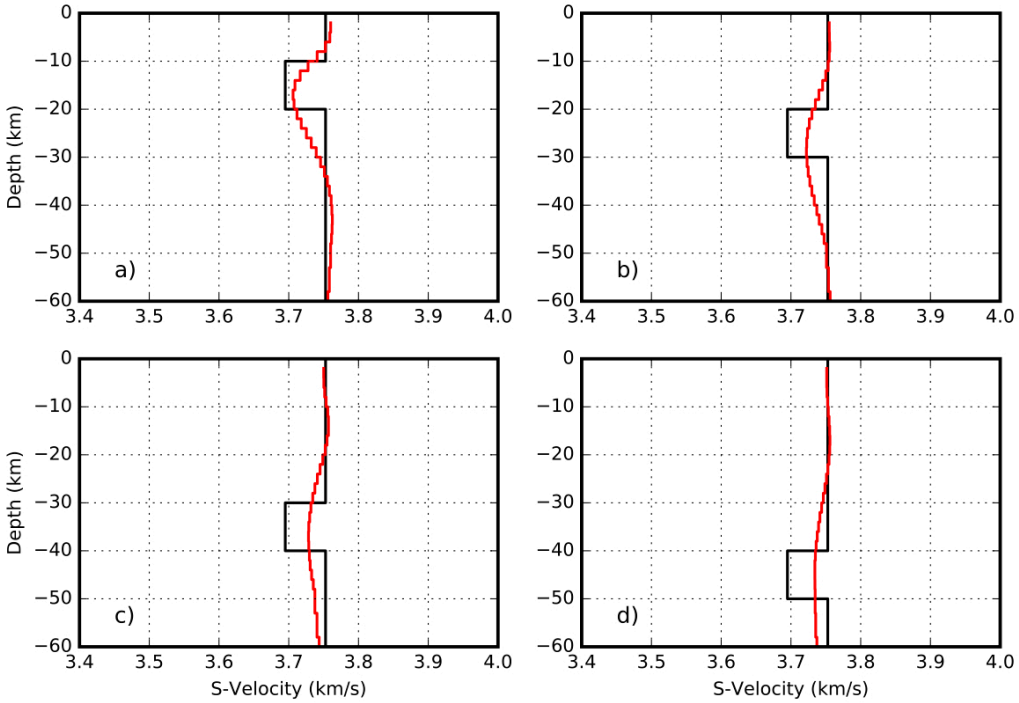

Figure S3. Synthetic tests to assess vertical resolution of the S-velocity models at different depths. Synthetic (black) and recovered (red) velocity models are shown for a low-velocity zone at (a) 10 km, (b) 20 km, (c) 30 km, and (d) 40 km. The low-velocity zone recovery is good down to ~35 km depth.

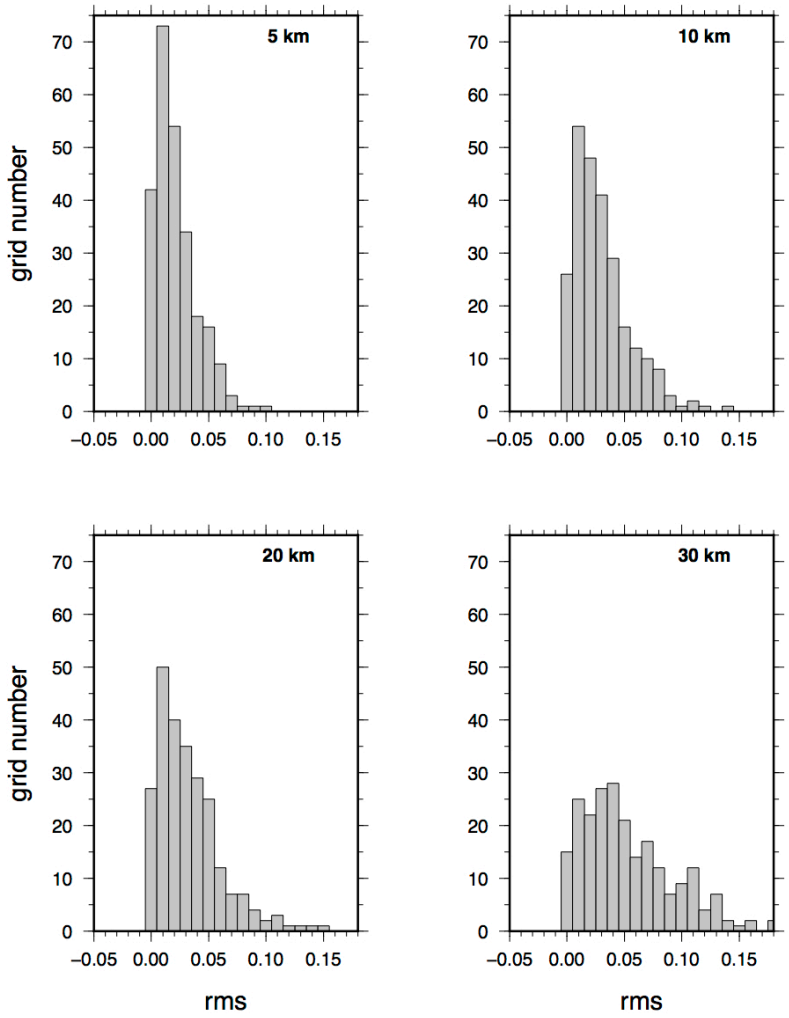

Figure S4. Histograms showing the number of nodes (in the 0.5˚ x 0.5˚ grid) with a given RMS average for S-wave velocity models developed from the two starting models described in the main text. Results are shown for 5, 10, 20, and 30 km depth.

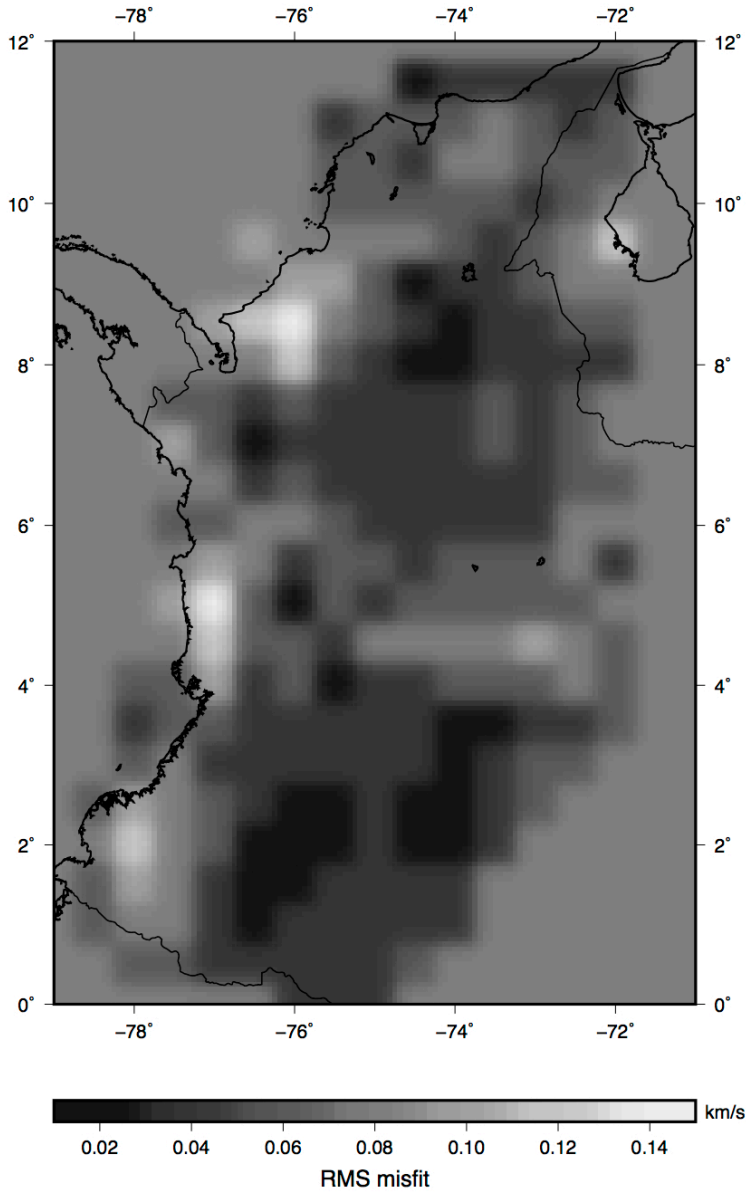

Figure S5. Misfit distribution from the NA inversion with the modified IASP91 starting model. Details are given in the main text.

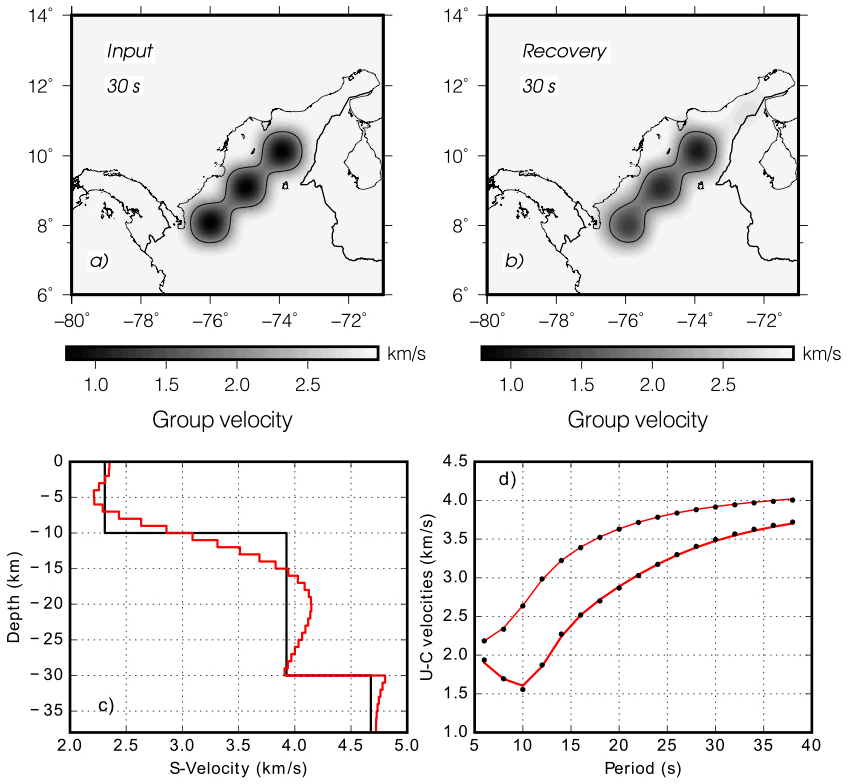

Figure S6. Resolution test for surface wave tomography and shear velocity inversion under Lower Magdalena Basin. (a) Input spike model for the 30 s group velocity inversion test, and (b) recovered group velocity model. (c) Input (black) and recovered (red) S-velocity profile, and (d) comparison between observed (symbols) and predicted (red line) Rayleigh-wave phase and group velocities.

Chapter 5

Investigating Active and Inactive Volcanism under the Colombian Andes with Radial Anisotropy (Paper II)

The following manuscript, entitled ***Investigating Active and Inactive Volcanism under the Colombian Andes with Radial Anisotropy from Ambient Noise and Surface Wave Tomography***, presents results on radial anisotropy for the Colombian Andes, inferred from the discrepancy between vertically (V_{SV}) and transverselly (V_{SH}) polarized S-velocities. A total of 1,264 empirical Green's functions were developed from ambient noise cross-correlations, and long-period (40 – 150 s) group velocities were determined from 11,000 fundamental-mode, surface-wave trains from earthquake sources at regional and teleseismic distances. The most important findings are related to regions of active and inactive volcanism, where negative/positive radial anisotropy in the upper-middle crust is observed, respectively, consistent with the presence/absence of feeding dykes. The manuscript also reports on positive radial anisotropy found at all crustal levels under the Lower Magdalena Valley, which is attributed to a combination of SPO (Shape Preferred Orientation) mechanisms including thick sedimentary sequences of alternating velocity, extensional stresses, and storage of asthenospheric magmas that breached the Caribbean flat slab. Additionally, it is argued that observed negative radial anisotropy in the Caribbean upper mantle might be characterizing the lateral extent of the Caribbean flat slab. This manuscript was submitted for publication in Tectonophysics on 02 AUG 2018.

Investigating Active and Inactive Volcanism under the Colombian Andes with Radial Anisotropy from Ambient Noise and Surface Wave Tomography

Esteban Poveda[1] and Jordi Julià[1, 2]

[1]Programa de Pós-Graduação em Geodinâmica e Geofísica, Universidade Federal do Rio Grande do Norte, Natal, RN CEP 59078-090, Brazil

[2]Departamento de Geofísica, Universidade Federal do Rio Grande do Norte, Natal, RN

Corresponding author: Esteban Poveda (esteban@ufrn.edu.br)

Key Points:

- Regions of active and inactive volcanism are underlain by negative and positive radial anisotropy, respectively, at upper- and mid-crustal depths.
- Positive radial anisotropy pervades the Colombian lower crust, suggesting widespread accumulation of subduction-related melts.
- Radial anisotropy in the upper mantle is generally small and can be disregarded.
- Negative radial anisotropy characterizes flat subduction under the Caribbean region at lithospheric depths.

Abstract

The relationship between crustal fluids and active/inactive volcanism under the Colombian Andes is investigated by mapping seismic radial anisotropy at crustal and upper mantle levels. Radial anisotropy is inferred from the discrepancy between

vertically (V_{SV}) and transverselly (V_{SH}) polarized S-velocities in horizontally propagating Rayleigh and Love waves, respectively. First, short-period (8 – 38 s) phase and group velocities are estimated from 1,264 empirical Green's functions from ambient noise cross-correlations, and long-period (40 – 150 s) group velocities are determined from 11,000 fundamental-mode, surface-wave trains from earthquake sources at regional and teleseismic epicentral distances. Dispersion velocities are then tomographically inverted to develop maps of phase and group velocity variation for periods between 8 and 38 s and 8 and 150 s, respectively. Finally, V_{SV} and V_{SH} velocity-depth profiles are constructed from the joint inversion of local group and phase velocity dispersion curves at each node in the tomographic grid down to 140 km depth. Our results reveal complex patterns of positive ($V_{SH} > V_{SV}$) and negative ($V_{SH} < V_{SV}$) radial anisotropy at both crustal and upper mantle depths. At upper to mid crustal levels radial anisotropy displays values of ±20%, with negative anisotropy coinciding with major tectonic terrains (Santa Marta Massif, Antioquia Batholith) and regions of active volcanism, and positive anisotropy characterizing major coastal basins (Lower Magdalena Basin, Tumaco Basin) and regions of inactive volcanism. Negative anisotropy under active volcanic regions is consistent with the presence of sub-vertical magmatic dykes feeding the volcanics, while positive anisotropy under inactive volcanic regions is consistent with magma storage along flat-lying sills. In tectonic terrains, negative anisotropy may be explained through escape tectonics, while positive anisotropy under the coastal basins could be resulting from a combination of flay-lying magmatic sills, extensional tectonics, and/or sub-horizontal shear. In the lower crust, positive anisotropy (up to 15%) is pervasive and interpreted as storage of subduction-related magmas, perhaps feeding

the dykes and sills at shallower crustal depths. Radial anisotropy in the upper mantle is generally small (< 2%), except in the Caribbean region where negative anisotropy up to 4% coincides with the postulated location of the Caribbean flat slab.

1. Introduction

The tectonic complexity of the northwestern Andes has been demonstrated through a number of geological and geophysical studies (Bernal-Olaya et al., 2015a; Chiarabba et al., 2016; Corredor, 2003; Cortés and Angelier, 2005; Idárraga-García et al., 2016; Pennington, 1981; Syracuse et al., 2016; Taboada et al., 2000; van der Hilst and Mann, 1994; Vargas and Mann, 2013; Wagner et al., 2017a; Yarce et al., 2014). Those studies demonstrate that the geometry of the Nazca and Caribbean plates is characterized by the presence of two Wadati-Benioff zones displaced by ~250 km at about 5.5°N and form a slab window. The first Benioff zone is located south of 5.5˚N and displays a well-defined, N-S trending line of active volcanoes. The second Benioff zone is located between latitudes 5.5˚N and 9˚N and, interestingly, has no active volcanism associated with it (see Fig. 1).

The geometry of the Nazca plate under NW South America can be divided into two segments, based on the angle of subduction from focal mechanisms and seismicity Pedraza-Garcia et al. (2007): a segment between 0°N and 3°N, with an angle that varies between 28° and 30°, and a second segment with an angle of 45° between 3°N and 5.5°N. The belt of associated volcanic activity is also segmented, with a volcanic gap between 2.92°N to 4.48°N possibly associated with the variation in the slab angle along the plate. South of the volcanic gap, volcanism is dominantly andesitic, with small

volumes of dacites and rhyolites and little explosive potential (e.g. Galeras Volcanic Complex). North of the volcanic gap (between ~4.5°N to ~5.5°N), several volcanic complexes are found (e.g. Nevado del Ruiz Volcano, Cerro Bravo volcano and Cerro Machín volcano), which are considered the most active and dangerous volcanoes in NW South America (Londoño and Sudo, 2003). The composition of these volcanoes ranges from basaltic andesites to dacites (Londoño and Sudo, 2003; Vatin-Pérignon et al., 1990). Recent studies (Londoño, 2016; Murcia et al., 2018) agree that the plumbing system under this volcanic segment is associated with vertical ducts in the shallow crust (between 5 – 20 km depth), fed by a common reservoir between 20 and 30 km depth under the entire volcanic segment. Lundgren et al. (2015), on the other hand, from interferometric synthetic aperture radar (InSAR) for the Nevado del Ruiz Volcano, propose that the magma ascent is associated with dike-generated conduits and lenses of magma stored at ~14 km depth.

The geometry of the Caribbean plate has not been accurately delineated, although several authors agree with very shallow subduction and oblique convergence of this plate below NW South America (Bernal-Olaya et al., 2015b; Mora-Bohórquez et al., 2017; Sanchez-Rojas and Palma, 2014; Sanchez and Mann, 2015; Taboada et al., 2000; van der Hilst and Mann, 1994). The shallow subduction angles postulated for this plate (5 – 10^{o}) have been invoked to explain the paucity of active surface volcanism in the overriding South American plate (Bernal-Olaya et al., 2015a; Mora-Bohórquez et al., 2017).

The presence of subduction-related melts within the overriding plate has been recently investigated in Poveda et al. (2018). In that study detailed velocity variations for

the Colombian Andes were recovered from ambient noise tomography (ANT) and inversion of Rayleigh-wave dispersion velocities. Low velocity values were reported in the upper crust coincident with sedimentary basins and quaternary deposits, such as the Sinú and San Jacinto belts (~2.4 km/s), the Maracaibo Basin (~2.7 km/s), and the Eastern Cordillera (EC) between 4°N and 5°N (~2.7 km/s), and along the Pacific coastal margins (~2.5 km/s). High velocity values were observed along the Central Cordillera (CC), coinciding with igneo-metamorphic rocks and batholits (eg., Ibague and Antioqua Batholiths). At mid-crustal levels (25-30 km) slow velocities were identified right under regions of active and inactive volcanism along the Central and Eastern Cordilleras, respectively, from which the presence of subduction-related melts were inferred. Why surface volcanism under the EC is inactive, however, remained unanswered. Even more intriguingly, similar slow velocities were reported under the Lower Magdalena Basin (LMB), right above the subducting Caribbean flat slab. The presence of Middle Miocene (13–14 Ma) mafic volcanism in the Caribbean continental margin, which might have reached the surface through a vertical tear in the Caribbean flat slab (Lara et al., 2013), let Poveda et al. (2018) propose that the slow velocities might reflect the presence of melts that breached the Caribbean slab and are now ponding at mid-crustal depths within the South American plate. Poveda et al. (2018), however, also acknowledged that those slow velocities could alternatively be related to fluid migration along major crustal faults (Corbeau et al., 2017) located under LMB (e.g. Romeral and Sinú faults).

Seismic anisotropy offers an excellent tool for investigating the stress and shear strain history associated with past deformation, magmatism and flow patterns resulting

from tectonic processes (e.g., *Moschetti et al.*, 2010a, 2010b). Traditionally, seismic anisotropy studies had utilized SKS phases from earthquake sources [e.g. *Porritt et al.*, 2014; *Bastow et al.*, 2015; *Idárraga-García et al.*, 2016] to infer orientation of fossil anisotropic fabrics in the lithosphere and/or flow patterns in the sublithospheric mantle; most recently, radial anisotropy has been considered for inferring patterns of fluid flow and/or direction of ductile deformation in the crust through the discrepancy between V_{SV} and V_{SH} velocities in Rayleigh and Love waves, respectively (Das and Rai, 2017; Lynner et al., 2018; Spica et al., 2017; Yudistira et al., 2017). Radially anisotropic media (or, equivalently, transversely isotropic media) are defined through a vertical symmetry axis [e.g *Xie et al.*, 2013], so that horizontally propagating waves travel at different wavespeeds depending on their vertical (V_{SV}) or horizontal (V_{SH}) sense of polarization. Radial anisotropy has been utilized to investigate crustal and/or mantle deformation on regional and global scales (Lynner et al., 2018; Moschetti et al., 2010b; Yudistira et al., 2017), as well as fluid flow in volcanic systems (Mordret et al., 2014; Spica et al., 2017). Radial anisotropy can be classified as positive ($V_{SV} > V_{SH}$), or negative ($V_{SH} < V_{SV}$), depending on which velocity is dominating.

Radial anisotropy can originate from either crystallographic preferred orientation (CPO) or shape preferred orientation (SPO). CPO is associated with alignment of the crystallographic axes of elastically anisotropic minerals, while SPO is related to structural controls exerted by geologic structures, such as sedimentary layering, magmatic intrusions, dykes, sills, melt lenses and partial melting (Babuska and Cara, 1991; Crampin, 1986, 1981; Leary et al., 1990; Shapiro, 2004). In the upper crust, the most important type of deformation for radial anisotropy is SPO (Karato, 2008). Positive

radial anisotropy is related to horizontal layering and/or aligned cracks and structures, such as horizontal bedding in sediments, fabric alignment created by extension and/or magma storage in flat-lying sills; negative radial anisotropy is attributed to vertically aligned structures such as vertical shear zones, high fault density in sedimentary sequences and/or dyke systems (Karato, 2008; Spica et al., 2017). Nevertheless, biotite and horblende can cause CPO anistropy in the crust. In the lower crust, plastic deformation is generally related to CPO of anisotropic minerals, such as amphibole and mica, during deformation along sub-horizontal shear zones at the upper-lower crust and the lower crust-lithospheric mantle boundaries (Gerbault and Willingshofer, 2004). In the upper mantle, horizontal, large-scale asthenospheric flow in the presence of strong anisotropic minerals, such as olivine or orthopyroxenes has been related to CPO, as well (Karato, 2008).

In this work, we compute transverse ambient seismic noise cross-correlations between all possible pairs of permanent stations in NW South America to extract empirical Green's functions for inter-station Love waves in the region, and develop maps of phase and group velocity variation between 8 and 26 s. The resulting ambient noise tomography (ANT) maps are then combined with those developed in *Poveda* et al. (2018) for Rayleigh waves to map radial anisotropy with depth through the Love-Rayleigh wave discrepancy (Lynner et al., 2018; Moschetti et al., 2010b; Spica et al., 2017). Moreover, group-velocity maps in the 40 to 150 s period range are additionally constructed through surface wave tomography (SWT) of Love and Rayleigh wave from regional and teleseismic earthquake sources, and combined with the shorter-period ANT results to develop joint V_{SV} and V_{SH} velocity models at crustal and upper mantle

depths (down to 140 km). In the upper crust, our results reveal positive anisotropy coinciding with the thick, sub-horizontal Quaternary sequences that fill the main sedimentary basins, and negative anisotropy under active surface volcanoes in igneous-metamorphic terrains. In the middle crust, negative anisotropy is again observed under active volcanic complexes, while positive anisotropy is found under inactive volcanoes, suggesting storage of subduction-related melts along vertically oriented (feeding) dykes and flat-lying sills, respectively. In the lower crust, positive anisotropy is pervasive throughout the study area. In the upper mantle negative radial anisotropy is generally small, but moderate negative anisotropy characterizes the lithospheric mantle under the LMB, perhaps delineating the area of Caribbean flat subduction.

2. Ambient noise and surface-wave tomography

2.1. Short-period dispersion velocities

The dataset utilized to develop short-period dispersion measurements consisted of continuous recordings of ambient seismic noise at up to 47 seismic stations operated by the Colombian Geological Survey and 3 nearby Global Seismograph Network stations in Ecuador, Venezuela, and Panamá. Recording time windows from January 2015 to December 2016 were considered. The combined seismic network consisted of a variety of seismic sensors and digitizers, which included Streckeisen STS-2, Streckeisen STS-2.5, Güralp CMG-3T, Güralp CMG3-ESP, Trillium 120p, Reftek 151A-120, and Reftek 151B-120 broadband and very broadband sensors, all with flat response in velocity down to 120 s, and high-gain digitizers (Quanterra Q330, Güralp

DM24 and Taurus) sampling continuously at 100 samples per second. The geographic distribution of the seismic stations is depicted in Figure 1.

Empirical Green's functions (EGFs) containing the Love wave train between all station pairs were obtained from the cross-correlation of up to two years (January 2015 – December 2016) of continuous data. We adopted the same procedure that *Poveda et al.* (2018) utilized to develop Rayleigh wave EGFs from the same dataset, which was based on the well-established approaches of *Bensen et al.* (2007) and *Lin et al.* (2008). At each station, data were first resampled to 1 sample per second and split into one-day segments, to then be demeaned, detrended, and have the instrument response removed. The resulting one day-long segments were next band-pass filtered between 0.01 and 0.2 Hz, and normalized in the time (one-bit) and frequency (spectral whitening) domains. The horizontal components (N, E) were then rotated into the great-circle-path according to interstation orientations to produce the radial (R) and transverse (T) components, and cross-correlated to develop radial-radial (RR) and transverse-transverse (TT) cross-correlations. Finally, the RR and TT cross-correlations were stacked through the time-frequency, phase-weighted procedure (tf-PWS) of *Schimmel and Paulssen* (1997) and *Schimmel et al.* (2011) to develop the EGFs. In total, 1264 Rayleigh (RR) and Love (TT) EGFs were obtained from the assembled data set (see Figure 2).

Phase and group velocity dispersion was measured in the Love-wave (TT) EGFs only, using the Automated Frequency–Time Analysis (AFTAN) of *Levshin and Ritzwoller* (2001), as Rayleigh-wave dispersion was already measured in the ZZ component by Poveda et al. (2018). Phase and group velocities were obtained for periods between 8

to 26 s for EGFs with a signal-to-noise ratio (SNR) > 7, and dispersion measurements with inter-station distances smaller than 3 wavelengths were eliminated (*Bensen et al.*, 2007). The intrinsic 2πN phase ambiguity of phase-velocity measurements was resolved using the global phase velocity reference model from the Preliminary Reference Earth Model (PREM) of *Dziewonski and Anderson* (1981). Additional details about data processing and measurement of dispersion velocities can be found in *Poveda et al.* (2018), along with Rayleigh-wave EGFs and dispersion measurements from ZZ (vertical-vertical) cross-correlations.

2.2. Long-period dispersion velocities

The dataset utilized to develop dispersion measurements at longer periods, consisted of local, regional and telesseismic waveforms recorded between 1994 and 2016 by 50 seismic stations operated by the National Seismological Network of Colombia (RSNC), and 9 additional Global Seismological Network (GSN) stations in Ecuador, Venezuela, Panama, Brazil and the Caribbean region. The time windows considered for each station and their geographical locations are listed in Table 1, and the location of the stations and earthquake sources are displayed in Figure 3. Hypocentral information was obtained from the National Earthquake Information Center (NEIC) for distant and regional events, and from the RSNC catalogue for local events. In total, we selected 430 local (< 1000 km), 270 regional (1000 – 2000 km) and 420 teleseismic (> 2000 km) earthquake sources with magnitudes larger than 4.5 and depths less than 30 km (see Figure S1, in the Supplemmentary Materials, for further details).

To develop dispersion measurements, the instrumental response was first removed from the recorded waveforms, which were then converted to displacement, demeaned, detrended and re-sampled to one sample per second. Fundamental-mode, group-velocities for Rayleigh and Love waves were then measured through the Multiple Filter Analysis of *Dziewonski et al.* (1969), as implemented in the PGSWMFA package (PGplot Surface Wave Multiple Filter Analysis) of *Ammon* (1998) , after isolating the fundamental mode through a phase-match filter (*Herrin and Goforth*, 1977). Rayleigh-wave dispersion was obtained from the vertical components, while Love-wave dispersion was measured on the rotated, transverse components. In total, over 11,000 wavetrains were analyzed, resulting in over 10,000 dispersion curves for Rayleigh wave and over 7,000 for Love waves. A detailed example of waveform processing for periods between 30 and 150 s is given in the Supplemmentary Materials (Figure S2). Dispersion measurements were obtained in a wide period range (10 – 150 s), although the range of periods for a given waveform varied according to waveform complexity, epicentral distance, and event magnitude.

A rigorous quality control was applied to the measured dispersion velocities to ensure that only high-quality group velocities were used in the tomographic inversion. First, in order to identify possible timing problems in the seismograms, P-wave travel times were computed with the TauP software of *Crotwell et al.* (1999) and compared to those picked from the waveforms. Those that did not agree within 5 s were rejected. Second, only group velocity estimates that formed continuous dispersion curves were considered, discarding measurements with abrupt jumps and/or gaps in the dispersion curve. Finally, as for the EGFs above, dispersion measurements with inter-station

distances smaller than 3 wavelengths were eliminated (Bensen et al., 2007). The final number of raypaths as a function of distance and period are displayed in Figure 4. Note that for periods between 20 and 60 s the number of measurement is larger than 8000 and 5000 for Rayleigh and Love waves, respectively; between 60 and 130 s, the number of raypaths gradually decreases from 8000 to 2000 for Rayleigh waves, and from 6000 to 1500 for Love waves (Figure 4a). The average distance travelled is similar for Rayleigh and Love waves (Figure 4c). Histograms for 50 s Rayleigh and Love wave raypaths reveal the most common distance is 10 degrees (Figs 4b,d).

2.3. Tomographic inversion

For the tomographic inversion, we used dispersion data between 8 to 26 s from EGFs (phase and group, Love) and 30 to 150 s from earthquake data (group only, Rayleigh and Love). Group velocities for periods below 30 s from earthquake sources were not considered, as they were found of lower quality when compared to those obtained from the ANT at similar periods, and no corresponding phase velocity estimates were developed. The FMST (Fast Marching Surface-wave Tomography) procedure of *Rawlinson and Sambridge* (2005) was utilized for either ambient noise or surface-wave dispersion measurements. The FMST solves the forward problem through the Eikonal equation, which allows for the description of the entire wavefront in time and space (Sethian and Popovici, 1999). The inverse problem was approached through an iterative, non-linear scheme driven by the subspace method, which minimizes the RMS misfit between observed and predicted dispersion velocities with damping and smoothness regularizations. Further details can be found in *Rawlinson and Sambridge* (2004, 2005).

For the tomographic inversion of ambient noise (Love waves, 8 – 26 s) and surface-wave dispersion velocities (Rayleigh and Love waves, 30 – 150 s), the study area was divided into cells of 0.5^o x 0.5^o and 1.0^o x 1.0^o, respectively. An average velocity was determined from all the observations at a given period, which was then utilized as both the starting model and for damping regularization. The regularization parameters in the objective function were estimated through the L-curve (*Aster et al.*, 2013), after exploring a wide variety of smoothness and damping values. Figure S3, in the Supplemmentary Materials, displays the L-curves for 26 and 110 s for Love wave. The regularization parameters ranged between 1 to 300 for smoothness and roughness, for all periods. Convergence was generally achieved after 6 iterations.

Tomographic images for Rayleigh and Love group velocities at 10, 50, and 100 s are displayed in Figure 5; similar images for Rayleigh and Love phase velocities can be found in Figure S4, along with checkerboard resolution tests (Figure S5). Recall that the ANT tomographic images for Rayleigh waves (phase and group) were borrowed from *Poveda et al.* (2018). As already noticed in that study, Rayleigh-wave group velocities at short periods (10 s) display a pattern of fast and slow dispersion that correlates well with surface geology: low velocity anomalies are found under coastal and intracontinental basins (LMB, MMV, EC), while fast velocities correlate with igneous-metamorphic complexes (SMM, AB, IB) and along the southern segment of the EC (which encompasses the Garzon Massif). At 50 s, Rayleigh-wave dispersion shows an inverse correlation with crustal thickness, with high velocities in regions of thin crust and low velocities in regions of thick crust. The Andean zone, where crustal thickness is larger than 50 km (*Poveda et al.*, 2015), is characterized by slow velocities, while fast

velocities characterize the Guiana craton, the Santa Marta Massif and the Maracaibo Block, where the crustal thickness is small (< 40 km). Finally, at long periods (100 s), low velocities are related to the asthenospheric mantle wedge above the subducting Nazca plate, while fast velocities are possibly associated with flat subduction of the Caribbean plate (*Bernal-Olaya et al.*, 2015b; *Mora-Bohórquez et al.*, 2017) and the presence of thick lithosphere under the EC.

Tomographic images for Love-wave dispersion display similar patterns, although the match to the corresponding Rayleigh-wave images is not perfect (Figure 5). At short periods the sedimentary basins (LMB, MMV, EC) still display slow velocities; however, velocities under the CC and SMM are not fast, but slow. At 50 s, Love and Rayleigh wave velocities are almost identical, probably reflecting the same variations in crustal thickness; yet, small discrepancies are still observed. At long periods (100 s) the transition from slow to fast velocity is shifted East with respect to that observed in the Rayleigh wave images at the same period. The reported discrepancies in the velocity patterns are due, in part, to the different depth-sensitivity of Rayleigh and Love waves at similar periods (e.g. *Lay and Wallace*, 1995); as demonstrated in the next section, the observed discrepancies also result from radial anisotropy.

3. Radial anisotropy patterns

3.1. Inversion for V_{SV} and V_{SH}

The tomographic dispersion estimates described in the previous section were next combined to build dispersion curves at each node making the 0.5^o x 0.5^o grid utilized in the ANT. Local dispersion curves (phase and group) for Rayleigh-waves were

constructed by combining the ambient noise tomography results of *Poveda et al.* (2018) between 7 to 38 s with group velocities developed in this work from earthquake sources between 40 and 150 s. Local dispersion curves were similarly built for Love waves by combining the Love-wave dispersion velocity estimates from ANT and from earthquake sources developed in this study. SV and SH velocity-depth profiles were then ~~developed~~ obtained from the joint inversion of Rayleigh and Love wave dispersion. Following Lynner et al. (2018), Rayleigh and Love-wave dispersion velocities were inverted separately.

To develop the 1D velocity-depth profiles we followed the linearized, iterative inversion scheme described in Julià et al. (2003), in which the RMS misfit between observed and predicted dispersion velocities is minimized in a least-squares sense, with smoothness constraints. The method was originally developed for the joint inversion of receiver functions and surface wave dispersion measurements, but can be easily applied to the inversion of dispersion curves by giving zero influence to the receiver function portion of the objective function. Smoothness is controlled through the *a priorily* defined smoothness parameter (θ), which is determined through analysis of the trade-off curve between RMS misfit and model roughness for each inversion (see e.g. *Ammon et al.*, 1990). The number of iterations was determined through inspection of the RMS misfit with iteration number.

The starting model was parametrized with a crust consisting of a S-velocity gradient from 3.3 to 4.0 km/s, using 2.5 km-thick layers that extended down to the local Moho depth reported in *Poveda et al.* (2018). In the upper mantle, we used S-velocity values from the PREM global velocity model (*Dziewonski and Anderson*, 1981),

parametrized in 5.0 km thick layers for depths between 70 and 150 km, and 10 km thick below 150 km depth. The crustal Vp/Vs ratio was set to the value reported by *Ojeda and Havskov* (2001) of 1.78 for NW South America, while densities were estimated from Vp through the well-established empirical relationship of *Berteussen* (1977).

A detailed example of the linearized dispersion curve inversion for V_{SV} and V_{SH} velocity is presented in Figure 6 for a node at 5.5°N, 73°W under the EC. The inversion results shows a fast V_{SH} with respect to V_{SV} for the middle crust, resulting in a marked peak of positive radial anisotropy (Vsh > Vsv) of 20% at 39 km depth. Figure 6 also shows a good match between observed and predicted Rayleigh and Love waves for both group and phase velocity. As shown in the Supplemmentary Materials (Figure S6), Rayleigh and Love dispersion curves could not be simultaneously matched using a single S-velocity model.

3.2. Radially anisotropic S-velocity structure

Radial anisotropy was inferred from the inverted V_{SV} and V_{SH} velocity models by first estimating isotropic S-velocity through the Voigt average

$$Voigt\ average = \sqrt{\frac{(2V_{SV}^2 - V_{SH}^2)}{3}} \qquad (1)$$

and then computing the percentage of radial anisotropy as

$$Radial\ anisotropy = \frac{2(V_{SH} - V_{SV})}{(V_{SH} + V_{SV})} \times 100\% \qquad (2)$$

(see e.g. Lynner et al., 2018). Figures 7 and 8 display the Voigt average and radial anisotropy percentage obtained from inverted V_{SV} and V_{SH} velocities for select depths

between 10 and 140 km. As expected (recall eq. 2), the variations in Voigt average are similar to those reported in *Poveda et al.* (2018) for V_{SV} where there is depth overlap.

More in detail, at 10 km depth fast velocities (3.4 km/s) and negative values of radial anisotropy are observed coinciding with igneous-metamorphic terrains along the AB (20%), the SMM (5%) and, perhaps, the SM (2%). South of the EC, under the Garzon massif (GM), negative radial anisotropy is observed with a value of 5% and a Voigt average of 3.3 km/s. Slow velocities and positive radial anisotropy patterns, on the other hand, are observed at the LMB (2.8 km/s - 12%), under the EC north of 4˚N (2.9 km/s – 3%), at the SSJB (2.9 km/s – 5 %), and at the TB (2.8 km/s - 10%). At 25 km depth, slow velocities and positive radial anisotropy are observed under the LMB, with values about of 3.3 km/s and 20%, respectively. Fast velocities and negative radial anisotropy are observed under the CC (north of 5.5˚N), the MMV and the SM, with values of 3.8-3.9 km/s and 5-10%, respectively. Below the CC (south of 5˚N), the WC and the TB, on the other hand, slightly slow velocities and positive radial anisotropy (3.4 km/s – 5%) are found. Note that active volcanism is found along the CC south of latitude 5˚N. Positive radial anisotropy (6%) and slow velocities (3.5 km/s) characterize the EC. At 40 km depth, positive radial anisotropy dominates the entire study area, with peaks of 10-15% under zones of active and inactive volcanism associated with slow velocities (3.4 to 3.9 km/s). Similarly, in the Maracaibo Basin (MaB) and regions limiting with Venezuela, positive radial anisotropy and slow velocities (18% - 3.7 km/s) are observed.

At 50 km depth, the Voigt average displays slow velocities (3.9 - 4.2 km/s) below the CC and the EC, likely due to crustal thicknesses over 50 km, and a marked positive

radial anisotropy of 10%. Fast velocities (4.4 km/s) under the LMB and the SMM and MaB (4.5 - 4.6 km/s) probably reflect the presence of upper mantle rocks. Except for the CC and the EC, radial anisotropy is slightly positive (2 - 3%) throughout the region. At 80 km depth, Voigt average velocities increase from West to East, with low values (4.4 km/s) under the Pacific coast, the WC, the CC, the TB and the Panama arc and high values under the MMV and the EC. Alternating patterns of small positive and negative radial anisotropy (1 - 2 %) are observed throughout, except under the LMB where negative values of radial anisotropy are larger. The velocity and anisotropy patterns at 120 km depth are similar to those reported at 80 km.

The vertical relationship between the velocity and anisotropy patterns described above is demonstrated through a number of cross-sections in Figures 9 through 11. Note how positive anisotropy of 7 – 20% pervades the entire lower crust, with values becoming largest under the CC and the EC and with correspondingly high values of isotropic shear velocities (3.8 - 4.0 km/s). More in detail, Figure 9a shows a cross-section through the Caribbean region. Under the LMB, positive anisotropy values for the entire crust are observed, along with slow velocities (2.8-3.4 km/s); in this area, the positive anisotropy layer located between 20-30 km seems to delimit the top of the Caribbean plate. Under the SLR high values of negative radial anisotropy and high Voigt averages, respectively (3.6 km/s – 10%), are found (Figure 9a).

The cross-section in Figure 9b crosses the CC and the EC at latitude 6˚N, where CC volcanism ceases, showing negative values of anisotropy in the upper (15%) and middle (5%) crust under the CC and slightly positive (5 %) under the EC, where the inactive Iza-Paipa volcanic complexes are located. Figure 10a displays another cross-

section through the CC and EC, now at latitude 4˚N. Regions with active volcanism (south of 5.5˚N) are characterized with negative anisotropy (5%) and slow velocity (3.4 km/s); intriguingly, a similar pattern is observed under the EC where no surface volcanism is observed. Finally, Figure 10b maps the volcanic complexes at latitude 2˚N, showing negative radial anisotropy and slow isotropic velocities (15% - 2.6 km/s) in the upper and middle crusts.

A SW-NE transect (Figure 11) is presented crossing the entire study area. As mentioned, slow isotropic velocities (3.4 km/s) are observed below the volcanic provinces, with negative anisotropy in the middle crust (5 - 10%). Absence of positive radial anisotropy between 30 and 50 km of depth coincides with the location of the volcanic gap under the CC (250 to 430 km along profile). A region with hight Voigt averages (4.0 km/s) between 20 - 35 km depth is observed under the CC, where the volcanism filnalizes (between 600 - 800 km along profile), with values of negative anisotropy of 5%. The lower crust, as mentioned before, displays positive radial anisotropy throughout.

4. Implications for fluid flow and deformation

One of the main findings reported in *Poveda et al.* (2018) was the presence of marked slow velocities within the crust (25 - 35 km depth), mimicking the track of the surface volcanism along the CC and EC. Such slow velocities were interpreted as resulting from subduction-related melts that pond at mid-crustal depths in the overriding plate. *Poveda et al.* (2018) further noticed that volcanism along the EC is inactive, and that the presence of slow velocities in the underlying crust implied that it was not extinct.

The Voigt averages obtained in this study extend the presence of such slow velocities under the surface volcanics down to 40 km depth (Figure 7e), with associated positive anisotropy (Figure 7f); more interestingly, estimates of radial anisotropy show that negative radial anisotropy characterizes the crust immediately above (< 25 km depth) under the CC, where volcanism is active, while positive radial anisotropy characterizes a similar depth-range under the EC, where volcanism is inactive (Figures 7b, 10). We speculate that the negative radial anisotropy might be related to some structural alignment in the vertical direction, for instance, emplacement of magmas intruding through sub-vertical feeding dykes. Indeed, recent studies (Londoño, 2016 and Murcia et al., 2018) from seismological and geochemical data reported a deep magmatic body emplaced at about 20–40 km depth north of the active volcanic segment at ~4.5°N that feed several active volcanoes in the area (e.g. Nevado del Ruiz Volcano, Cerro Bravo volcano and Cerro Machín volcano). Moreover, Lundgren et al. (2015), reported the existence of dykes in the shallow crust under the Nevado del Ruiz Volcano from InSAR modelling. On the other hand, under the Iza-Paipa volcanic complex in the EC, positive radial anisotropy is observed, which is consistent with the proposal that volcanism in this area is inactive but not extinct (Bernet et al., 2016; Poveda et al., 2018). The profile in Figure 09b clearly shows a low-velocity zone under eastern side of EC at depths between 25 and 35 km associated with an area with strong positive radial anisotropy, suggesting the presence of horizontally lying magma bodies. The absence of negative radial anisotropy immediatelly above would indicate the absence of dyke systems feeding the surface volcanoes.

In the Caribbean region, positive radial anisotropy is found under the LMB at all crustal levels (Figures 7 and 9) overlying the Caribbean flat slab. In this region, Poveda et al. (2018) found ~~a~~ the crust is characterized by slow S-velocity (V_{SV}), as also observed through the Voigt average in this work, and raised two hypotheses. The first hypothesis was related to the presence of Middle Miocene (13–14 Ma) mafic volcanism within the Caribbean continental margin, as reported by Lara et al. (2013). Those authors proposed that asthenospheric magmas might have breached the Caribbean flat slab through a preexisting vertical tear, and that they are now ponding at mid-crustal depths within the overriding plate. Indeed, this hypothesis would be consistent with positive anisotropy, provided that melts were ponding in flay-lying structures such as sills. Note that, if this were correct, the preferred storage of the melts along horizontal structures (rather than vertical structures such as feeding dykes) would additionally explain the paucity of surface volcanism in the region. The second hypothesis was related to fluid migration along major crustal faults (Corbeau et al., 2017; Zhao et al., 1996); this hypothesis would be inconsistent with positive anisotropy, as SPO from vertical structures such as faults would be expected to yield negative anisotropy (Yudistira et al., 2017).

Alternatively, crustal extension might also explain positive anisotropy. The Plato (PB) and San Jorge Basins (SJB), which are part of the LMB, have been suggested to result from extensional stresses produced by a Miocene to Recent, 23°–30° clockwise rotation of the Santa Marta Massif (Montes et al., 2010), with a total of 50–56 km of east-west shortening in the Cesar-Rancheria Basin (CRB) and 115 km of extensión throughout the LMB. In the shallow crust, the deposition of thick, flat-lying sedimentary

sequences (Lara et al., 2013; Montes et al., 2010; Vernette et al., 1992), with alternating layers of fast and slow S-velocity, might be responsible for the observed positive radial anisotropy (Xie et al., 2013; Yudistira et al., 2017); in the middle crust, positive radial anisotropy could result from subhorizontal alignment of anisotropic minerals due to CPO associated to the extensional process. Additionally, dragging through coupling with the Caribbean flat slab right under the LMB might have induced sub-horizontal shear in the upper plate, which might in turn have further contributed to positive radial anisotropy (Gerbault and Willingshofer, 2004; Karato, 2008).

Radial anisotropy in the lower crust is commonly explained by CPO of minerals due to sub-horizontal plastic or ductile channel flow (Karato, 2008). This mechanism of deformation has been invoked in Tibet (e.g. (Guo et al., 2012; Shapiro, 2004; Xie et al., 2013), where crustal thickness is more than 50 km, to explain the extensional setting and crustal thinning of the region (Shapiro, 2004). Most recently, it has also been invoked to explain positive radial anisotropy in the middle and lower crust in some parts of the Central Andes (Lynner et al., 2018). This mechanism produces sub-horizontal shear zones at the boundaries between the upper and lower crusts, and between the lower crust and lithospheric mantle, and might be playing a role in the pervasive positive radial anisotropy reported in this study for the Colombian Andes (Figure 7h). However, we note that the magnitude of positive anisotropy is stronger where active and inactive volcanism are found, and that it is coincident with slow S-velocities. This makes as think that magmatic storage in flat-lying sills is more plausible. The mechanism under CC is more likely to be related to horizontally aligned magmatic addition, which can also play a role in thickening the crust (Poveda et al. 2015) and agrees with the proposal of

Weber et al. (2002) of magmatic addition from the upper mantle wedge. Under the EC, a combination of SPO and CPO due to horizontally lying magma bodies and upper mantle flow (Yarce et al. 2014) could be a plausible explanation for the observe positive radial anisotropy, as it would explain non-isostatic residual topography associated with subduction.

In the upper mantle, radial anisotropy is generally small (2 %) and can probably be ignored. However moderate (4 %) negative radial anisotropy is observed north of latitude 8°N below 80 km depth (Figures 08 and 09). According to *Bernal-Olaya et al.* (2015a), the Caribbean plate subducts under NW South America with an anomalous low angle of 3-8° over a distance of 200 km into the South American continent from the trench zone. If the Caribbean plate is indeed characterized by negative radial anisotropy, we can then suggest that the southern termination of the Caribbean slab occurs at around of 8°N. This suggests that the Nazca plate can extend to at least 8°N, which implies that the limit at 5.5 N (seismicity offset) represents a slab tear as proposed by *Chiarabba et al.* (2016), *Syracuse et al.* (2016), and *Wagner et al.* (2017) rathern than a boundary between two separate plates (e.g. *Bernal-Olaya et al.*, 2015b; *Yarce et al.* (2014); *Cortés and Angelier*, 2005; *Taboada et al.*, 2000).

Finally, negative radial anisotropy also characterizes the upper crust of some tectonic blocks, such as the SMM, AB, SM, SRL and IB (Figure 7b). The SMM, SM, SRL and IB they are of plutonic nature and represents a NNE-trending batholitic record of Late Triassic - Jurassic age associated with volcanic rocks distributed along of the Central Cordillera and the middle and upper Magdalena Valley (UMV) (*Bustamante et*

al., 2016; *Spikings et al.*, 2015). In particular, the AB is the most important intrusive body of the northern segment of the Central Cordillera (*Restrepo-Moreno et al.*, 2009). The origin of those magmatic pulses have been associated to oblique subduction of the Farallon plate, which explains the segmented distribution of these batholiths along the CC (*Bustamante et al.* 2016). The intrusive nature of these bodies, especially the SMM, SM, SRL and IB, with similar ages and genesis, can explain the negative anisotropy through vertical shape preferred orientation (SPO). Furthermore, *Restrepo-Moreno et al.*, (2009) reported long-term erosional exhumation of the Antioqueño plateau, which includes the AB, along with deformation related to uplift, shortening and high fault angles making negative radial anisotropy more likely. Also, the modern stress regime is accommodated by major structures within the North Andean Block through lateral escape at 6±2 mm/a to the northeast, with the South American plate acting as a rigid body, while the Panama-arc (or Panama-Choco Block) is in active collision at a rate of ~25 mm/yr (*Egbue et al.*, 2014; *Trenkamp et al.*, 2002). Escape tectonics could be triggering a combined shortening-and-upplift deformation that would be consistent with negative radial anisotropy, especially under the CC.

5. Conclusions

Combined Rayleigh and Love wave tomography using seismic ambient noise (7 – 38 s) and earthquake sources (40 – 150 s) revealed the radial anisotropic structure under NW South America. Anisotropic parameters were obtained through a linearized inversion scheme that estimated 3-D variation in V_{SV} and V_{SH} in the crust and upper mantle. Positive anisotropy is pervasive in the lower crust, especially under the CC and EC, consistent with the accumulation of subduction-related magmas along flat-lying

structures. Positive radial anisotropy if found under the LMB at all crustal levels, perhaps due to a combination of SPOs from extensional stresses, drag by the Caribbean flat slab, and storage of asthenospheric magmas breaching the slab. Negative radial anisotropy characterizes the upper and middle crusts under the CC, where surface volcanism is active, which can be related magmatic alignment along sub-vertical feeding dykes, positive radial anisotropy is observed at similar depth-ranges under the EC, suggesting storage of magmas along flat-lying sills. Weak negative radial anisotropy is observed throghout the upper mantle, except under the LMB, perhaps marking the lateral exteng of the Caribbean flat slab.

Acknowledgements

The authors want to express their gratitude to the Colombian Geological Survey (Servicio Geológico Colombiano, SGC) for generously providing the data for conducting this study; in particular to Marta Calvache, technical director of geological hazards of Colombian Geological Survey and Viviana Dionicio, Head of the Seismological Network (Red Sismológica Nacional de Colombia, RSNC). Raw data can be freely available and accesible to the scientific community through written request and justification addressed to the Colombian Geological Survey (sismologo@sgc.gov.co). EP acknowledges support from the *Coordenação de Aperfeiçoamento de Pessoal de Nível Superior* (CAPES) through a 4-year scholarship to complete his Ph.D. JJ thanks the *Conselho Superior de Desenvolvimento Científico e Tecnológico* (CNPq) for his research fellowship (process number 304421/2015-4). Most of the figures have been plotted with matplotlib (Hunter, 2007) and the Generic Mapping Tools (GMT) (Wessel and Smith, 1998). We thank to Martin Schimmel for making his cross-correlations and stacking codes available to us.

Figure Captions

Figure 1. Simplified tectonic and geologic map of northwestern South America. Geologic provinces are from *Gómez et al.* (2007) and major faults from *Veloza et al.* (2012). Plate motions relative to South America are from *Trenkamp et al.* (2002). The gray thick line marks the boundary of the North Andean Block (NAB); the area with vertical lines marks the location of the Panamá-arc. Red triangles are active volcanoes; Blue triangles are inactive volcanoes. SMM: Santa Marta Massif; Mab: Maracaibo Block; SMBF: Santa Marta- Bucaramanga Fault; SM: Santander Massif; MA: Merida Andes; SSJB: Sinú and San Jacinto Basin; CRB: Cesár-Rancheria Basic; PB: Plató Basin; LMV: Lower Magdalena Valley; SJB: San Jorgé Basin; SLR: San Lucas Range; AB: Antioqueño Batholith; BR: Baudo Range; MMV: Middle Magdalena Valley; RS-: Romeral Suture; CPB: Panamá arc Block; AB: Antioqueño Batholith; CC: Central Cordillera; EC: Eastern Cordillera; LIB: Llanos Basin; LFS: Llanos Faults system; WC: Western Cordillera; CV: Cauca Valley; IB: Ibagué Batholith; SMV: Superior Magdalena Valley; QM: Quetame Massif; GM: Garzón Massif and CV: Cauca Valley; MR: Macarena Ranges; TB: Túmaco Basin.

Figure 2. Reconstructed Love (a) and Rayleigh waves (b) EGFs from ambient noise cross-correlations. All traces are band-pass filtered between 10 to 50 seconds and normalized to maximum amplitude. Only cross correlations with SNR > 10 are included.

Figure 3. Global distribution of Mw > 4.5 earthquakes for the period 1994-2016 and depth < 50 km (top); Stations used in this study for SWT (bottom).

Figure 4. (a) Number of paths for Rayleigh waves (dashed line) and Love waves (solid line) as a function of period. (b) Distribution of epicentral distances for 50 s period Love waves. (c). Path lenght as function of period. (d) Distribution of epicentral distances for 50 s period Rayleigh waves.

Figure 5. Rayleigh and Love-wave group velocity maps for selected periods of 10, 50 and 100 s. Major faults (black lines) are superimposed from *Veloza et al.* (2012). Insets show path coverage at each period. Red and blue triangles show active and inactive volcanoes, respectively.

Figure 6. Detailed inversion results at node -73°W,5.5°N (EC); a) Inverted V_{SV}, V_{SH} and Voigt average; b) Radial anisotropy from V_{SV} and V_{SH}; c) Location of inversion node (-73°W, 5.5°N); d) Comparison between observed (gray) and predicted Love (blue) and Rayleigh (purple) phase dispersion curves; e) Comparison between observed (gray) and predicted Love (blue) and Rayleigh (purple) group dispersion curves.

Figure 7. Voigt average and radial anisotropic maps for 10, 30 and 50 km depth. Depth is indicated in the lower right corner of each map. Red and blue triangles indicate active and inactive volcanoes, respectively; major faults (blue lines) are superimposed from Veloza et al. (2012). Dashed black lines in (a) mark the locations of cross-sections in Figures 11 and 12.

Figure 8. Voigt average and radial anisotropic maps for 80, 100 and 140 km depths. Depth is indicated in the lower right corner of each map. Red and blue triangles indicate the active and inactive volcanoes, respectively; major faults (blue lines) are

superimposed from Veloza et al. (2012). Dashed black lines in (a) mark the locations of cross-sections in Figures 11 and 12.

Figure 9. a) Cross-sections across the Caribbean and Andean regions A-A' (see figure 8) with topography on top. Top and bottom panels display Voigt average and radial anisotropy, respectively. Dashed lines represent the Caribbean slab from *Mora-Bohórquez et al.* (2017)**;** b) Cross-sections on Andean region B-B', with topography on top. Top and bottom panels display Voigt average and radial anisotropy, respectively. White circles represent hypocentral locations.

Figure 10. a) Cross-sections along C-C' (see figure 8), with topography on top. Top and bottom panels display Voigt average and radial anisotropy, respectively; b) Cross-sections along Andean region D-D', with topography. Top and bottom panels display Voigt average and radial anisotropy, respectively. White circles represent hypocentral locations, dashed lines mark the upper boundary of the subducting Nazca plate (from Hayes et al., 2012).

Figure 11. Cross-section along E-E' (see Figure 8), with associated topography on top panel. The top and bottom panels display the Voigt average and radial anisotropy, respectively.

References

Ammon, C.J., 1998. Notes on surface-wave tomography. Part I: Group velocity estimation.

Ammon, C.J., Randall, G.E., Zandt, G., 1990. On the nonuniqueness of receiver function inversions. J. Geophys. Res. 95, 15303. doi:10.1029/JB095iB10p15303

Aster, R.C., Borchers, B., Thurber, C.H., 2013. Chapter Four - Tikhonov Regularization, in: Aster, R.C., Borchers, B., Thurber, C.H. (Eds.), Parameter Estimation and Inverse Problems (Second Edition). Academic Press, Boston, pp. 93–127. doi:https://doi.org/10.1016/B978-0-12-385048-5.00004-5

Babuska, V., Cara, M., 1991. Seismic Anisotropy in the Earth. Publishers Kluwer Academic, Dordrecht.

Bastow, I.D., Julià, J., do Nascimento, A.F., Fuck, R.A., Buckthorp, T.L., McClellan, J.J., 2015. Upper mantle anisotropy of the Borborema Province, NE Brazil: Implications for intra-plate deformation and sub-cratonic asthenospheric flow. Tectonophysics 657, 81–93. doi:10.1016/j.tecto.2015.06.024

Bensen, G.D., Ritzwoller, M.H., Barmin, M.P., Levshin, A.L., Lin, F., Moschetti, M.P., Shapiro, N.M., Yang, Y., 2007. Processing seismic ambient noise data to obtain reliable broad-band surface wave dispersion measurements. Geophys. J. Int. 169, 1239–1260. doi:10.1111/j.1365-246X.2007.03374.x

Bernal-Olaya, R., Mann, P., Vargas, C.A., 2015a. Earthquake, Tomographic, Seismic

Reflection, and Gravity Evidence for a Shallowly Dipping Subduction Zone beneath the Caribbean Margin of Northwestern Colombia. Mem. 108 Pet. Geol. Potential Colomb. Caribb. Margin 247–270. doi:10.1306/13531939M1083642

Bernal-Olaya, R., Sanchez, J., Mann, P., Murphy, M., 2015b. Along-strike Crustal Thickness Variations of the Subducting Caribbean Plate Produces Two Distinctive Styles of Thrusting in the Offshore South Caribbean Deformed Belt, Colombia, in: Memoir 108: Petroleum Geology and Potential of the Colombian Caribbean Margin. AAPG, pp. 295–322. doi:10.1306/13531941M1083645

Bernet, M., Urueña, C., Amaya, S., Peña, M.L., 2016. New thermo and geochronological constraints on the Pliocene-Pleistocene eruption history of the Paipa-Iza volcanic complex, Eastern Cordillera, Colombia. J. Volcanol. Geotherm. Res. doi:10.1016/j.jvolgeores.2016.08.013

Berteussen, K.-A., 1977. Moho depth determinations based on spectral-ratio analysis of NORSAR long-period P waves. Phys. Earth Planet. Inter. 15, 13–27. doi:10.1016/0031-9201(77)90006-1

Bustamante, C., Archanjo, C.J., Cardona, A., Vervoort, J.D., 2016. Late Jurassic to Early Cretaceous plutonism in the Colombian Andes: A record of long-term arc maturity. Geol. Soc. Am. Bull. 128, 1762–1779. doi:10.1130/B31307.1

Chiarabba, C., De Gori, P., Faccenna, C., Speranza, F., Seccia, D., Dionicio, V., Prieto, G.A., 2016. Subduction system and flat slab beneath the Eastern Cordillera of Colombia. Geochemistry, Geophys. Geosystems 17, 16–27.

doi:10.1002/2015GC006048

Corbeau, J., Rolandone, F., Leroy, S., Guerrier, K., Keir, D., Stuart, G., Clouard, V., Gallacher, R., Ulysse, S., Boisson, D., Bien-aimé Momplaisir, R., Saint Preux, F., Prépetit, C., Saurel, J.M., Mercier de Lépinay, B., Meyer, B., 2017. Crustal structure of western Hispaniola (Haiti) from a teleseismic receiver function study. Tectonophysics 709, 9–19. doi:10.1016/j.tecto.2017.04.029

Corredor, F., 2003. Seismic strain rates and distributed continental deformation in the northern Andes and three-dimensional seismotectonics of northwestern South America. Tectonophysics 372, 147–166. doi:10.1016/S0040-1951(03)00276-2

Cortés, M., Angelier, J., 2005. Current states of stress in the northern Andes as indicated by focal mechanisms of earthquakes. Tectonophysics 403, 29–58. doi:10.1016/j.tecto.2005.03.020

Crampin, S., 1986. Anisotropy and Transverse Isotropy. Geophys. Prospect. 34, 94–99. doi:10.1111/j.1365-2478.1986.tb00454.x

Crampin, S., 1981. A review of wave motion in anisotropic and cracked elastic-media. Wave Motion 3, 343–391. doi:10.1016/0165-2125(81)90026-3

Crotwell, H.P., Owens, T.J., Ritsema, J., 1999. The TauP Toolkit: Flexible Seismic Travel-time and Ray-path Utilities. Seismol. Res. Lett. 70, 154–160.

Das, R., Rai, S.S., 2017. Extensive seismic anisotropy in the lower crust of Archean metamorphic terrain, South India, inferred from ambient noise tomography.

Tectonophysics 694, 164–180. doi:10.1016/j.tecto.2016.12.002

Dziewonski, A., Bloch, S., Landisman, M., 1969. A technique for the analysis of transient seismic signals. Bull. Seismol. Soc. Am. 59, 427–444.

Dziewonski, A.M., Anderson, D.L., 1981. Preliminary reference Earth model. Phys. Earth Planet. Inter. 25, 297–356. doi:10.1016/0031-9201(81)90046-7

Egbue, O., Kellogg, J., Aguirre, H., Torres, C., 2014. Evolution of the stress and strain fields in the Eastern Cordillera, Colombia. J. Struct. Geol. 58, 8–21. doi:10.1016/j.jsg.2013.10.004

Gerbault, M., Willingshofer, E., 2004. Lower crust indentation or horizontal ductile flow during continental collision? Tectonophysics 387, 169–187. doi:10.1016/j.tecto.2004.06.012

Gómez, J., Nivia, A., Montes, N.E., Jiménez, D.M., Tejada, M.L., Sepúlveda, M.J., Osorio, J.A., Gaona, T., Diederix, H., Uribe, H., Mora, M., 2007. Mapa Geologico Colombia.

Guo, Z., Gao, X., Wang, W., Yao, Z., 2012. Upper- and mid-crustal radial anisotropy beneath the central Himalaya and southern Tibet from seismic ambient noise tomography. Geophys. J. Int. 189, 1169–1182. doi:10.1111/j.1365-246X.2012.05425.x

Hayes, G.P., Wald, D.J., Johnson, R.L., 2012. Slab1.0: A three-dimensional model of global subduction zone geometries. J. Geophys. Res. Solid Earth 117, n/a-n/a.

doi:10.1029/2011JB008524

Herrin, E., Goforth, T., 1977. Phase-matched filters: Application to the study of Rayleigh waves. Bull. Seismol. Soc. Am. 67, 1259–1275.

Hunter, J.D., 2007. Matplotlib: A 2D Graphics Environment. Comput. Sci. Eng. 9, 90–95. doi:10.1109/MCSE.2007.55

Idárraga-García, J., Kendall, J.-M., Vargas, C.A., 2016. Shear wave anisotropy in northwestern South America and its link to the Caribbean and Nazca subduction geodynamics. Geochemistry, Geophys. Geosystems 17, 3655–3673. doi:10.1002/2016GC006323

Karato, S., 2008. Seismic anisotropy and its geodynamic implications, in: Deformation of Earth Materials: An Introduction to the Rheology of Solid Earth. Cambridge University Press, pp. 391–411. doi:10.1017/CBO9780511804892.022

Lara, M., Cardona, A., Monsalve, G., Yarce, J., Montes, C., Valencia, V., Weber, M., De La Parra, F., Espitia, D., López-Martínez, M., 2013. Middle Miocene near trench volcanism in northern Colombia: A record of slab tearing due to the simultaneous subduction of the Caribbean Plate under South and Central America? J. South Am. Earth Sci. 45, 24–41. doi:10.1016/j.jsames.2012.12.006

Lay, T., Wallace, T.C., 1995. Modern Global Seismology.

Leary, P.C., Crampin, S., McEvilly, T. V., 1990. Seismic fracture anisotropy in the Earth's crust: An overview. J. Geophys. Res. 95, 11105.

doi:10.1029/JB095iB07p11105

Levshin, A.L., Ritzwoller, M.H., 2001. Automated Detection, Extraction, and Measurement of Regional Surface Waves. Pure Appl. Geophys. 158, 1531–1545. doi:10.1007/PL00001233

Lin, F.C., Moschetti, M.P., Ritzwoller, M.H., 2008. Surface wave tomography of the western United States from ambient seismic noise: Rayleigh and Love wave phase velocity maps. Geophys. J. Int. 173, 281–298. doi:10.1111/j.1365-246X.2008.03720.x

Londono, J.M., 2016. Evidence of recent deep magmatic activity at Cerro Bravo-Cerro Machín volcanic complex, central Colombia. Implications for future volcanic activity at Nevado del Ruiz, Cerro Machín and other volcanoes. J. Volcanol. Geotherm. Res. 324, 156–168. doi:10.1016/j.jvolgeores.2016.06.003

Londoño, J.M., Sudo, Y., 2003. Velocity structure and a seismic model for Nevado del Ruiz Volcano (Colombia). J. Volcanol. Geotherm. Res. 119, 61–87. doi:10.1016/S0377-0273(02)00306-2

Lundgren, P., Samsonov, S. V., López Velez, C.M., Ordoñez, M., 2015. Deep source model for Nevado del Ruiz Volcano, Colombia, constrained by interferometric synthetic aperture radar observations. Geophys. Res. Lett. 42, 4816–4823. doi:10.1002/2015GL063858

Lynner, C., Beck, S.L., Zandt, G., Porritt, R.W., Lin, F.-C., Eilon, Z.C., 2018. Mid-crustal deformation in the Central Andes constrained by radial anisotropy. J. Geophys.

Res. Solid Earth. doi:10.1029/2017JB014936

Montes, C., Guzman, G., Bayona, G., Cardona, A., Valencia, V., Jaramillo, C., 2010. Clockwise rotation of the Santa Marta massif and simultaneous Paleogene to Neogene deformation of the Plato-San Jorge and Cesar-Ranchería basins. J. South Am. Earth Sci. 29, 832–848. doi:10.1016/j.jsames.2009.07.010

Mora-Bohórquez, J.A., Ibánez-Mejia, M., Oncken, O., de Freitas, M., Vélez, V., Mesa, A., Serna, L., 2017. Structure and age of the Lower Magdalena Valley basin basement, northern Colombia: New reflection-seismic and U-Pb-Hf insights into the termination of the central andes against the Caribbean basin. J. South Am. Earth Sci. 74, 1–26. doi:10.1016/j.jsames.2017.01.001

Mordret, A., Rivet, D., Landès, M., Shapiro, N.M., 2014. Three-dimensional shear velocity anisotropicmodel of Piton de la Fournaise Volcano (La Réunion Island) fromambient seismic noise. J. Geophys. Res. Solid Earth 120, 1–22. doi:10.1002/2014JB011654.We

Moschetti, M.P., Ritzwoller, M.H., Lin, F.-C., Yang, Y., 2010a. Crustal shear wave velocity structure of the western United States inferred from ambient seismic noise and earthquake data. J. Geophys. Res. 115, B10306. doi:10.1029/2010JB007448

Moschetti, M.P., Ritzwoller, M.H., Lin, F., Yang, Y., 2010b. Seismic evidence for widespread western-US deep-crustal deformation caused by extension. Nature 464, 885–889. doi:10.1038/nature08951

Murcia, H., Borrero, C., Németh, K., 2018. Overview and plumbing system implications

of monogenetic volcanism in the northernmost Andes' volcanic province. J. Volcanol. Geotherm. Res. doi:10.1016/j.jvolgeores.2018.06.013

Ojeda, A., Havskov, J., 2001. Crustal structure and local seismicity in Colombia. J. Seismol. 5, 575–593. doi:10.1023/A:1012053206408

Pedraza Garcia, P., Vargas, C.A., Monsalve J., H., 2007. Geometric model of the Nazca plate subduction in Southwest Colombia. Earth Sci. Res. J.

Pennington, W.D., 1981. Subduction of the Eastern Panama Basin and seismotectonics of northwestern South America. J. Geophys. Res. Solid Earth 86, 10753–10770. doi:10.1029/JB086iB11p10753

Porritt, R.W., Becker, T.W., Monsalve, G., 2014. Seismic anisotropy and slab dynamics from SKS splitting recorded in Colombia. Geophys. Res. Lett. 41, 8775–8783. doi:10.1002/2014GL061958

Poveda, E., Julià, J., Schimmel, M., Perez-Garcia, N., 2018. Upper and Middle Crustal Velocity Structure of the Colombian Andes From Ambient Noise Tomography: Investigating Subduction-Related Magmatism in the Overriding Plate. J. Geophys. Res. Solid Earth. doi:10.1002/2017JB014688

Poveda, E., Monsalve, G., Vargas, C.A., 2015. Receiver functions and crustal structure of the northwestern Andean region, Colombia. J. Geophys. Res. Solid Earth 120, 2408–2425. doi:10.1002/2014JB011304

Rawlinson, N., Sambridge, M., 2005. The fast marching method: an effective tool for

tomographic imaging and tracking multiple phases in complex layered media. Explor. Geophys. 36, 341. doi:10.1071/EG05341

Rawlinson, N., Sambridge, M., 2004. Multiple reflection and transmission phases in complex layered media using a multistage fast marching method. Geophysics 69, 1338–1350. doi:10.1190/1.1801950

Restrepo-Moreno, S., Foster, D., Stockli, D., Parra-Sanchez, L., 2009. Long-term erosion and exhumation of the “Altiplano Antioqueño”, Northern Andes (Colombia) from apatite (U–Th)/He thermochronology. Earth Planet. Sci. Lett. 278, 1–12. doi:10.1016/j.epsl.2008.09.037

Sanchez-Rojas, J., Palma, M., 2014. Crustal density structure in northwestern South America derived from analysis and 3-D modeling of gravity and seismicity data. Tectonophysics 634, 97–115. doi:10.1016/j.tecto.2014.07.026

Sanchez, J., Mann, P., 2015. Integrated Structural and Basinal Analysis of the Cesar–Rancheria Basin, Colombia: Implications for its Tectonic History and Petroleum Systems, in: Memoir 108: Petroleum Geology and Potential of the Colombian Caribbean Margin. AAPG. doi:10.1306/13531945M1083648

Schimmel, M., Paulssen, H., 1997. Noise reduction and detection of weak, coherent signals through phase-weighted stacks. Geophys. J. Int. 130, 497–505. doi:10.1111/j.1365-246X.1997.tb05664.x

Schimmel, M., Stutzmann, E., Gallart, J., 2011. Using instantaneous phase coherence for signal extraction from ambient noise data at a local to a global scale. Geophys.

J. Int. 184, 494–506. doi:10.1111/j.1365-246X.2010.04861.x

Sethian, J.A., Popovici, A.M., 1999. 3-D traveltime computation using the fast marching method. GEOPHYSICS 64, 516–523. doi:10.1190/1.1444558

Shapiro, N.M., 2004. Thinning and Flow of Tibetan Crust Constrained by Seismic Anisotropy. Science (80-.). 305, 233–236. doi:10.1126/science.1098276

Spica, Z., Perton, M., Legrand, D., 2017. Anatomy of the Colima volcano magmatic system, Mexico. Earth Planet. Sci. Lett. 459, 1–13. doi:10.1016/j.epsl.2016.11.010

Spikings, R., Cochrane, R., Villagomez, D., Lelij, R. Van Der, Vallejo, C., Winkler, W., Beate, B., 2015. The geological history of northwestern South America : from Pangaea to the early collision of the Caribbean Large Igneous Province (290 – 75 Ma). Gondwana Res. 27, 95–139. doi:10.1016/j.gr.2014.06.004

Syracuse, E.M., Maceira, M., Prieto, G.A., Zhang, H., Ammon, C.J., 2016. Multiple plates subducting beneath Colombia, as illuminated by seismicity and velocity from the joint inversion of seismic and gravity data. Earth Planet. Sci. Lett. 444, 139–149. doi:10.1016/j.epsl.2016.03.050

Taboada, A., Rivera, L.A., Fuenzalida, A., Cisternas, A., Philip, H., Bijwaard, H., Olaya, J., Rivera, C., 2000. Geodynamics of the northern Andes: Subductions and intracontinental deformation (Colombia). Tectonics 19, 787–813. doi:10.1029/2000TC900004

Trenkamp, R., Kellogg, J.N., Freymueller, J.T., Mora, H.P., 2002. Wide plate margin

deformation, southern Central America and northwestern South America, CASA GPS observations. J. South Am. Earth Sci. 15, 157–171. doi:10.1016/S0895-9811(02)00018-4

van der Hilst, R., Mann, P., 1994. Tectonic implications of tomographic images of subducted lithosphere beneath northwestern South America. Geology 22, 451–454. doi:10.1130/0091-7613(1994)022

Vargas, C.A., Mann, P., 2013. Tearing and Breaking Off of Subducted Slabs as the Result of Collision of the Panama Arc-Indenter with Northwestern South America. Bull. Seismol. Soc. Am. 103, 2025–2046. doi:10.1785/0120120328

Vatin-Pérignon, N., Goemans, P., Oliver, R.A., Palacio, E.P., 1990. Evaluation of magmatic processes for the products of the Nevado del Ruiz Volcano, Colombia from geochemical and petrological data. J. Volcanol. Geotherm. Res. 41, 153–176. doi:10.1016/0377-0273(90)90087-V

Veloza, G., Styron, R., Taylor, M., Mora, A., 2012. Open-source archive of active faults for northwest South America. GSA Today 22, 4–10. doi:10.1130/GSAT-G156A.1

Vernette, G., Mauffret, A., Bobier, C., Briceno, L., Gayet, J., 1992. Mud diapirism, fan sedimentation and strike-slip faulting, Caribbean Colombian Margin. Tectonophysics 202, 335–349. doi:10.1016/0040-1951(92)90118-P

Wagner, L.S., Jaramillo, J.S., Ramírez-Hoyos, L.F., Monsalve, G., Cardona, A., Becker, T.W., 2017a. Transient slab flattening beneath Colombia. Geophys. Res. Lett. 44, 6616–6623. doi:10.1002/2017GL073981

Wagner, L.S., Jaramillo, J.S., Ramírez-Hoyos, L.F., Monsalve, G., Cardona, A., Becker, T.W., 2017b. Transient slab flattening beneath Colombia. Geophys. Res. Lett. 44, 6616–6623. doi:10.1002/2017GL073981

Weber, M.B.I., Tarney, J., Kempton, P.D., Kent, R.W., 2002. Crustal make-up of the northern Andes : evidence based on deep crustal xenolith suites, Mercaderes, SW Colombia. Tectonophysics 345, 49–82.

Wessel, P., Smith, W.H.F., 1998. New, improved version of generic mapping tools released. Eos, Trans. Am. Geophys. Union 79, 579–579. doi:10.1029/98EO00426

Xie, J., Ritzwoller, M.H., Shen, W., Yang, Y., Zheng, Y., Zhou, L., 2013. Crustal radial anisotropy across Eastern Tibet and the Western Yangtze Craton. J. Geophys. Res. Solid Earth 118, 4226–4252. doi:10.1002/jgrb.50296

Yarce, J., Monsalve, G., Becker, T., Cardona, A., Poveda, E., Alvira, D., Ordonez-Carmona Oswaldo, 2014. Seismological observations in Northwestern South America: Evidence for two subduction segments, contrasting crustal thicknesses and upper mantle flow. Tectonophysics 637, 57–67. doi:10.1016/j.tecto.2014.09.006

Yudistira, T., Paulssen, H., Trampert, J., 2017. The crustal structure beneath The Netherlands derived from ambient seismic noise. Tectonophysics 721, 361–371. doi:10.1016/j.tecto.2017.09.025

Zhao, D., Kanamori, H., Negishi, H., Wiens, D., 1996. Tomography of the Source Area of the 1995 Kobe Earthquake: Evidence for Fluids at the Hypocenter? Science (80-.

). 274, 1891–1894. doi:10.1126/science.274.5294.1891

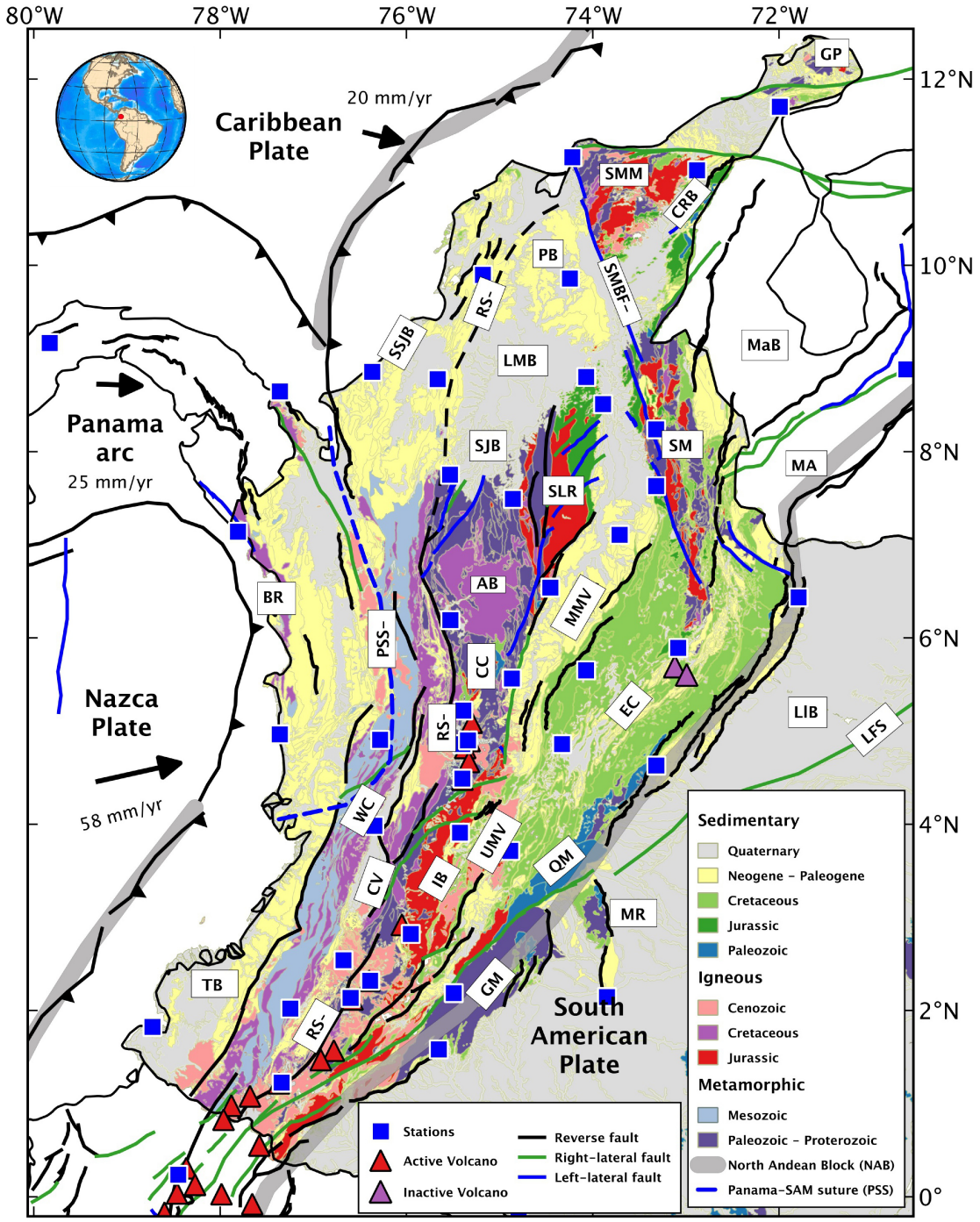
80°W
78°W
76°W
74°W
72°W
12°N
10°N
8°N
6°N
4°N
2°N
0°
Caribbean Plate
20 mm/yr
Panama arc
25 mm/yr
Nazca Plate
58 mm/yr
South American Plate
GP
SMM
CRB
PB
SMBF-
RS-
SSJB
LMB
MaB
SJB
SM
SLR
MA
AB
MMV
BR
PSS-
CC
EC
LIB
LFS
WC
UMV
QM
CV
IB
MR
TB
GM
Stations
Active Volcano
Inactive Volcano
Reverse fault
Right-lateral fault
Left-lateral fault
Sedimentary
Quaternary
Neogene - Paleogene
Cretaceous
Jurassic
Paleozoic
Igneous
Cenozoic
Cretaceous
Jurassic
Metamorphic
Mesozoic
Paleozoic - Proterozoic
North Andean Block (NAB)
Panama-SAM suture (PSS)

Figure 1

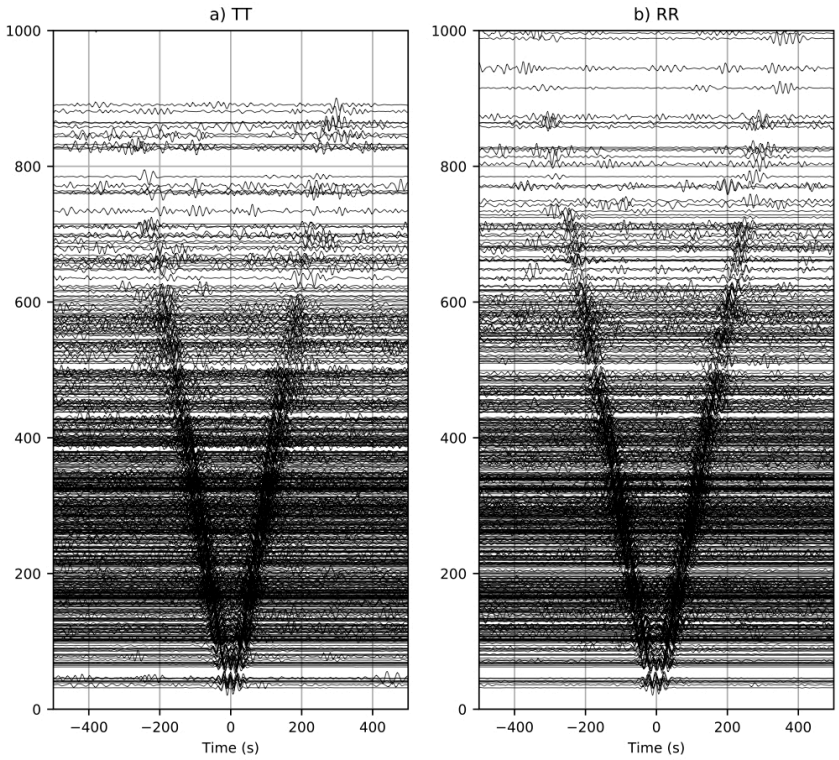

Figure 2

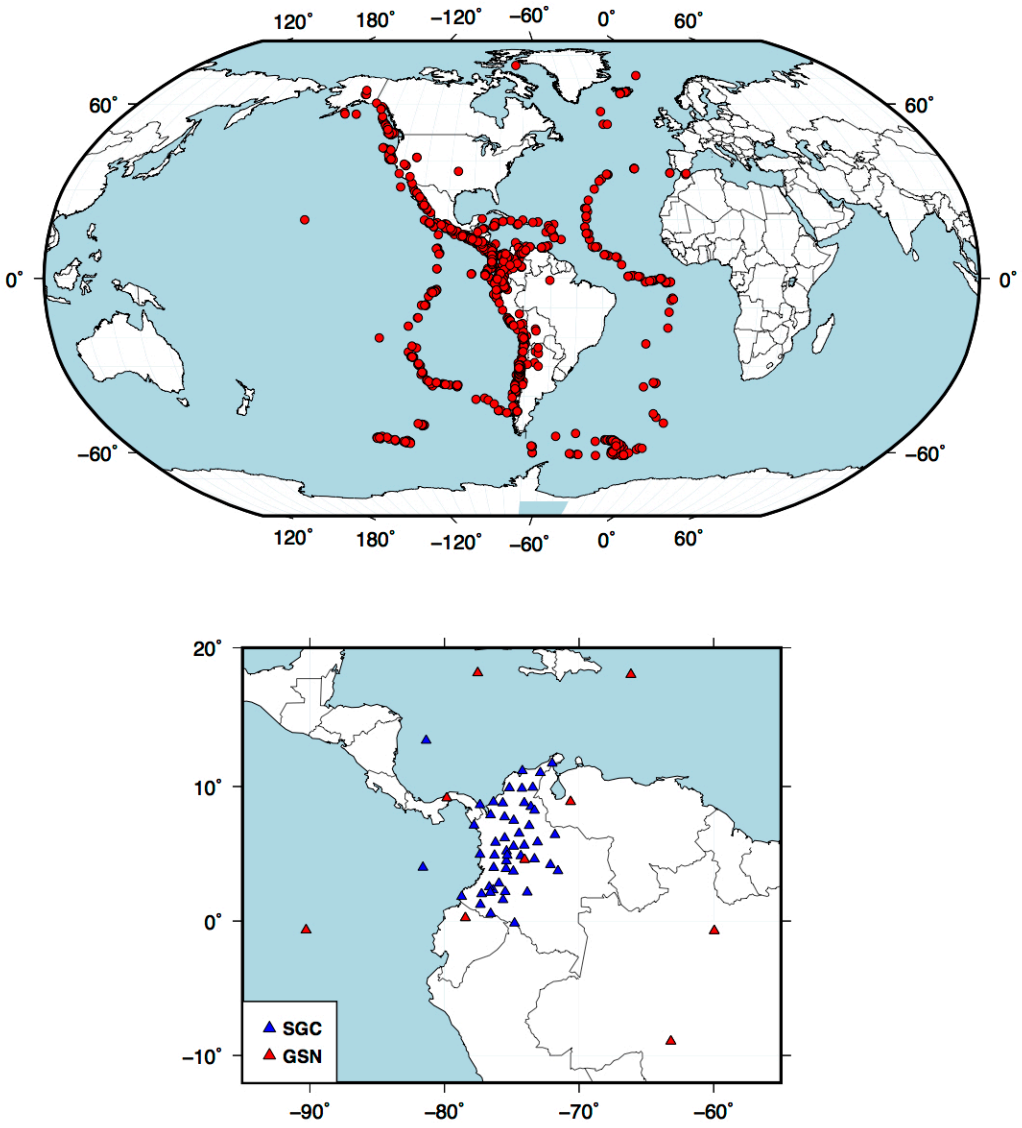

Figure 3

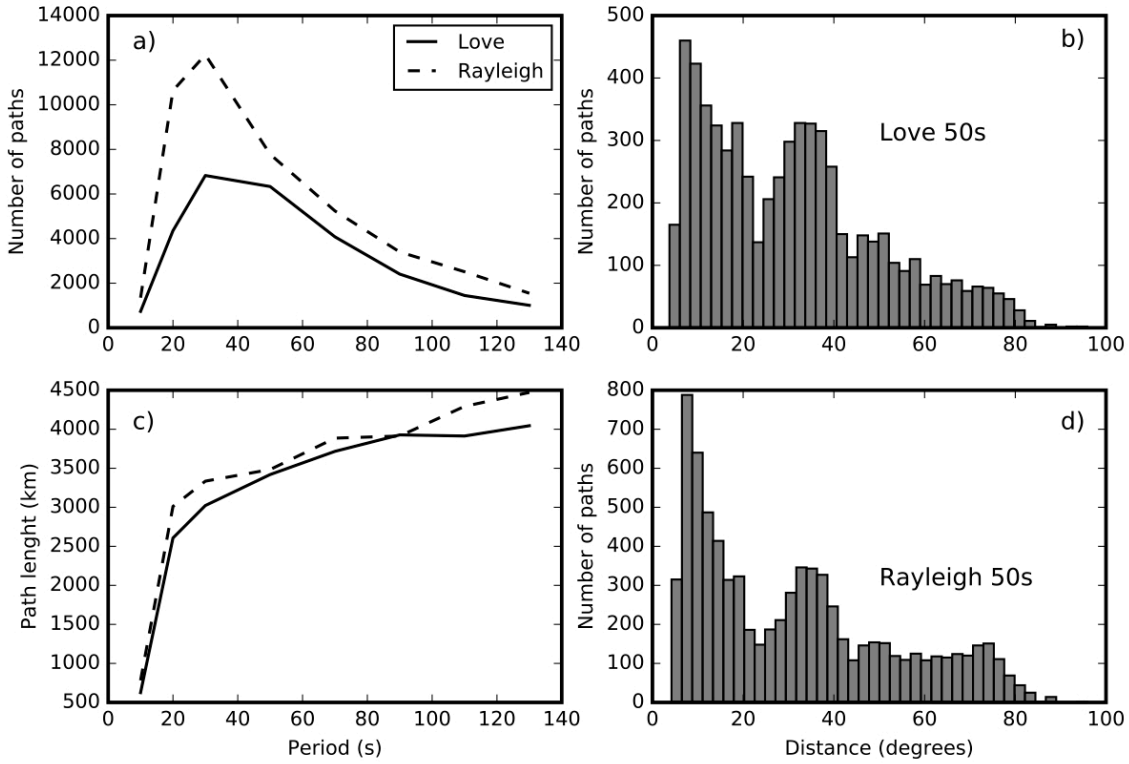
a)
Love
Rayleigh
Number of paths
b)
Love 50s
Number of paths
c)
Path lenght (km)
Period (s)
d)
Rayleigh 50s
Number of paths
Distance (degrees)

Figure 4

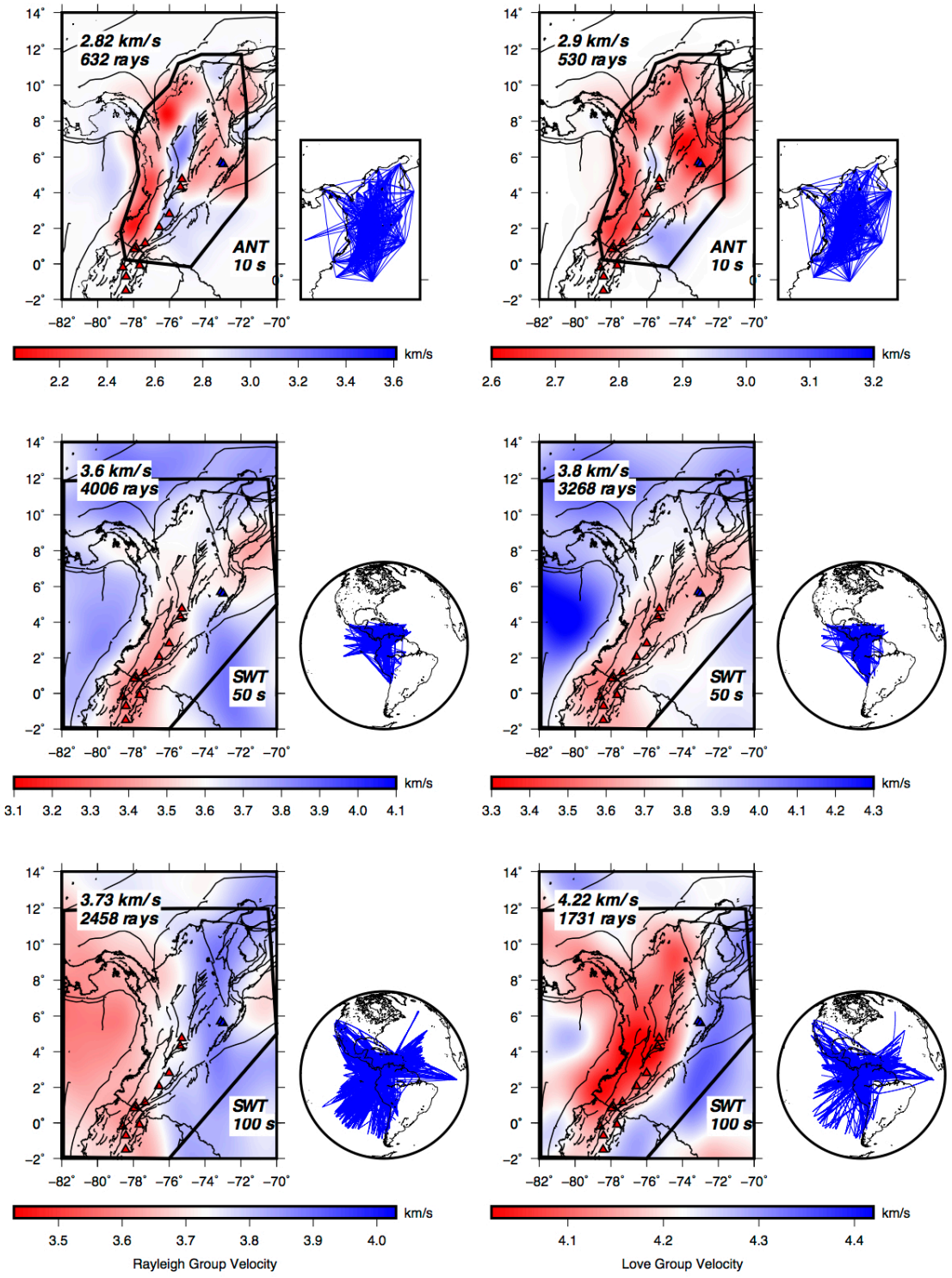
2.82 km/s
632 rays
ANT
10 s
km/s
2.2 2.4 2.6 2.8 3.0 3.2 3.4 3.6
2.9 km/s
530 rays
ANT
10 s
km/s
2.6 2.7 2.8 2.9 3.0 3.1 3.2
3.6 km/s
4006 rays
SWT
50 s
km/s
3.1 3.2 3.3 3.4 3.5 3.6 3.7 3.8 3.9 4.0 4.1
3.8 km/s
3268 rays
SWT
50 s
km/s
3.3 3.4 3.5 3.6 3.7 3.8 3.9 4.0 4.1 4.2 4.3
3.73 km/s
2458 rays
SWT
100 s
km/s
3.5 3.6 3.7 3.8 3.9 4.0
Rayleigh Group Velocity
4.22 km/s
1731 rays
SWT
100 s
km/s
4.1 4.2 4.3 4.4
Love Group Velocity

Figure 5

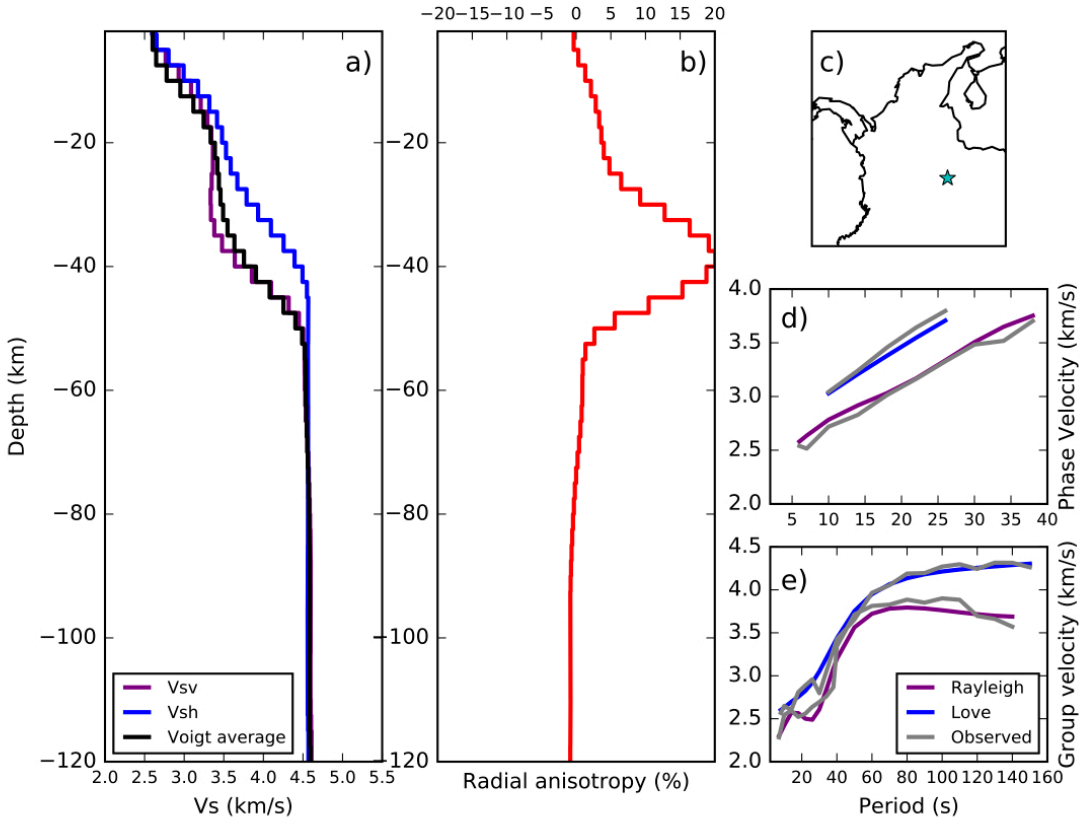
a)
b)
c)
d)
e)
Depth (km)
Vs (km/s)
Vsv
Vsh
Voigt average
Radial anisotropy (%)
Phase Velocity (km/s)
Group velocity (km/s)
Period (s)
Rayleigh
Love
Observed

Figure 6

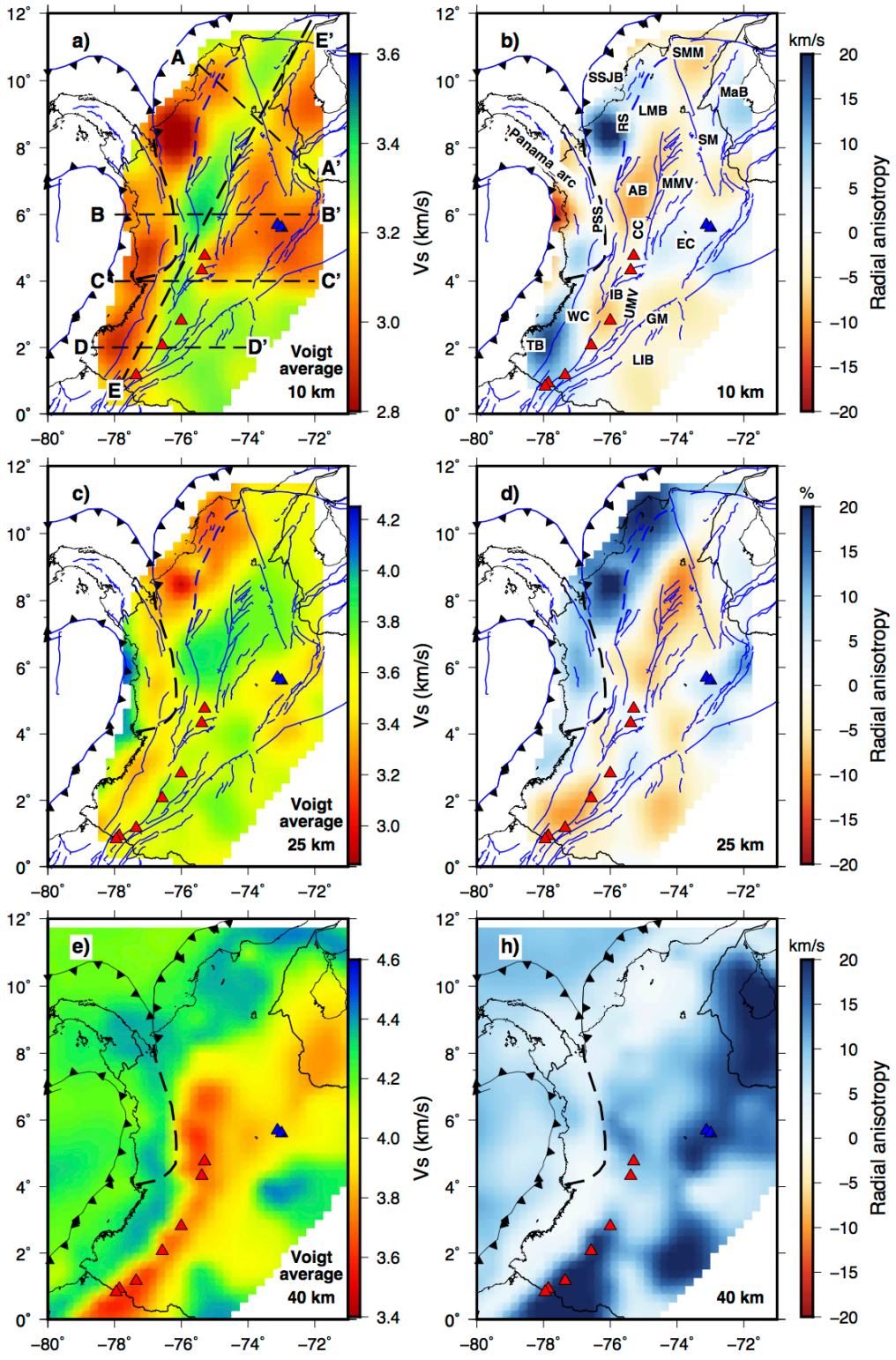
a)
A
A'
B
B'
C
C'
D
D'
E
E'
Voigt average 10 km
b)
SMM
SSJB
MaB
LMB
RS
SM
Panama arc
AB
MMV
PSS
CC
EC
IB
UMV
WC
GM
TB
LIB
10 km
Vs (km/s)
km/s
Radial anisotropy
c)
Voigt average 25 km
d)
25 km
%
e)
Voigt average 40 km
h)
40 km
12°
10°
8°
6°
4°
2°
0°
−80°
−78°
−76°
−74°
−72°

Figure 7

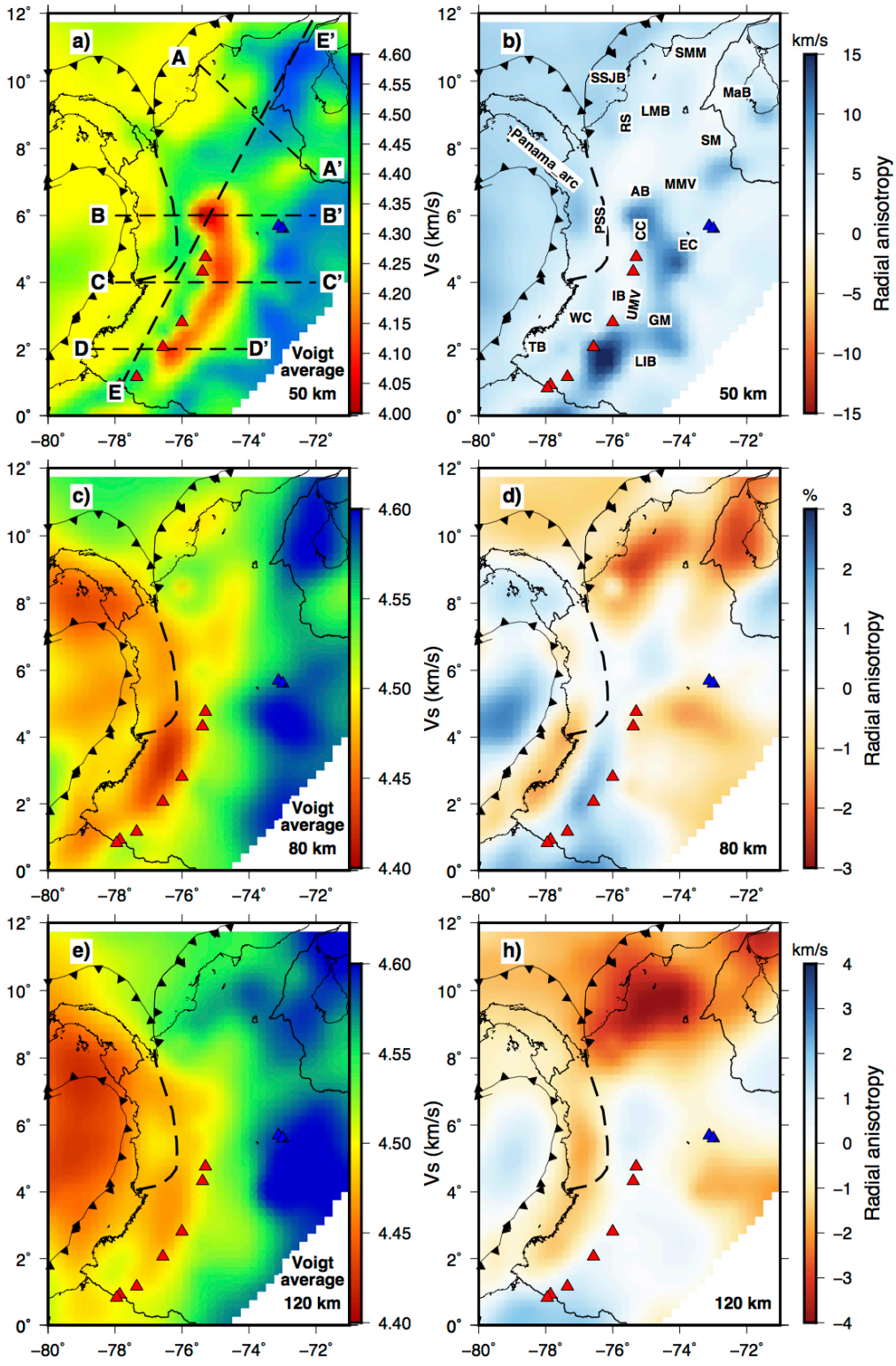
a)
A
A'
B
B'
C
C'
D
D'
E
E'
Voigt average 50 km
b)
SMM
SSJB
MaB
LMB
RS
SM
Panama arc
AB
MMV
PSS
CC
EC
IB
UMV
WC
GM
TB
LIB
50 km
Vs (km/s)
km/s
Radial anisotropy
c)
Voigt average 80 km
d)
80 km
%
e)
Voigt average 120 km
h)
120 km
12°
10°
8°
6°
4°
2°
0°
−80°
−78°
−76°
−74°
−72°
4.60
4.55
4.50
4.45
4.40
4.35
4.30
4.25
4.20
4.15
4.10
4.05
4.00
15
10
5
0
−5
−10
−15
3
2
1
0
−1
−2
−3
4
−4

Figure 8

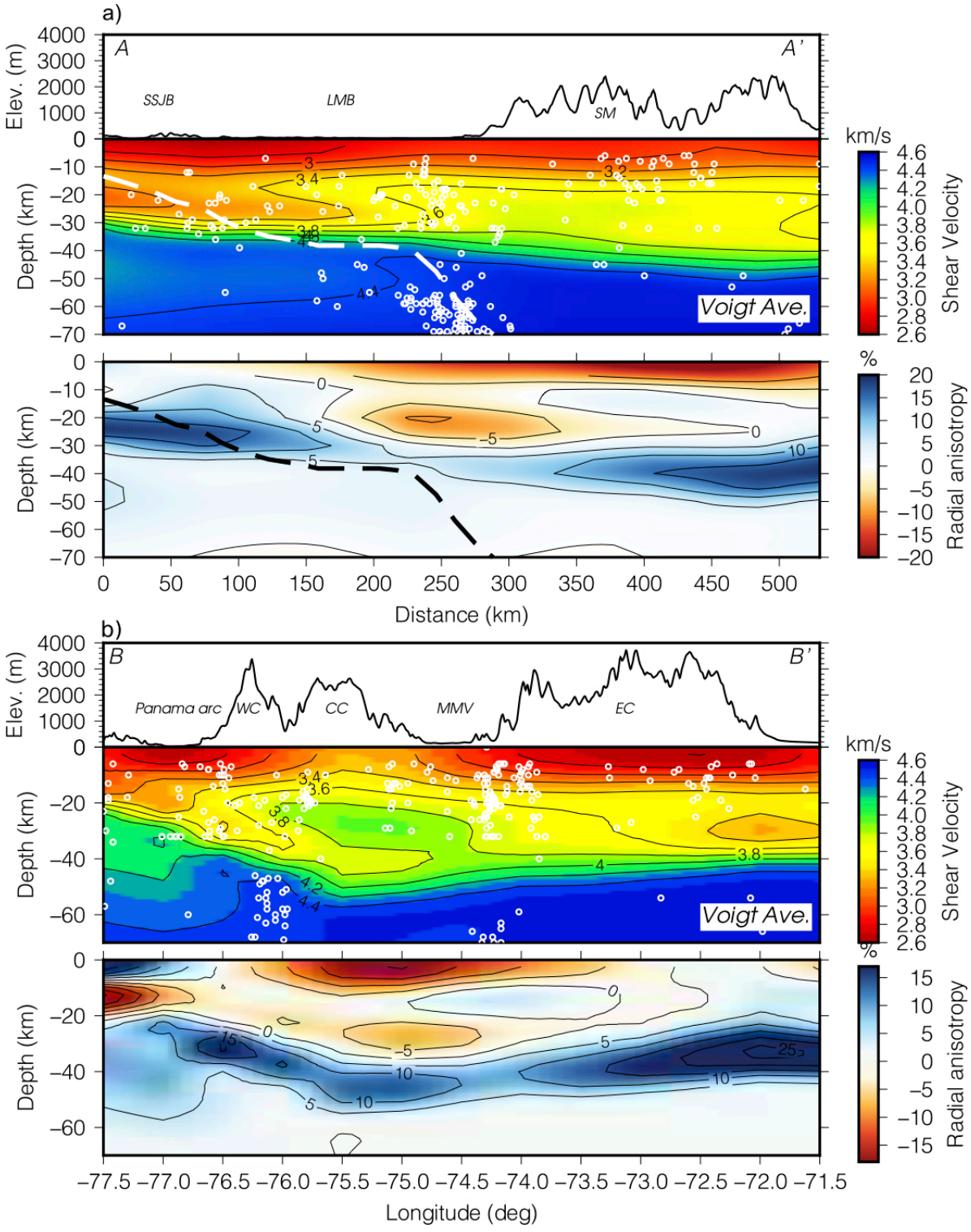
a)
A
A'
SSJB
LMB
SM
Elev. (m)
Depth (km)
Voigt Ave.
km/s
Shear Velocity
%
Radial anisotropy
Distance (km)
b)
B
B'
Panama arc
WC
CC
MMV
EC
Longitude (deg)

Figure 9

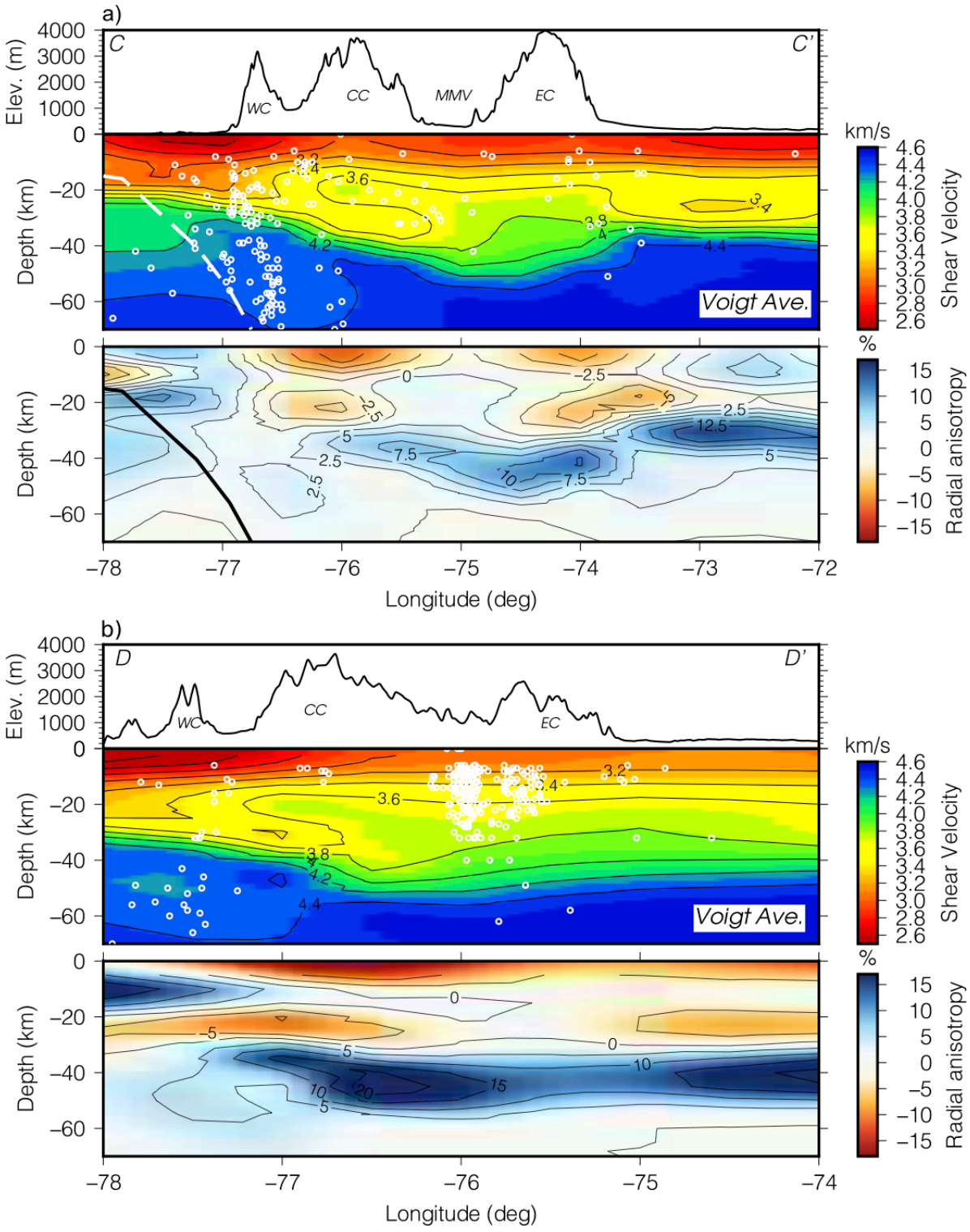
a)
C
C'
WC
CC
MMV
EC
Elev. (m)
Depth (km)
Voigt Ave.
km/s
Shear Velocity
%
Radial anisotropy
Longitude (deg)
b)
D
D'
WC
CC
EC
Elev. (m)
Depth (km)
Voigt Ave.
km/s
Shear Velocity
%
Radial anisotropy
Longitude (deg)

Figure 10

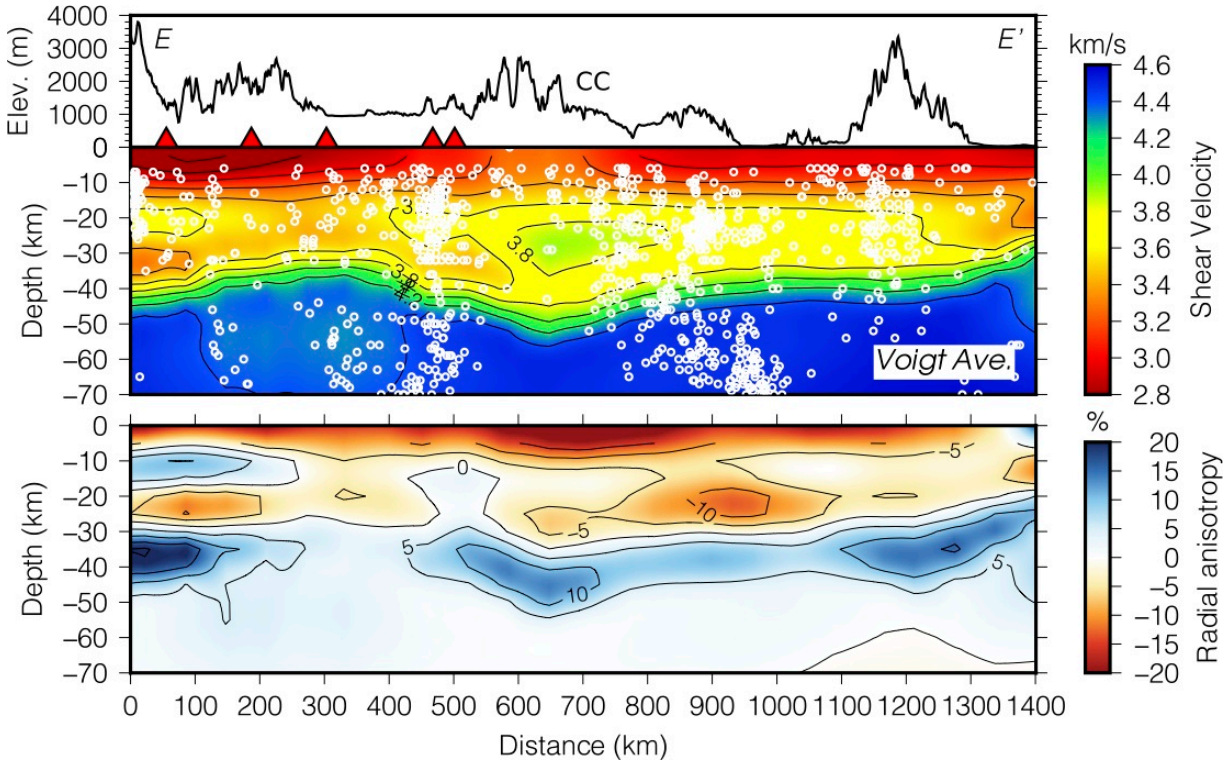
E
E'
CC
Elev. (m)
4000
3000
2000
1000
0
Depth (km)
−10
−20
−30
−40
−50
−60
−70
3
3.8
Voigt Ave.
km/s
4.6
4.4
4.2
4.0
3.8
3.6
3.4
3.2
3.0
2.8
Shear Velocity
%
20
15
10
5
0
−5
−10
−15
−20
Radial anisotropy
0
−5
−10
5
10
0 100 200 300 400 500 600 700 800 900 1000 1100 1200 1300 1400
Distance (km)

Figure 11

Station	Latitude (deg)	Longitude (deg)	Recording time used (MONTH/DAY/JULIAN DAY/YEAR)	
AGCC	8.512	-73.585	JAN 04 (004), 2016	OCT 05 (279), 2016
ANIL	4.490	-75.400	JAN 12 (018), 2010	OCT 28 (301), 2015
APAC	7.910	-76.580	DEC 06 (341), 2016	DEC 27 (362), 2016
ARGC	9.858	-74.246	APR 28 (118), 2013	DEC 28 (362), 2016
BBAC	2.021	-77.247	APR 28 (118), 2013	DEC 11 (346), 2016
BCIP	9.166	-79.830	JAN 20 (020), 2007	DEC 28 (363), 2016
BOCO	4.587	-74.043	JUN 06 (157), 1994	AUG 05 (218), 1996
BRR	7.107	-73.712	AUG 28 (241), 2008	DEC 28 (363), 2016
CAP2	8.646	-77.359	SEP 18 (262), 2008	SEP 03 (247), 2016
CBOC	5.864	-76.210	AUG 12 (224), 2013	DEC 28 (363), 2016
CHI	4.630	-73.318	AUG 28 (241), 2008	DEC 28 (363), 2016
COD	9.935	-73.444	SEP 13 (256), 2011	APR 10 (100), 2014
CRJC	11.02	-72.881	DEC 08 (342), 2014	DEC 28 (363), 2016
FLO2	1.583	-75.653	SEP 18 (262), 2008	DEC 28 (363), 2016
GARC	2.187	-75.493	JUL 26 (207), 2014	DEC 28 (363), 2016
GCUF	1.226	-77.340	AUG 28 (241), 2008	DEC 28 (363), 2016
GUY	5.220	-75.390	JAN 12 (012), 2010	DEC 28 (363), 2016
HEL	6.191	-75.529	AUG 28 (241), 2008	OCT 31 (305), 2016
LCBC	8.857	-76.368	NOV 25 (329), 2013	DEC 28 (363), 2016
MACC	2.145	-73.848	MAY 27 (147), 2013	DEC 28 (363), 2016
MAP	4.004	-81.606	AUG 03 (215), 2009	DEC 28 (363), 2016
MARA	2.822	-75.954	NOV 13 (317), 2009	DEC 28 (363), 2016
MON	8.778	-75.665	MAY 10 (130), 2009	MAR 28 (088), 2016
MTDJ	18.227	-77.534	DEC 13 (347), 2007	DEC 08 (342), 2014
NOR	5.564	-74.869	AUG 15 (228), 2012	DEC 28 (363), 2016
OCA	8.239	-73.320	MAY 18 (139), 2012	OCT 24 (298), 2016
ORTC	3.909	-75.426	JUN 14 (165), 2013	DEC 28 (363), 2016
OTAV	0.237	-78.450	OCT 21 (295), 2000	OCT 06 (280), 2016
PAL	4.906	-76.283	NOV 17 (321), 2011	DEC 28 (363), 2016
PAYG	-0.674	-90.286	AUG 05 (217), 1998	DEC 08 (342), 2014
PCON	2.320	-76.390	AUG 28 (241), 2008	MAY 16 (136), 2014
PGA1	3.747	-71.571	MAY 13 (133), 2014	NOV 08 (313), 2016
PIZC	4.965	-77.360	SEP 26 (269), 2013	DEC 28 (363), 2016
POP2	2.540	-76.676	SEP 12 (255), 2009	SEP 28 (272), 2016
PRA	3.714	-74.886	AUG 28 (241), 2008	DEC 11 (346), 2016
PRV	13.376	-81.364	APR 16 (107), 2012	DEC 28 (363), 2016
PTA	7.140	-77.809	SEP 05 (249), 2012	DEC 25 (360), 2016
PTB	6.540	-74.456	DEC 13 (347), 2011	DEC 28 (363), 2016
PTGA	-0.731	-59.960	DEC 01 (335), 1995	DEC 08 (342), 2010
PTGC	4.199	-72.134	SEP 26 (269), 2013	DEC 28 (363), 2016
PTLC	-0.170	-74.797	DEC 09 (344), 2012	OCT 27 (301), 2016
PUAC	0.550	-76.570	MAY 13 (133), 2014	JAN 10 (010), 2015
ROSC	4.860	-74.330	JAN 04 (004), 2006	DEC 28 (363), 2016
RREF	4.910	-75.340	AUG 28 (241), 2008	JUN 20 (171), 2015
RUS	5.893	-73.083	AUG 28 (241), 2008	DEC 28 (363), 2016
SAML	-8.949	-63.183	MAY 14 (134), 2003	DEC 08 (342), 2014
SDV	8.883	-70.634	SEP 01 (244), 1994	DEC 28 (363), 2016
SJC	9.897	-75.180	SEP 13 (256), 2011	DEC 28 (363), 2016
SJG	18.109	-66.150	JUN 06 (157), 1994	DEC 08 (342), 2014
SMAR	11.160	-74.220	SEP 05 (249), 2012	DEC 28 (363), 2016
SML	8.801	-74.071	NOV 07 (312), 2012	MAY 08 (129), 2016
SOTA	2.135	-76.600	SEP 24 (268), 2008	DEC 28 (363), 2016
SPBC	5.652	-74.072	AUG 12 (224), 2013	NOV 08 (313), 2016
TAM	6.435	-71.791	JUN 28 (180), 2012	DEC 28 (363), 2016
TUM	1.824	-78.727	OCT 11 (285), 2008	DEC 28 (363), 2016
URE	7.752	-75.533	MAY 18 (139), 2012	DEC 28 (363), 2016
URI	11.702	-71.993	DEC 18 (353), 2008	DEC 28 (363), 2016
YOT	3.983	-76.345	JAN 10 (010), 2012	DEC 28 (363), 2016
ZAR	7.492	-74.858	SEP 13 (256), 2011	DEC 28 (363), 2016

Table 1

Supplementary Materials for

Investigating Active and Inactive Volcanism under the Colombian Andes with Radial Anisotropy from Ambient Noise and Surface Wave Tomography

Esteban Poveda[1], Jordi Julià[1, 2]

[1]Programa de Pós-Graduação em Geodinâmica e Geofísica, Universidade Federal do Rio Grande do Norte, Natal, RN CEP 59078-090, Brazil

[2]Departamento de Geofísica, Universidade Federal do Rio Grande do Norte, Natal, RN CEP 59078-970, Brazil

Contents of this file

Figures S1 to S6

Introduction

This supporting information contains six figures. All figures are cited in the main text and described in detail through their figure captions. Raw data can be obtained from the Servicio Geológico Colombiano (SGC) upon request.

Figure S1 displays a number of histograms on earthquake source distribution for surface wave tomography. Figure S2 contains a detailed example of group-velocity measurement for periods between 30 and 200 s with the PGSWMFA software. Trade-off curves for 26 s Rayleigh-wave ambient noise tomography and 110 s Rayleigh-wave surface wave tomography are presented in Figure S3. Figure S4 displays Rayleigh- and Love-wave phase-velocity maps at select periods between 7 and 30 s. The resolution of the inverted tomographic images, assessed through a number of checkerboard tests, is

displayed in Figure S5. Finally, figure S6, displays a dispersion curve inversion test in which Love- and Rayleigh-wave dispersion curves are inverted simultaneously, demonstrating the impossibility to match the observations with a single Earth model, especially for short periods.

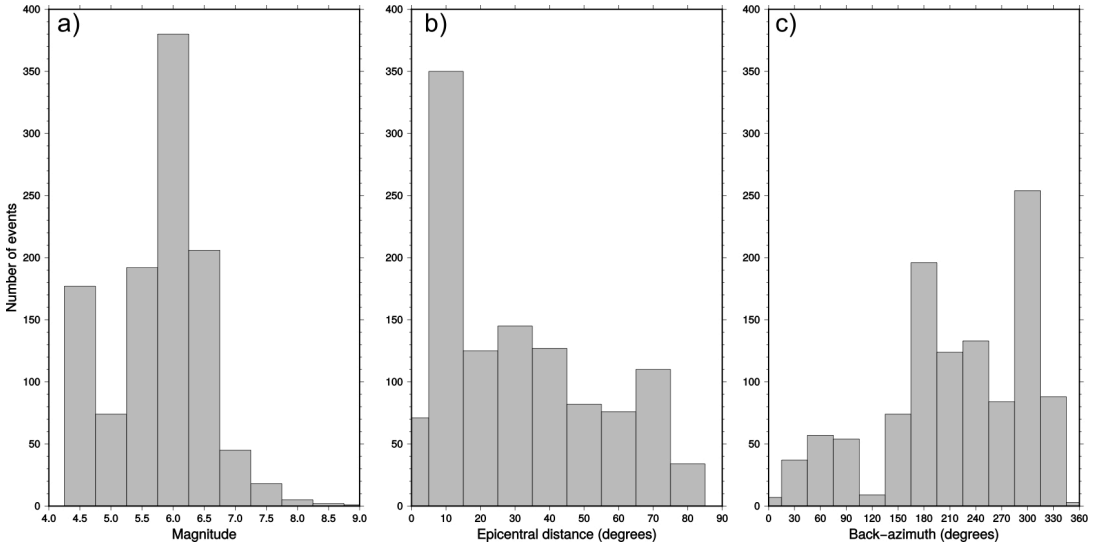

Figure S1. Histograms of source properties correspondint to events used in the surface wave tomography: a) Magnitude; b) Epicentral distance and c) Back-azimuth.

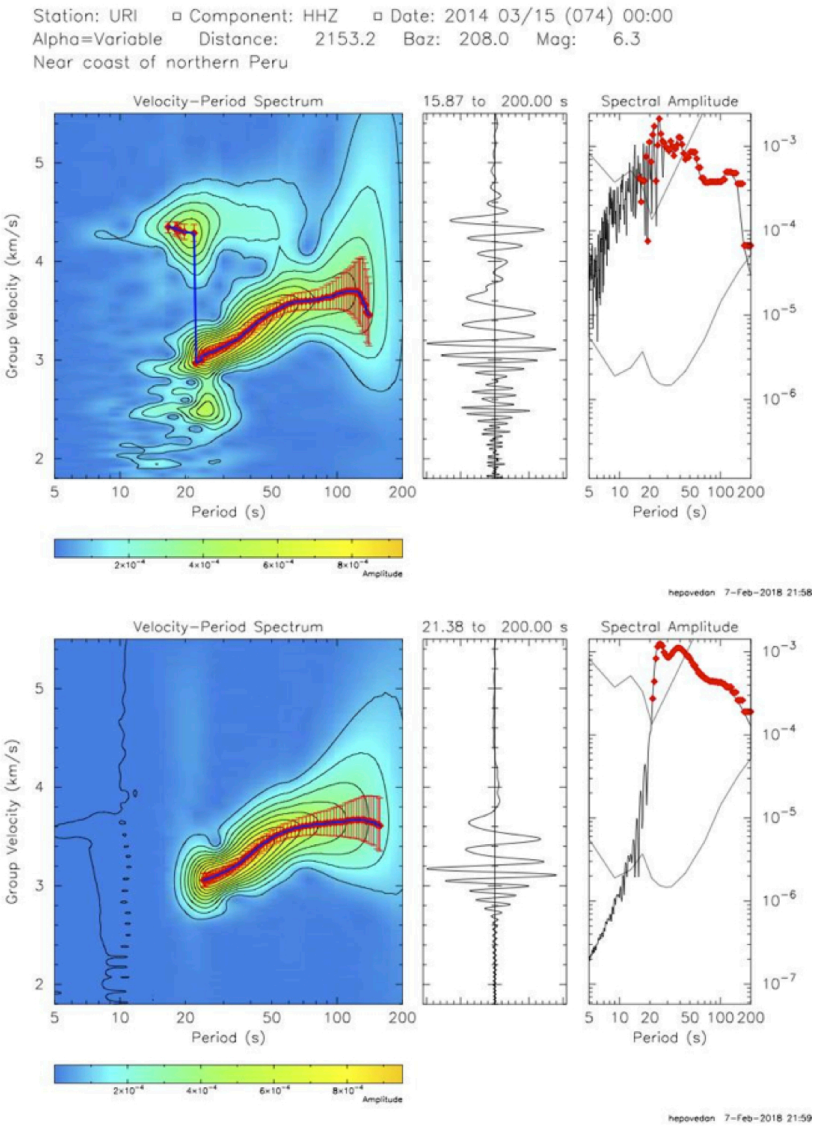

Figure S2. (Top) Example of group velocity measurement using the PGSWMFA software for station URI, in the Guajira peninsula. The left panel shows the contours of the frequency-time surface (in the velocity-period domain), which are used to estimate the dispersion measurements, along with uncertainty. The center panel shows the corresponding Rayleigh waveform, and the panel shows the amplitude spectrum of the waveform. (Bottom) Same panels after application of a phase-match filter to the Rayleigh waveform.

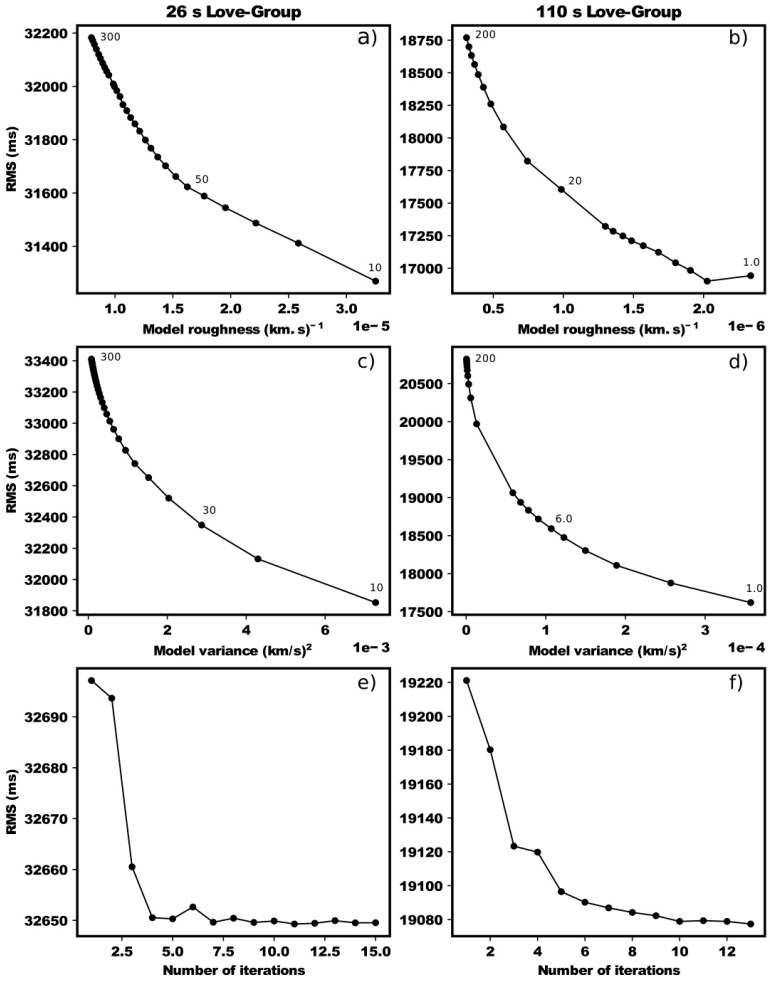

Figure S3. L-curves and RMS reduction curves for 26 and 110 s Love-wave group-velocity tomography; (a) and (b) - RMS misfit *vs* model roughness; selected values of the smoothness parameter were 50 and 20 for 26 and 110 s curves, respectively; (c) and (d) - RMS misfit *vs* model variance; selected values for the damping parameter were 30 and 6 for 22 and 110 s curves, respectively; (e) and (f) - RMS variation with number of iterations; note that after 6 iterations convergence is reached.

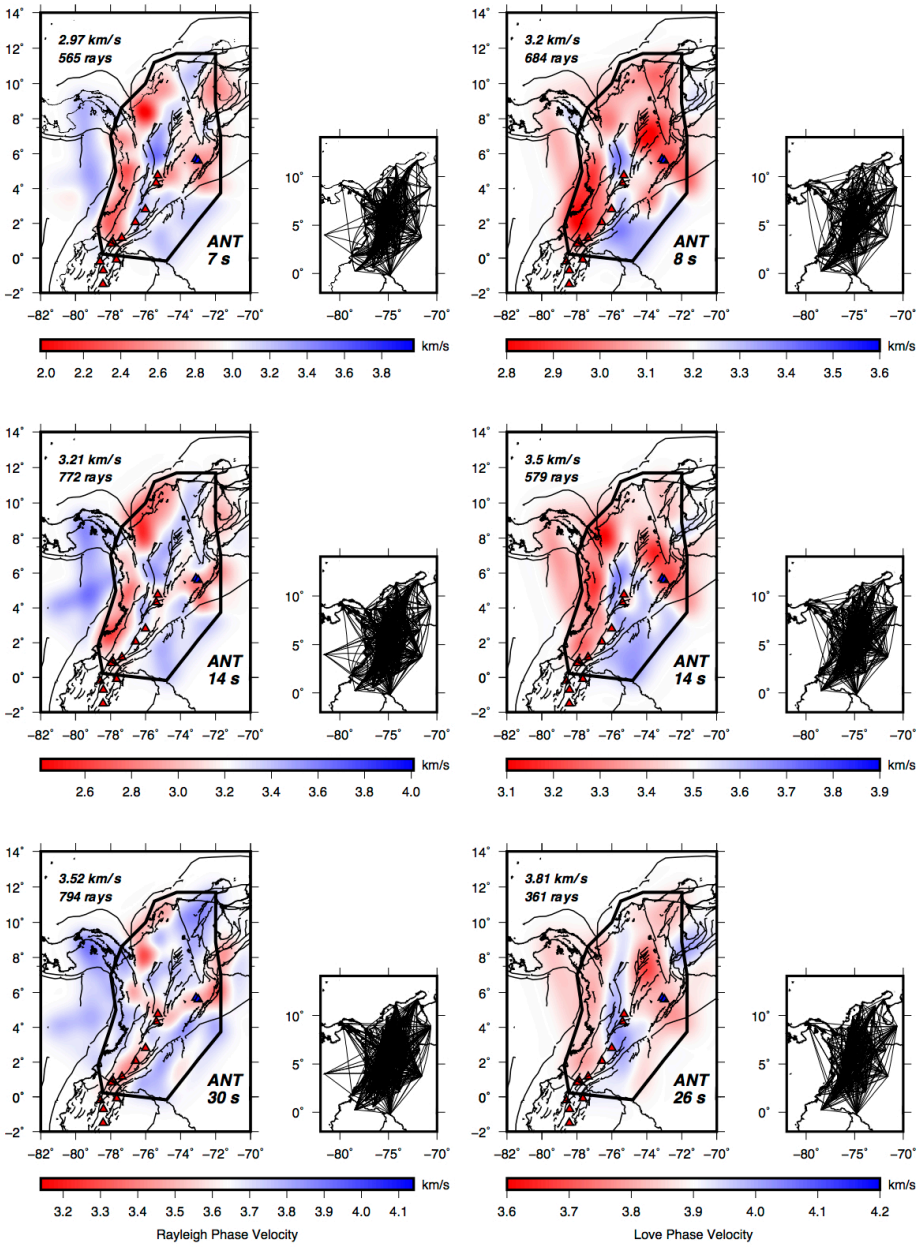

Figure S4. Rayleigh- and Love-wave phase velocity maps for select periods between 7 to 30 s. Major faults (black lines) are superimposed from *Veloza et al.* (2012). Small insets on the sides show raypath coverage for each period. Red and blue triangles show active and inactive volcanoes, respectively.

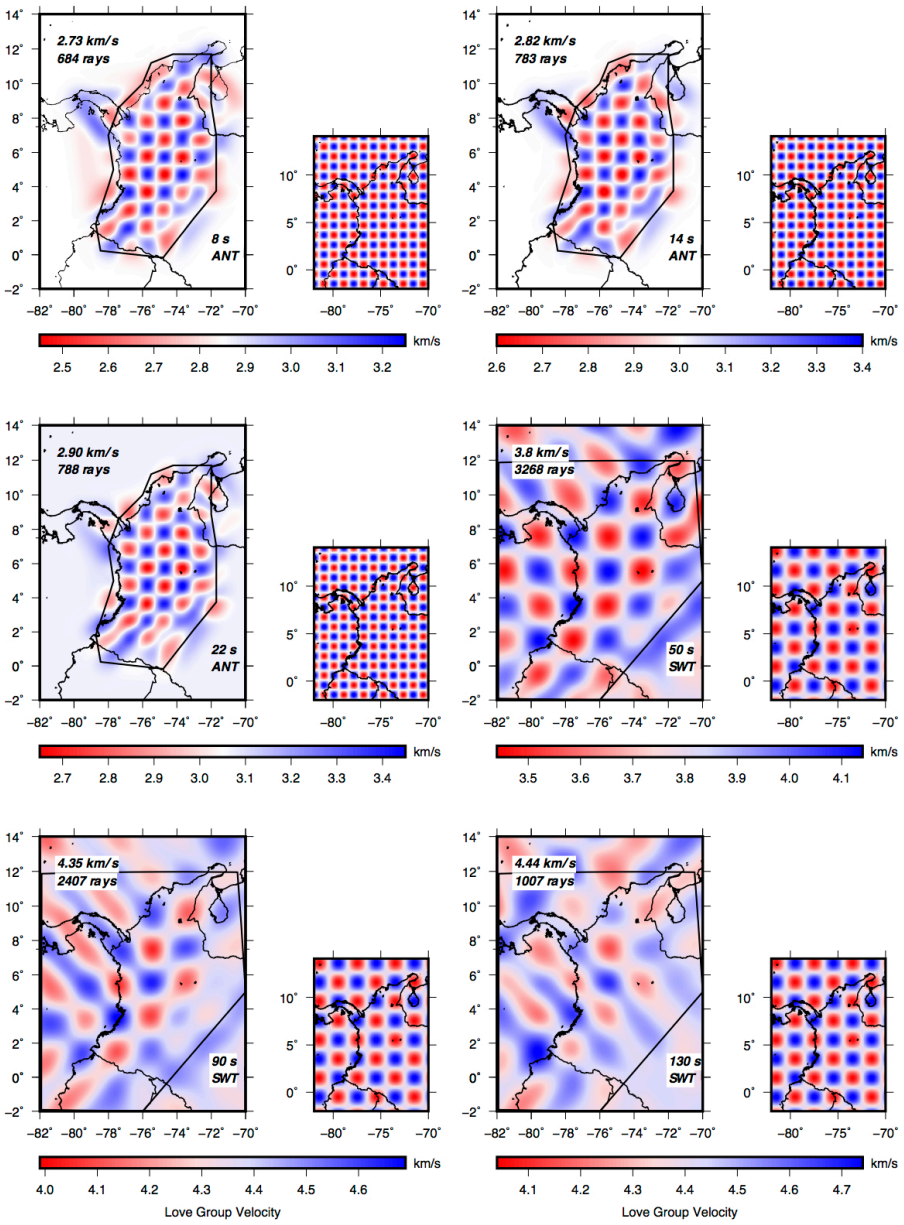

Figure S5. Checkerboard resolution tests for group velocities at 8, 14, 22, 50, 90, and 130 s (large maps). The black polygon encompasses the region used for modeling crustal and upper mantle shear velocities (Figs 8 and 9), and the numbers in the upper-left corner show mean group velocity and number of raypaths. Small maps on each side show input checkerboard model for each period.

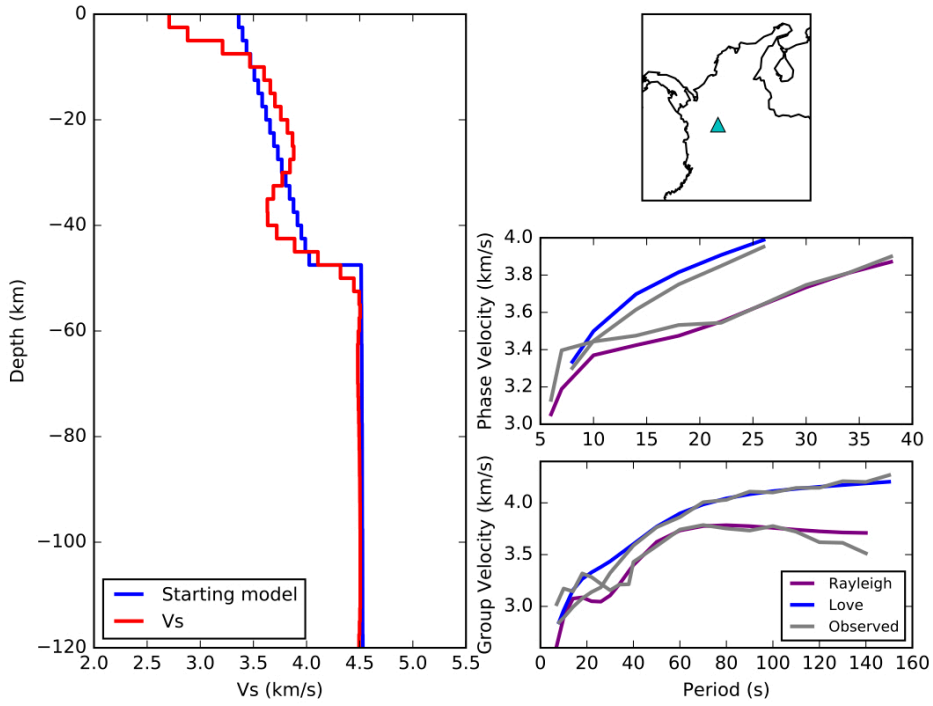

Figure S6. (Left) 1-D velocity-depth profile from the joint inversion of Rayleigh and Love phase and group dispersion curves. (Right) From top to bottom, location of node, match to phase-velocity curves, and match to group-velocity curves. Note how the match in the short periods degrades when attempting to explain both Rayleigh and Love curves with a single model (see main text for details).

Chapter 6

Discussion

The manuscripts presented in the previous chapters have reported on two tomographic studies that map the structure of the crust and upper mantle under NW South America in unprecedented detail. The most important features revealed by the S-wave velocity model developed from the seismic tomographies are: (i) The strong correlation between slow S velocities at mid-crustal depths (25–35 km) and surface volcanism in the CC; (ii) The presence of even slower S-velocities in the mid-crust under the inactive volcanoes of the EC (Paipa and Iza); (iii) The presence of similarly slow S velocities under the Lower Magdalena Basin, where slower-than-average S velocities are found for almost the entire depth range; (iv) Positive radial anisotropy throughout the lower crust, particularly under CC and EC; (v) Negative radial anisotropy in middle crust under the CC, where volcanism is active, and positive radial anisotropy under the EC, where volcanism is inactive; (vi) Negative anisotropy at mid-crustal levels where major tectonic terrains (e.g., SMM, IB, AB, SLR) and regions of active volcanism are located; (vii) Positive anisotropy characterizing major coastal basins (e.g., LMB, TB); (viii) Positive radial anisotropy under the LMB at all crustal levels; (ix) Moderate (4 %) negative radial anisotropy in the upper mantle under the LMB.

The joint interpretation of isotropic (Voigt) S-velocities and radial anisotropy has al-

lowed to investigate the relationship between crustal fluids and active/inactive volcanims under NW South America. The main conclusions have been that: (i) Under active volcanims along the CC, slow velocities and negative radial anisotropy might be related to emplacement of magmas along intruding, sub-vertical dyke systems feeding the volcanics; (ii) Slow velocities and positive radial anisotropy under the Iza-Paipa volcanic complex in the EC is consistent with storage of magmas in flat-lying sills, reinforcing the proposal that volcanism in this area is inactive but not extinct; (iii) The presence of positive radial anisotropy in all the crust under the LMB is consistent with horizontal structures in this area, suggesting that the effect of migration of fluids in faults may be minimal or negligible; (iv) Negative anisotropy under the LMB at upper mantle depths, seems to map the shallow flat subduction of the Caribbean plate, suggesting that the limit between the Nazca and the Caribbean plates is around latitude 8°N.

In the following, the interpretation of our results and their implications are discussed in more detail.

6.1 Comparison with independent studies

The S-velocity model for the upper and middle crusts shows a generally good agreement with previous studies in southern Colombia, such as the Nariño Project active-source profiling survey (Meissnar et al. 1976, Meyer et al. 1976, Mooney et al. 1979, Flueh et al. 1981). The results of Meissnar et al. (1976) for the region at 1°N and 4°N and 82°W and 76°W, for instance, showed that P-wave velocities ranged between 6.0 and 6.8 km/s for the upper and lower crusts and ∼8.0 km/s for the underlying mantle. Through conversion of these values into S-wave velocity, after assuming a Vp/Vs of 1.78 (Ojeda & Havskov 2001), it is observed that this range of velocities compares similarly to the results reported in this thesis.

At shallow crustal levels, S-velocities in this study are consistent with major surface

geological features (Gómez et al. 2007, Veloza et al. 2012). Slow S-wave velocities correlate with the main sedimentary basins and with offshore regions (LMB, TB, MMV, MaB, EC), while high velocities are consistent with the regions where the main massifs, metamorphic rocks, batholiths and plutons are located (SMM, SM, AB, SLR, IB, GM). Alternated low and high velocities are correlated with the main fault systems: the Romeral fault system, from the LMB to the northern segment of the CC; the Bucaramanga-Santa Marta Fault System, which divides the LMB from the SMM; and the Otú-Pericos Faults System, which separates the CC and the MMV.

Our results are consistent with reported values of sedimentary thickness in Laske & Masters (1997) (Figure 6.1) for the upper crust. The slow velocity region in the lower Magdalena Valley coincides with sediment thickness values up to 7 km; similarly, in the Pacific coast under the Túmaco basin and the Eastern Cordillera, sediment thickness values are between 3 and 5 km and are associated with slow shear wave velocities. In contrast, regions with thin sedimentary layers (<2 km) such as the Central Cordillera and the Santa Marta Massif are imaged with high velocities in the tomographic slices.

The results presented in this work are also comparable to those produced by Syracuse et al. (2016), where images of lateral P wave and S wave velocity variation down to 155 km depth were developed for the Colombian Andes and adjacent regions. Their S-velocity depth slices at 12.5 km and 32.5 km (see Figure 6 in Syracuse et al., 2016) have similar dimensions to our S-velocity maps at 10 and 35 km depth, displaying similar S-velocity patterns throughout the area. At shallow crustal depths, both studies show slow velocities in the LMB and the Eastern Llanos, separated by faster velocities in the intervening cordilleras; at intermediate crustal depths, both studies display slow velocities in the LMB and under the volcanic areas of the EC and CC. Due to the inclusion of shorter periods in our velocity models, however, our velocity images have better resolution at short wavelengths. Our images, for instance, clearly depict the fast velocities characterizing the Antioqueño batholith at shallow depths and successfully image intra-crustal slow velocity

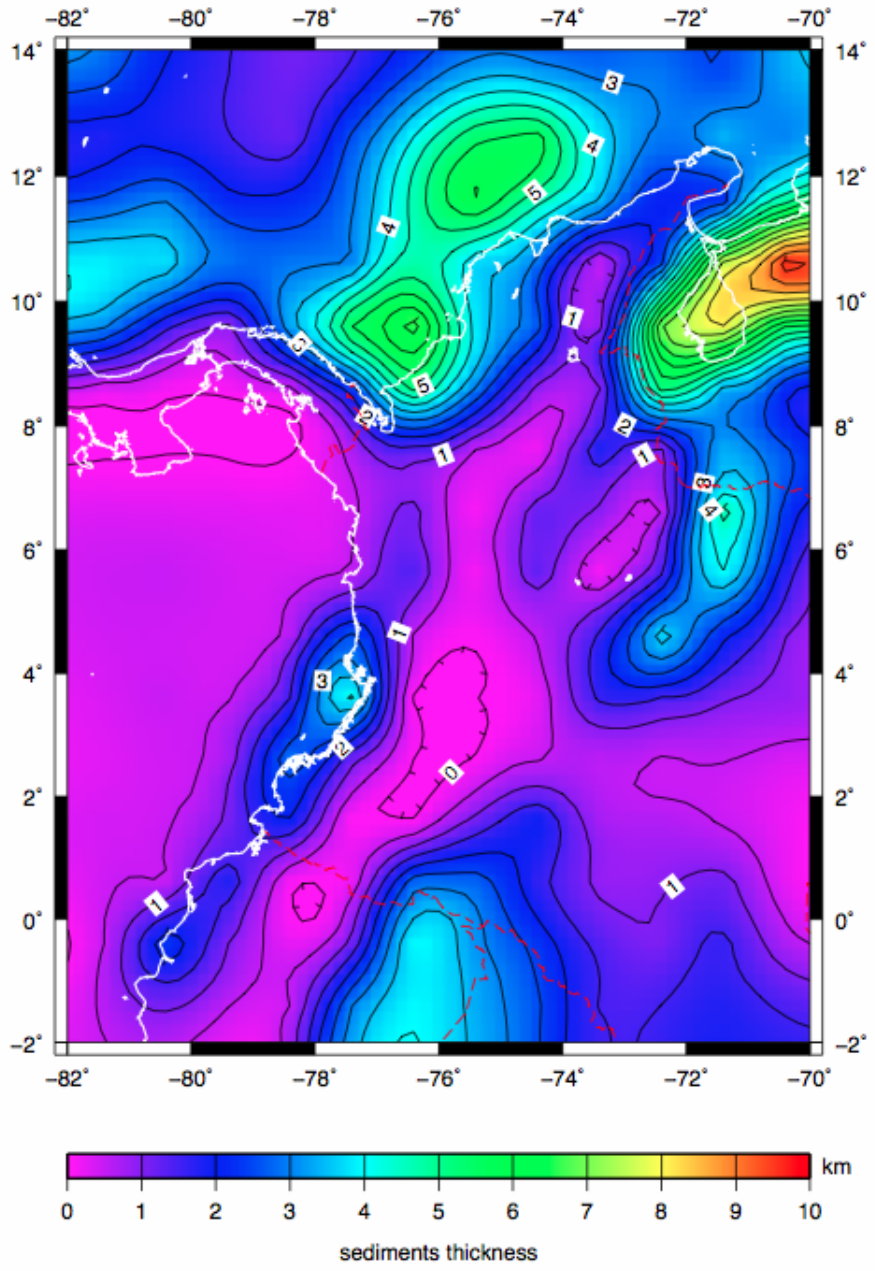

Figure 6.1: Compilation of sediments thickness from Laske and Masters (1997). The Colombia area is taken from the global compilation

regions that mimic the patterns described by surface volcanism.

Similarly, it is possible to compare our results for the upper mantle with the results presented in Syracuse et al. (2016). At 100 km depth, both studies show high velocities under the LMB, SMM, MMV and the EC, while low velocities are found under the Panamá arc and under active volcanism. Their results, however, differ from ours below the WC and the TB, where low velocities are found for our study in contrast with high velocities resolved in Syracuse et al. (2016). The differences may be related to the use of different datasets and methodologies; while Syracuse et al. (2016) used 134 local events (< 1000 km) to make Rayleigh dispersion measurements, 1340 events with P- and S-wave readings, and gravity data, we used a larger selection of 430 local (< 1000 km), 270 regional (1000 – 2000 km) and 420 teleseismic (> 2000 km) earthquake sources with magnitudes larger than 4.5 and depths less than 30 km. This resulted in a total of 1120 events, and over 10.000 dispersion curves for Rayleigh wave and 7.000 for Love waves covering all NW South America. Additionally, the methodology used in Syracuse et al. (2016) consisted of a combined body-wave velocity tomography algorithm (tomoDD) (Zhang & Thurber 2006), and a joint inversion algorithm for surface wave dispersion curves and gravity anomalies (Maceira & Ammon 2009). The body-wave, surface-wave and gravity data are combined in a single system of equations with weighting factors that control the contributions of each data types to the solution. The method seems quite sensitive to the chosen weight values for each dataset, if over-fitting of observables is to be avoided (Zhang et al. 2014). An LSQR approach is used to solve the system of equations (Paige & Saunders 1982).

6.2 Shear Velocities and Radial anisotropy

One of the most common forms of anisotropy is radial anisotropy, which is also know as transverse isotropy. It may develop, for instance, for a stack of layered materials (Stein

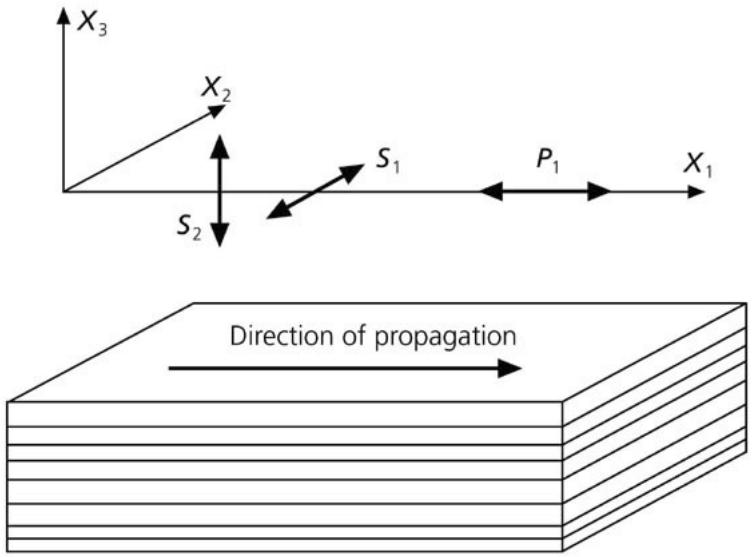

Figure 6.2: Schematic diagram showing radial anisotropy due to layering, with displacements of P and S waves propagating in the x_1 direction. The S_1 wave (SH) travels faster than the S_2 (SV), because the latter travel across layering. (Adapted from Stein and Wysession, 2003).

& Wysession 2003), where each layer is isotropic in their properties, but these properties differ from layer to layer. A transversely isotropic material is one with physical properties which are symmetric about an axis that is normal to a plane of isotropy. In this case, the elastic properties do not depend on the azimuth of propagation of the waves in the horizontal plane, but differ in the perpendicular direction (Babuska & Cara 1991).

For transverselly isotropic media, the elastic tensor c_{ijkl} contains five independent elastic constants; this is a particular case of anisotropy, because the two quasi-shear wave polarizations correspond to SH and SV (Shearer 2009). Transverse isotropy is frequently invoked in seismic reflection surveys and sedimentary layering of the crust and, more recently, in ambient noise tomography studies that investigate past and ongoing crustal deformation (Moschetti et al. 2010b, Lynner et al. 2018, Yudistira et al. 2017). In the upper mantle, it is generally utilized to account for discrepancies between Love and Rayleigh surface-wave velocities.

A case where radial anisotropy develops is illustrated in Figure 6.2. Let's consider

a medium with horizontal layers, with waves propagating in the x_1 direction. The shear velocities will depend on the polarization of the particle motions, with waves polarized in one plane traveling faster (s_1) than those polarized in the other plane (s_2). Commonly, horizontal layering is observed in the Earth and resulting in transverse anisotropy with vertical axis of symmetry. V_{SH} is generally faster than V_{SV}, since the V_{SH} displacement is in the plane of the layering. This is called *positive radial anisotropy* ($V_{SH} > V_{SV}$); on the other hand, when $V_{SH} < V_{SV}$, the term adopted is *negative radial anisotropy*.

Radial anisotropy is inferred from V_{SV} and V_{SH} velocity models by first estimating isotropic S-velocity through the Voigt average

$$V_S = \sqrt{(2V_{SV}^2 + V_{SH}^2)/3} \tag{6.1}$$

and then computing the percentage of radial anisotropy (γ) as

$$\gamma = \frac{2(V_{SH} - V_{SV})}{(V_{SH} + V_{SV})} \times 100\% \tag{6.2}$$

Anisotropy can originate through two primordial processes: (i) Crystal Preferred Orientation (CPO), in which anisotropy emerges from a preferred orientation of intrinsically anisotropic crystals; and (ii) Shape Preferred Orientation (SPO), in which the material is isotropic at fine scales but anisotropic at coarser scales, inducing seismic anisotropy at long wavelengths compared to the scale of the heterogeneity (Shearer 2009).

SPO is associated to geological structures, such as sedimentary layering, magmatic intrusions, dykes, sills, melt lenses and partial melting (Spica et al. 2017, Yudistira et al. 2017). Those include fine alternating layers of fast and slow material or small aligned cracks within a rock, which can cause radial anisotropy when the wavelength exceeds the dimensions of the layer or crack spacing. This mechanism is the most important to explain radial anisotropy in the upper and middle crusts (Karato 2008). As mentioned earlier, negative radial anisotropy is generated when V_{SV} propagates faster than V_{SH}, which

can be explained through SPO due to vertically aligned structures such as vertical shear zones, high fault density in sedimentary sequences and/or dyke system. Positive radial anisotropy ($V_{SH} > V_{SV}$) by SPO, on the other hand, is related to horizontal layering and/or aligned cracks and structures, such as horizontal bedding in sediments, fabric alignment created by extension and/or magma storage in flat-lying sills.

Radial anisotropy induced by CPO of micas, has been invoked by Shapiro et al. (2004) to explain horizontal flow in the middle crust due to crustal thinning in Tibet. The CPO mechanism is more dominant in the lower crust and upper mantle (Karato 2008), due to the presence of strongly anisotropic minerals such as olivine or orthopyroxenes. These minerals present strong anisotropy, with seismic velocities often differing by 20% or more among the different directions defined by the symmetry axes. Large-scale asthenospheric flow, for instance, has been related to CPO (Karato 2008, Shearer 2009). Moreover, CPO in anisotropic minerals, such as amphibole and mica, can generate positive radial anisotropy during deformation at sub-horizontal shear zones in the upper-lower crust and the lower crust-lithospheric mantle boundaries.

6.3 Tectonic and geological implications

6.3.1 Magmatic overprinting in the Eastern Cordillera

The Eastern Cordillera was uplifted during the Cenozoic because of compression of the North Andean Block. Former extensional basins were thus inverted through fault reactivation, facilitating the shortening of the crust and surface uplift of the EC (Kellogg et al. 1995, Taboada et al. 2000, Egbue et al. 2014). The crust in this area has been significantly thickened, reaching values over 50 km (Poveda et al. 2015). The presence of a few isolated, inactive volcanoes (extinct about 6 Ma) may be unrelated to modern arc magmatism (Bernet et al. 2016).

One of the thickening mechanisms may be associated to the shortening of the crust

due to a combination of compression and escape tectonics (Trenkamp et al. 2002). The greatest shortening and high topography formation in the EC began in the Miocene, in response to the accretion of the Panama arc along the western margin of Colombia (Taboada et al. 2000). An alternative mechanism for crustal thickening may be associated to magmatic addition, as evidenced through the Pliocene volcanim reported in (Pardo et al. 2005, Bernet et al. 2016). Our results display a low velocity zone in the middle crust overlying a wide area of positive radial anisotropy down to the lower crust. If shortening were the predominant mechanism, deformation would likely have generated negative radial SPO anisotropy due to vertically oriented structures such as the high-angle faults that bound the EC. However, positive radial anisotropy is observed instead, making some sort of magmatic addition along horizontally lying magma bodies more likely.

Moreover, in the upper crust positive radial anisotropy might be related to sub-horizontal structures that prevent magmas from reaching the surface. Although shortening of the EC cannot be ruled out, we suggest that the dominating mechanism is magmatic addition. The mechanims of magmatic addition could be related to mantle flow or some other convective disturbance below the EC, as those would explain non-isostatic residual topography associated with subduction reported by Yarce et al. (2014).

6.3.2 Implications for extension and melts in the Lower Magdalena Basin

The Lower Magdalena Basin is an Oligocene to Recent basin, located between two basement massifs: the Central Cordillera and Sierra Nevada de Santa Marta (Santa Marta Massif), and the Sinú and San Jacinto fold belts (Mora-Bohórquez et al. 2017). This area includes the Plató (PB) and San Jorge Basins (SJB). The evolutionary characteristics of this basin indicate that from the Oligocene it behaves as a set of rotational and extensional basins (Montes et al. 2010, Mora-Bohórquez et al. 2017), due to the oblique and shallow

subduction of the Caribbean Plate without subduction-related volcanims.

In this area, we have reported slow shear velocities with positive radial anisotropy throughout the crust. In the upper crust, the slow velocities seem to be controlled structurally by the Romeral Fault and the trench zone below Sinu and San Jacinto, which may be related to the dense sedimentary cover reported for this area (Vernette et al. 1992, Lara et al. 2013, Mora-Bohórquez et al. 2017). In the middle and lower crust slow velocities and positive radial anisotropy extend throughout the LMB. Two hypotheses were proposed to explain the low velocities in the middle and upper crust. The first hypothesis was related to the presence of Middle Miocene (13–14 Ma) mafic volcanism within the Caribbean continental margin, as reported by Lara et al. (2013). Those authors proposed that asthenospheric magmas might have breached the Caribbean flat slab through a preexisting vertical tear, and that they are now ponding at mid-crustal depths within the overriding plate. The second hypothesis was related to fluid migration along major crustal faults (Zhao et al. 1996, Corbeau et al. 2017). Taking the observations of positive radial anisotropy for this region into account, it is easy to rule out the effect of fault migration, since negative radial anisotropy related to vertical faults should be observed. Nonetheless, the presence of the Romeral fault system in the LMB, could indeed be the object of fluid migration, and negative radial anisotropy should be expected under the Sinú and San Jacinto fold belts. Observations of positive radial anisotropy and low velocity dominate the entire LMB, suggesting the first hypothesis is more plausible. Moreover, if this hypothesis is considered, the storage of the melts along horizontal structures located in the middle and lower crusts would explain the paucity of surface volcanism in the region.

An additional mechanism that can contribute to generate positive radial anisotropy under the LMB is extension in the area, which has been active since the Early Cenozoic. Montes et al. (2005) document a recent, 23°–30° clockwise rotation of the Santa Marta Massif, with a total of 50–56 km of east-west shortening in the Cesar-Rancheria Basin (CRB) and 115 km of extensión throughout the LMB. This is consistent with a small

crustal thickness in the Caribbean Plains between 25 and 31 km (Poveda et al. 2015). Under that mechanism, positive radial anisotropy could result from sub-horizontal realignment of crystals due to extension.

6.3.3 Implications for fluid flow and deformation in the Central cordillera

The Central Cordillera hosts active volcanism and keeps a Late Triassic to Late Jurassic record of magmatism between 203 and 145 Ma (Aspden et al. 1987, Spikings et al. 2015, Bustamante et al. 2016), which includes large NW-NE batholiths associated with volcanic rocks distributed along the eastern margin of the Central Cordillera and the middle and upper Magdalena River Valley (UMV). Our results show high velocities in the upper crust that mark the footprint of those batholiths (Ibague, Antioquia, and Segovia in the San Lucas Range). Radial anisotropy is predominantly negative, which may indicate an intrusive nature for these bodies, especially the SMM, SM, SRL and IB. With similar ages and genesis, it can explain negative anisotropy through vertical shape preferred orientation (SPO). Negative anisotropy with high velocities can also be consistent with the modern stress regime, through accommodation by major structures within the North Andean Block, deformation related to uplift, shortening, and high fault angles (Restrepo-Moreno et al., 2008), and exhumation of the Antioqueño Plateau including the AB.

One of the most important results of this thesis is that subduction-related melts are marked by slow velocities within the crust (25 - 35 km depth), while estimates of radial anisotropy show a negative character throughout the crust immediately above (< 25 km depth). We suggest that negative radial anisotropy is consistent with structural alignment in the vertical direction, through sub-vertical feeding dykes and an SPO mechanim. In the lower crust, positive anisotropy with slow velocities are observed, similar to the EC,

suggesting the presence of horizontally lying magma bodies. Recent studies (Londono 2016, Murcia et al. 2018) have proved the existence of a common magmatic body about 20–40 km depth that feeds the volcanoes of northern Colombia, which is consistent with our interpretation.

6.3.4 Negative radial anisotropy of the Caribbean plate

The radial anisotropy found in the upper mantle is generally small ($\pm 2\%$) and can likely be disregarded. However, a moderate value of 4% and negative sign is found under the Lower Magdalena Valley. According to several authors (van der Hilst & Mann 1994, Taboada et al. 2000, Vargas & Mann 2013) the Caribbean plate subducts under NW South America with an anomalous low angle over a distance of 200 km into the South American continent. According to (Bowland & Rosencratz 1988) the Caribbean plate is a thick oceanic plateau, with a crustal thicknesses that can reach $\sim$20 km. The Caribbean plate may have formed in an intrusive environment, which would be consistent with the observed negative anisotropy. Our observations would then imply that the southern termination of the Caribbean slab occurs at around of 8°N, and that the Nazca plate might be extending north to 8°N. If correct, the offset in seismicity at 5.5°N would represent a slab tear (Chiarabba et al. 2016, Syracuse et al. 2016, Wagner et al. 2017) rather than a boundary between two separate plates (Yarce et al. 2014, Cortés et al. 2006, Taboada et al. 2000).

Chapter 7

Conclusions and future work

Through cross-correlation of long time series, from 2012 to 2016, of ambient seismic noise between stations, we have obtained Rayleigh and Love wave phase and group velocity dispersion curves at periods between 7 s and 38 s. From earthquake sources at regional and teleseismic distances, group velocity curves of Rayleigh and Loves wave have been determined from 11,000 surface-wave trains at periods from 40 to 150 s. Surface wave tomographic maps between 7 to 150 s, have been used to estimated 3-D variations in V_{SV} and V_{SH} in the crust and upper mantle down to 140 km depth. These results have then been used to infer shear velocity Voigt average and radial anisotropy maps for NW South america with unprecedent resolution. The results resolve geological features with high accuracy at shallow levels, as well as features associated with magmatism, revealing the relationship between crustal fluids and active/inactive volcanims under NW South America. In the middle crust, negative anisotropy is found under active volcanics, consistent with sub-vertical magmatic dykes; in contrast, positive radial anisotropy is observed under inactive volcanism along the EC, suggesting storage along flat-lying sills. Positive radial anisotropy pervades the entire lower crust, suggesting widespread accumulation of subduction-related melts. In the upper mantle, negative radial anisotropy under the LMB is found consistent with the proposed extent of Caribbean flat subduction.

Future research that can be based on the results of this thesis include:

- Investigate the most important seismic discontinuities in NW South America from the Common-Conversion-Point stacking of receiver functions (Dueker & Sheehan 1997, Frassetto et al. 2010), in order to find phase conversions that can improve the results of crustal thickness found in Poveda et al. (2015) and the main discontinuites in the upper mantle. However, due to the strong lateral hetereogeneities of the Andean the crust (dipping boundaries and/or anisotropic structures), it would be advisable to develop the migration of the isotropic part of the receiver functions, after application of harmonic decomposition (Bianchi et al. 2010).

- Taking advantage of the isotropic receiver functions, the joint inversion of receiver functions and surface waves dispersion observations (Julià et al. 2000) could be applied, gaining greater control of the main interfaces in the crust and the upper mantle.

- Improve the upper mantle seismic structure beneath NW South America from P- and S-wave regional and teleseimic traveltime tomography (Schimmel et al. 2003, Rocha et al. 2011), perhaps jointly inverting with group delays from the surface-wave dispersion curves develop in this thesis (West et al. 2004).

Bibliography

Aki, Keiiti (1957), Space and Time Spectra of Stationary Stochastic Waves, Vol. 35.

Aldrich, L.T., D.E. James, A.T. Linde, G.R. Ocola, G.R. Poe & I. S. Sacks (1973), 'Project Nariño', Carnegie Institute Washington, Yearb **72**, 247–249.

Ammon, Charles J., George E. Randall & George Zandt (1990), 'On the nonuniqueness of receiver function inversions', Journal of Geophysical Research **95**(B10), 15303.
URL: *http://doi.wiley.com/10.1029/JB095iB10p15303*

Aspden, J. A., W. J. McCourt & M. Brook (1987), 'Geometrical control of subduction-related magmatism: the Mesozoic and Cenozoic plutonic history of Western Colombia', Journal of the Geological Society **144**(6), 893–905.
URL: *http://jgs.lyellcollection.org/cgi/doi/10.1144/gsjgs.144.6.0893*

Babuska, V. & M. Cara (1991), Seismic Anisotropy in the Earth, Publishers Kluwer Academic, Dordrecht.

Bastow, Ian D., J. Julià, A.F. do Nascimento, R.A. Fuck, T.L. Buckthorp & J.J. McClellan (2015), 'Upper mantle anisotropy of the Borborema Province, NE Brazil: Implications for intra-plate deformation and sub-cratonic asthenospheric flow', Tectonophysics **657**, 81–93.
URL: *http://linkinghub.elsevier.com/retrieve/pii/S0040195115003558*

Becker, Thorsten W., Bogdan Kustowski & Göran Ekström (2008), 'Radial seismic anisotropy as a constraint for upper mantle rheology', Earth and Planetary Science Letters **267**(1-2), 213–227.
URL: *http://linkinghub.elsevier.com/retrieve/pii/S0012821X07007728*

Behr, Y., J. Townend, S. Bannister & M. K. Savage (2010), 'Shear velocity structure of the Northland Peninsula, New Zealand, inferred from ambient noise correlations', Journal of Geophysical Research **115**(B5), B05309.
URL: *http://doi.wiley.com/10.1029/2009JB006737*

Bensen, G. D., M. H. Ritzwoller, M. P. Barmin, A. L. Levshin, F. Lin, M. P. Moschetti, N. M. Shapiro & Y. Yang (2007), 'Processing seismic ambient noise data to obtain reliable broad-band surface wave dispersion measurements', Geophysical Journal International **169**(3), 1239–1260.

Bensen, G. D., M.H. Ritzwoller & N. M. Shapiro (2008), 'Broadband ambient noise surface wave tomography across the United States', Journal of Geophysical Research **113**, B05306.
URL: *http://doi.wiley.com/10.1029/2007JB005248*

Bernal-Olaya, Rocio, Paul Mann & Carlos A. Vargas (2015), 'Earthquake, Tomographic, Seismic Reflection, and Gravity Evidence for a Shallowly Dipping Subduction Zone beneath the Caribbean Margin of Northwestern Colombia', Memoir 108: Petroleum Geology and Potential of the Colombian Caribbean Margin pp. 247–270.
URL: *http://search.datapages.com/data/doi/10.1306/13531939M1083642*

Bernet, Matthias, Cindy Urueña, Sergio Amaya & Mary L Peña (2016), 'New thermo and geochronological constraints on the Pliocene-Pleistocene eruption history of the Paipa-Iza volcanic complex, Eastern Cordillera, Colombia', Journal of Volcanology

and Geothermal Research .

URL: *http://dx.doi.org/10.1016/j.jvolgeores.2016.08.013*

Bianchi, I., J. Park, N. Piana Agostinetti & V. Levin (2010), 'Mapping seismic anisotropy using harmonic decomposition of receiver functions: An application to Northern Apennines, Italy', Journal of Geophysical Research **115**(B12), B12317.

URL: *http://doi.wiley.com/10.1029/2009JB007061*

Bowland, C L & E Rosencratz (1988), 'Upper Crustal structure of the Western Colombian basin, Caribbean sea', Geological Society of America Bulletin **100**(4), 534–546.

Bracewell, R. N. (1965), The Fourier transform and its applications.

Bromirski, Peter D (2009), 'Earth Vibrations', **324**(5930), 1026–1027.

Bustamante, Camilo, Carlos J. Archanjo, Agustín Cardona & Jeffrey D. Vervoort (2016), 'Late Jurassic to Early Cretaceous plutonism in the Colombian Andes: A record of long-term arc maturity', Geological Society of America Bulletin **128**(11-12), 1762–1779.

URL: *http://gsabulletin.gsapubs.org/lookup/doi/10.1130/B31307.1*

Capon, J (1973), 'Signal Processing and Frequency-Wavenumber Spectrum Analysis for a Large Aperture Seismic Array', Meth.˜in Comp.˜Phys., Volume 13, p.˜1-59 **13**, 1–59.

Cardona, A., V. A. Valencia, G. Bayona, J. Duque, M. Ducea, G. Gehrels, C. Jaramillo, C. Montes, G. Ojeda & J. Ruiz (2011), 'Early-subduction-related orogeny in the northern Andes: Turonian to Eocene magmatic and provenance record in the Santa Marta Massif and Rancheria Basin, northern Colombia', Terra Nova **23**(1), 26–34.

URL: *http://doi.wiley.com/10.1111/j.1365-3121.2010.00979.x*

Case, J. E., L. G. Duran S, LopezR. Alfonsp & W. R. Moore (1971), 'Tectonic Investigations in Western Colombia and Eastern Panama', Geological Society of America Bulletin **82**(10), 2685.
URL: *http://gsabulletin.gsapubs.org/cgi/doi/10.1130/0016-7606(1971)82[2685:TIIWCA]2.0.CO;2*

Cediel, Fabio, Robert Shaw & Carlos Cáceres (2003), 'Tectonic Assembly of the Northern Andean Block', eds., The Circum-Gulf of Mexico and the Caribbean: Hydrocarbon habitats, basin formation, and plate tectonics **79**, 815–848.

Chang, Ying, Linda M. Warren & Germán A. Prieto (2017), 'Precise Locations for Intermediate-Depth Earthquakes in the Cauca Cluster, Colombia', Bulletin of the Seismological Society of America **107**(6), 2649–2663.
URL: *https://pubs.geoscienceworld.org/bssa/article-lookup?doi=10.1785/0120170127*

Chiarabba, Claudio, Pasquale De Gori, Claudio Faccenna, Fabio Speranza, Danilo Seccia, Viviana Dionicio & Germán A. Prieto (2016), 'Subduction system and flat slab beneath the Eastern Cordillera of Colombia', Geochemistry, Geophysics, Geosystems **17**(1), 16–27.
URL: *http://doi.wiley.com/10.1002/2015GC006048*

Condie, Kent C. (2005), 'High field strength element ratios in Archean basalts: a window to evolving sources of mantle plumes?', Lithos **79**(3-4), 491–504.
URL: *http://linkinghub.elsevier.com/retrieve/pii/S0024493704003202*

Corbeau, J., F. Rolandone, S. Leroy, K. Guerrier, D. Keir, G. Stuart, V. Clouard, R. Gallacher, S. Ulysse, D. Boisson, R. Bien-aimé Momplaisir, F. Saint Preux, C. Prépetit, J. M. Saurel, B. Mercier de Lépinay & B. Meyer (2017), 'Crustal structure of western Hispaniola (Haiti) from a teleseismic receiver function study', Tectonophysics

709(April 2013), 9–19.

URL: *http://dx.doi.org/10.1016/j.tecto.2017.04.029*

Corredor, Freddy (2003), 'Seismic strain rates and distributed continental deformation in the northern Andes and three-dimensional seismotectonics of northwestern South America', Tectonophysics **372**(3-4), 147–166.

Cortés, Martin, Bernard Colletta & Jacques Angelier (2006), 'Structure and tectonics of the central segment of the Eastern Cordillera of Colombia', Journal of South American Earth Sciences **21**(4), 437–465.

Das, Ritima & S.S. Rai (2017), 'Extensive seismic anisotropy in the lower crust of Archean metamorphic terrain, South India, inferred from ambient noise tomography', Tectonophysics **694**, 164–180.

URL: *http://linkinghub.elsevier.com/retrieve/pii/S0040195116305960*

Dengo, C. A. & M. C. Covey (1993), 'Structure of the Eastern Cordillera of Colombia: implications for trap styles and regional tectonics'.

Dueker, Kenneth G & Anne F Sheehan (1997), 'Mantle discontinuity structure from midpoint stacks of converted P to S waves across the Yellowstone hotspot track', Journal of Geophysical Research: Solid Earth **102**(B4), 8313–8327.

URL: *https://agupubs.onlinelibrary.wiley.com/doi/abs/10.1029/96JB03857 http://doi.wiley.com/10.1029/96JB03857*

Dunkin, John W (1965), 'Computation of modal solutions in layered, elastic media at high frequencies', Bulletin of the Seismological Society of America **55**(2), 335–358.

URL: *http://www.bssaonline.org/content/55/2/335.abstract*

Duque-Caro, H (1990), 'The Choco Block in the northwestern corner of South America : Structural , tectonostratigraphic , and paleogeographic implications', Journal of South American Earth Sciences **3**(I), 71–84.

Dziewonski, A, S Bloch & M Landisman (1969), 'A technique for the analysis of transient seismic signals', Bulletin of the Seismological Society of America **59**(1), 427–444.
URL: *http://dx.doi.org/*

Dziewonski, Adam M. & Don L. Anderson (1981), 'Preliminary reference Earth model', Physics of the Earth and Planetary Interiors **25**(4), 297–356.
URL: *http://linkinghub.elsevier.com/retrieve/pii/0031920181900467*

Efron, Bradley & Robert J. Tibshirani (1993), 'An Introduction To The Bootstrap'.

Egbue, Obi, James Kellogg, Hector Aguirre & Carolina Torres (2014), 'Evolution of the stress and strain fields in the Eastern Cordillera, Colombia', Journal of Structural Geology **58**, 8–21.
URL: *http://dx.doi.org/10.1016/j.jsg.2013.10.004*
http://linkinghub.elsevier.com/retrieve/pii/S0191814113001752

Escalona, Alejandro & Paul Mann (2011), 'Tectonics, basin subsidence mechanisms, and paleogeography of the Caribbean-South American plate boundary zone', Marine and Petroleum Geology **28**(1), 8–39.
URL: *http://dx.doi.org/10.1016/j.marpetgeo.2010.01.016*

Farris, David W, Carlos Jaramillo, German Bayona, Sergio A Restrepo-moreno, Camilo Montes, Agustin Cardona, Andres Mora, Robert J Speakman, Michael D Glascock & Victor Valencia (2011), 'Fracturing of the Panamanian Isthmus during initial collision with South America', Geology **39**(11), 1007–1010.

Feng, Mei, Marcelo Assumpção & Suzan Van der Lee (2004), 'Group-velocity tomography and lithospheric S-velocity structure of the South American continent', Physics of the Earth and Planetary Interiors **147**(4), 315–331.
URL: *http://linkinghub.elsevier.com/retrieve/pii/S0031920104002924*

Flinch, J F (2003), 'Structural Evolution of the Sinu-Lower Magdalena Area (Northern Colombia)', AAPG Memoir **79**, 776–796.

Flueh, E.R., B. Milkereit, R. Meissner, R. P. Meyer, J. E. Ramirez, J. C. Quintero & A. Udias (1981), Seismic refraction observations in northwestern Colombia at latitude 5.5°N,, em U.Miller & U.Rosenfeld, eds., 'Zentralblatt fuer Geologie und Palaeontologie', vol 3-4ª edição, Angew., Reg. Hist. Geol, Germany, pp. 231–242.

Frassetto, A., G. Zandt, H. Gilbert, T. J. Owens & C. H. Jones (2010), 'Improved imaging with phase-weighted common conversion point stacks of receiver functions', Geophysical Journal International **182**(1), 368–374.

Freymueller, Jeffrey T., James N. Kellogg & Victor Vega (1993), 'Plate Motions in the north Andean region', Journal of Geophysical Research: Solid Earth **98**(B12), 21853–21863.
URL: *http://doi.wiley.com/10.1029/93JB00520*

Gómez-Alba, Sebastián, Carlos Eduardo Fajardo-Zarate & Carlos Alberto Vargas (2016), 'Stress field estimation based on focal mechanisms and back projected imaging in the Eastern Llanos Basin (Colombia)', Journal of South American Earth Sciences **71**, 320–332.
URL: *http://linkinghub.elsevier.com/retrieve/pii/S089598111530047X*

Gómez, J., A. Nivia, N.E. Montes, D.M. Jiménez, M.L. Tejada, M.J. Sepúlveda, J.A. Osorio, T. Gaona, H. Diederix, H. Uribe, Mora M. & Compilers (2007), 'Geological Map of Colombia', INGEOMINAS, Project Geological Map of Colombia, Bogotá, Colombia. Available at: http://www2.sgc.gov.co/ getattachment/Geologia/Mapa-geologico-de-Colombia/ GMC_2007_1000K.pdf.aspx .

Gutscher, Marc-André, Wim Spakman, Harmen Bijwaard & E Robert Engdahl (2000), 'Geodynamics of flat subduction: Seismicity and tomographic constraints from the

Andean margin', Tectonics **19**(5), 814–833.
URL: *http://doi.wiley.com/10.1029/1999TC001152*

Herrin, Eugene & Tom Goforth (1977), 'Phase-matched filters: Application to the study of Rayleigh waves', Bulletin of the Seismological Society of America **67**(5), 1259–1275.

Idárraga-García, J., J.-M. Kendall & C. A. Vargas (2016), 'Shear wave anisotropy in northwestern South America and its link to the Caribbean and Nazca subduction geodynamics', Geochemistry, Geophysics, Geosystems **17**(9), 3655–3673.
URL: *http://doi.wiley.com/10.1002/2016GC006406*
http://doi.wiley.com/10.1002/2016GC006323

Julià, J., C J Ammon, R B Herrmann & A M Correig (2000), 'Joint inversion of receiver function and surface wave dispersion observations', Geophysical Journal International **143**(1), 99–112.
URL: *http://doi.wiley.com/10.1046/j.1365-246x.2000.00217.x*

Kao, Honn, Yannik Behr, Claire A. Currie, Roy Hyndman, John Townend, Fan-Chi Lin, Michael H. Ritzwoller, Shao-Ju Shan & Jiangheng He (2013), 'Ambient seismic noise tomography of Canada and adjacent regions: Part I. Crustal structures', Journal of Geophysical Research: Solid Earth **118**(11), 5865–5887.
URL: *http://doi.wiley.com/10.1002/2013JB010535*

Karato, Shun-ichiro (2008), Seismic anisotropy and its geodynamic implications, em 'Deformation of Earth Materials: An Introduction to the Rheology of Solid Earth', Cambridge University Press, p. 391–411.

Kellogg, James N., Victor Vega, T. C. Stailings, Carlos L.V. Aiken & James N. Kellogg (1995), Tectonic development of Panama, Costa Rica, and the Colombian Andes:

Constraints from Global Positioning System geodetic studies and gravity, pp. 75–90.

URL: *https://pubs.geoscienceworld.org/books/book/441/chapter/3798922/*

Kennett, B. L. N., M. S. Sambridge & P. R. Williamson (1988), 'Subspace methods for large inverse problems with multiple parameter classes', Geophysical Journal International **94**(2), 237–247.

URL: *http://gji.oxfordjournals.org/cgi/doi/10.1111/j.1365-246X.1988.tb05898.x*

Köhler, Andreas, Christian Weidle & Valérie Maupin (2012), 'Crustal and uppermost mantle structure of southern Norway: results from surface wave analysis of ambient seismic noise and earthquake data', Geophysical Journal International **191**(3), 1441–1456.

URL: *http://gji.oxfordjournals.org/cgi/doi/10.1111/j.1365-246X.2012.05698.x https://academic.oup.com/gji/article-lookup/doi/10.1111/j.1365-246X.2012.05698.x*

Lara, M., A. Cardona, G. Monsalve, J. Yarce, C. Montes, V. Valencia, M. Weber, F. De La Parra, D. Espitia & M. López-Martínez (2013), 'Middle Miocene near trench volcanism in northern Colombia: A record of slab tearing due to the simultaneous subduction of the Caribbean Plate under South and Central America?', Journal of South American Earth Sciences **45**, 24–41.

URL: *http://dx.doi.org/10.1016/j.jsames.2012.12.006 http://linkinghub.elsevier.com/retrieve/pii/S0895981113000023*

Larose, Eric (2004), 'Imaging from one-bit correlations of wideband diffuse wave fields', Journal of Applied Physics **95**(12), 8393.

URL: *http://scitation.aip.org/content/aip/journal/jap/95/12/10.1063/1.1739529*

Levshin, A. L. & M. H. Ritzwoller (2001), 'Automated Detection, Extraction, and Measurement of Regional Surface Waves', Pure and Applied Geophysics **158**(8), 1531–1545.

URL: *http://link.springer.com/10.1007/PL00001233*

Lin, Fan C., Morgan P. Moschetti & Michael H. Ritzwoller (2008a), 'Surface wave tomography of the western United States from ambient seismic noise: Rayleigh and Love wave phase velocity maps', Geophysical Journal International **173**(1), 281–298.

Lin, Fan-Chi, Morgan P. Moschetti & Michael H. Ritzwoller (2008b), 'Surface wave tomography of the western United States from ambient seismic noise: Rayleigh and Love wave phase velocity maps', Geophysical Journal International **173**(1), 281–298.

URL: *https://academic.oup.com/gji/article-lookup/doi/10.1111/j.1365-246X.2008.03720.x*

Lomax, Anthony & Roel Snieder (1994), 'Finding sets of acceptable solutions with a genetic algorithm with application to surface wave group dispersion in Europe', Geophysical Research Letters **21**(24), 2617–2620.

URL: *http://doi.wiley.com/10.1029/94GL02635*

Londono, John Makario (2016), 'Evidence of recent deep magmatic activity at Cerro Bravo-Cerro Machín volcanic complex, central Colombia. Implications for future volcanic activity at Nevado del Ruiz, Cerro Machín and other volcanoes', Journal of Volcanology and Geothermal Research **324**, 156–168.

URL: *http://dx.doi.org/10.1016/j.jvolgeores.2016.06.003 http://linkinghub.elsevier.com/retrieve/pii/S0377027316301299*

Lynner, Colton, Susan L. Beck, George Zandt, Robert W. Porritt, Fan-Chi Lin & Zachary C. Eilon (2018), 'Mid-crustal deformation in the Central Andes constrained

by radial anisotropy', Journal of Geophysical Research: Solid Earth .
URL: *http://doi.wiley.com/10.1029/2017JB014936*

Maceira, Monica & Charles J. Ammon (2009), 'Joint inversion of surface wave velocity and gravity observations and its application to central Asian basins shear velocity structure', Journal of Geophysical Research **114**(B2), B02314.
URL: *http://doi.wiley.com/10.1029/2007JB005157*

McNamara, Daniel E (2004), 'Ambient Noise Levels in the Continental United States', Bulletin of the Seismological Society of America **94**(4), 1517–1527.
URL: *http://dx.doi.org/10.1785/012003001 https://pubs.geoscienceworld.org/bssa/article/94/4/15*
1527/121021

Meissnar, R.O., E.R. Flueh, F. Stibane & E. Berg (1976), 'Dynamics of the active plate boundary in southwest colombia according to recent geophysical measurements', Tectonophysics **35**(1-3), 115–136.
URL: *http://linkinghub.elsevier.com/retrieve/pii/0040195176900329*

Meyer, R. P., W. D. Mooney, A. L. Hales, C. E. Helsley, G. P. Woollard, D. M. Hussong, L. W. Kroenke & J. E. Ramirez (1976), Project Nariño III: Refraction observation across a leading edge, Malpelo Island to the Colombian cordillera occidental, pp. 105–132.
URL: *http://www.agu.org/books/gm/v019/GM019p0105/GM019p0105.shtml*

Montes, Camilo, Georgina Guzman, German Bayona, Agustin Cardona, Victor Valencia & Carlos Jaramillo (2010), 'Clockwise rotation of the Santa Marta massif and simultaneous Paleogene to Neogene deformation of the Plato-San Jorge and Cesar-Ranchería basins', Journal of South American Earth Sciences **29**(4), 832–848.
URL: *http://linkinghub.elsevier.com/retrieve/pii/S0895981109001059*

Mooney, Walter D, Robert P Meyer, Joseph P Laurence, Hansjurgen Meyer & J Emilio Ramírez (1979), 'Seismic refraction studies of the Western Cordillera, Colombia', Bulletin of the Seismological Society of America **69**(6), 1745–1761.
URL: *http://www.bssaonline.org/content/69/6/1745.abstract*

Mora-Bohórquez, J. Alejandro, Mauricio Ibánez-Mejia, Onno Oncken, Mario de Freitas, Vickye Vélez, Andrés Mesa & Lina Serna (2017), 'Structure and age of the Lower Magdalena Valley basin basement, northern Colombia: New reflection-seismic and U-Pb-Hf insights into the termination of the central andes against the Caribbean basin', Journal of South American Earth Sciences **74**, 1–26.
URL: *http://linkinghub.elsevier.com/retrieve/pii/S0895981117300019*

Moschetti, M. P., M. H. Ritzwoller, F.-C. Lin & Y. Yang (2010a), 'Crustal shear wave velocity structure of the western United States inferred from ambient seismic noise and earthquake data', Journal of Geophysical Research **115**(B10), B10306.
URL: *http://doi.wiley.com/10.1029/2010JB007448*

Moschetti, M. P., M. H. Ritzwoller, F. Lin & Y. Yang (2010b), 'Seismic evidence for widespread western-US deep-crustal deformation caused by extension', Nature **464**(7290), 885–889.
URL: *http://www.nature.com/articles/nature08951*

Murcia, H., C. Borrero & K. Németh (2018), 'Overview and plumbing system implications of monogenetic volcanism in the northernmost Andes' volcanic province', Journal of Volcanology and Geothermal Research .
URL: *https://linkinghub.elsevier.com/retrieve/pii/S0377027317305942*

Ocola, Leonidas C, L T Aldrich, J F Gettrust, R P Meyer & J E Ramirez (1975), 'Project Nariño I: Crustal structure under southern Colombian-northern Ecuador Andes from seismic refraction data', Bulletin of the Seismological Society of America

65(6), 1681–1695.

URL: *http://www.bssaonline.org/content/65/6/1681.abstract*

Ojeda, Anibal & Jens Havskov (2001), 'Crustal structure and local seismicity in Colombia', Journal of Seismology **5**(4), 575–593.

URL: *http://dx.doi.org/10.1023/A:1012053206408*
http://link.springer.com/10.1023/A:1012053206408

Paige, C C & M A Saunders (1982), 'LSQR: An Algorithm for Sparse Linear Equations and Sparse Least Squares', **8**, 43–71.

Pardo, Natalia, Héctor Cepeda & José Maria Jaramillo (2005), 'The Paipa Volcano, Easter Cordillera of Colombia,South America: Volcanic Stratigraphy', Earth Sciences Research Journal **9**(1), 3–18.

Pennington, Wayne D. (1981), 'Subduction of the Eastern Panama Basin and seismotectonics of northwestern South America', Journal of Geophysical Research: Solid Earth **86**(B11), 10753–10770.

URL: *http://doi.wiley.com/10.1029/JB086iB11p10753*

Pindell, J. & L. Kennan (2009), 'Dextral shear, terrane accretion and basin formation in the Northern Andes: best explained by interaction with a Pacific-derived Caribbean Plate?', Geological Society, London, Special Publications **328**(1), 487–531.

Porritt, Robert W., Thorsten W. Becker & Gaspar Monsalve (2014), 'Seismic anisotropy and slab dynamics from SKS splitting recorded in Colombia', Geophysical Research Letters **41**(24), 8775–8783.

URL: *http://doi.wiley.com/10.1002/2014GL061958*

Poveda, Esteban, Gaspar Monsalve & Carlos Alberto Vargas (2015), 'Receiver functions and crustal structure of the northwestern Andean region, Colombia', Journal of

Geophysical Research: Solid Earth **120**(4), 2408–2425.

URL: *http://doi.wiley.com/10.1002/2014JB011304*

Prieto, G. A., J. F. Lawrence & G. C. Beroza (2009), 'Anelastic Earth structure from the coherency of the ambient seismic field', Journal of Geophysical Research **114**(B7), B07303.

URL: *http://doi.wiley.com/10.1029/2008JB006067*

Prieto, German a (2012), 'Imaging the deep Earth.', Science **338**, 1037–8.

URL: *http://www.ncbi.nlm.nih.gov/pubmed/23180851*

Prieto, Germán A., Gregory C. Beroza, Sarah A. Barrett, Gabriel A. López & Manuel Florez (2012), 'Earthquake nests as natural laboratories for the study of intermediate-depth earthquake mechanics', Tectonophysics **570-571**, 42–56.

URL: *http://linkinghub.elsevier.com/retrieve/pii/S0040195112004374*

Rawlinson, N. & M. Sambridge (2003), SEISMIC TRAVELTIME TOMOGRAPHY OF THE CRUST AND LITHOSPHERE, em 'Advances in Geophysics', Vol. 46, pp. 81–198.

URL: *http://linkinghub.elsevier.com/retrieve/pii/S0065268703460020*

Rawlinson, N. & M. Sambridge (2004), 'Multiple reflection and transmission phases in complex layered media using a multistage fast marching method', Geophysics **69**(5), 1338–1350.

URL: *http://library.seg.org/doi/abs/10.1190/1.1801950*

Rawlinson, N., S. Pozgay & S. Fishwick (2010), 'Seismic tomography: A window into deep Earth', Physics of the Earth and Planetary Interiors **178**(3-4), 101–135.

URL: *http://linkinghub.elsevier.com/retrieve/pii/S0031920109002106*

Rawlinson, Nicholas & Malcolm Sambridge (2005), 'The fast marching method: an effective tool for tomographic imaging and tracking multiple phases in complex layered

media', Exploration Geophysics **36**(4), 341.
URL: *http://www.publish.csiro.au/?paper=EG05341*

Restrepo, J. & J. Toussaint (1988), 'Terranes and continental accretion in the Colombian Andes', Episodes **11**, 189–193.

Restrepo-Moreno, S, D Foster, D Stockli & L Parra-Sanchez (2009), 'Long-term erosion and exhumation of the "Altiplano Antioqueño", Northern Andes (Colombia) from apatite (U–Th)/He thermochronology', Earth and Planetary Science Letters **278**(1-2), 1–12.
URL: *http://dx.doi.org/10.1016/j.epsl.2008.09.037*
http://linkinghub.elsevier.com/retrieve/pii/S0012821X08006390

Ritsema, Jeroen, Hendrik Jan van Heijst & John H. Woodhouse (2004), 'Global transition zone tomography', Journal of Geophysical Research: Solid Earth **109**(B2).
URL: *http://doi.wiley.com/10.1029/2003JB002610*

Rocha, Marcelo Peres, Martin Schimmel & Marcelo Assumpção (2011), 'Upper-mantle seismic structure beneath SE and Central Brazil from P- and S-wave regional traveltime tomography', Geophysical Journal International **184**(1), 268–286.
URL: *https://academic.oup.com/gji/article-lookup/doi/10.1111/j.1365-246X.2010.04831.x*

Romanowicz, B (1991), 'Seismic Tomography of the Earth's Mantle', Annual Review of Earth and Planetary Sciences **19**(1), 77–99.
URL: *https://doi.org/10.1146/annurev.ea.19.050191.000453*
http://www.annualreviews.org/doi/10.1146/annurev.ea.19.050191.000453

Rosa, María Laura, Bruno Collaço, Marcelo Assumpção, Nora Sabbione & Gerardo Sánchez (2016), 'Thin crust beneath the Chaco-Paraná Basin by surface-wave tomo-

graphy', Journal of South American Earth Sciences **66**(February 2016), 1–14.
URL: *http://linkinghub.elsevier.com/retrieve/pii/S0895981115300900*

Sabra, Karim G., Peter Gerstoft, Philippe Roux, W. A. Kuperman & Michael C. Fehler (2005), 'Surface wave tomography from microseisms in Southern California', Geophysical Research Letters **32**(14), n/a–n/a.
URL: *http://doi.wiley.com/10.1029/2005GL023155*

Sambridge, Malcolm (1999), 'Geophysical inversion with a neighbourhood algorithm - I. Searching a parameter space', Geophysical Journal International **138**(2), 479–494.

Schimmel, M., E. Stutzmann & J. Gallart (2011), 'Using instantaneous phase coherence for signal extraction from ambient noise data at a local to a global scale', Geophysical Journal International **184**(1), 494–506.

Schimmel, M. & J. Gallart (2007), 'Frequency-dependent phase coherence for noise suppression in seismic array data', Journal of Geophysical Research: Solid Earth **112**(B4).
URL: *http://doi.wiley.com/10.1029/2006JB004680*

Schimmel, M., M. Assumpção & J. C. VanDecar (2003), 'Seismic velocity anomalies beneath SE Brazil from P and S wave travel time inversions', Journal of Geophysical Research: Solid Earth **108**(B4).
URL: *http://doi.wiley.com/10.1029/2001JB000187*

Schimmel, Martin (1999), 'Phase cross-correlations: Design, comparisons, and applications', Bulletin of the Seismological Society of America **89**(5), 1366–1378.
URL: *http://dx.doi.org/*

Schimmel, Martin & Hanneke Paulssen (1997), 'Noise reduction and detection of weak, coherent signals through phase-weighted stacks', Geophysical Journal International

130(2), 497–505.

URL: *http://gji.oxfordjournals.org/cgi/doi/10.1111/j.1365-246X.1997.tb05664.x*

Sen, Mrinal K. & Paul L. Stoffa (1991), 'Nonlinear one-dimensional seismic waveform inversion using simulated annealing', GEOPHYSICS **56**(10), 1624–1638.

URL: *http://library.seg.org/doi/abs/10.1190/1.1442973*

Sethian, J. A. (1996), 'A fast marching level set method for monotonically advancing fronts.', Proceedings of the National Academy of Sciences **93**(4), 1591–1595.

URL: *http://www.pnas.org/cgi/doi/10.1073/pnas.93.4.1591*

Shapiro, N. M. & M. Campillo (2004), 'Emergence of broadband Rayleigh waves from correlations of the ambient seismic noise', Geophysical Research Letters **31**(7), 8–11.

Shearer, P M (2009), Introduction to Seismology, Cambridge University Press.

URL: *https://books.google.com.co/books?id=VV0mV4lF0RUC*

Snieder, Roel (2004), 'Extracting the Green's function from the correlation of coda waves: a derivation based on stationary phase.', Physical review. E, Statistical, nonlinear, and soft matter physics **69**(4 Pt 2), 046610.

Spica, Zack, Mathieu Perton & Denis Legrand (2017), 'Anatomy of the Colima volcano magmatic system, Mexico', Earth and Planetary Science Letters **459**, 1–13.

URL: *http://linkinghub.elsevier.com/retrieve/pii/S0012821X16306446*

Spikings, Richard, Ryan Cochrane, Diego Villagomez, Roelant Van Der Lelij, Cristian Vallejo, Wilfried Winkler & Bernado Beate (2015), 'The geological history of northwestern South America : from Pangaea to the early collision of the Caribbean Large Igneous Province (290 – 75 Ma)', Gondwana Research **27**(1), 95–139.

URL: *http://dx.doi.org/10.1016/j.gr.2014.06.004*

Stein, Seth & Michael Wysession (2003), An introduction to seismology, earthquakes, and earth structure

Stockwell, R.G., L. Mansinha & R.P. Lowe (1996), 'Localization of the complex spectrum: the S transform', IEEE Transactions on Signal Processing **44**(4), 998–1001.
URL: *http://ieeexplore.ieee.org/lpdocs/epic03/wrapper.htm?arnumber=492555*

Syracuse, Ellen M., Monica Maceira, Germán A. Prieto, Haijiang Zhang & Charles J. Ammon (2016), 'Multiple plates subducting beneath Colombia, as illuminated by seismicity and velocity from the joint inversion of seismic and gravity data', Earth and Planetary Science Letters **444**, 139–149.
URL: *http://linkinghub.elsevier.com/retrieve/pii/S0012821X16301455*

Taboada, Alfredo, Luis A. Rivera, Andrés Fuenzalida, Armando Cisternas, Hervé Philip, Harmen Bijwaard, José Olaya & Clara Rivera (2000), 'Geodynamics of the northern Andes: Subductions and intracontinental deformation (Colombia)', Tectonics **19**(5), 787–813.
URL: *http://doi.wiley.com/10.1029/2000TC900004*

Tanimoto, Toshiro (2007), 'Excitation of microseisms', Geophysical Research Letters **34**(5).
URL: *http://doi.wiley.com/10.1029/2006GL029046*

Tikhonov, A N & V I A Arsenin (1977), Solutions of ill-posed problems, Scripta series in mathematics, Winston.
URL: *https://books.google.com.co/books?id=ECrvAAAAMAAJ*

Toto, El Arbi & J.N. Kellogg (1992), 'Structure of the Sinu-San Jacinto fold belt — an active accretionary prism in northern Colombia', Journal of South American Earth Sciences **5**(2), 211–222.
URL: *http://linkinghub.elsevier.com/retrieve/pii/0895981192900392*

Trenkamp, Robert, James N. Kellogg, Jeffrey T. Freymueller & Hector P. Mora (2002), 'Wide plate margin deformation, southern Central America and northwestern South America, CASA GPS observations', Journal of South American Earth Sciences **15**(2), 157–171.

URL: *http://linkinghub.elsevier.com/retrieve/pii/S0895981102000184*

Turcotte, Donald L. & Gerald Schubert (2002), Geodynamics, Cambridge University Press, Cambridge.

URL: *http://ebooks.cambridge.org/ref/id/CBO9780511807442*

van der Hilst, Rob & Paul Mann (1994), 'Tectonic implications of tomographic images of subducted lithosphere beneath northwestern South America', Geology **22**(5), 451–454.

URL: *http://geology.gsapubs.org/content/22/5/451.abstract*

Vargas, C. A. & P. Mann (2013), 'Tearing and Breaking Off of Subducted Slabs as the Result of Collision of the Panama Arc-Indenter with Northwestern South America', Bulletin of the Seismological Society of America **103**(3), 2025–2046.

URL: *http://www.bssaonline.org/cgi/doi/10.1785/0120120328*

Veloza, Gabriel, Richard Styron, Michael Taylor & Andrés Mora (2012), 'Open-source archive of active faults for northwest South America', GSA Today **22**(10), 4–10.

URL: *http://www.geosociety.org/gsatoday/archive/22/10/abstract/i1052-5173-22-10-4.htm*

Vernette, G., A. Mauffret, C. Bobier, L. Briceno & J. Gayet (1992), 'Mud diapirism, fan sedimentation and strike-slip faulting, Caribbean Colombian Margin', Tectonophysics **202**(2-4), 335–349.

URL: *http://linkinghub.elsevier.com/retrieve/pii/004019519290118P*

Villaseñor, Antonio, Yingjie Yang, Michael H. Ritzwoller & Josep Gallart (2007), 'Ambient noise surface wave tomography of the Iberian Peninsula: Implications for shallow seismic structure', Geophysical Research Letters **34**(11), L11304.
URL: *http://doi.wiley.com/10.1029/2007GL030164*

Wagner, L. S., J. S. Jaramillo, L. F. Ramírez-Hoyos, G. Monsalve, A. Cardona & T. W. Becker (2017), 'Transient slab flattening beneath Colombia', Geophysical Research Letters **44**(13), 6616–6623.

Wapenaar, Kees, Deyan Draganov, Roel Snieder, Xander Campman & Arie Verdel (2010), 'Tutorial on seismic interferometry: Part 1 — Basic principles and applications', Geophysics **75**(5), 195–75.

Wathelet, Marc (2008), 'An improved neighborhood algorithm: Parameter conditions and dynamic scaling', Geophysical Research Letters **35**(9), 1–5.

Weaver, Richard & Oleg Lobkis (2002), 'On the emergence of the Green's function in the correlations of a diffuse field: Pulse-echo using thermal phonons', Ultrasonics **40**(1-8), 435–439.

Weber, M., J. Gómez-Tapias, A. Cardona, E. Duarte, A. Pardo-Trujillo & V.A. Valencia (2015), 'Geochemistry of the Santa Fé Batholith and Buriticá Tonalite in NW Colombia – Evidence of subduction initiation beneath the Colombian Caribbean Plateau', Journal of South American Earth Sciences **62**, 257–274.
URL: *http://linkinghub.elsevier.com/retrieve/pii/S0895981115000528*

West, Michael, Wei Gao & Stephen Grand (2004), 'A simple approach to the joint inversion of seismic body and surface waves applied to the southwest U.S', Geophysical Research Letters **31**(15), L15615.
URL: *http://doi.wiley.com/10.1029/2004GL020373*

Yang, Yingjie, Michael H. Ritzwoller, Anatoli L. Levshin & Nikolai M. Shapiro (2007), 'Ambient noise Rayleigh wave tomography across Europe', Geophysical Journal International **168**(1), 259–274.

Yarce, Jefferson, Gaspar Monsalve, Thorsten Becker, Agustin Cardona, Esteban Poveda, Daniel Alvira & Ordonez-Carmona Oswaldo (2014), 'Seismological observations in Northwestern South America: Evidence for two subduction segments, contrasting crustal thicknesses and upper mantle flow', Tectonophysics **637**, 57–67.

Yudistira, Tedi, Hanneke Paulssen & Jeannot Trampert (2017), 'The crustal structure beneath The Netherlands derived from ambient seismic noise', Tectonophysics **721**, 361–371.
URL: *http://linkinghub.elsevier.com/retrieve/pii/S0040195117304018*

Zarifi, Zoya, Jens Havskov & Andrzej Hanyga (2007), 'An insight into the Bucaramanga nest', Tectonophysics **443**(1-2), 93–105.

Zhang, Haijiang & Clifford Thurber (2006), 'Development and Applications of Double-difference Seismic Tomography', Pure and Applied Geophysics **163**(2-3), 373–403.
URL: *http://link.springer.com/10.1007/s00024-005-0021-y*

Zhang, Haijiang, Monica Maceira, Philippe Roux & Clifford Thurber (2014), 'Joint Inversion of Body-Wave Arrival Times and Surface-Wave Dispersion for Three-Dimensional Seismic Structure Around SAFOD', Pure and Applied Geophysics **171**(11), 3013–3022.
URL: *http://link.springer.com/10.1007/s00024-014-0806-y*

Zhao, D., H. Kanamori, H. Negishi & D. Wiens (1996), 'Tomography of the Source Area of the 1995 Kobe Earthquake: Evidence for Fluids at the Hypocenter?', Science **274**(5294), 1891–1894.
URL: *http://www.sciencemag.org/cgi/doi/10.1126/science.274.5294.1891*

Zhu, Lupei & Hiroo Kanamori (2000), 'Moho depth variation in southern California from teleseismic receiver functions', Journal of Geophysical Research: Solid Earth **105**(B2), 2969–2980.

URL: *http://doi.wiley.com/10.1029/1999JB900322*

Appendix A

Crustal thickness estimates

The crustal thickness map presented in Poveda et al. (2015) from receiver function analysis has been updated in this thesis, following the procedures described in their study. We include 11 new stations that improve the sampling of the Caribbean region, the WC and the CC. We include new receiver functions at previous stations, as well. In the table A.1 results of crustal thickness with associated uncertainties are presented, with misfit obtained with bootstrap method (Efron & J. Tibshirani 1993) with 500 replications. About 5000 receiver functions recorded in 43 stations were analyzed. In the Figures A.1 and A.2 the distribution of events ordered by ray parameter and back-azimuth are displayed. In figures (A.3 to A.11) the $h - \kappa$ stacks (Zhu & Kanamori 2000) for new stations not included in the previous study are displayed.

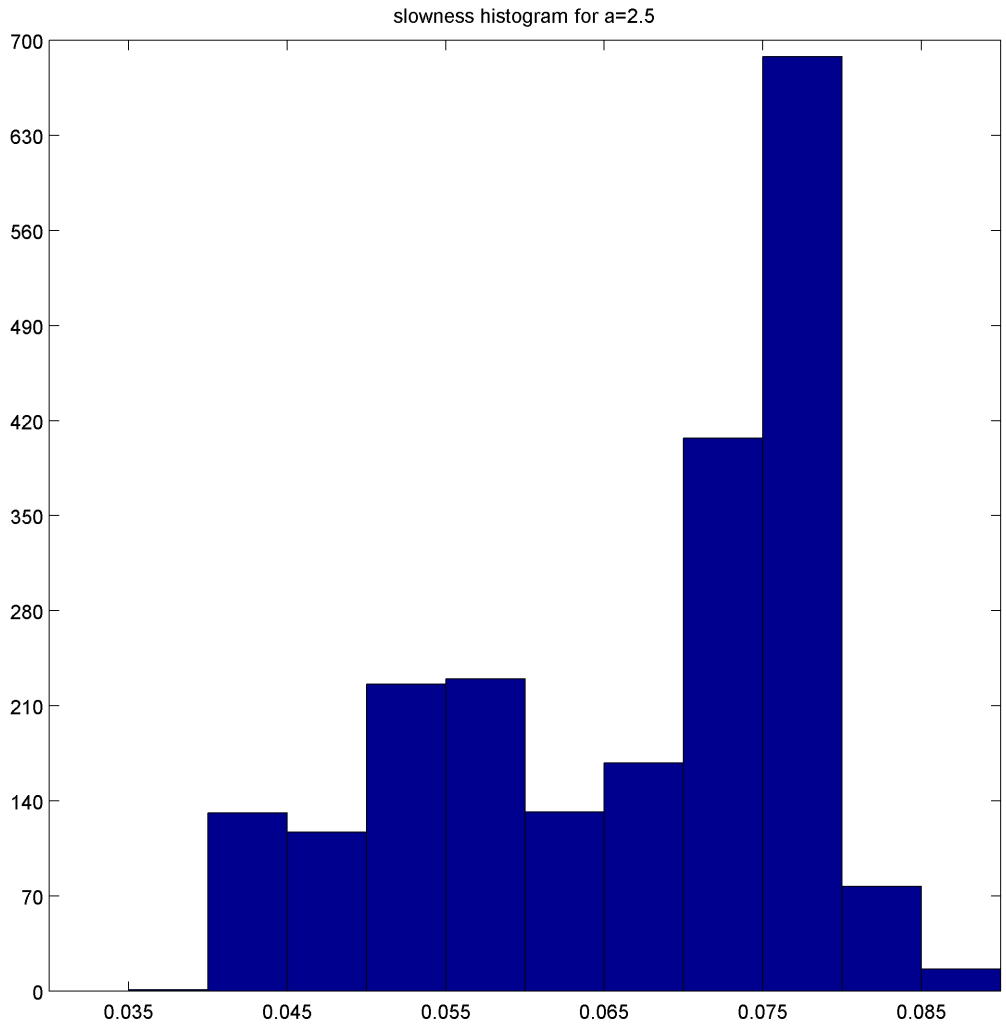

Figure A.1: Events ordered by ray parameter (s/km).

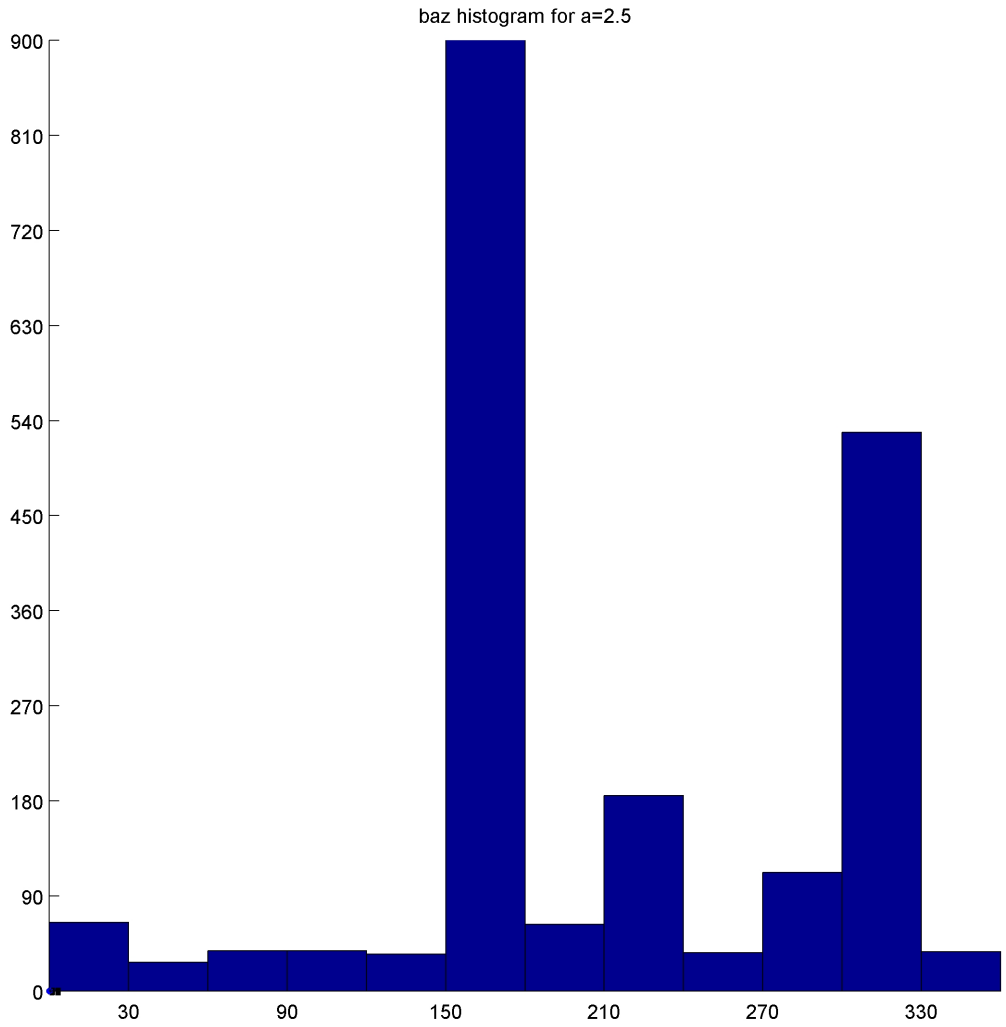

Figure A.2: Events ordered by back-azimuth (degrees).

STATION	H (km)	Uncertainty (km)	Number of RFs.
ANIL	53,5	2,8	101
ARGC	27,6	1,7	57
BBAC	33,0	1,5	65
BOCO	59,5	4,4	19
BRR	49,0	1,9	122
CAP2	36,3	1,9	90
CBOC	36,0	1,2	65
CHI	51,0	1,4	163
COD	37,5	1,2	51
CRJC	37,6	1,2	24
FLO2	37,0	5,1	113
GCUF	56,0	4,1	89
GUY2C	39,3	1,9	84
HEL	56,5	1,9	319
MACC	40,0	2,1	72
MAP	17,24	1,2	25
MARA	45,0	2,4	62
MON	24,5	1,2	85
OCA	45,7	2,1	32
ORTC	41,6	1,2	75
OTAV	49,5	2,3	153
PAL	35,0	2,9	59
PAM	55,0	4,2	87
PCON	49,5	2,4	85
POP2	34,0	2,2	116
PRA	44,0	2,0	187
PTLC	28,0	1,8	85
ROSC	60,0	2,0	153
RREF	42,85	1,1	75
RUS	46,5	2,1	148
SJC	37,15	2,9	127
SMAR	42,4	3,1	92
SPBC	45,7	2,1	75
SOTA	53,0	3,5	125
TAM	41,72	6,4	61
TUM	22,5	2,2	81
URE	41,5	1,4	89
URI	29,5	3,7	111
VIL	31,35	3,2	30
YOT	36,24	4,7	106
ZAR	57,81	2,9	79

Table A.1: Crustal thickness estimations from receiver functions analysis from Poveda et al. (2015) and new stations included

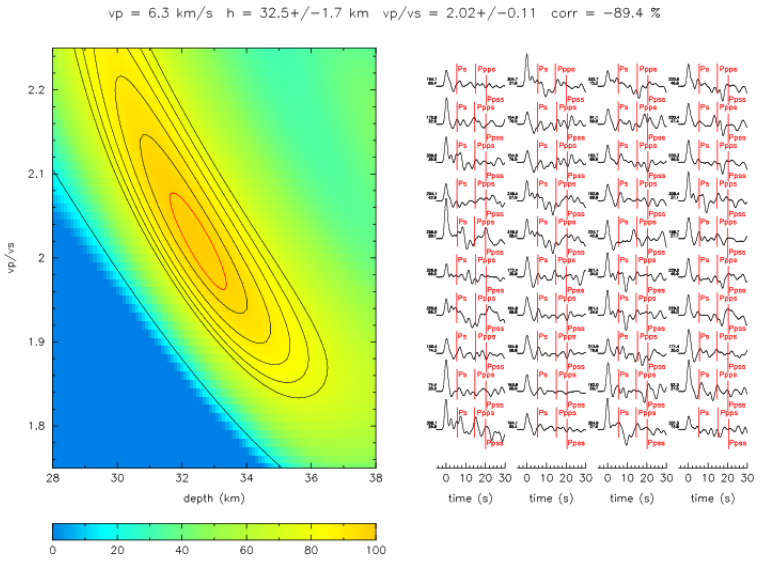

Figure A.3: $h - \kappa$ stack for station BBAC. The V_p, the V_p/V_s and the fit are shown above each panel.

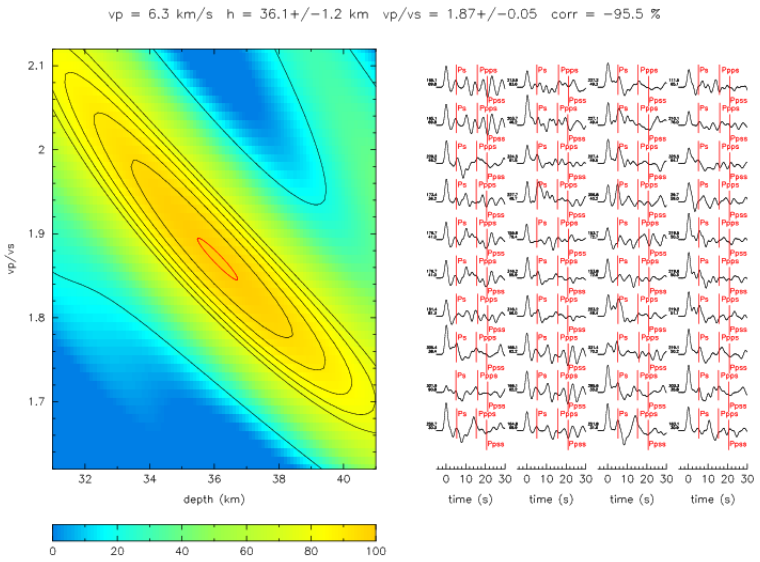

Figure A.4: $h - \kappa$ stack for station CBOC. The V_p, the V_p/V_s and the fit are shown above each panel.

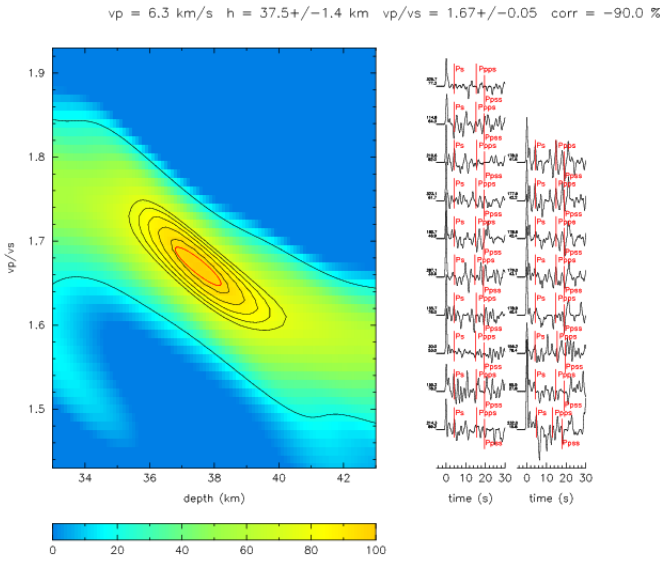

Figure A.5: $h - \kappa$ stack for station CRJC. The V_p, the V_p/V_s and the fit are shown above each panel.

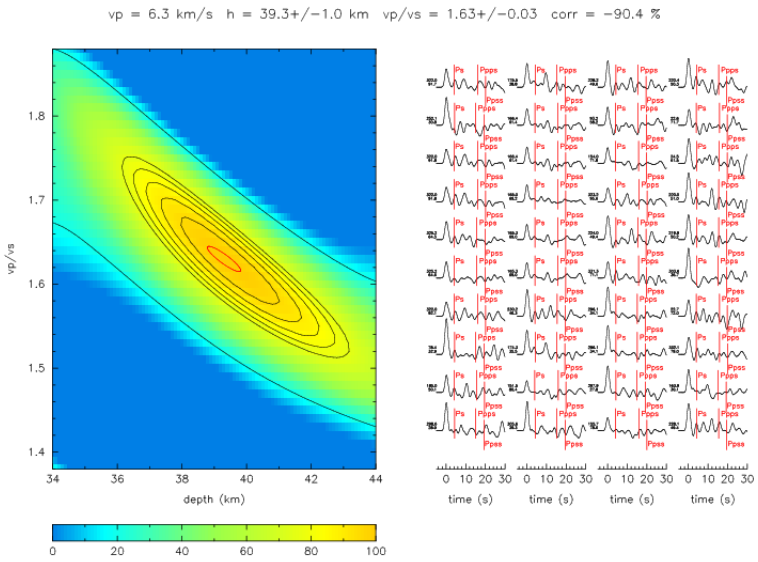

Figure A.6: $h - \kappa$ stack for station GUY2C. The V_p, the V_p/V_s and the fit are shown above each panel.

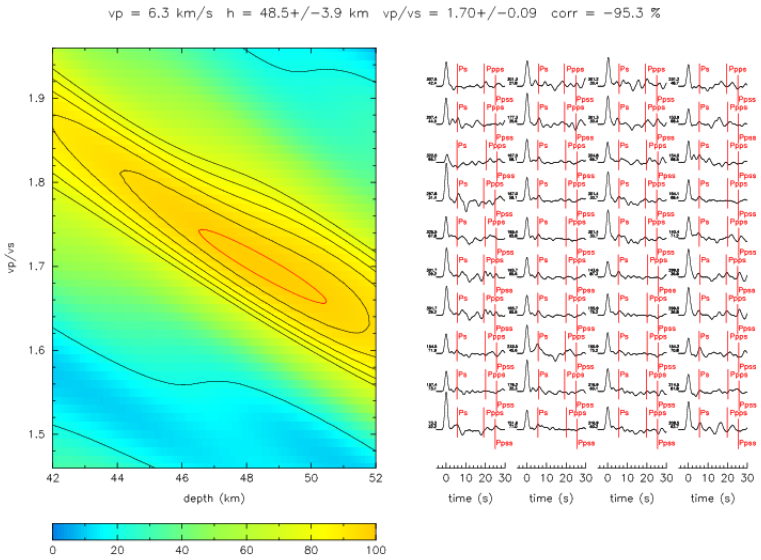

Figure A.7: $h - \kappa$ stack for station MACC. The V_p, the V_p/V_s and the fit are shown above each panel.

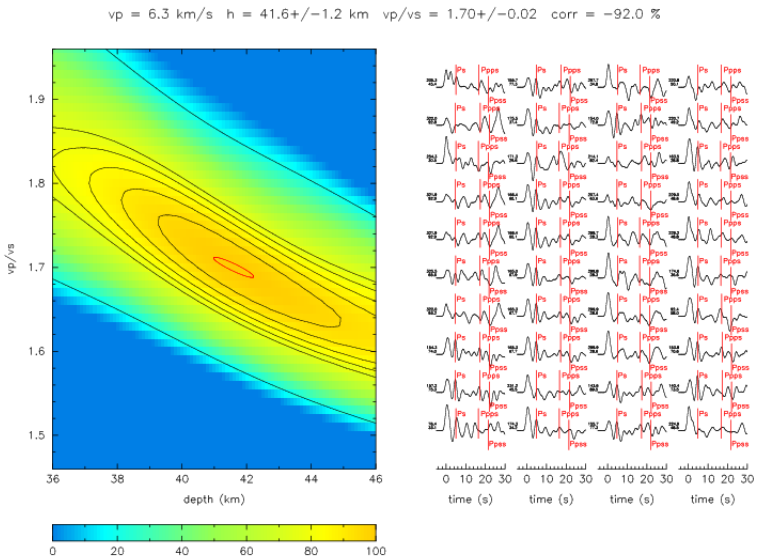

Figure A.8: $h - \kappa$ stack for station NOR. The V_p, the V_p/V_s and the fit are shown above each panel.

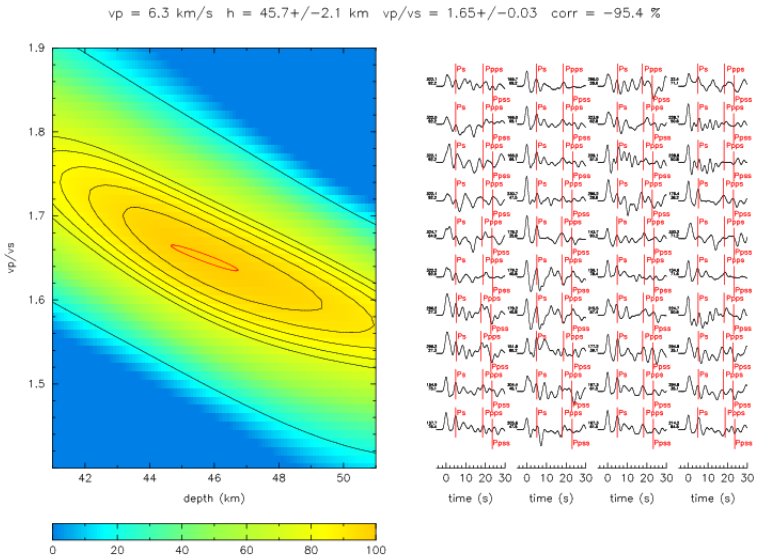

Figure A.9: $h - \kappa$ stack for station SPBC. The V_p, the V_p/V_s and the fit are shown above each panel.

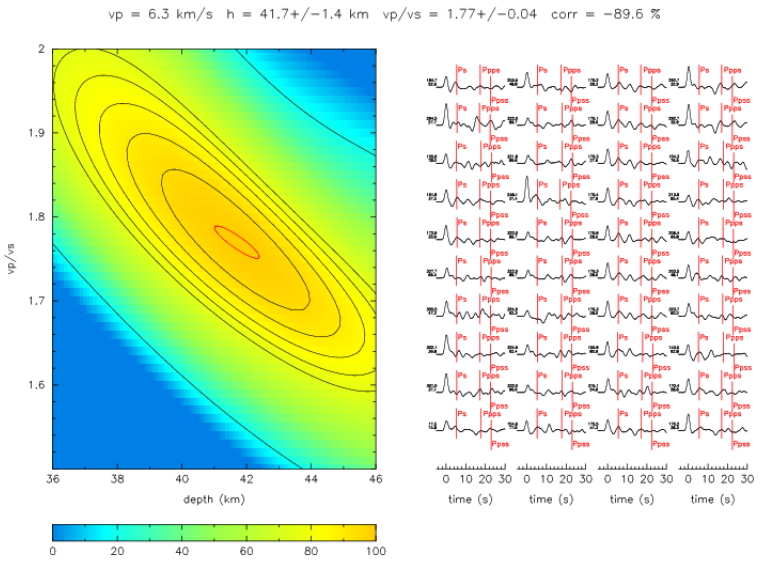

Figure A.10: $h - \kappa$ stack for station URE. The V_p, the V_p/V_s and the fit are shown above each panel.

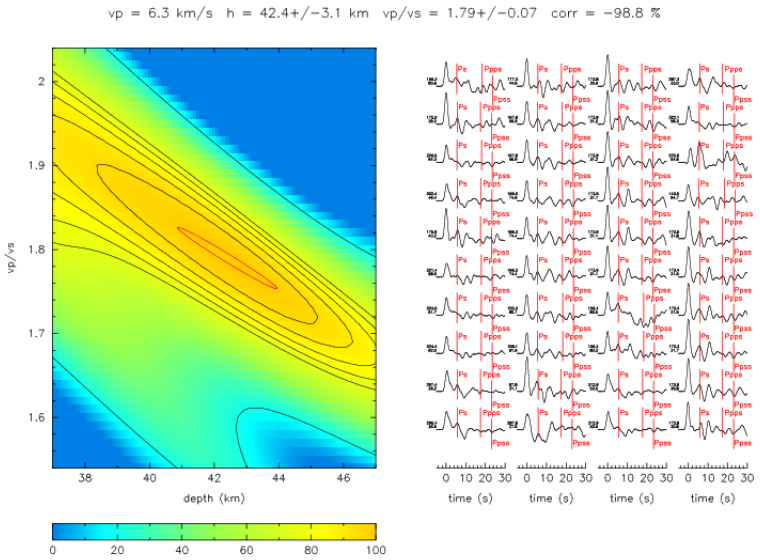

Figure A.11: $h - \kappa$ stack for station SMAR. The V_p, the V_p/V_s and the fit are shown above each panel.